Failure Characterization of Hot Formed Boron Steels with Tailored Mechanical Properties

by

Lukas ten Kortenaar

A thesis

presented to the University of Waterloo

in fulfillment of the

thesis requirement for the degree of

Master of Applied Science

in

Mechanical Engineering

Waterloo, Ontario, Canada, 2016

I hereby declare that I am the sole author of this thesis. This is a true copy of the thesis, including any required final revisions, as accepted by my examiners.

I understand that my thesis may be made electronically available to the public.

ABSTRACT

This thesis presents the results from characterization of the failure behaviour of hot stamped USIBOR® 1500-AS steel sheet with tailored properties. A phenomenological approach is used in which failure strain is characterized as a function of stress state and as-hot stamped condition, based on the results of an extensive experimental campaign. A range of material quench conditions are investigated, resulting in a multitude of material microstructures.

Considering the framework for tailored hot stamping using in die heating to achieve different material responses, six different material quench conditions were considered in this work, ranging from fully martensitic (Vickers microhardness of 485HV) to a mixed ferrite-bainite microstructure (185HV). Four of the material quench conditions investigated were produced using laboratory equipment, while the remainder were obtained from tailored axial crush components that were quenched with die temperatures of 400 and 700 °C.

Miniature shear, butterfly, hole expansion, hole tensile, and hemispherical dome tests were developed for fracture characterization of sheet metal and digital image correlation (DIC) techniques were used extensively in order to obtain fracture strains and strain paths for the different experiments. Notched tensile specimens were also tested, however these specimens were not used for fracture characterization, due to their non-proportional loading paths and indeterminate fracture locations.

Considering fracture strain to be a function of stress state and assuming the material investigated in this work to be isotropic and von Mises yielding, the equivalent strain at fracture and stress triaxiality of each experiment was determined from DIC-measured major and minor strains. Fracture loci were then calibrated for different material quench conditions. The validity of the experimental fracture locus was probed using a number of non-proportional loading

experiments, in which specimens were initially pre-strained in equi-biaxial tension, before being subjected to loading states of simple shear or uniaxial tension. Additionally, work was done to adapt and apply the experimental fracture loci to impact simulations of hot stamped components with tailored properties, requiring development of "model dependent fracture loci".

There was found to be an inverse relationship between material hardness and measured fracture strain, with the fully martensitic material quench condition (485HV) possessing the lowest ductility, while the greatest fracture strains were measured in the samples produced through die quenching at 700 °C (185HV). For the range of material conditions considered, the lowest fracture strains corresponded to a plane strain loading condition, while the fracture strains measured in simple shear were considerably greater. The material quench conditions, ordered in increasing ductility, are as follows (fracture strains for simple shear and plane-strain tension included in parentheses): fully martensitic (0.54, 0.15), intermediate forced air quench (0.68, 0.22), fully bainitic (0.90, 0.36), 400 °C die quench (1.01, 0.38), and 700 °C die quench (1.05, 0.44).

ACKNOWLEDGEMENTS

First and foremost, I would like to thank my supervisor, Professor Michael Worswick for providing the opportunity to contribute to this project while developing my understanding of both hot stamping and fracture characterization. His guidance and support over the past three years has been invaluable.

I would also like to thank Professor Cliff Butcher, without whom this work would have existed in a very different form. His experience with and knowledge of fracture characterization were fundamental in shaping this work. None of the fracture loci presented in this work would have been possible without his involvement.

Thanks to Alexander Bardelcik and Ryan George for their knowledge of hot stamping and wrapping up this project. Thanks also to Jose Imbert Boyd for his expertise with cluster-related issues, as well as the numerous conversations about smoking and fermenting.

The support for this project provided by Honda R&D Americas, Promatek Research Centre, ArcelorMittal, Automotive Partnership Canada, the Natural Science and Engineering Research Council, the Ontario Research Fund, and the Canada Research Chair Secretariat is gratefully acknowledged.

Helping me when I had to get my hands dirty were the ever helpful research technologists: Andy Barber for being there whenever there were 407 or FlexTest issues, Howie Barker for his troubleshooting and machining expertise, Eckhard Budziarek for shearing, grilling, driving, and keeping things on track, Tom Gawel for keeping the lab up and running and providing a place to live, Rich Gordon for sharing his various tools and toys, and Jeff Wemp for cleaning too many cameras and lenses to count. Also helping me when it came to ever-exciting

hardness measurements, co-op students Sam Kim, Chris Thompson, and Ping Zhang. Your help made this aspect of work more manageable.

Ensuring that I had specimens to test, I would like to express my gratitude to the engineering machine shop: Fred Bakker, Charlie Boyle, Jorge Cruz, Rick Forgett, Karl Janzen, Rob Kaptein, Rob Kraemer, Mark Kuntz, and Phil Laycock.

These past three years would not have been possible without the company of all the other grad students: office talks of football, off-road vehicles, and masterful shearing with Armin Abedini, late night hockey with Jeff Barker, squash and other things with Khaled Boqaileh, dance floor destruction with Norman Fong, grilling and smoking sessions spearheaded by Chris Kohar, road pie and walks around campus with Kaab Omer, and driving with Rohit Verma. Shout outs to Sante DiCecco, Nikky Pathak, Yonathan Prajogo, Taamjeed Rahmaan, Dilaver Singh, and Amir Zhumagulov. Thanks also to Huey Tran and Kayleigh Wilson for their role in making my near-weekly pad Thai.

Thanks to my parents and siblings for their support and encouragement. Also, special thanks to Brittany Codrington for putting up with the seemingly never-ending thesis and beard.

Finally, thanks to everybody who was involved in adventures in and around Dearborn, Luleå, Columbus, Evanston, Toronto, and Columbia. You know who you are.

Dedicated to the Defenders of the Steel

TABLE OF CONTENTS

LIST OF FIGURES

LIST OF TABLES

1 INTRODUCTION

1.1 Motivation and Objective

As automotive manufacturers continue to develop more fuel efficient vehicles, extensive efforts have been undertaken to reduce vehicle mass through the development and application of lighter weight materials. However, due to occupant safety requirements, automotive manufacturers must produce lighter weight vehicles without sacrificing structural integrity and crash worthiness. A means of providing superior occupant safety while simultaneously decreasing chassis weight is through the use of materials with enhanced specific strength, such as ultra-high strength steel (UHSS). Boron steel sheets can be used to produce components with an ultimate tensile strength of 1500 MPa through the Hot Forming Die Quenching (HFDQ) process, also known as hot stamping or press hardening. This process entails pre-heating a blank to temperatures in excess of the austenizing temperature in order to induce a phase transformation from austenite to martensite during forming in a cooled die. A more recent advancement in the HFDQ process features the use of dies with discrete, temperature-controlled sections, in order to induce different cooling rates, thereby resulting in the formation of softer, more ductile phases such as bainite or ferrite, in order to allow for additional deformation compared to a fully martensitic part.

In addition, as material modeling developments allow manufacturers to create increasingly sophisticated computer simulations, there is growing attention being paid to how material failure can be modeled with the goal of further improving simulation accuracy. Modeling of material failure is of particular interest when considering parts with tailored properties produced in the hot stamping process, since the various microstructures present possess drastically disparate

ductility. Therefore, the principal objective of this work is to develop a failure model, which can be applied to models featuring hot stamped parts and accurately predict fracture.

1.2 The Hot Stamping Process

First developed in Sweden as a method of manufacturing stamped components with fully martensitic microstructure [1], hot stamping has recently risen to prominence as an innovative manufacturing technique that can be used to reduce the mass of structural components. Currently, the hot stamping process can be characterized as direct or indirect, where the direct process involves heating a blank in a furnace above the austenizing temperature and then quenching the part as it is formed, while the indirect process begins with a cold formed part which is then heated and subsequently quenched during a calibration operation in order to achieve the desired final geometry. Heating of the blank results in increased ductility and decreased flow stress, improving formability [2]. Steel grades used for hot stamping include 22 MnB5, 27MnCrB5, and 37MnB4, with 22MnB5 being the most commonly used grade. Boron steels are used since boron has a large influence on hardenability and also suppresses the transformation into softer microstructures, such as ferrite, due to precipitation of boron carbide at grain boundaries and boron segregation [3]. Manganese is a substitutional solid solution element and is required for hardenability but has only a slight influence on post-quenching strength. In this work, only the direct hot stamping process is considered.

The direct hot stamping process generally consists of heating the blank above the austenizing temperature (over 900 °C) for at least 5 minutes. The austenized blank is quickly transferred from the furnace to the forming press and is then stamped. A cooling rate in excess of 27 °C/s will yield a diffusionless martensitic phase transformation beginning at 425 °C, resulting in a final part with strength in excess of 1500 [MPa] [4].

1.2.1 Hot Stamping with Tailored Properties

While the hot stamping process was originally devised as a material forming process that could produce parts with outstanding strength, a more recent area of research has the use of hot stamping to form parts with tailored microstructures. Some of the methods used to achieve various microstructures in a single component include tailor-welded blanks, tool tempering, and blank tempering. Tailor-welded blanks typically consist of two different materials, a heat-treatable steel and a non-heat-treatable steel, welded together to form a stamping blank for a single part. During the HFDQ process, the heat-treatable section undergoes a phase transformation, resulting in a martensitic microstructure, while the microstructure of the non-heat-treatable section is less affected. Tool-tempering utilizes dies designed to induce varying cooling rates in order to yield different microstructures, such as through the use of temperature-controlled die sections. By heating or cooling different sections of the dies, a single part can be created with softer or harder sections, providing control over the local mechanical properties of the final part. Finally, blank-tempering is a means of producing hot stamped components with tailored properties by controlling the temperature of different regions of a single blank. By only heating certain regions of the blank in excess of the austenizing temperature, only these regions will undergo a phase transformation to a fully martensitic microstructure when formed in a cooled die, while the sections that were not heated to this temperature will retain the original microstructure.

Since the strength and ductility of the final part depend on the cooling rate during the quenching process, different microstructures can be achieved through the means described above. In order to achieve a crash response with improved energy absorption, in comparison to a fully martensitic hot stamped part, George *et al.* [5] demonstrated that control of die temperature

can be used to create parts that feature softer sections, consisting of microstructures containing bainite and ferrite.

1.2.2 Modeling of Hot Stamped Material

Currently, various models have been developed to predict the stress-strain response of USIBOR® 1500-AS, either as a function of cooling rate [6] or as a function of microhardness [7]. Generally speaking, it has been considered adequate to model the stress-strain response of this material using isotropic constitutive models [8], taking into consideration the effect of microstructure [9]. However, work done to predict the failure response of this material has been fairly limited thus far, with only a limited number of microstructures considered. In order to improve modeling capabilities of hot stamped parts with tailored properties, this work aims to develop a fracture model for USIBOR® 1500-AS, which considers a range of material quench conditions.

1.3 Failure Characterization

In addition to characterizing material plasticity, there are also benefits in being able to accurately predict how a material ultimately fails. Numerous approaches for doing so exist, with varying degrees of physical basis. Specific physical and phenomenological approaches are discussed in more detail in subsequent sections.

From a broader perspective, the main motivation for the characterization of failure for a range of microstructures present in hot stamped parts with tailored properties is to enhance the accuracy of finite element simulations of the crash response of vehicles that feature tailored hot stamped components. As a result of the tailored hot stamping process, parts are produced which feature microstructures that possess disparate levels of ductility. In order to confidently develop

and optimize the impact behaviour of new hot stamped components with tailored properties, failure must be accurately characterized.

1.3.1 Failure of (Ultra high strength) Steels

The current literature on the topic of failure of ultra-high strength steels is rather limited. Eller *et al*. [9] have looked at failure of USIBOR® 1500-AS for the purpose of calibrating failure model to be used in automotive crash simulations. Their work looked at characterizing material failure as a function of stress state for three material conditions (quenched in cooled tooling, slow cooled in heated tooling, and as-received) using five different experiments to vary stress state. Similar work looking at the influence of microhardness on equivalent failure strain for two notched tensile specimens has been completed by Östlund [10]. This work investigated four conditions of material that were obtained through quenching in temperature-controlled tooling. These material conditions included the following compositions: (i) fully martensitic; (ii) 97% lower bainite; with a small amount of austenite and martensite; (iii) 75% upper bainite with a mixture of irregular ferrite, martensite, lower bainite, and austenite; and, (iv) 95% irregular ferrite with small amounts of upper bainite, martensite, austenite, and polygonal ferrite.

Looking at fully hardened MBW1500 + AS, a boron steel produced by ThyssenKrup, Mohr and Ebnoether characterized fracture under plane stress conditions [8]. Initial dogbone tensile tests indicated that the material could be considered isotropic. In order to understand fracture behaviour, hemispherical dome and butterfly specimens were tested. The butterfly specimen features a reduced-thickness central gage section and was tested in various orientations to encompass stress states corresponding to pure shear, combined shear-tension, and plane-strain tension. For validation, experiments using three different notched tensile specimen geometries were carried out. Unlike the butterfly tests used to calibrate the fracture locus, the notched tensile

specimens produced non-constant stress states, which evolved over time, making them more suitable for model validation rather than calibration.

Outside of these studies, there is a dearth of literature on the topic of failure characterization of HFDQ boron steel. However, much more common in the literature is research on the failure of various high strength steels (HSS), advanced high strength steels (AHSS), transformation induced plasticity (TRIP) steels, and dual phase (DP) steels. In characterizing fracture of TRIP780 steel as a function of stress state, Dunand utilized a tensile test specimen with a central hole, notched tensile tests, and a hemispherical punch dome test [11]. These tests were used to obtain uniaxial tensile, intermediate uniaxial-biaxial, and nearly equi-biaxial tensile failure strains, respectively. While the stress state was fairly constant for both the central hole and hemispherical punch dome tests, the notched tensile specimens yielded evolving stress states as deformation localized. Further work by Dunand and Mohr on the failure characterization of TRIP780 steel led to the development of a butterfly specimen, an optimized geometry with a gauge section of reduced thickness (shown in Figure 1), in order to assess fracture for combined shear-tension stress states [12].

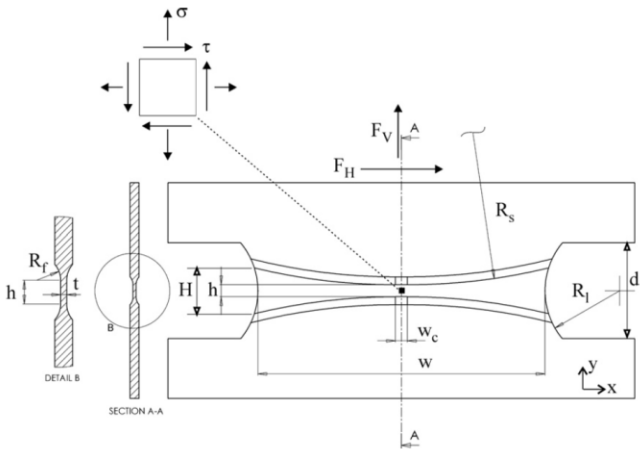

Figure 1: Geometry of butterfly specimen proposed by Dunand and Mohr [12]

The butterfly test makes it possible to carry out fracture experiments on a single apparatus, with one specimen geometry, however it has complexities when compared to a simple tensile or hemispherical punch dome test, namely the machining of test specimens, apparatus calibration, and modelling of experiments. In characterizing fracture of DP780 steel, considering both stress state and strain rate, Walters utilized butterfly specimens and Hasek specimens (hemispherical punch dome tests with varying specimen geometry) in order to develop a fracture locus [13]. In that work, it was determined that, when considering strain-rate effects on failure, the Hasek specimens are superior to the butterfly experiments, since the complex geometry of the butterfly specimen was found to diffract stress waves passing through the specimen, preventing equilibrium from ever being achieved at high rates of strain. Björklund *et al*. [14] used in-plane shear tests, plane strain tests, and Nakajima tests to characterize failure of Docol 600 DP (dual phase) and Docol 1200M (martensitic) steels. In order to characterize failure of DP980 steel, Lou and Huh conducted tensile tests, utilizing a multitude of geometries to address a range of stress states [15]. Specimen geometries include dog-bone, central hole, plane strain, and in-plane shear, as well as 3 different notched tensile and 3 different shear geometries, shown in Figure 2. As with the similar experiments in [8] and [11], most of these specimen geometries produced an evolving stress state.

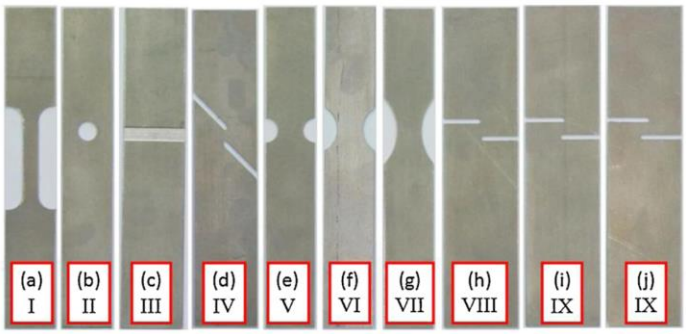

Figure 2: Specimens used by Lou & Huh for fracture characterization of DP980 AHSS [15]

1.3.2 Damage Modeling

Mechanical damage models can be broadly grouped as belonging to one of two categories: either micromechanical damage models or continuum damage models. Micromechanical damage models are physically based, treating material as being comprised of inhomogeneous cells and attempting to model the nucleation, growth, and coalescence of voids and microcracks, which lead to material softening and eventually fracture. Such models typically contain a yield function which triggers a loss of load bearing ability upon reaching a critical value. One of the most widely used micromechanical damage models is the Gurson model [16], the yield function of which is:

$$\Phi = \frac{\sigma_{eq}^2}{\bar{\sigma}^2} + 2f\cosh\left(\frac{3\sigma_m}{2\bar{\sigma}^2}\right) - [1 + f^2] = 0$$

where $\bar{\sigma}$ is the undamaged material's yield stress, f is the void volume fraction, σ_{eq} and σ_m are the macroscopic equivalent (von Mises) stress and mean stress, respectively. Damage evolution is then given as:

$$\Delta f = \Delta f_{growth} + \Delta f_{nucleation}$$

where Δf is the incremental void volume fraction, and Δf_{growth} and $\Delta f_{nucleation}$ are the incremental void volume changes due to void growth and void nucleation, respectively.

While micromechanical models account for the physical phenomena that occur in a material [17] [18], due to their complexity, they require considerable computing resources, making them unsuitable for application to automotive crashworthiness simulations, which involve very large-scale computations.

Approaches more common to continuum mechanics models consider the macroscopic response of the material, and are often calibrated in a phenomenological manner, rather than

attempting to model the phenomena at play at a microstructural level, and calculate damage separately from material plasticity.

In its simplest form, modeling material failure has been achieved using a critical level of equivalent plastic strain which corresponds to that at material failure, as suggested by Huber:

$$\bar{\varepsilon} = \bar{\varepsilon}_f$$

where $\bar{\varepsilon}$ is equivalent plastic strain and $\bar{\varepsilon}_f$ is equivalent plastic strain at failure. While this criterion for material failure is relatively simple, in theory requiring only a single experiment to calibrate, this approach assumes that failure strain is stress state independent.

One approach of incorporating loading state (typically defined as stress ratio or strain ratio) into modeling of material failure is to extend the widely used forming limit diagram (FLD) to fracture, yielding a fracture forming limit diagram (FFLD). Like the FLD used frequently in metal forming to identify the necking limit of material for a range of strain paths, the FFLD plots major and minor strains. Calibration of this fracture criterion is fairly rudimentary, using experiments which induce uniaxial tension and equibiaxial tension, given by:

$$\varepsilon_{1f} + \varepsilon_{2f} = -\varepsilon_{3f} = C$$

A drawback of using the FFLD to predict fracture is the fact that the majority of FFLDs are determined using proportional loading methods and don't make allowances for cases where non-proportional loading occurs. Furthermore, as FFLDs have largely been developed as an extension of FLDs, the range of stress states that such a failure criterion considers are somewhat limited.

A commonly adopted continuum model of fracture is the Johnson and Cook model to predict fracture strain [19], which also features allowances for strain rate and temperature:

$$\varepsilon_f(\eta) = (D_1 + D_2 e^{-D_3\eta})\left[1 + D_4 \ln\left(\dot{\varepsilon}_p \Big/ \dot{\varepsilon}_0\right)\right]\left[1 + D_5 \frac{T - T_0}{T_m - T_0}\right]$$

where ε_f is the fracture strain, D_1, D_2, D_3, D_4, D_5 are material constants, η is stress triaxiality (the ratio of average stress over equivalent stress), T, T_0, T_m are the temperature, room temperature, and melting temperature, respectively, and $\dot{\varepsilon}_p$ and $\dot{\varepsilon}_0$ are the equivalent plastic and reference strain rates, respectively.

Continuum damage mechanics has produced models which feature a coupling of damage with stress-strain response, in order to account for the loss of load bearing capacity that results from the cross-sectional decreasing as a result of voids and cracks. For instance, as a phenomenological means of capturing the material softening that results from void nucleation, growth, and coalescence, Børvik *et al*. [20] developed an extension to the Johnson-Cook continuum model. The model proposed by Johnson and Cook expressed material flow stress as a function of strain, strain rate, and temperature:

$$\bar{\sigma} = [A + B\varepsilon^n][1 + C \ln \dot{\varepsilon}^*][1 - T^{*m}]$$

where ε is equivalent plastic strain, A, B, n, C, and m are material constants, $\dot{\varepsilon}^* = {\dot{\varepsilon}}/{\dot{\varepsilon}_o}$ is dimensionless plastic strain rate for $\dot{\varepsilon}_o = 1.0\ s^{-1}$, and T^* is homologous temperature [21]. Børvik *et al*. introduced a term for damage-induced softening:

$$\bar{\sigma} = (1 - \beta D)[A + B\varepsilon^n][1 + C \ln \dot{\varepsilon}^*][1 - T^{*m}]$$

In this model D is the damage variable, ranging between 0 (undamaged) and 1 (broken), and β is a coupling parameter, coupling the flow stress definition with damage when set equal to 1.

However, when it comes to modeling multi-stage processes, difficulties can arise if a single damage model is used for all steps. For instance, some of the previously outlined damage models only considered the strain at fracture for predicting material failure. In such cases, if the strain path changes, accurate failure prediction becomes difficult.

Considering the modeling of automotive crash simulations, such simulations were historically conducted on vehicle models without accounting for the deformation that various components underwent in their respective forming processes. However, given the prevalence of forming processes in the production of automotive components, it is thought that simulations would be more accurate if the stresses and strains that result from forming are accounted for.

1.3.3 Generalized Incremental Stress State dependent damage MOdel (GISSMO)

LS-DYNA includes a continuum damage model, used to model material failure as a function of stress state. This model, termed the "**G**eneralized **I**ncremental **S**tress **S**tate dependent damage **MO**del" (GISSMO), was recently developed by Daimler and DYNAmore for modeling the failure of ductile materials [22] [23]. GISSMO is phenomenological in nature and is thus calibrated using experimental results. The primary motivation for the GISSMO model has arisen from improving the accuracy of numerical simulations of multistage processes. Although some other damage models define damage as a tensor quantity [24] [25], the GISSMO model uses a scalar parameter to define damage in the following form:

$$D = \left(\frac{\varepsilon_p}{\varepsilon_f}\right)^n$$

where ε_p is the equivalent plastic strain and ε_f is the equivalent plastic strain at failure. Since equivalent plastic strain at failure is dependent on the loading condition, this relation is only applicable for proportional loading, that is, the ratio of stress components remains constant. Therefore, in order to determine the damage that results from a process which features varying stress states, and is thus path-dependent, an incremental measure of damage is utilized.

The model for incremental damage at a material point is given below:

$$dD = \frac{n}{\varepsilon_f(\eta, \xi)} D^{\frac{n-1}{n}} d\varepsilon_p$$

where dD is the incremental damage, n is an exponent used to introduce non-linearity, D is the current damage, $d\varepsilon_p$ is the incremental plastic strain, and ε_f is the plastic strain at failure, which has been determined to be a function of stress triaxiality and Lode angle.

To determine the current damage, the above term is integrated:

$$D = \int \frac{n}{\varepsilon_f(\eta, \xi)} D^{\frac{n-1}{n}} d\varepsilon_p$$

Once the value of the current damage reaches unity, failure is considered to have occurred. In the context of finite element simulation, an element is deleted once its damage reaches unity.

In addition to providing damage accumulation, the GISSMO model can also be used to consider effects of the onset of localization (necking) and material instability [26]. To do so, an incremental measure of forming intensity is used, which has a form similar to that of the damage increment and is given below:

$$dF_r = \frac{n}{\varepsilon_{p,l}(\eta)} F_r^{\frac{n-1}{n}} d\varepsilon_p$$

where dF_r is the incremental forming intensity, n is an exponent used to introduce non-linearity, F_r is the forming intensity, $d\varepsilon_p$ is the incremental plastic strain, and $\varepsilon_{p,l}$ is the plastic strain at the onset of instability, for the current loading state (a function of stress triaxiality). Similar to the damage increment, in order to obtain the current forming intensity, the above term is integrated and is considered to have reached a critical point upon attaining a value of unity. It should be noted that, unlike the damage accumulation of the GISSMO model, the parameters used for determining the onset of material instability can be difficult to obtain experimentally, and are instead typically determined through a reverse engineering of multi-stage deformation processes.

Prior to the current forming intensity reaching a value of unity, the stress operative within a material is determined from the constitutive model. However, as soon as the forming intensity takes a value of unity, the critical damage level is reached and the calculation of material stresses becomes coupled to the damage model. This coupling can be expressed using the concept of effective stress in the form of the following two inequalities:

$$\sigma^* = \sigma \; if \; D \leq D_{crit}$$

$$\sigma^* = \sigma\left(1 - \left(\frac{D - D_{crit}}{1 - D_{crit}}\right)^m\right) \text{ if } D > D_{crit}$$

where m is termed a "fading exponent" that can be defined depending on element size and which governs the rate of stress reduction (fading) due to material softening. The concept of effective stress is used because the damage variable in the GISSMO damage model has no physical meaning [27].

The GISSMO model allows a single damage model to be used in simulation of both forming as well as impact, simulations which have different requirements with regard to modeling. As such, the mesh size used in crashworthiness simulations is appreciably larger than that used in forming simulations. Since the parameters in the GISSMO model are usually initially calibrated to numerical simulations of the experiments used, a fine mesh is initially used. However, to be applicable to crashworthiness simulations, this model must also be accurate when a larger mesh size is used. As a means of regularizing the energy dissipated during crack development, the effective stress exponent m can be defined as a function of element size, varying the stress reduction that occurs during the fadeout of elements based on their size [22].

To calibrate GISSMO for use in numerical simulations, the minimum required information is plastic strain at fracture as a function of triaxiality, a typical plot of which is shown in Figure 3.

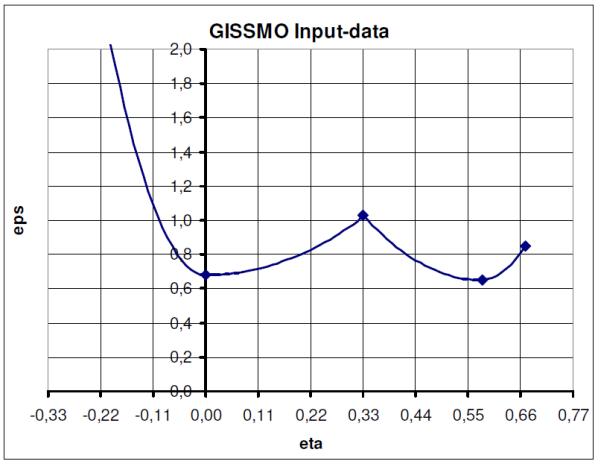

Figure 3: Plot of triaxiality and plastic strain at fracture [28]

Such input data is applicable for plane stress loading cases ($\sigma_3 = 0$), where there is a direct relationship between stress triaxiality (η) and Lode angle parameter (ξ) [29]:

$$\xi = -\frac{27}{2}\eta\left(\eta^2 - \frac{1}{3}\right)$$

However, in loading cases which cannot be simplified to the plane stress state, it has been shown that there is an influence of the Lode angle on the plastic strain at fracture. Therefore, as input data, a fracture surface for the material is required, a typical example of which is shown in Figure 4.

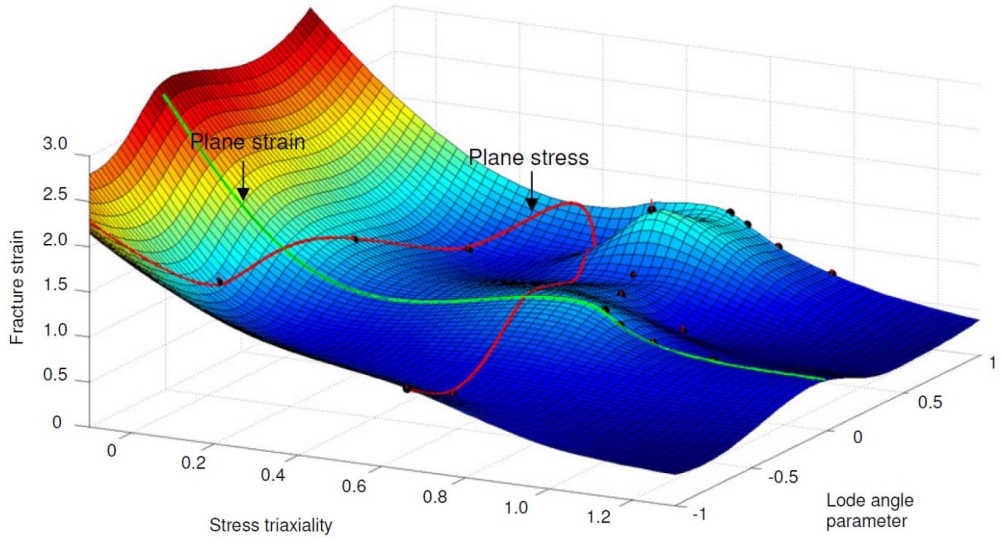

Figure 4: Example Fracture Surface [29]

In order to interpolate a fracture surface using results obtained from fracture characterization experiments, numerous fracture loci have been presented in literature. As an example, Bai and Wierzbicki developed the following fracture locus [30]:

$$\hat{\varepsilon}_f(\eta,\xi) = \left[\frac{1}{2}(C_1 e^{-C_2\eta} + C_5 e^{-C_6\eta}) - C_3 e^{-C_4\eta}\right]\xi^2 + \frac{1}{2}(C_1 e^{-C_2\eta} - C_5 e^{-C_6\eta})\xi + C_3 e^{-C_4\eta}$$

in which $C_1 - C_6$ are material constants. Similarly, the modified Mohr-Coulomb fracture locus is also somewhat common in literature, being described in the work of Wierzbicki [31] [32], as well as that of Mohr [12]. The equation for this fracture locus is given below:

$$\hat{\varepsilon}_f(\eta,\xi) = \left\{\frac{C_1}{C_2}\left[C_3 + \frac{\sqrt{3}}{2-\sqrt{3}}(1-C_3)\left(\sec\left(\frac{\xi\pi}{6}\right) - 1\right)\right]\right.$$

$$\left.\times\left[\sqrt{\frac{1+C_4^2}{3}}\cos\left(\frac{\xi\pi}{6}\right) + C_4\left(\eta + \frac{1}{3}\sin\left(\frac{\xi\pi}{6}\right)\right)\right]\right\}^{\frac{-1}{C_5}}$$

where $C_1 - C_5$ are material constants.

Since the plastic strain at fracture has been shown to be dependent on the loading case, a means of uniquely describing the load case is required.

Considering the stress tensor:

$$\sigma_{ij} = \begin{bmatrix} \sigma_{11} & \sigma_{12} & \sigma_{13} \\ \sigma_{21} & \sigma_{22} & \sigma_{23} \\ \sigma_{31} & \sigma_{32} & \sigma_{33} \end{bmatrix}$$

The stress state can be uniquely described through the 3 principal stresses (note that this assumes material anisotropy), which are obtained when the stresses on the principal planes are considered. Such that:

$$\sigma_{ij} = \begin{bmatrix} \sigma_1 & 0 & 0 \\ 0 & \sigma_2 & 0 \\ 0 & 0 & \sigma_3 \end{bmatrix}$$

In the literature, it has been proposed to represent the principal stresses as a vector in the Haigh-Westgaard space, a Cartesian coordinate system with axes in the directions of the principal stresses. Such a depiction of the stress state is shown in Figure 5.

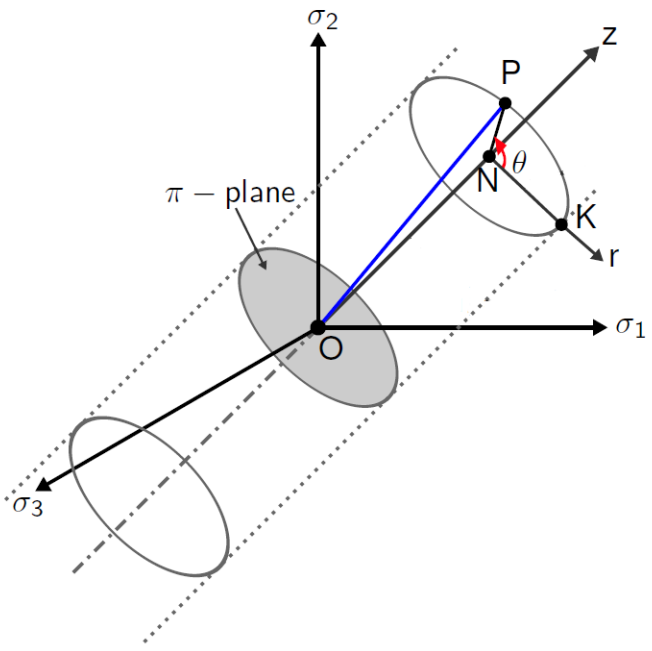

Figure 5: Principal stress vector in Haigh-Westergaard space [33]

Further, a cylindrical coordinate system can be represented in this space, as shown in Figure 5. This coordinate system is described in terms of (r, θ, z), or more clearly, $(\sigma_{eq}, \theta, \sigma_m)$ where z is axis of hydrostatic stress (σ_m) and σ_{eq} is the equivalent (von Mises) stress.

Evidently, the stress state can be completely described by the vector summation of $\overrightarrow{ON}$, the component of the principal stress vector along the hydrostatic axis, and $\overrightarrow{NP}$, a vector on the deviatoric plane, defined by $r \,\&\, \theta$. Historically, the stress invariants I_1, J_2, and J_3, have been utilized due to their physical meanings pertaining to mean stress, shear stress magnitude, and shear stress direction, respectively.

Considering the first stress invariant, and the second and third deviatoric stress invariants, the equivalent stress, mean stress and Lode angle (θ) can be defined [29]:

$$\sigma_m = \frac{1}{3}(\sigma_1 + \sigma_2 + \sigma_3) = \frac{1}{3} I_1$$

$$\sigma_{eq} = \frac{1}{\sqrt{2}} \sqrt{(\sigma_1 - \sigma_2)^2 + (\sigma_1 - \sigma_3)^2 + (\sigma_2 - \sigma_3)^2} = \sqrt{3 J_2}$$

$$\theta = \frac{1}{3} \cos^{-1}\left(\frac{3\sqrt{3} J_3}{2 {J_2}^{3/2}}\right)$$

While these three terms can fully define a material stress state, it is conventional to use dimensionless parameters based on these terms, namely, the stress triaxiality and Lode angle parameter, η and ξ, respectively. Where:

$$\eta = \frac{\sigma_m}{\sigma_{eq}} = \frac{\frac{1}{3} I_1}{\sqrt{3 J_2}}$$

$$\xi = \cos(3\theta) = \frac{27}{2} \frac{J_3}{{\sigma_{eq}}^3} = \frac{3\sqrt{3}}{2} \frac{J_3}{{J_2}^{3/2}}$$

The tests used to calibrate the GISSMO model to a specific material depend somewhat on the characteristics of the material. Since there is no consideration for material anisotropy in the GISSMO model, it has been most commonly used in modelling steels which are assumed not to exhibit material anisotropy.

In summary, the current state of phenomenological fracture characterization involves utilization of multiple tests in order to assess fracture strain across a range of stress states. However, there is only limited work investigating fracture characterization of hot stamped steels with tailored properties. The goal of this work is to characterize fracture of hot stamped steel quenched to various microstructural conditions in order to improve the accuracy of crash simulations of vehicles that feature tailored hot stamped components. Considering the previous work presented above, it is evident a variety of test specimens are required, investigating a multitude of stress states. The experimental program used to achieve this goal includes butterfly, mini shear, hole expansion, notched- and hole-tensile, Nakajima-type dog bone, and equi-biaxial specimens. The experimental testing program is discussed in further detail in Chapter 2. The results obtained from the various experiments are presented in Chapters 3 and 4. Chapter 5 focuses on calibration of fracture loci, while Chapter 6 is a brief discussion of a validation approach. Application of fracture loci to impact simulations of hot stamped components is the focus of Chapter 7. Conclusions and recommendations are summarized in Chapter 8.

2 EQUIPMENT AND EXPERIMENTAL TESTING PROGRAM

2.1 Material

The material considered in this research is USIBOR® 1500-AS, which is a boron steel produced by ArcelorMittal. For direct hot-stamping processes, this steel features an aluminum silicon coating that transforms to aluminum-iron-silicon intermetallic layers during heating in the furnace, thereby preventing the formation of scale and inhibiting oxidation [4]. The chemical composition is given in Table 1.

Table 1: Composition of USIBOR® 1500-AS [4]

Element	Composition (weight %)
Carbon (C)	0.22
Manganese (Mn)	1.23
Phosphorus (P)	0.008
Sulfur (S)	0.001
Silicon (Si)	0.25
Copper (Cu)	0.03
Nickel (Ni)	0.02
Molybdenum (Mo)	0.02
Chromium (Cr)	0.2
Columbium (Cb)	0.008
Vanadium (V)	0.008
Aluminum (Al)	0.03
Tin (Sn)	0.01
Titanium (Ti)	0.037
Nitrogen (N)	0.044
Boron (B)	0.004
Iron (Fe)	Remaining

All of the material that was quenched specifically for the work presented in this thesis had a nominal thickness of 1.2 mm. As the work of Bardelcik conducted extensive tensile testing while assuming USIBOR® 1500-AS to be isotropic [7], this same assumption was adopted in the current work. It should be noted, some tensile tests were later conducted outside of this thesis, in order to assess the validity of this assumption. Using ASTM E8 tensile specimens machined in the rolling and transverse directions of the material, for both fully bainitic and fully martensitic

quench conditions, R-values of approximately 1.1 were measured. In addition, 2 further microstructures investigated were after the majority of the experimental work had been completed. These two material conditions were produced through in-die heating of hot stamped axial crush rails and the material used for these microstructures had a nominal thickness of 1.8 mm.

In its as-received state, this material has a ferritic-pearlitic microstructure. The CCT for USIBOR® 1500-AS is shown in Figure 6. The cooling rates obtained for the quenching of the material with a sheet thickness of 1.2 mm are overlaid.

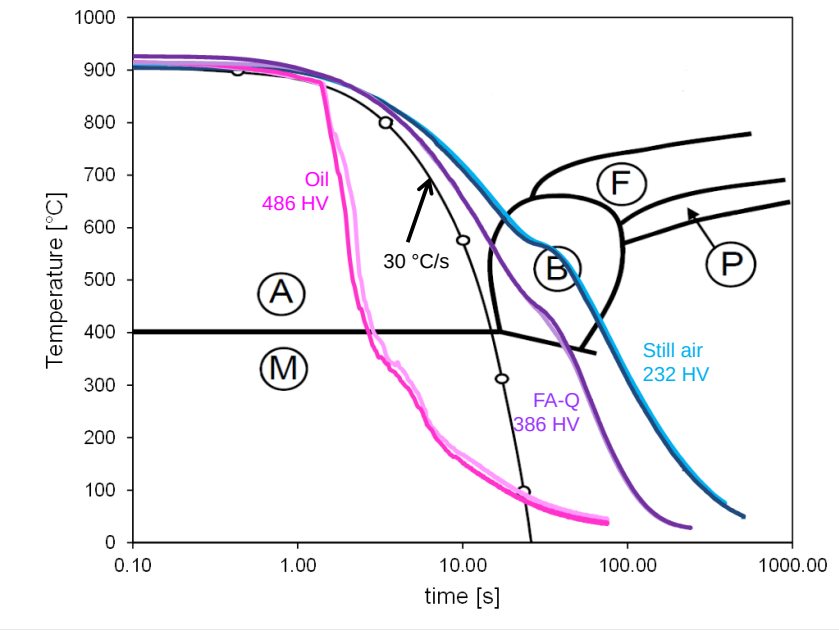

Figure 6: CCT for USIBOR® 1500-AS adapted from Bardelcik [34]. Three quench conditions overlaid on the CCT correspond to the fully martensitic, intermediate forced air quench, and fully bainitic, denoted by magenta, purple, and blue. The critical cooling rate of 30 °C/s to obtain a fully martensitic microstructure is also shown.

To achieve a fully martensitic microstructure in a part using the HFDQ process, a cooling rate of 30 °C/s or greater is necessary. Slower cooling rates can be utilized in the HFDQ process to produce microstructures that contain varying amounts of martensite, bainite, ferrite, and pearlite.

2.1.1 Quench conditions

Since this work is being done in the context of improving existing models of hot stamped parts with tailored properties, failure characterization is required for a variety of microstructures, produced as a result of various quench conditions. The as-quenched microstructures (conditions) considered for the 1.2 mm sheet include fully bainitic, fully martensitic, and an intermediate quench (consisting of approximately 70 % martensite and 30 % bainite).

The fully bainitic microstructure was produced by austenizing blanks in a furnace to 930 °C, holding at this temperature for 6.5 minutes, and then removing it from the furnace, allowing it to cool in still air. This quench yielded a microhardness of approximately 232 HV. An example of this microstructure are shown in Figure 7.

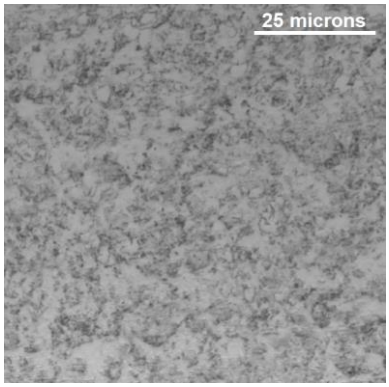

Figure 7: Fully bainitic microstructure

Fully martensitic blanks were produced following the same austenization process used to produce fully bainitic blanks, however, after removal from the furnace, the blank was transferred to still oil in order to quench it. This quench process yielded material with an average microhardness of 486 HV. Examples of this microstructure are shown in Figure 8.

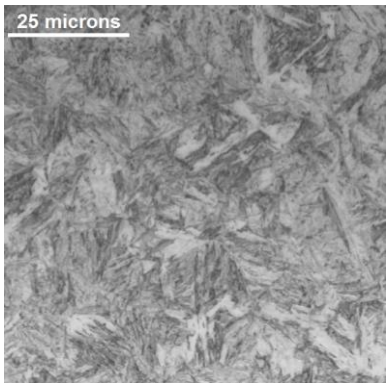

Figure 8: Fully martensitic microstructure

The intermediate microstructure considered for this work resulted from using forced air as the quench medium following the same austenizing process used for the previously described quench conditions. The forced air quench apparatus (FAQA), shown in Figure 9, developed by Bardelcik [35], was used to produce an intermediate quench condition. This apparatus was later revised (and thus renamed Forced Air Quench 2, abbreviated as FA-Q 2,) to adapt it for quenching blanks for hole expansion, biaxial dome, plane strain dome, and butterfly specimens. (The mechanical testing program is detailed in Section 2.2.) The FA-Q 2 was calibrated so that all of the blanks produced using this quench method had an average microhardness of 386 HV.

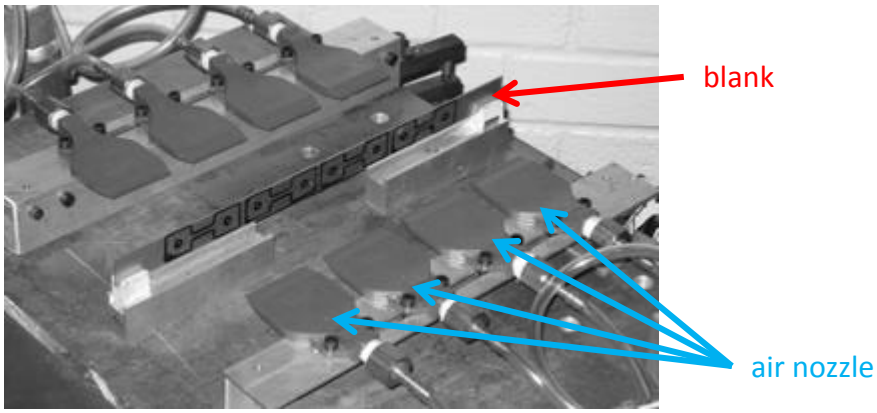

Figure 9: FAQA

The work of Barcellona and Palmeri [3] and Bardelcik *et al*. [36] demonstrated that deformation during quenching can affect the CCT, causing a shift of the bainite nose, as illustrated in Figure 10, yielding a martensitic-bainitic-ferritic microstructure.

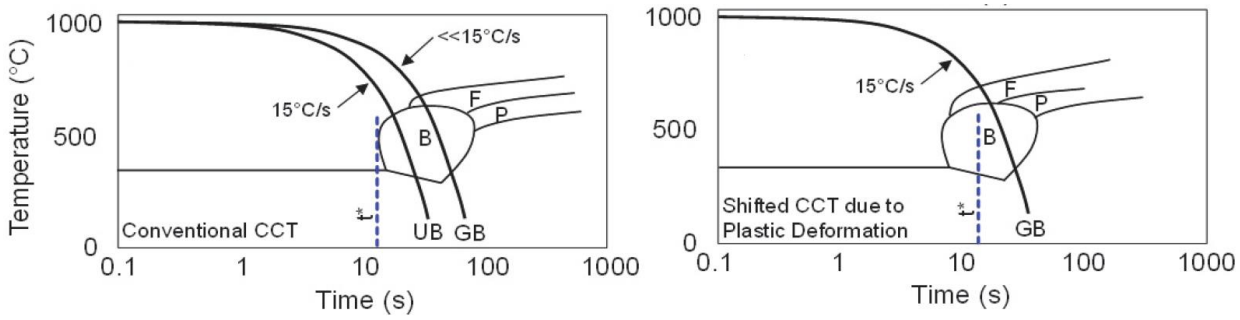

Figure 10: Comparison of conventional and shifted CCT [34], adapted from [3].

In light of this work, an additional quench condition was considered, following the method used by Bardelcik *et al*. [36], who deformed the specimen in a Gleeble thermo-mechanical simulator by elongating it by 10 mm starting at 600 °C while quenching at a constant cooling rate of 15 °C/s. This deformation resulted in approximately 20% engineering strain imposed in the area from which the specimen gauge length would be machined, at a strain rate of 0.4 s^{-1}. Figure 11 shows the region of the blank used in the Gleeble apparatus from which specimens were machined, as well as the location of the control thermocouple. The average measured micro

hardness of this material was approximately 288 HV. The resulting microstructure is shown in Figure 12.

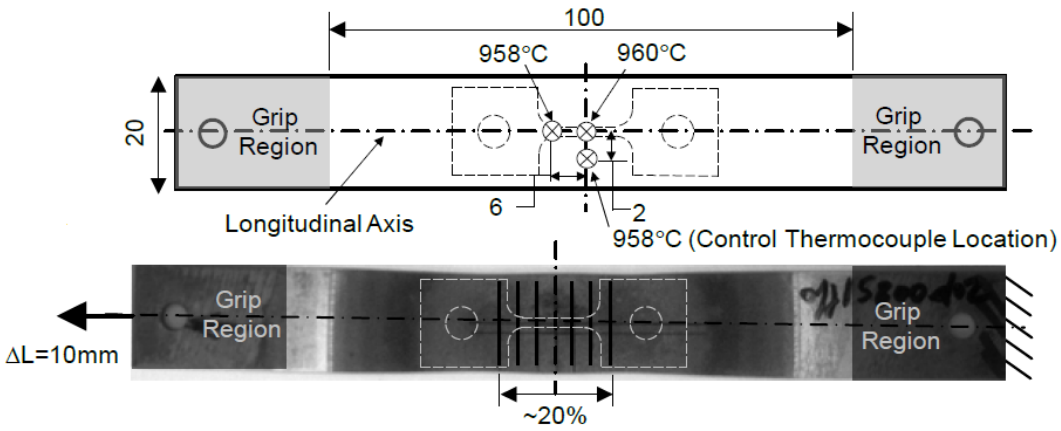

Figure 11: Blank used in Gleeble thermo-mechanical simulator, indicating thermocouple locations and region from which specimens were machined [36]

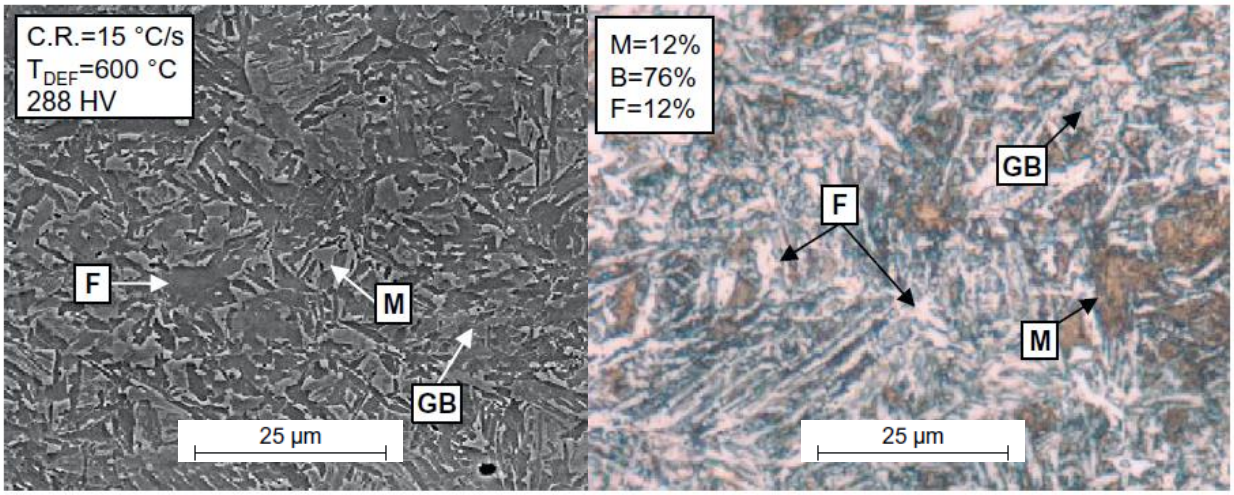

Figure 12: Microstructure of material simultaneously quenched and deformed using Gleeble apparatus. F, GB, and M denote ferrite, granular bainite, and martensite, respectively [36].

Unlike the previously described quench conditions, due to the deformation induced by the quenching process on the Gleeble, the blanks used to produce these specimens had slightly greater variation in thickness. For consistency, prior to machining, all blanks produced on the Gleeble apparatus were ground to produce a consistent thickness of 1.0 mm.

After the testing of specimens produced with each of the fully bainitic, fully martensitic, intermediate forced air, and intermediate Gleeble quench conditions was completed, there was interest in testing specimens produced from actual tailored hot stamped "top hat" sections (shown in Figure 13) produced in heated dies with temperature of 400 and 700 °C. The forming of these parts is described in [37]. Due to the relatively small area of the top hats, limitations were imposed on the quantity and type of specimens that could be produced. Furthermore, since only one-half of the part is quenched in a heated die, care was required to ensure that no specimens were produced from the material in the transition region, in the middle of the part. For fracture characterization of these quench conditions, a limited series of tests was considered: mini shear specimen, mini dog bone uniaxial tensile specimen, mini hole tensile specimen, and two butterfly specimens. Figure 13 shows the specimens produced from each part, as well as their location on the top hat section.

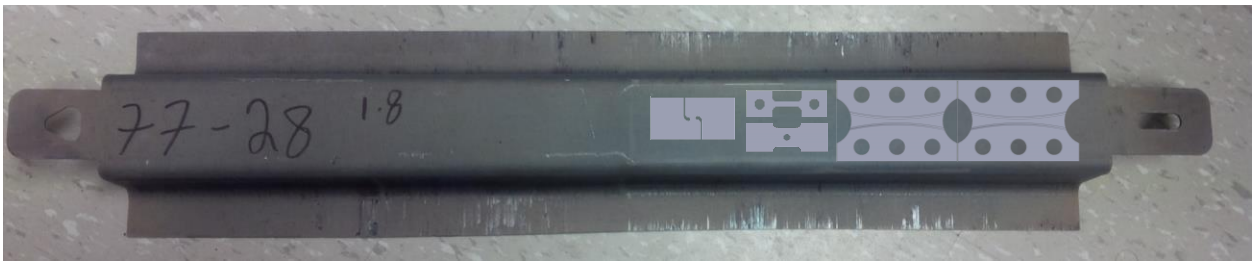

Figure 13: Depiction of specimens produced from tailored hot stamped parts formed at 400 and 700 °C. Specimens shown, from left to right: mini shear, mini dog bone and hole tensile, and two butterfly specimens

2.2 Constitutive and Fracture Characterization Testing Program

The experimental testing program described in this thesis may appear somewhat inconsistent when considered in its entirety. The initial approach for characterizing the failure of tailored hot stamped USIBOR® 1500-AS intended to use a variety of tensile specimen geometries, in order to produce tests of varying stress state through the use of various notched specimen. While this approach somewhat limited the range of stress states which could be evaluated, it would allow

for a consistent group of tests to be conducted across a range of strain rates, with the aim of enabling any strain rate effects on fracture behaviour to be observed. To probe other stress states, a number of different butterfly tests would be conducted. To tie the experimental results into the calibration of a failure criterion, a hybrid experimental-numerical approach, similar to [38] and [13], among others, would be employed to evaluate the stress state properties of each experiment. However, since this approach is heavily reliant on the results of finite element simulations, an alternative approach was developed over the course of the experimental testing program. Ignoring the effect of strain rate, tests other than those mentioned above were considered in order to assess the influence of stress state on failure strain for the different quench conditions investigated. To this extent, tests with largely proportional strain paths were developed and utilized. Additionally, rather than relying on the FE models of each test to provide failure strain information, tests from which this could easily be measured were considered. For the sake of completeness, the results of all of the experiments conducted are presented in the following paragraphs, however, subsequent sections that discuss failure criterion calibration will detail which experiments were ultimately employed for failure characterization.

2.2.1 Quasi-static Tensile Experiments

A hydraulic Instron mechanical testing apparatus was used to carry out quasi-static testing of uniaxial tensile, notched tensile, and hole tensile specimens. The geometry of the uniaxial, notched, and hole tensile specimens are shown in Figure 14-Figure 17. These miniature samples were adopted to ensure geometric compatibility with future experiments on the influence of strain rate on failure behaviour. Mini dogbone specimens were used in [7] for high strain rate testing. For certain materials, stress-strain data acquired using these specimens has shown acceptable correlation between this miniaturized geometry and the standard ASTM E8 geometry

up until uniform elongation [39] [40]. For this research, the mini dog bone tensile geometry was used exclusively, but validation of this geometry for this material was outside of the scope of investigation. The notched tensile geometries have been selected in order to maintain a gauge width consistent with the miniature uniaxial tensile specimens [41]. For the work involving material which underwent simultaneous quenching and deformation on the Gleeble apparatus, the size of blank used was very limited due to the size of the Gleeble grips and quench head. As a result, a mini hole tensile specimen was used to increase the number of unique stress states which could be tested. The work of Bao [42] was used for guidance when developing the hole tensile specimen geometry, since that work demonstrated that a ratio of ligament width to sheet thickness of four produced the best results in terms of consistent failure at the hole edge, where the stress triaxiality of in the material is 1/3, corresponding to pure uniaxial tension. For the fully martensitic, forced air intermediate, and fully bainitic quench conditions, all specimens were produced from sheet material with a nominal thickness of 1.2 mm, while the specimens machined from material quenched on the Gleeble apparatus had a nominal thickness of 1.0 mm. The specimens produced from the tailored hot stamped top hat sections had a nominal thickness of 1.8 mm.

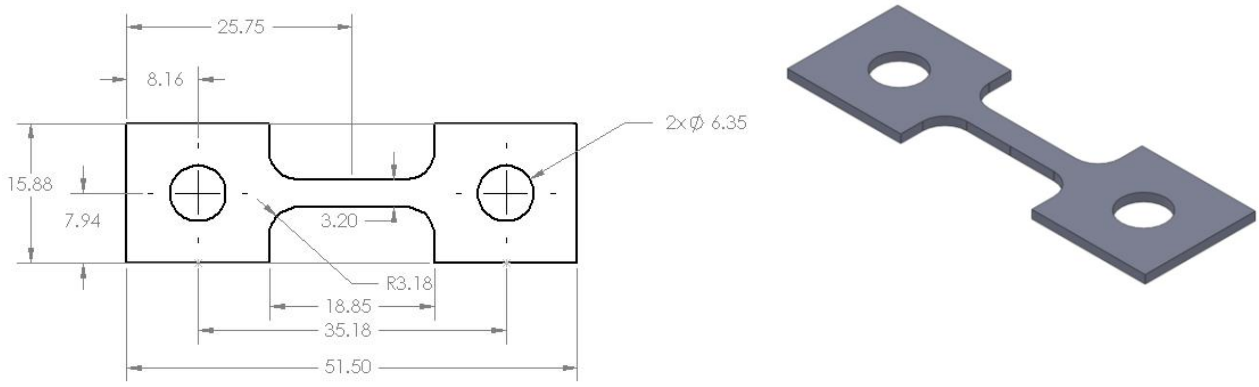

Figure 14: Uniaxial tensile specimen geometry

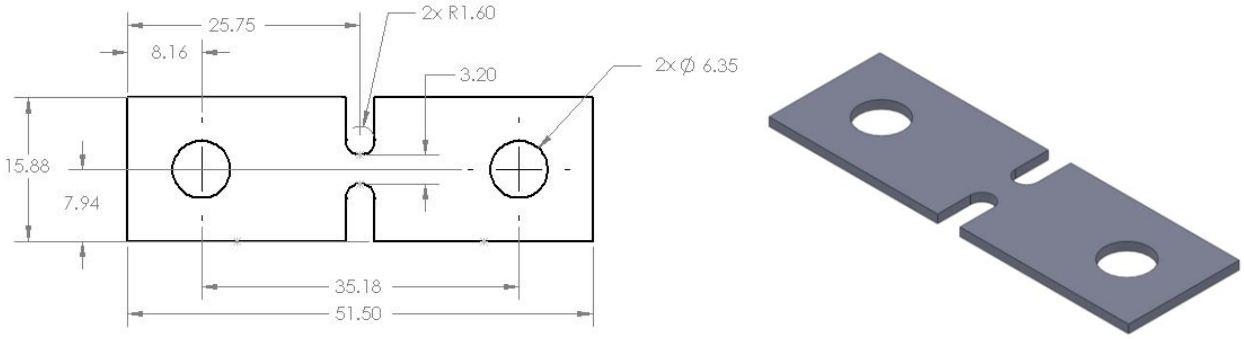

Figure 15: 1a notch tensile specimen geometry

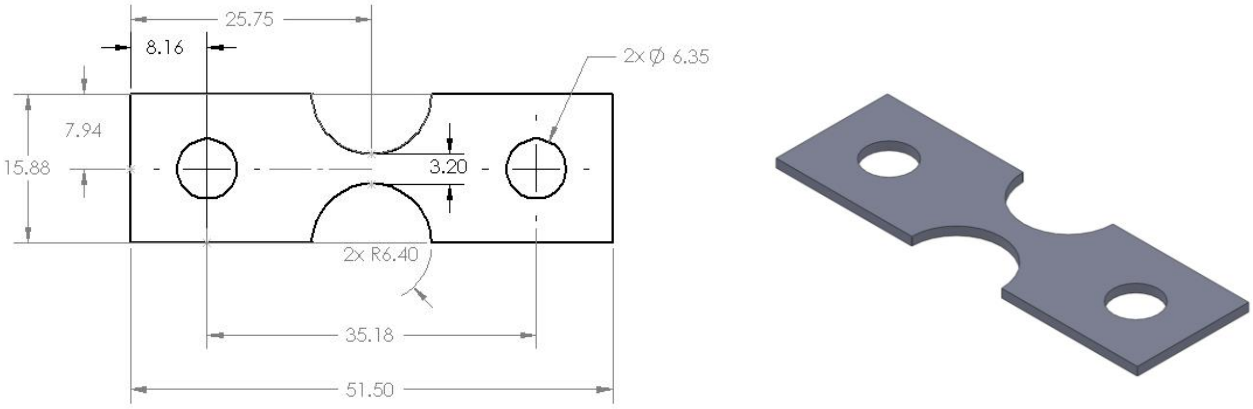

Figure 16: 4a notch tensile specimen geometry

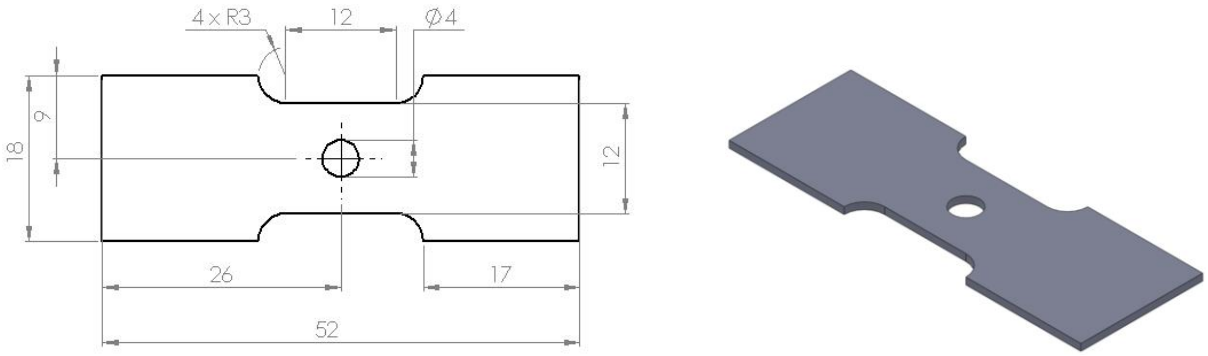

Figure 17: Hole tensile specimen geometry (Gleeble)

For these experiments, the Instron Model 1331 servohydraulic mechanical testing apparatus was fitted with a 111,206 N (25,000 lbf) load cell. This apparatus is shown in Figure 18. All experiments were performed at a strain rate of 0.003 s^{-1}, which could be considered quasi-static. For the mini dog bone uniaxial tensile geometry, this was achieved using a cross-head speed of 0.0375 mm/s. For the 4a and 1a notched tensile specimens, the gauge length was considered to be two times the notch radius, resulting in cross-head speed of 0.0384 and 0.0096 mm/s being used. While the hole tensile specimen doesn't feature an obvious geometric feature which could be considered a gauge length, for the purposes of selecting a crosshead speed, the gauge length was chosen as three times the hole diameter.

Figure 18: Instron Model 1331servohydraulic mechanical testing apparatus

Digital Image Correlation (DIC) was utilized to measure displacements and to compute experimental surface strains for these experiments. For the fully bainitic, forced air intermediate, and fully martensitic material conditions, a single Point Grey Research GZL-CL-41C6M-C 4.1MP camera fitted with a Sigma DG 28-300mm f/3.5-6.3 macro lens was used to record images in order to apply in-plane 2-D DIC. For the specimens produced on the Gleeble, stereoscopic Point Grey Research GRAS-50S5M-C 5.0MP cameras fitted with a Kenko 1.4X TELEPLUS Pro 300 tele adapter and Tamron SP 180mm f/3.5 Di macro lenses and were used to capture images so that 3-D DIC could be applied. Frame rates were selected based on the

expected displacement to failure for each material condition and test specimen geometry, with the intention of capturing 100-300 images per test. The frame rates used for the tests described above are listed in Table 2.

Table 2: Camera frame rates for different experiments

Material – Specimen Geometry	Frame Rate [frames/s]
100% Bainite – Uniaxial	4
100% Bainite – 4a	4
100% Bainite – 1a	2
100% Martensite – Uniaxial	4
100% Martensite – 4a	4
100% Martensite – 1a	2.5
Intermediate FAQA – Uniaxial	4
Intermediate FAQA – 4a	4
Intermediate FAQA – 1a	4
Intermediate Gleeble – Uniaxial	4
Intermediate Gleeble – 4a	5
Intermediate Gleeble – 1a	4
Intermediate Gleeble – Hole Tensile	4

For DIC, the image capture and analysis package from Correlated Solutions was used, using VIC-2D 2009 and VIC-3D 7 for 2-D and 3-D analysis, respectively. Rustoleum Painter's Touch white primer was sprayed on each specimen, on top of which a fine random speckle pattern was applied using Rustoleum Painter's Touch flat black spray paint. This speckle pattern enables the DIC software to compute displacement and strain fields to be determined by comparing images of the deformed specimen with those of the specimen in its previous state.

2.2.2 Hole Expansion Experiments

For obtaining uniaxial tensile failure strains for fully martensitic, intermediate, and fully bainitic material conditions, a hole expansion test was used. The specimen geometry for this experiment is shown in Figure 19. While this test is commonly applied in industry to quickly assess material edge or stretch flange formability [43], because this test induces a proportional

loading case at the top edge of the hole that is essentially constant right up until material failure, this experiment is an excellent means of determining the failure strain for the uniaxial stress state. However, it is also considered to be quite useful for assessing formability of sheared edge conditions as shown by Butcher [44] and Levy [45]. The hole expansion apparatus at the ArcelorMittal Research and Development facility in Hamilton was used for this experiment. The sample incorporates a 127 mm x 127 mm (5” x 5”) blank with a 10 mm diameter reamed hole (to avoid the influence of sheared edge effects) in the centre. Ferrocote MAL HCL 1 lubricant was applied around the hole on the bottom surface of the blank that contacts the punch.

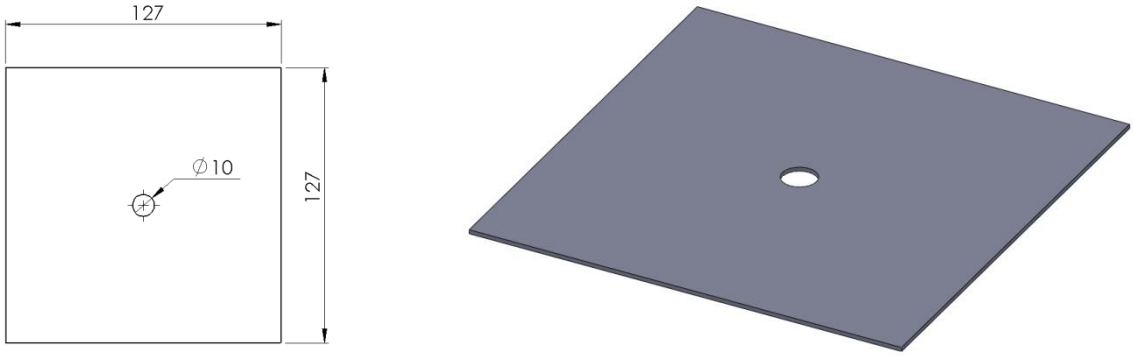

Figure 19: Hole expansion specimen geometry

This apparatus consists of a binder which applies a clamping force to the blank while a conical punch is forced through the reamed hole until a crack appears through the thickness of the material. It should be noted, that while a range of variations of this test exist, utilizing flat, hemispherical, or conical punches, using a flat or hemispherical punch for this test typically results in failure behind the hole edge, where the material experiences a stress state closer to that of equi-biaxial tension, rather than the uniaxial stress state achieved with a conical punch [46]. The conical punch also serves to supress necking at the hole edge, where the material fails in this test, yielding an extremely consistent stress state for the duration of the test. It is for this reason that the conical punch was used in this experiment. Unlike the other experiments carried out in

this work, DIC was not used, as the tester at ArcelorMittal has an integrated camera system with a semi-automated measurement system, which allows the strain at failure to be measured directly from the diameter of the specimen at failure. The view provided by the camera system during a test is shown in Figure 20.

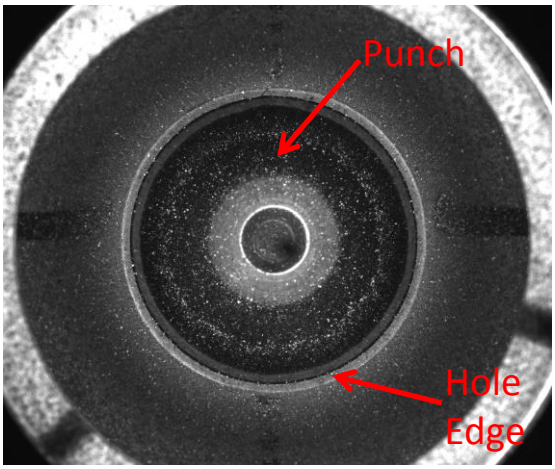

Figure 20: ArcelorMittal hole expansion specimen

2.2.3 Hemispherical Dome Experiments

To obtain experimental failure strains for stress states corresponding to biaxial tension and in plane-plane strain, an MTS dome tester apparatus with a hemispherical punch was used. This apparatus is shown in Figure 21. The biaxial specimens consisted of 203.2 mm x 203.3 mm (8" x 8") blanks, as shown in Figure 22. The plane strain specimens were of a notched geometry in accordance with the ISO guidelines for plane strain testing [47], with the dimensions shown in Figure 23. Although often used to characterize material formability, dome tests are also frequently used in stress-state dependent material fracture characterization. Maclean [48] and Beese [49], among others [50], [51], have utilized a near-equi-biaxial dome test for fracture characterization in a biaxial tensile stress state.

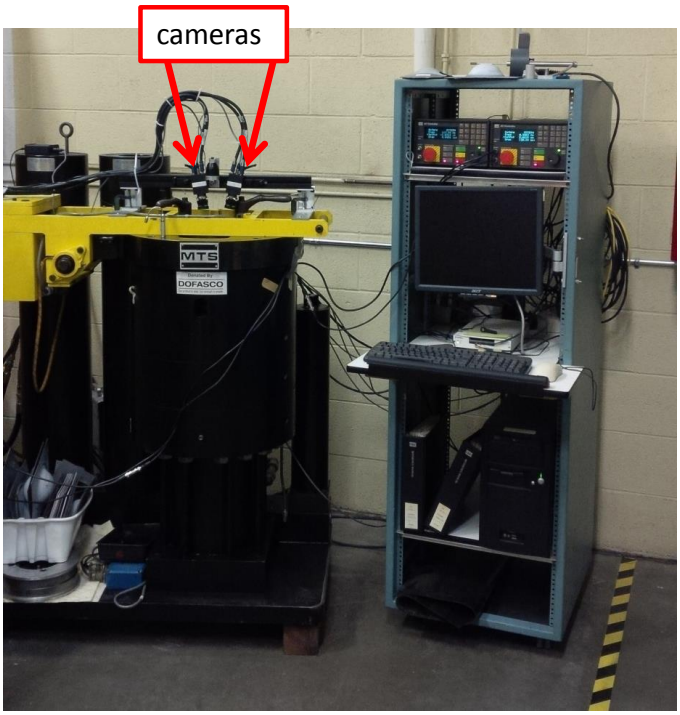

Figure 21: MTS dome tester apparatus

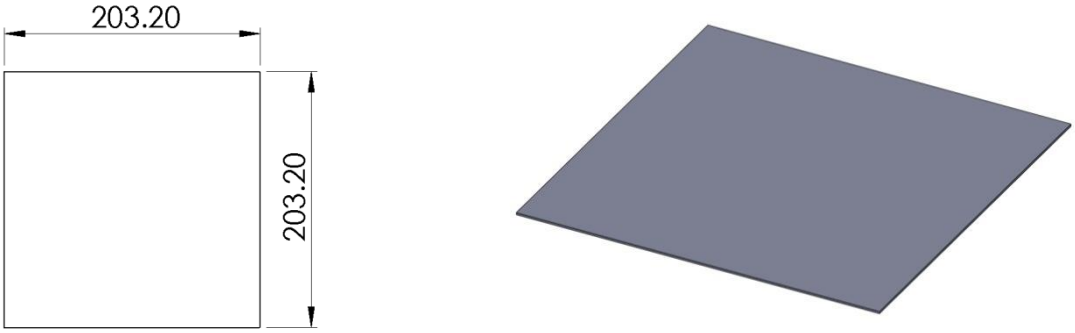

Figure 22: Biaxial dome test specimen geometry

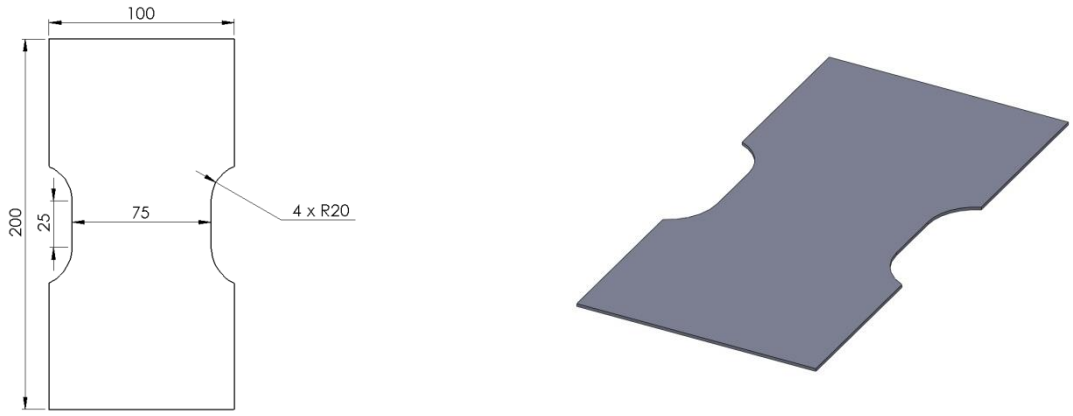

Figure 23: Plane strain dome test specimen geometry

The dome tester consists of upper and lower lock bead sections and a hemispherical punch. The various dome tester tooling components are shown in Figure 24 and their dimensions are listed in Table 3. Given the high strength of the material tested, the lock bead was essential for this test. However, the brittle nature of the martensitic and intermediate quench specimens necessitated clamping the blanks prior to heat treating in order to pre-form the lock bead geometry. Clamping the material in its as-received state, when the material is relatively ductile, served two purposes. Firstly, it prevents fracture at the lock bead when the specimen is clamped just before testing and secondly, it serves to stiffen the blank, preventing warping during the oil and forced air quenches used to produce martensitic and intermediate quenched specimens.

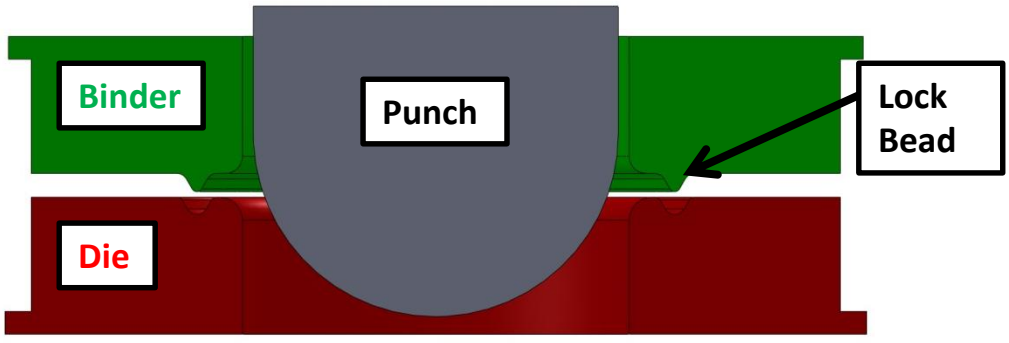

Figure 24: Dome test apparatus tooling components. Blank is placed between die and binder

Table 3: MTS dome tester tooling dimensions

Tooling Component	Dimension [mm]
Punch diameter	101.6
Lock bead midpoint diameter	133
Die inner diameter	107.6
Die entry profile radius	6.35
Lockbead height	4.7

From this apparatus, punch force and stroke were obtained, while 3-D DIC was used in order to measure dome height and strains. To achieve quasi-static strain rates, a punch speed of 0.25 [mm/s] was used for all tests. Stereoscopic Point Grey Research GRAS-50S5M-C 5.0MP cameras fitted Schneider Xenoplan 1.4/17mm Compact C-Mount lenses were used to capture images during the experiments. As with the quasi-static tensile tests, the camera frame rate was selected in order to record approximately 300 to 400 images per test. The frame rates for the different material conditions and specimen geometries are listed in Table 4. For post-processing of the captured images, the DIC subset size varied slightly based on speckle pattern quality, but was typically 21-25 pixels. For computation of true logarithmic strains, step and strain filter sizes were 5 and 7 pixels, respectively. A 1.2 mm diameter circle was centred at the location of the first visible crack in order to evaluate strains at the onset of fracture. In work outside the scope of this thesis, it was found that the influence of step and strain filter size had miniscule influence on true strain measured at the onset of fracture.

Table 4: Frame rates for hemispherical punch dome tests

Material – Specimen Geometry	Frame Rate [frames/s]
100% Bainite – Equi-biaxial	3
100% Bainite – Plane strain	4
100% Martensite – Equi-biaxial	3
100% Martensite – Plane strain	6
Intermediate FAQA – Equi-biaxial	4
Intermediate FAQA – Plane strain	5

In order to obtain consistent dome height measurements, considerable lubrication, consisting of three sheets of Teflon with petroleum jelly applied between each as well as to the blank and the punch, was used. This particular approach to lubrication was selected after carrying out experiments in which the quantities of both Teflon and petrolatum used were varied. It was found that this particular lubrication approach consistently resulted in fracture occurring at the centre of the specimen.

2.2.4 Butterfly

The butterfly test is utilized to obtain failure strains for a range of stress states, from simple shear through to tensile plane strain, under quasi-static loading conditions [12] . The apparatus, shown in Figure 25, occupies a hydraulic load frame and consists of indexable grips, which can be rotated in increments of 5°. This apparatus is configured in a manner such that "0°" corresponds to simple shear and "90°" corresponds to tensile plane strain [52]. For this work, tests were carried out on fully bainitic, fully martensitic, and intermediate forced air quenched microstructures, using grip orientations of 0°, 10°, and 30°, resulting in stress states of simple shear, combined shear-tension, and combined shear-tension. For the butterfly specimens machined from axial crush members formed in dies with temperatures of 400 and 700 °C, grip orientations of 15° and 90° were used. These orientations correspond to stress states of combined shear-tension and plane strain tension, respectively

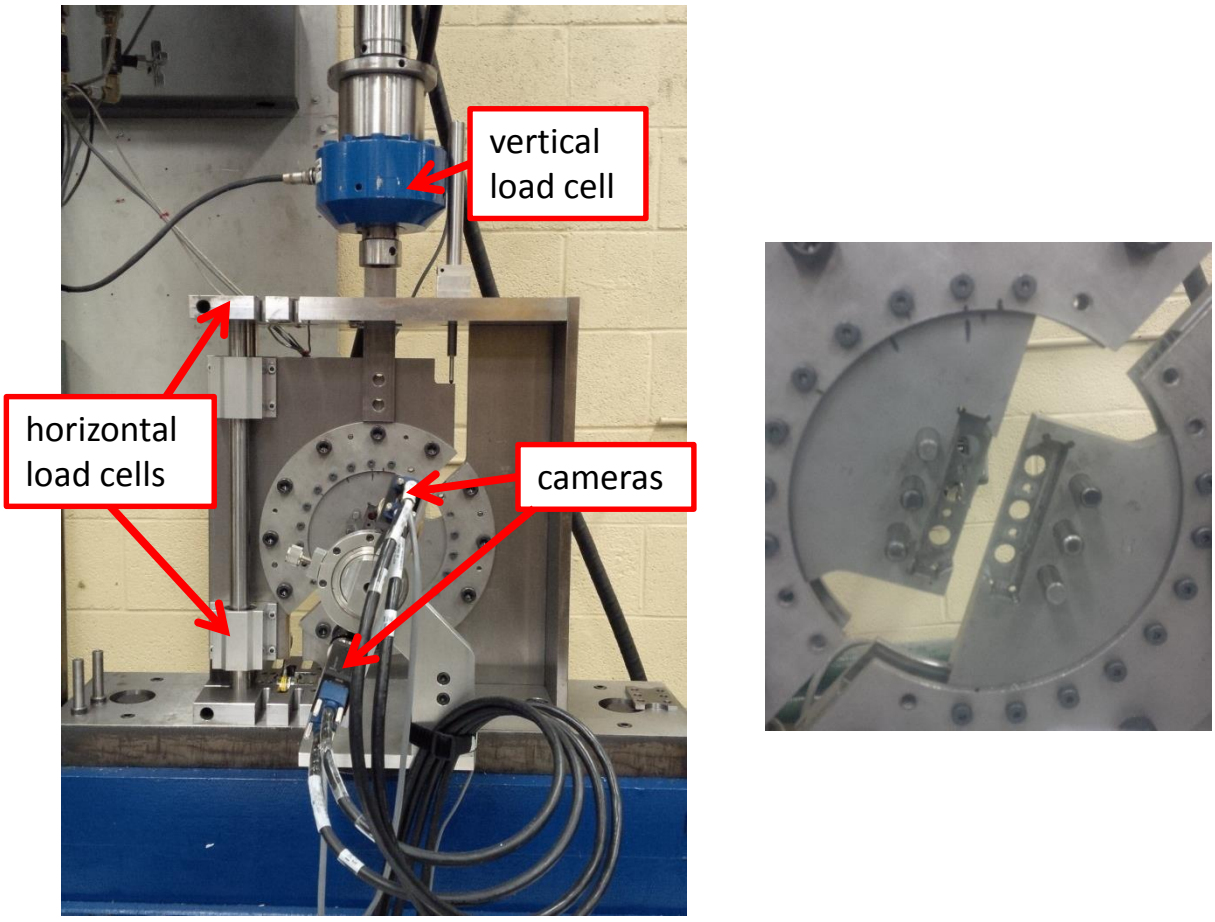

Figure 25: Butterfly apparatus, with close up of grips

The hydraulic load frame utilizes a 111,206 N (25,000 lbf) load cell. The specimen is securely clamped in a pair of grips, one of which remains stationary while the other is connected to the hydraulic actuator. While the hydraulic actuator is only capable of applying vertical displacement, the grip orientation can be rotated, controlling how the specimen is loaded. In order to measure both vertical and horizontal loads applied to the specimen, the apparatus is also fitted with two load cells, oriented horizontally, with capacities of 44,482 N (10,000 lbf). In order to analyze displacement and strain fields, 3-D DIC is used, recording images using stereoscopic Point Grey Research GZL-CL-41C6M-C 4.1MP cameras fitted with Schneider Xenoplan 1.9/35mm Compact C-Mount lenses. The cameras are positioned on a rotatable camera mount, shown in Figure 26, which can be oriented from 0° to 90°, in increments of 5°, like the

specimen grips. For the purpose of recording any rotation of the test specimen during testing, each of the grips feature two tracking markers which can be tracked using stereoscopic DIC. Post-processing of captured images was carried out using Vic 3-D 7. For the majority of tests, a subset size in the range 23-27 pixels proved suitable. A step size of 4 pixels and strain filter size of 5 pixels were used to compute true logarithmic strains. A 1.2 mm diameter was centred at the location of a visible crack in order to obtain strain measurements at the onset of fracture.

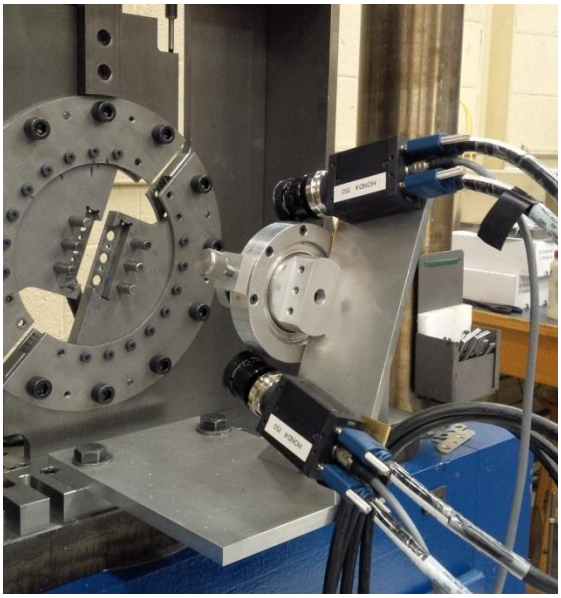

Figure 26: Indexable mount for cameras on butterfly apparatus

The specimen used in this test is shown in Figure 27 and has a tapered centre section machined down to half of the sheet thickness in order to localize deformation away from the specimen edge. Since the apparatus was under development while most of the experiments were being carried out, the gripped sections of the fully bainitic specimens tested at 0° differ slightly from the other material conditions and orientations investigated, since the grips were revised to improve ease of use after the fully bainitic specimens were machined and tested. The boundary condition imposed by the grips for both specimens is the same, but the newer grips make loading and unloading of specimens easier as well as providing a means of measuring displacement of

the grip which was initially assumed to be stationary. The specimen geometries are otherwise identical.

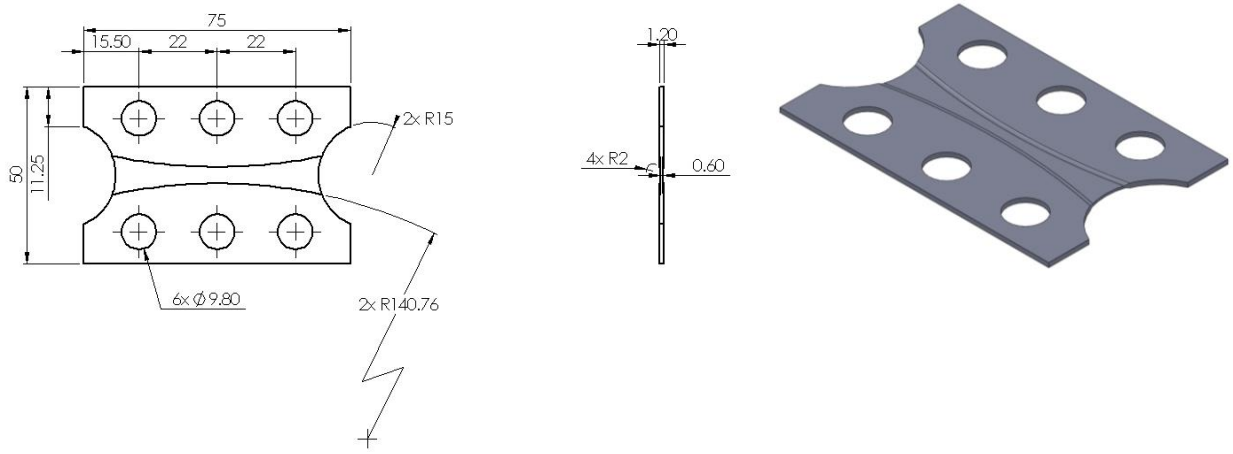

Figure 27: Butterfly specimen geometry [12]

2.2.5 Mini Shear

For the axial crush rails hot stamped and quenched in 400 and 700 °C dies, since the area from which specimens could be machined from each rail was limited, as was the number of parts available, an alternative to the butterfly specimen was used to obtain fracture strains for the simple shear stress state. This geometry is smaller than the butterfly and was developed by Peirs *et al.* [53]. Previous work at the University of Waterloo has found it to be an extremely clever and effective method of characterizing material in simple shear [54]. The geometry of this specimen is shown in Figure 28. In the gauge section, a state of simple shear is induced. However, due to the resulting rotation of the gauge section, the geometry features a slight eccentricity between the cut-outs in order to ensure a relatively consistent stress state up to larger strains.

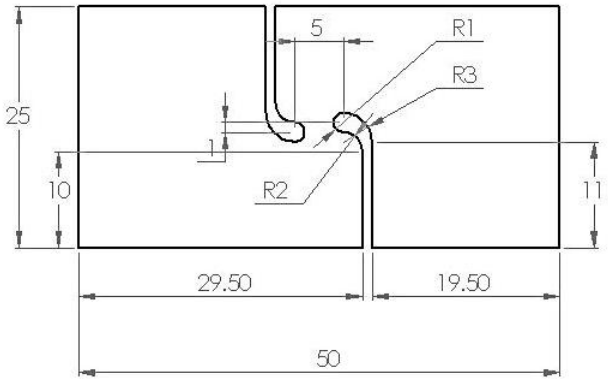

Figure 28: Mini shear specimen geometry

Since these parts were to be produced from axial crush rails, the tear-drop shaped cut-out was machined in the rail, followed by machining the outer dimensions of the specimen. Figure 13 shows the location of the rail from which this specimen was machined. Work done by Omer [37] showed that the microstructure of the rail in this region is uniform, with average micro hardnesses of 245 and 195HV for the 400 and 700 °C rails, respectively.

The mini shear specimens were tested using the hydraulic Instron Model 1331 tensile apparatus. A crosshead velocity of 0.03 [mm/s] was used, as this was found to induce a nominal strain rate of 0.01 s^{-1}. Although this specimen doesn't typically exhibit any thinning [54], as would be expected for simple shear, stereoscopic DIC was utilized in spite of the fact that 2-D DIC could have been considered sufficient. For capturing images of this test, two Point Grey Research GRAS-50S5M-C 5.0MP cameras fitted with Tamron SP 180mm f/3.5 Di macro lenses were used. Frame rates were selected to yield between 300-400 images for each test. For computation of true logarithmic strains at the onset of fracture, a circle with a diameter of 1.2 mm was located in the centre of the gage section. A subset size of 29-31 pixels was used for DIC analysis, with a step size of 5 and strain filter size of 7.

3 UNIAXIAL AND NOTCHED TENSILE EXPERIMENTS AND SIMULATIONS

This chapter presents the data obtained from the uniaxial and notched tensile tests that were conducted. While these tests were conducted for the fully bainitic, fully martensitic, intermediate forced air quench, and intermediate Gleeble material conditions, only the results for the fully bainitic material quench condition are presented here, while the results from the remainder of the material conditions are included in Appendix A-Appendix D. Experimental data presented in this chapter includes plots of load-displacement response as well as a summary of selected mechanical properties. Additionally, for each test, local area strains were obtained by measuring the cross sections of the fracture specimen.

In addition to the experimental results from the uniaxial and notched tensile tests, results from finite element simulations of these tests are also provided in this chapter. A brief description of the modeling approach is provided, as well as pictures of the mesh used for each specimen geometry.

It should be noted, over the course of testing the notched tensile specimens and developing corresponding finite element models for each experiment, the use of these specimens for fracture characterization came under scrutiny, and have ultimately not been used for developing the fracture loci presented in Chapter 5. Although results from these experiments and simulations have been published [55], it was not possible to definitively identify the location of fracture initiation in the experiments. Of additional concern with these experiments was the fact that the stress state continually evolves as the specimen is tested, prompting question over the use of such tests for calibration of stress state-dependent fracture loci.Uniaxial Tensile – Fully bainitic material quench condition

For each of the material conditions, the first test done was the uniaxial tensile test at quasi-static strain rates (0.003 s^{-1}). The specimen geometry is shown in Figure 14. Load-displacement response was obtained for each test using load measurements from the load cell mounted on the Instron and displacements obtained from 2-D (fully bainitic, fully martensitic, and intermediate forced air) and 3-D DIC (intermediate Gleeble, 400 and 700 °C tailored). To derive engineering stress-engineering strain data, the dimensions of each of the specimens were measured prior to testing. Rather than mounting a physical extensometer, virtual extensometers were placed along the gauge length of the specimens using Vic-2D or Vic-3D. Ideally, local strain paths and failure strains could be determined by computing the strains locally in the region where necking occurs. Unfortunately, due to issues of paint adhesion, seemingly a result of the aluminum silica coating on hot stamped USIBOR® 1500-AS [4], analysis of the necked region proved extremely difficult. Instead, failure strains were determined by measuring area reduction in extended depth of field (EDOF) images of the fracture surfaces. Figure 29 shows EDOF images of one specimen as an example. The measured area reduction takes into consideration the effect of the fracture surface angle. All of the EDOF images are included in Appendix A.

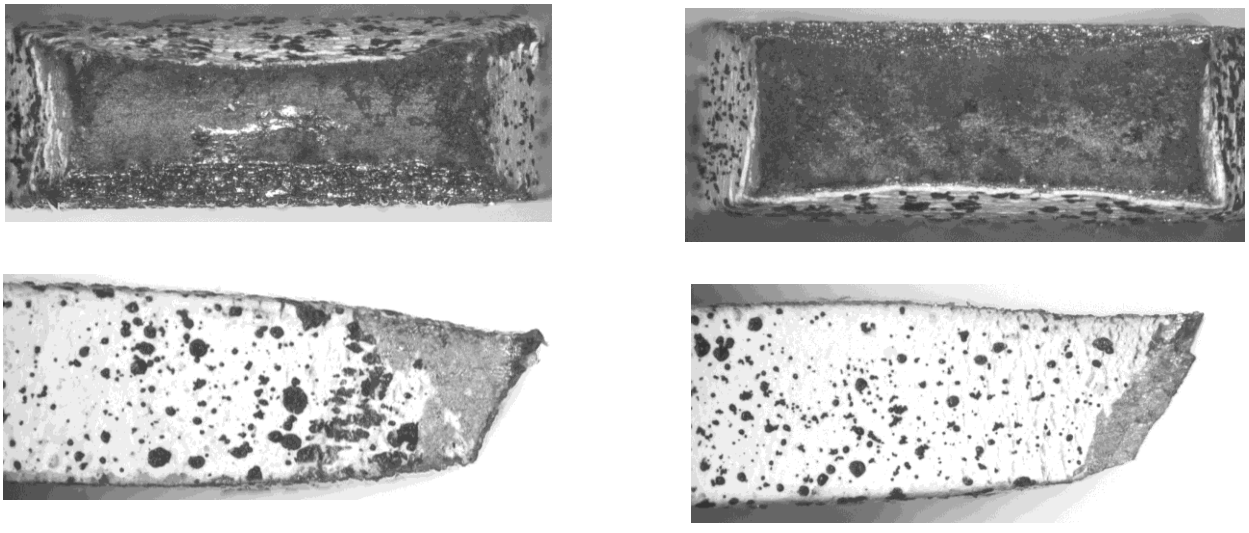

Figure 29: Extended depth of field images for measuring area reduction at failure (left: fully bainitic condition, right: fully martensitic condition)

The fully bainitic uniaxial specimens exhibited reasonable repeatability in terms of engineering stress-engineering strain response, as Figure 30 shows. For the fully bainitic material condition, the ductility of the material resulted in some of the paint applied for DIC flaking off in the area of the neck. While this would influence the fidelity of local strain measurements in that area, the virtual extensometer is still capable of capturing the macroscopic response of the material, as the paint remained intact in the other areas at the ends of the gauge length. A typical contour plot of equivalent strain is also shown in Figure 30.

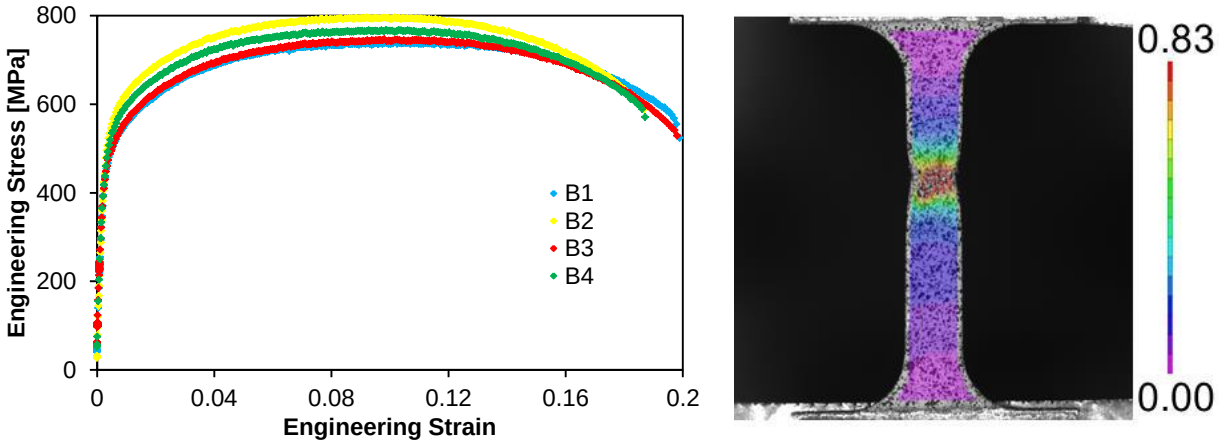

Figure 30: Engineering stress-strain curve for fully bainitic uniaxial tensile tests and typical contour plot of equivalent strain one frame before fracture. Note paint separation in necked region of specimen

Table 5 details the local strains at failure from the area reduction of the fully bainitic uniaxial tensile specimens.

Table 5: Properties of fully bainitic uniaxial tensile specimens

Sample	B1	B2	B3	B4	Average	Standard Deviation
UTS (MPa)	739	795	746	767	**762**	**21.8**
Elongation	0.20	0.19	0.20	0.19	**0.19**	**0.01**
Initial Area (mm^2)	3.79	3.63	3.70	3.80	**3.73**	**0.07**
Final Area (mm^2)	1.54	1.80	1.49	1.87	**1.67**	**0.16**
Area strain	0.86	0.72	0.88	0.71	**0.79**	**0.08**

For the material quench conditions included in Appendix B:

- Three fully martensitic uniaxial tensile specimens were tested and exhibited reasonably consistent engineering stress-engineering strain response. When the EDOF images were being produced in order to measure area, specimen M2 could not be located. Thus, only the area strains of specimens M1 and M3 area included in Table 27.
- While the forced air quench apparatus was being calibrated to produce an intermediate microstructure, repeated microhardness measurements of the material produced indicated greater variability than the material quenched either in still air or still oil. However, the five intermediate forced-air quench uniaxial tensile specimens tested demonstrated acceptable repeatability. Total elongation is similar to the fully martensitic material quench condition, but greater area strains were measured.
- Five intermediate Gleeble quench uniaxial tensile specimens were tested. Good repeatability was observed in terms of UTS, total elongation, and area strain at fracture. In comparison with the intermediate forced air quench uniaxial tensile specimens, the intermediate Gleeble specimens exhibited greater elongation but lower area strains at fracture.
- The five uniaxial tensile specimens tested from each of the tailored hot stamped axial crush rails were tested using an electromechanical MTS Criterion 45 tensile apparatus fitted with a 100 kN loadcell, rather than the servohydraulic Instron 1331.
- While the 400 °C tailored hot stamped parts had measured microhardness similar to that of the fully bainitic material quench condition [37], the measured area strains were considerably greater.

3.1 Uniaxial Tensile Simulations

To simulation the uniaxial tensile test, the specimen geometry was sectioned to create a quarter-symmetry model, as shown in Figure 31. Through the gauge section, the mesh features elements with a length of 0.1 mm. This mesh consists of 29,712 constant stress, hexahedral elements. Additional meshes were created with other element sizes in the gauge section, in order to assess convergence. These meshes are included in Appendix E. For the purpose of model simplicity, the holes that exist for fixing the specimen in the grips of the tensile frame are not considered in the model. Instead, the geometry was truncated at the location of the centre of the specimen holes (specimen geometry shown in Figure 14). Boundary conditions are applied at the ends of the mesh, fully constraining one end, while allowing for displacement only in the x-direction at the opposite end. The nodes at the end where x-direction displacement is unconstrained make up a node set, which is assigned a velocity-control boundary condition.

Figure 31: Mesh for quarter-symmetry uniaxial tensile model

Since the explicit dynamic solver is used, time and mass scaling could be applied [56], however, in this case, only time scaling is applied. Linear piecewise plasticity, a simple isotropic model using the von Mises yield criterion [57] is used. As this work does not consider strain rate

sensitivity, the velocity-time curve applied to the uniaxial tensile models is accelerated when compared to the quasi-static strain rate used in the experiments, 0.003 [s^{-1}]. Because the explicit solver is used, the time step is determined by the Courant criterion [58], and is thus governed by the smallest element in this model. A time step convergence study is not applicable to explicit simulations. However, to understand the influence of any dynamic effects, the model was initially simulated with various velocity-time history curves to ensure that subsequent simulations were free of time-scaling related dynamic (inertial) artefacts. In order to calibrate the material model to capture the post-uniform behaviour of the uniaxial tensile test, the approach suggested by Ling [59] was used. This approach was used for each of the material conditions investigated, using the averaging the true stress and effective plastic strain data obtained from the uniaxial tensile tests in order to generate a mean flow stress curve for each material condition. The following equation was used to extrapolate the flow stress curve for the post-uniform regime of the tensile test:

$$\sigma = \sigma_u \left[q(1 + \varepsilon - \varepsilon_u) + (1 - q)\left(\frac{\varepsilon^{\varepsilon_u}}{\varepsilon_u^{\varepsilon_u}}\right)\right]$$

where σ is true stress, σ_u is true stress at UTS, ε is effective plastic strain, ε_u is effective plastic strain at UTS, and q is a weighting constant which is varied between 0 and 1, serving to modulate a combination of linear hardening and power law hardening. Increments in q of 0.2 were used to fit the constitutive response and, from each simulation, engineering stress-strain data was extracted and plotted against the experimental results. Since the objective of this work is characterize fracture strain as a function of stress state, a common approach in literature is to consider the element in which the greatest effective plastic strain is observed and then utilize the strain at failure and stress triaxiality and Lode angle parameter in this element. This approach was employed in the current work.

The hardening curve used for all of the fully bainitic condition models is shown in Figure 32. The results from the other material quench conditions are included in Appendix B.

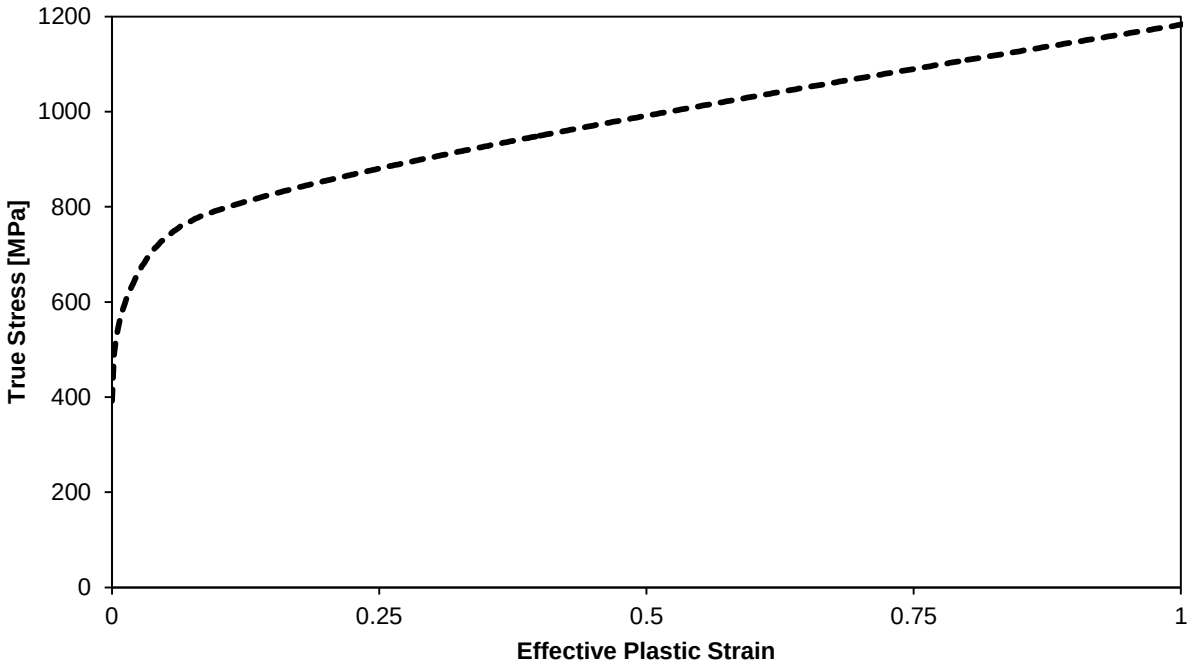

Figure 32: Flow stress curve for fully bainitic material condition

The predicted engineering stress-strain curve using the fully bainitic hardening curve (Figure 32) and the corresponding measured data are shown in Figure 33, indicating good correlation with the experiments. From this model, the evolution of the stress state at the centre element, where plastic strain is highest, can also be obtained. Stress triaxiality and Lode angle parameter are also plotted as function of engineering strain in Figure 33. Over the course of elongation, once the specimen begins to neck, the stress triaxiality and Lode angle parameter both begin to deviate from their values for a uniaxial state of stress. Considering plastic strain evolution, the greatest increase in effective plastic strain in the centre element does not occur under a state of uniaxial tension. An alternative means of highlighting this stress state evolution is in Figure 34, in which both stress triaxiality and Lode angle parameter are plotted as a function of effective plastic strain. Given the slight variation in elongation to fracture observed in the experiments,

potential variation in stress state and effective plastic strain at fracture is highlighted, with the solid and dashed lines corresponding to the minimum and maximum elongations to fracture, respectively.

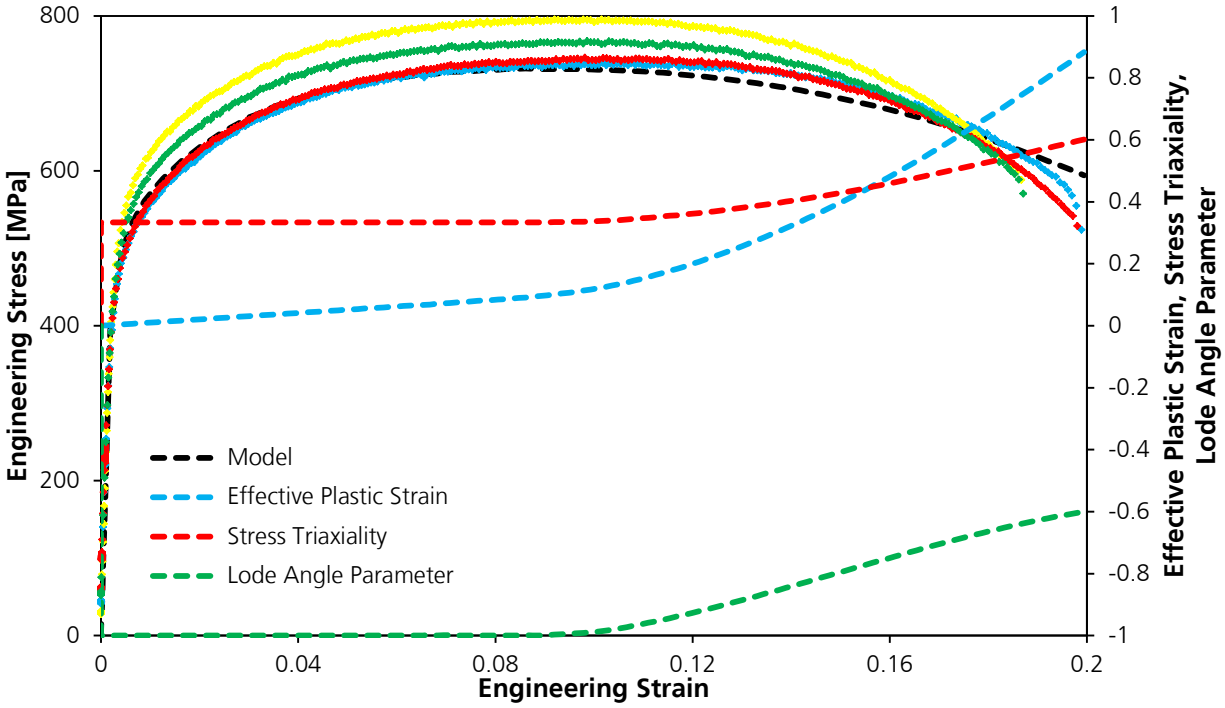

Figure 33: Uniaxial tensile model results for fully bainitic material condition

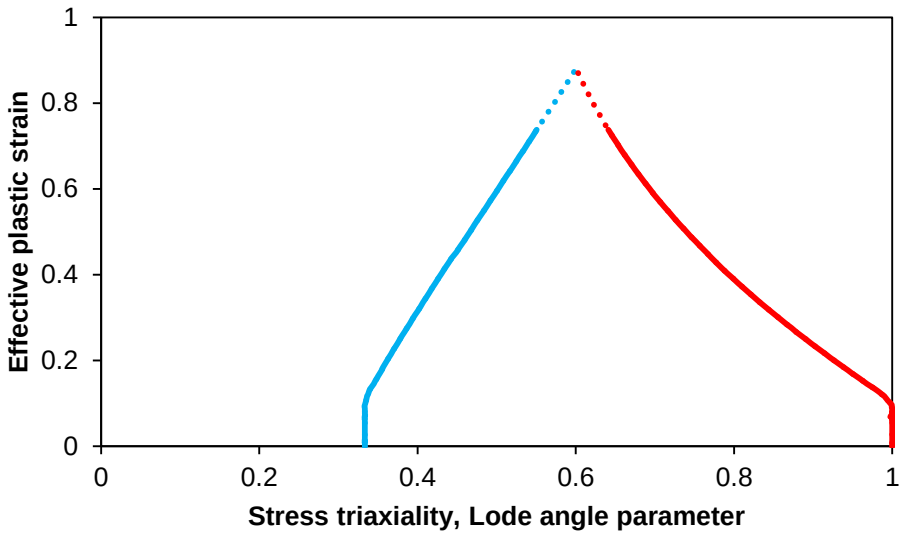

Figure 34: Stress state evolution for fully bainitic quench uniaxial tensile specimen

For each of the different material conditions for which uniaxial tensile specimens were tested, the results from the numerical simulation, consisting namely of equivalent plastic strain at failure, stress triaxiality, and Lode angle parameter, are summarized in Table 6.

Table 6: Summary of results from uniaxial tensile specimen models

Material Condition	Equivalent Plastic Strain	Stress Triaxiality-at fracture	Stress Triaxiality - averaged	Lode Angle Parameter – at fracture	Lode Angle Parameter - averaged
100% Bainite	0.81	0.58	0.37	0.62	0.91
100% Martensite	0.72	0.73	0.41	0.46	0.85
Intermediate FA-Q2	0.61	0.67	0.40	0.53	0.87
Intermediate Gleeble	0.50	0.50	0.35	0.69	0.94

3.2 4a Notched Tensile – Fully Bainitic Material Quench Condition

With the intention of using a tensile apparatus to obtain failure strain data for stress states other than uniaxial tension and additional strain rates other than solely quasi-static, a series of notched tensile specimen geometries were devised by Anderson and Kraehling [60]. One of these

geometries is referred to as the ‘4a’ notch, since the length of the notch, from shoulder to shoulder, is four times that of the ligament width. This specimen geometry is shown in Figure 16. Numerous notched tensile geometries have been used in recent works, such as [61], [29], [62], and [38], among others [63], however, pioneering work into the use of notched specimens was originally carried out by Bridgman [64]. Unlike the sheet material used in this work, axisymmetric specimen geometries were the focus of Bridgman’s work.

The 4a notch geometry presented similar issues to the uniaxial tensile specimens during testing, with regard to the adhesion of the painted on speckle pattern. Virtual extensometer techniques analogous to those used with the uniaxial tensile specimens were applied to the 4a notches as a means of obtaining displacement measurements. However, as the paint flaked off in the region of necking, where the highest local strains would be found, it was not possible to obtain local strain measurements using DIC. For this reason, it was also impossible to obtain experimental strain paths for the region in which deformation localizes. EDOF images of the specimen cross-sectional area were measured instead as a means of obtaining local strains at failure. Appendix A shows the EDOF images.

For the fully bainitic material condition, three repeats of the 4a notched tensile specimen were tested. Figure 35 shows the nominal stress-strain curves obtained from experiments. Since the specimens shown in this plot exhibited very similar stress-strain response, as well as very similar elongation at failure, only 3 repeats were completed.

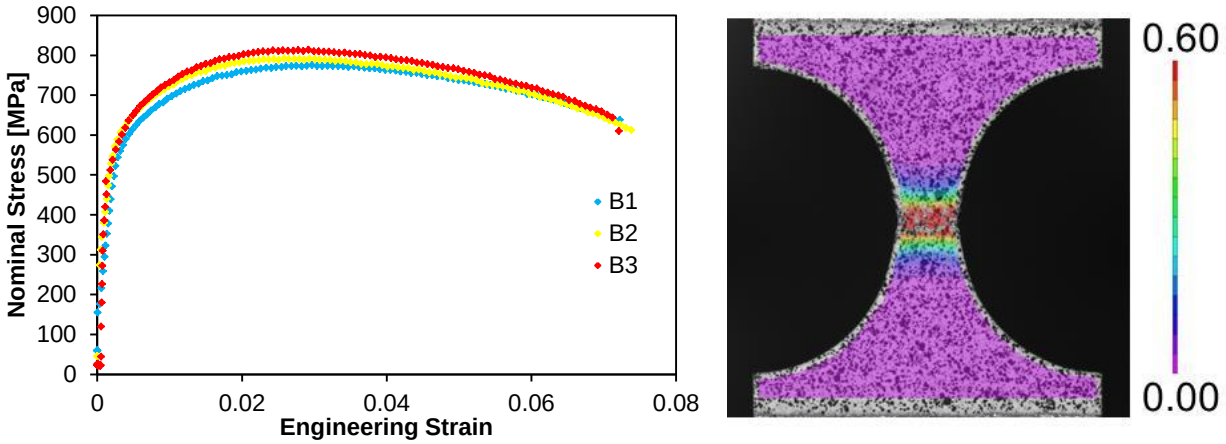

Figure 35: Nominal stress-strain curve for fully bainitic 4a notch tensile tests

In terms of local strains measured at failure, Table 7 lists the initial and final areas of each specimen as well as the resulting true area strain for each. B2 and B3 had nearly identical area strains at failure, both of which were considerably greater than those of B1. Table 7 also lists the measured mechanical properties of the three specimens tested. Of the three tests completed, B1 also possessed the lowest strength.

Table 7: Properties of fully bainitic 4a notch tensile specimens

Sample	B1	B2	B3	Average
UTS (MPa)	775	792	813	**793**
Elongation	0.07	0.07	0.07	**0.07**
Initial Area (mm^2)	3.80	3.89	3.86	**3.85**
Final Area (mm^2)	2.03	1.79	1.75	**1.86**
Area strain	0.62	0.78	0.79	**0.73**

For the material quench conditions included in Appendix C:

- Repeat tests of each material quench condition produced very consistent results.

3.3 4a Notched Tensile Simulations

As a means of utilizing a tensile apparatus to obtain fracture strains for stress states other than uniaxial tension, various notched tensile geometries had been developed, as outlined in Section 2.2.1. For modeling the 4a notch, the approach used for the uniaxial tensile models was applied to this geometry. Identical symmetry planes and boundary conditions were used. Also,

the velocity-time profile used in the uniaxial models was used for the 4a notch, since the same crosshead speed was used in the tests for both of these geometries. While the data shown corresponds to that obtained from simulations that featured an element size of 0.1 mm at the centre of the notch, additional models with other mesh densities were also considered. Figure 36 shows the 0.1 mm mesh, while the other meshes considered are included in Appendix E. The 0.1 mm mesh consists of 30,720 hexahedral, constant stress elements.

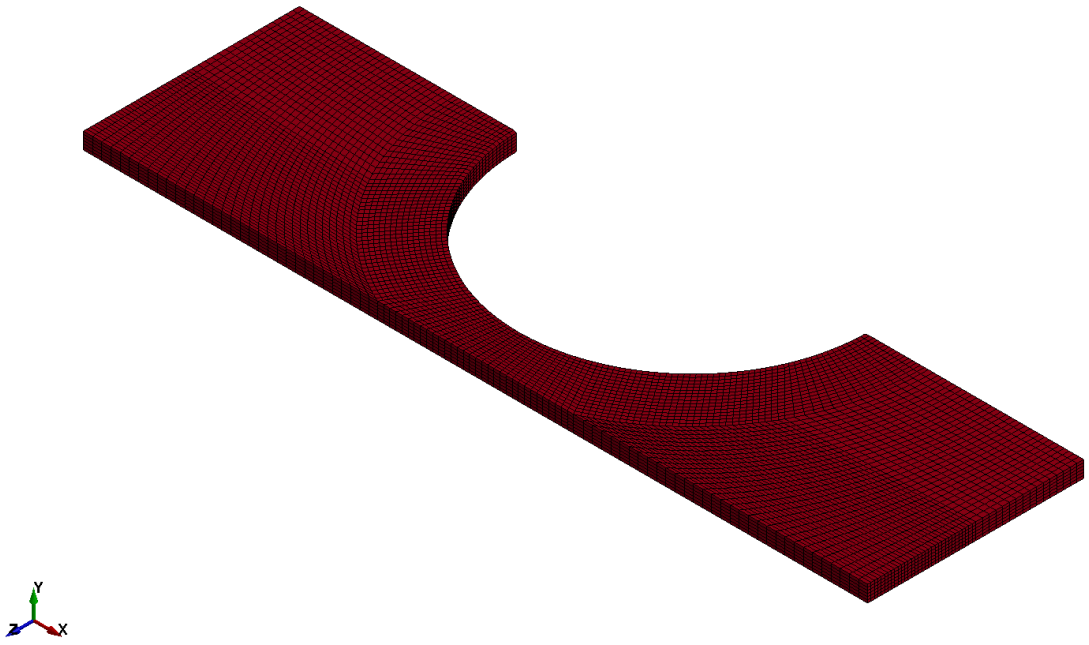

Figure 36: Mesh for quarter-symmetry 4a notched tensile model

For each of the different material conditions for which 4a notched tensile specimens were tested, the results from the numerical simulation, consisting namely of equivalent plastic strain at failure, stress triaxiality, and Lode angle parameter, are summarized in Table 8.

Table 8: Summary of results from 4a notched tensile specimen models

Material Condition	Equivalent Plastic Strain	Stress Triaxiality-at fracture	Stress Triaxiality - averaged	Lode Angle Parameter – at fracture	Lode Angle Parameter - averaged
100% Bainite	0.46	0.57	0.46	0.63	0.67
100% Martensite	0.40	0.68	0.54	0.47	0.57

Intermediate FA-Q2	0.48	0.71	0.51	0.47	0.59
Intermediate Gleeble	0.35	0.56	0.59	0.47	0.66

For the 4a notch in the fully bainitic material condition, the macroscopic response of this model is shown in the form of an nominal stress-strain curve, shown in Figure 37. The effective plastic strain, stress triaxiality, and Lode angle parameter corresponding to the element with the maximum effective plastic strain at failure are also included in this figure. Unlike the uniaxial tensile specimens, the parameters used to characterize the stress state in centre element continuously evolve over the course of the test. In comparison with the ductility noted in the uniaxial tensile model of the fully bainitic material condition, the effective plastic strain at failure in the fully bainitic 4a notch is approximately half as much.

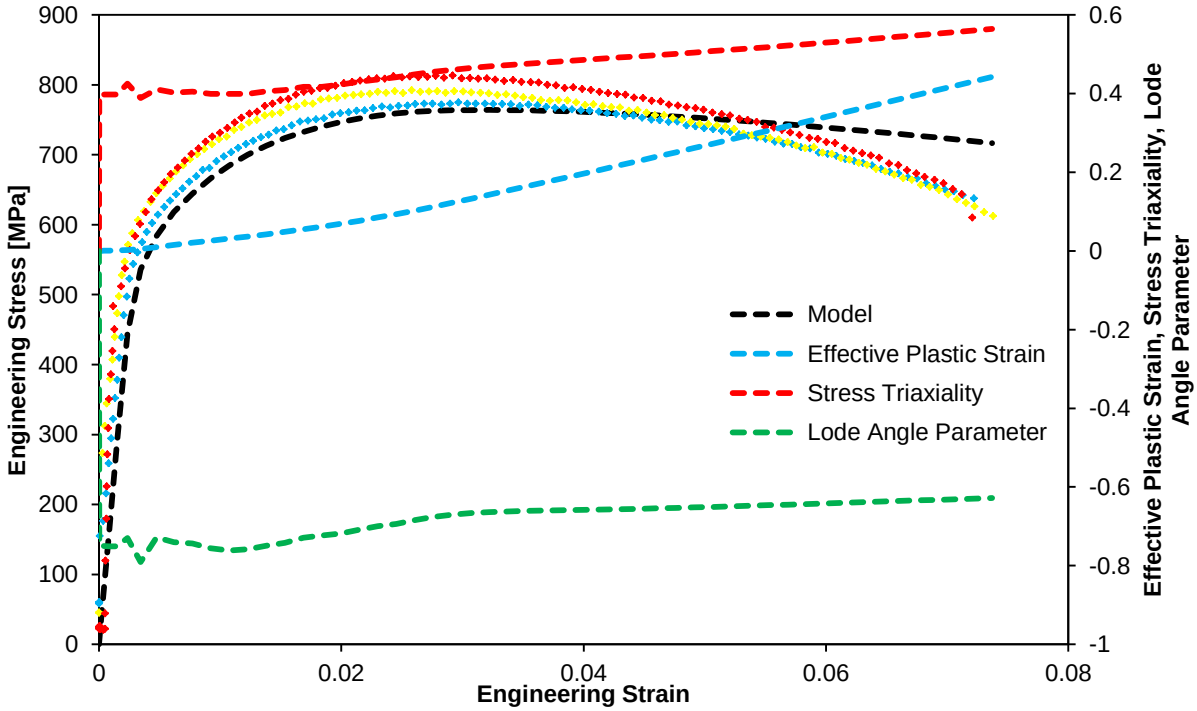

Figure 37: 4a notched tensile model results for fully bainitic material condition

The evolution of the stress state for this test, obtained by considering stress triaxiality and Lode angle parameter as a function of equivalent plastic strain, is further highlighted in Figure 38. Given the reasonable experimental repeatability in terms of elongation to fracture, the range of stress states and fracture strains suggested by the model is relatively narrow.

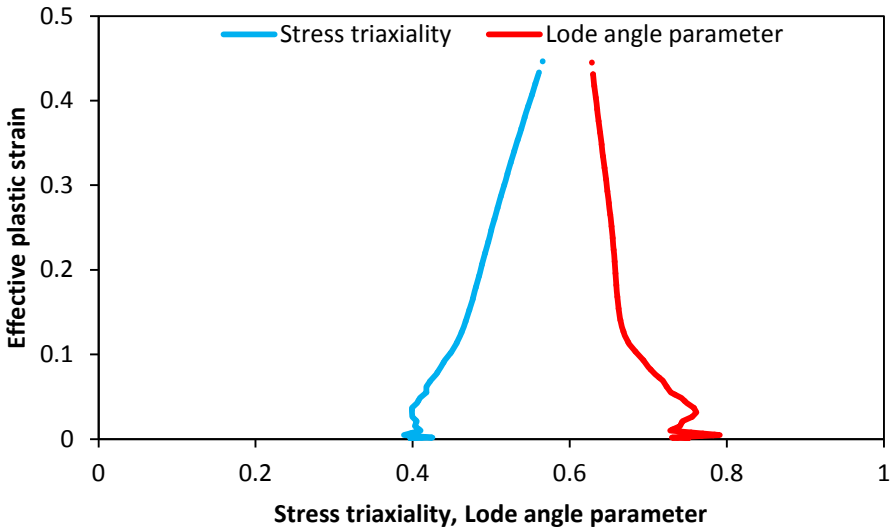

Figure 38: Stress state evolution of fully bainitic 4a notched tensile specimen

Since the stress state that results from this test is not consistent over the course of the test, both the stress triaxiality and Lode angle parameter were also averaged as a function of equivalent plastic strain. These values are also tabulated. The results from the other material quench conditions are included in Appendix C.

3.4 1a Notched Tensile – Fully Bainitic Material Quench Condition

As with the 4a notched tensile geometry, the 1a notched tensile geometry was proposed by Anderson and Kraehling [60]. Comparatively, the 1a notch is a much tighter notch geometry than the 4a notch, with the ligament width equalling the shoulder to shoulder length, hence the name of 1a.

For the fully bainitic material condition, the nominal stress-strain response of the 1a notches is plotted in Figure 39. Plotted as engineering strain, elongation appears comparable to the uniaxial tensile tests of this material condition, however, it should be noted that the gauge length of the mini dog bone tensile specimens is nearly 4 times that of the 1a notch. To compare macroscopic elongation of the 1a notched tensile specimen with the mini dog bone tensile specimens tested, overall displacement measured at the ends of the gauge section is a better means of comparing these two different specimen geometries.

For the fully bainitic 1a notched tensile specimens tested, the macroscopic response of the specimens is fairly consistent. Based on measurements of the specimens prior to testing, the three specimens tested had very consistent dimensions. The cross-sectional areas measured after testing was completed were also very similar for two of the samples tested, with the third specimen exhibiting a somewhat larger measured area, and thus lower fracture strain.

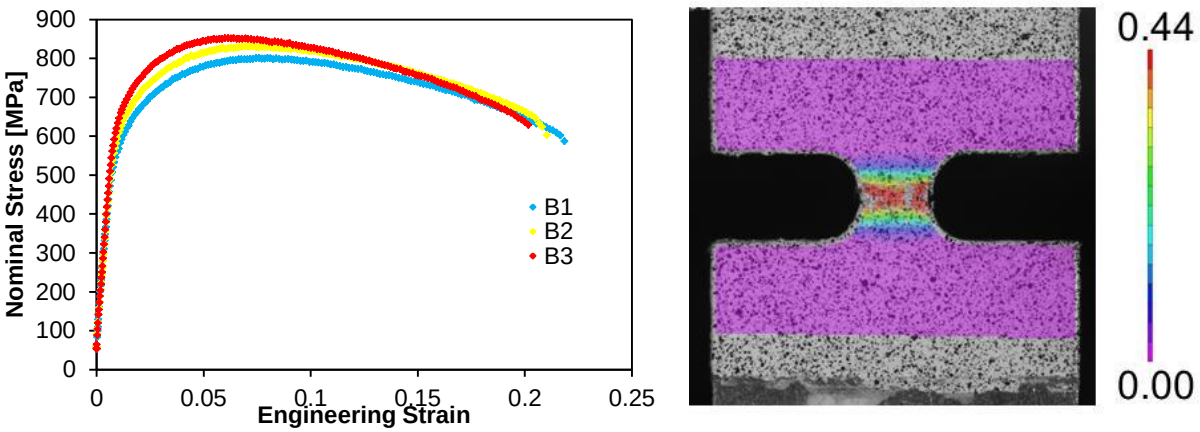

Figure 39: Nominal stress-strain curve for fully bainitic 1a notch tensile tests

Table 9: Properties of fully bainitic 1a notch tensile specimens

Sample	B1	B2	B3	Average
UTS (MPa)	801	831	852	**828**
Elongation	0.22	0.21	0.20	**0.21**
Initial Area (mm^2)	3.78	3.74	3.74	**3.75**
Final Area (mm^2)	1.82	1.97	1.83	**1.87**
Area strain	0.73	0.64	0.72	**0.70**

For the material quench conditions included in Appendix D:

- Repeat tests of each material quench condition produced very consistent results.

3.5 1a Notched Tensile

Similarly to the uniaxial and 4a notched tensile specimens, numerical simulations of the 1a notched tensile geometry were created in order to be able to obtain parameters to characterize fracture, specifically the effective plastic strain, stress triaxiality, and Lode angle parameter of the centre element of the specimen. For each of the four different material conditions tested and modeled, the centre element of the specimen coincided with the location of the largest plastic strain and these results are tabulated in Table 10. Like the other two tensile geometries, quarter symmetry boundary conditions were also applied to the mesh of the 1a notched tensile specimen. The gauge section consists of 0.1 mm solid elements, in order to maintain consistency with the other two previously discussed tensile geometries. However, since the gauge length for the notch geometries considered in this work is taken to be the distance shoulder to shoulder, the applied velocity control boundary condition is one quarter the magnitude of that applied to the other two geometries. The solid element formulation used in LS-DYNA is type 1 (constant stress). The model consists of 51,456 solid elements. The mesh is shown in Figure 40.

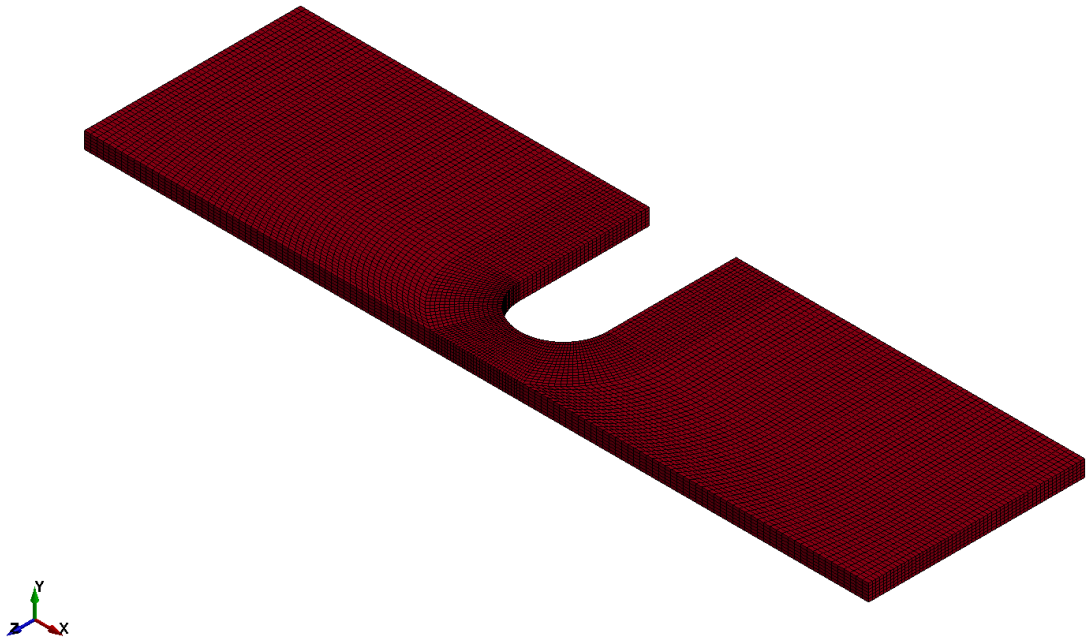

Figure 40: Mesh for quarter-symmetry 1a notched tensile model

Table 10: Summary of results from 1a notched tensile specimen models

Material Condition	Equivalent Plastic Strain	Stress Triaxiality-at fracture	Stress Triaxiality - averaged	Lode Angle Parameter – at fracture	Lode Angle Parameter - averaged
100% Bainite	0.52	0.70	0.58	0.27	0.26
100% Martensite	0.35	0.75	0.59	0.16	0.19
Intermediate FA-Q2	0.42	0.78	0.60	0.15	0.18
Intermediate Gleeble	0.37	0.67	0.58	0.25	0.27

The model of the 1a notched tensile specimen in the fully bainitic material condition produced results that were largely similar to the other two geometries that were discussed in the previous sections. For this model, the peak loads are similar to those observed in the experiment, however, like the 4a notch geometry, the load drop in the model after the maximum load is reached deviates somewhat from the experimental results. Figure 41 plots the engineering stress strain result obtained from the model against that of the experiments. Additionally, effective plastic strain, stress triaxiality, and Lode angle parameter are also plotted against engineering

strain in this figure. While the Lode angle parameter remains relatively constant over the duration of the deformation of the specimen, the stress triaxiality increases from approximately 0.54 to 0.71. At the displacement corresponding to failure, the model also indicates a maximum effective plastic strain of 0.56. To more clearly indicate how the stress triaxiality and Lode angle parameter vary over the course of the test, these two parameters are plotted as a function of effective plastic strain in Figure 42. The results from the other material quench conditions are included in Appendix D.

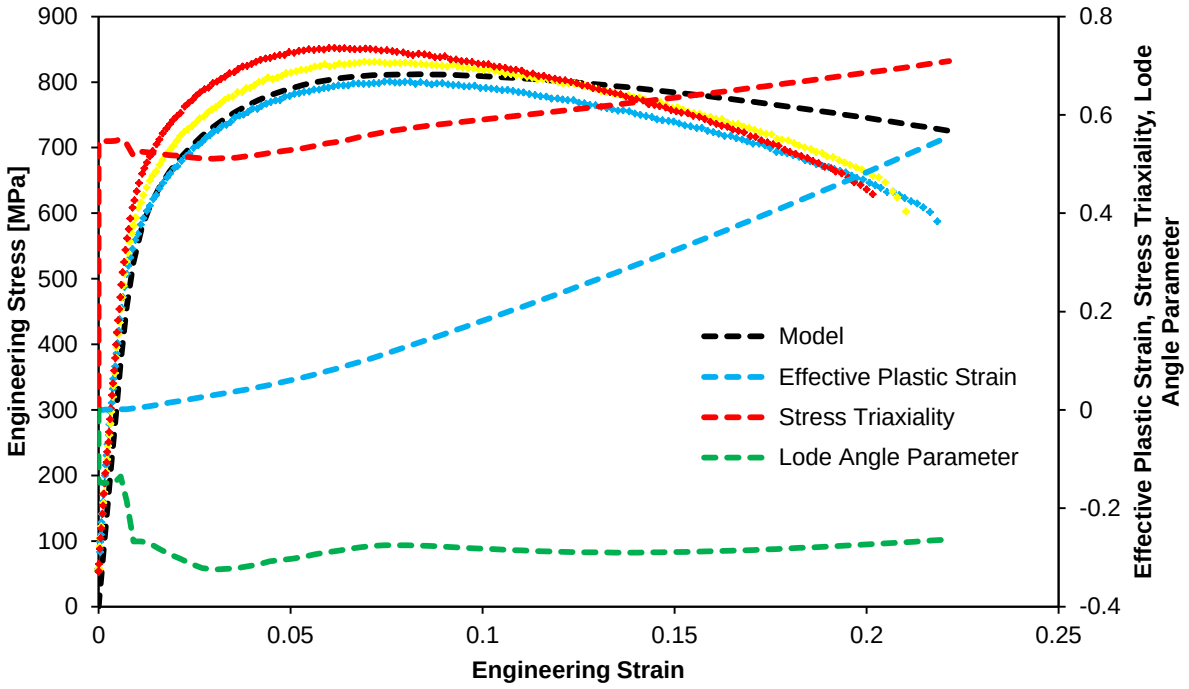

Figure 41: 1a notched tensile model results for fully bainitic material condition

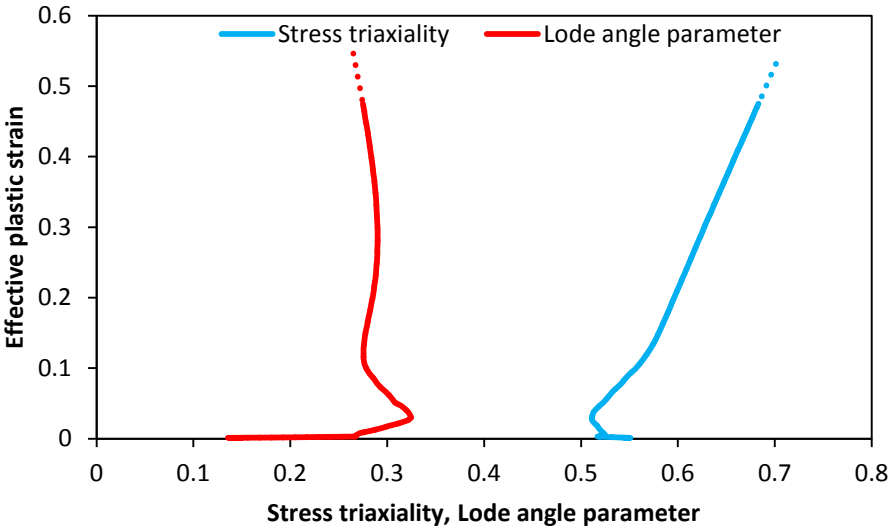

Figure 42: Stress state evolution for fully bainitic 1a notched tensile specimen

4 FRACTURE EXPERIMENT RESULTS

In the interest of brevity, the experimental fracture results are discussed in detail for only one material quench condition for each test. For the tests performed on the material quenched in the lab, the fully bainitic material quench condition is presented. Additionally, for the hole tensile test, the intermediate Gleeble quench material condition is presented, while any additional tests outside of those encompassed by these two material quench conditions are presented for the tailored hot stamped axial crush rails quenched at a die temperature of 700 °C. Where applicable, the differences between the different material quench conditions are discussed in brief comments. The remainder of the experimental results can be found in Appendix F-Appendix O.

Note that this chapter focuses on presenting results from the individual experiments and specimen types, including measured load-displacement response and local strains at onset of failure. These failure strains are combined to produce fracture loci comprising failure strain versus stress triaxiality, as presented in Chapter 5 which includes fracture loci for all material conditions. The experiments presented in this chapter are ordered increasing in triaxiality, beginning with simple shear and ending with equi-biaxial tension.

4.1 0° Butterfly – Fully Bainitic Material Quench Condition

The 0° butterfly test is used to obtain failure strains corresponding to the simple shear stress state. For this case, the specimen orientation and boundary conditions are shown in Figure 43. The specimen is aligned vertically, in the direction of the load frame. For each test, the load displacement data presented has been normalized over the specimen thickness in the gauge section. Measurement of specimens indicated that there was some inconsistency in the machined gauge section. While the most poorly machined specimens were not tested, some marginal specimens were tested to round out data sets for some test conditions.

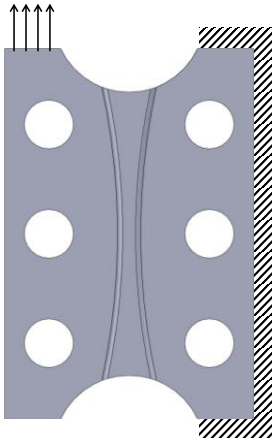

Figure 43: 0° butterfly specimen orientation

For the fully bainitic material condition, 7 repeats were tested, with very consistent results. Figure 44 shows the force-displacement response for these experiments. The true strains at failure measured on the surface of the specimen are listed in Table 11 for each of the repeats. Regarding the DIC analysis of these specimens, due to the severe deformations induced by this test, incremental correlation was used. The vertical load-displacement response measured for each specimen is plotted in Figure 44. Figure 45 shows the major and minor surface strains for these experiments. For each test, it is evident that the strain state corresponds to that of simple shear since $\varepsilon_1 = -\varepsilon_2$. For this particular test, the fracture location appeared to be in the centre of the gauge section for some, but not all of the tests. In some tests, it appeared that fracture initiated at the machined through thickness radius.

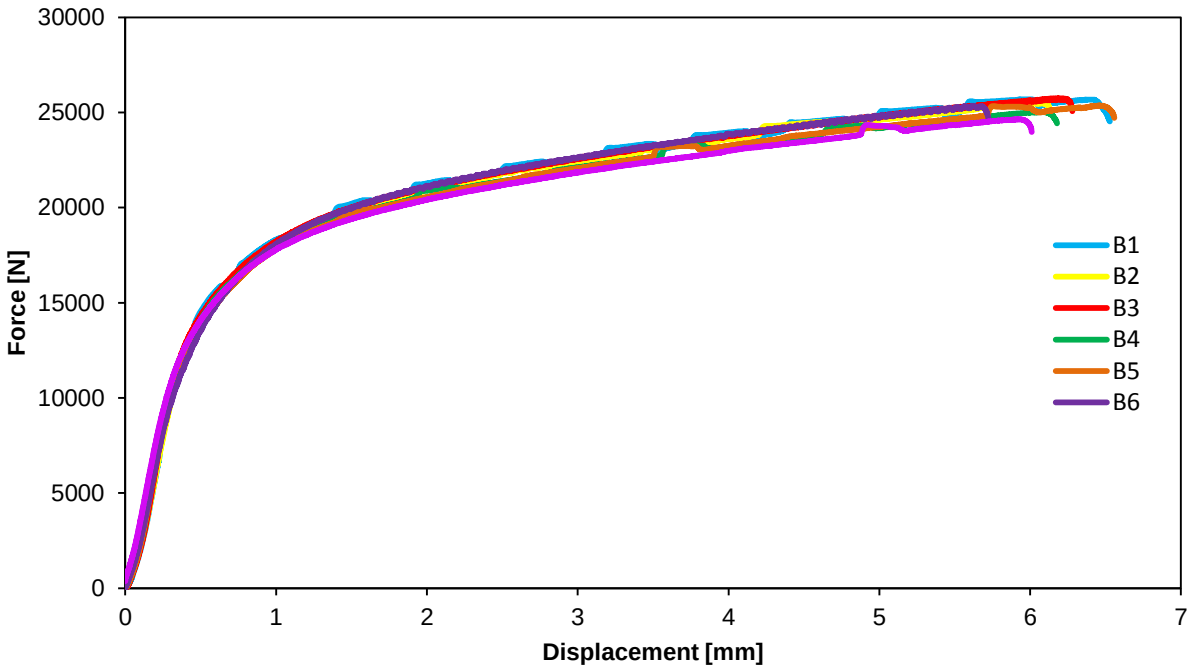

Figure 44: Load-displacement response for fully bainitic 0° butterfly test

The strain paths at the location of maximum strain for each repeat are evidently extremely proportional and no evidence of thinning was observed. In addition to the presented strain paths of each of the tests, the major, minor, and equivalent true strains at failure are listed in Table 11. This table also includes the maximum measured vertical force and displacement at failure for each specimen. The measured failure strains are quite similar, indicating very good consistency in this test.

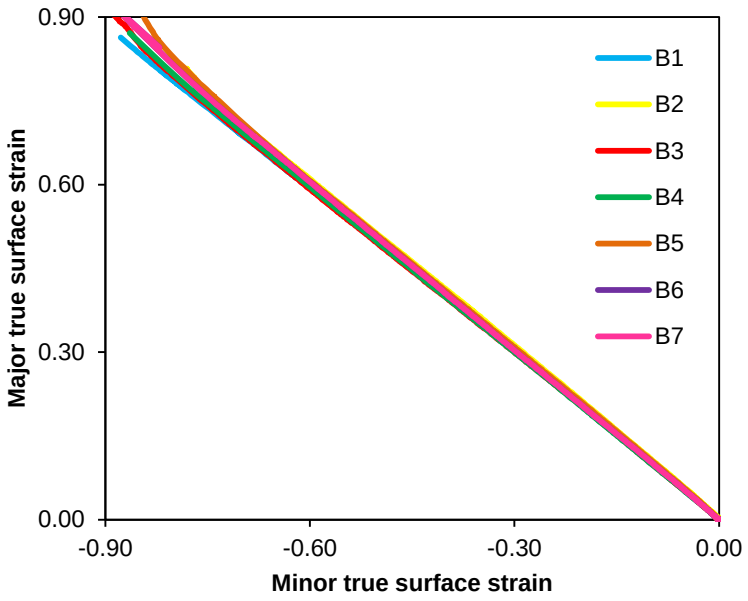

Figure 45: Major true surface strain vs. minor true surface strain for fully bainitic 0° butterfly test

Table 11: Failure strains for fully bainitic 0° butterfly test

Sample	1	2	3	4	5	6	7	Average	Standard Deviation
ε_1	0.86	0.75	0.78	0.81	0.82	0.68	0.77	**0.78**	**0.06**
ε_2	-0.88	-0.74	-0.79	-0.81	-0.79	-0.67	-0.76	**-0.78**	**0.06**
ε_{eq}	1.01	0.86	0.91	0.94	0.93	0.78	0.89	**0.90**	**0.07**

For the material quench conditions included in Appendix F:

- In contrast to the fully bainitic case, comparatively greater variability is observed in the fully martensitic specimens, both in terms of displacement at failure as well as strains at fracture. In all cases, the fracture of martensite was very abrupt, appearing to initiate in most cases at the centre of the gauge section.
- While the results from the five repeats of the intermediate forced air quench material condition conducted are presented here, additional repeats had to be conducted in order to yield five consistent results, due to the poor consistency of this quenching methodology when attempting to quench the comparatively larger blank size required for the butterfly

specimen. Considerable time was spent adjusting the FA-Q2 in order to yield relatively homogenous blanks, which possessed similar microhardness to the previously tested specimens produced using the FA-Q2.

4.2 Mini shear – 700 °C Tailored Hot Stamped

As discussed in section 2.2.5, the mini shear geometry was used to obtain fracture strains in simple shear for the material produced by hot stamping followed by die quenching at either 400 or 700 °C. For each material condition, five repeats of this test were conducted. For the mini shear specimens machined from the axial crush rails hot stamped and quenched in 700 °C dies, the load-displacement response obtained from this test is shown in Figure 46. The material response of the specimens tested is extremely consistent in terms of elongation to failure. In this figure, onset of fracture is indicated. This corresponds to the average elongation at fracture of the specimens tested. Locally analyzing the DIC results of this test, local strains were obtained. Considering the major and minor strains measured in each specimen, strain paths were extracted. Figure 47 shows the strain paths obtained from the centre of the gauge section. In this figure, the dashed black line denotes the theoretical strain path for simple shear, which the experimental strain paths are generally extremely close to. Due to paint issues compromising the speckle pattern for one of the specimens tested, the strain paths of four repeats are included in this figure. A summary of the mechanical properties obtained from the mini shear test for this material quench condition is included in Table 12.

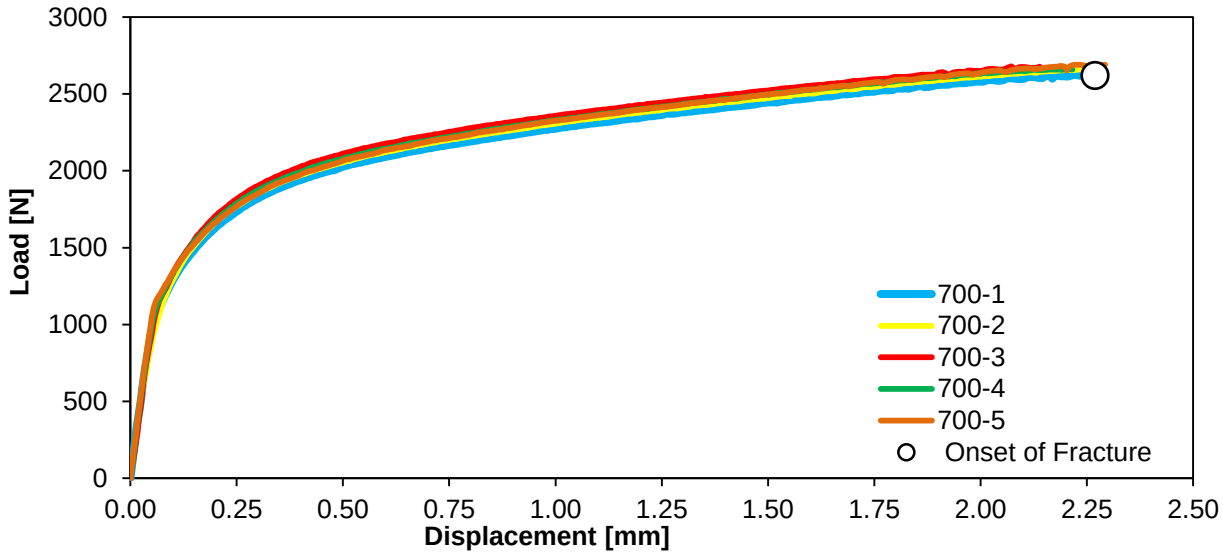

Figure 46: Load-displacement response for 700 °C quench mini shear test

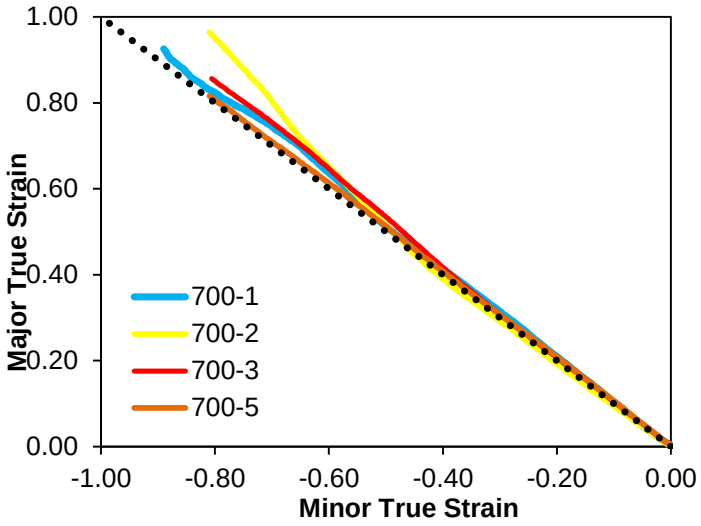

Figure 47: Major true surface strain vs. minor true surface strain for 700 °C quench mini shear test

Table 12: Properties of 700 °C quench mini shear specimens

Sample	700-1	700-2	700-3	700-4	700-5	Average	Standard Deviation
Peak Load [N]	2619	2666	2677	2659	2691	**2662**	**27.1**
Elongation [mm]	2.27	2.28	2.14	2.22	2.29	**2.24**	**0.06**
ε_1	0.93	0.96	0.86		0.82	**0.89**	**0.07**
ε_2	-0.89	-0.81	-0.81		-0.81	**-0.83**	**0.04**
ε_{eq}	1.12	1.11	1.00		0.99	**1.05**	**0.07**

For the material quench condition included in Appendix G:

- For each of the 400 °C tailored hot stamped material conditions, four of the five specimens tested produced very consistent strain data. For the specimen that did not, this was a result of a compromised speckle pattern in the gage section of the specimen. Otherwise, these tests were extremely repeatable.

4.3 10° Butterfly – Fully Bainitic Material Quench Condition

The butterfly specimen was tested in the 10° orientation in order to obtain failure strains for a stress state between simple shear and uniaxial tension. The orientation of the specimen for this test is shown in Figure 48. This particular orientation highlights an advantage of this test apparatus, as it enables fracture characterization of shear, combined tension-shear, and plane strain tension stress states simply by altering the orientation of the grips in the apparatus. Additionally, since the specimen rotates with the grips, the cameras used for the stereoscopic DIC setup are mounted on a fixture which can also be rotated, ensuring that the same camera window orientation is used for all tests conducted on the butterfly apparatus.

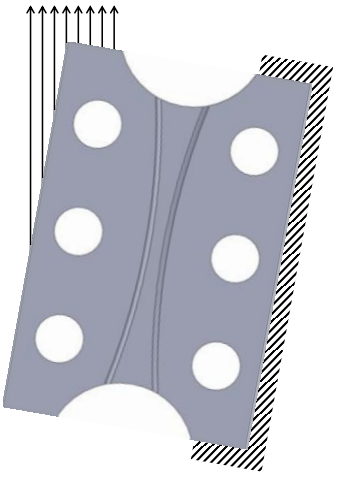

Figure 48: 10° butterfly specimen orientation

For the fully bainitic material condition, four repeats were completed, with reasonable repeatability observed. The macroscopic force-displacement response of the specimen is shown in Figure 49. The overall response is rather similar to that of the fully bainitic butterfly specimens tested in the 0° orientation. This test was very repeatable, with extremely similar load displacement response for the four samples tested.

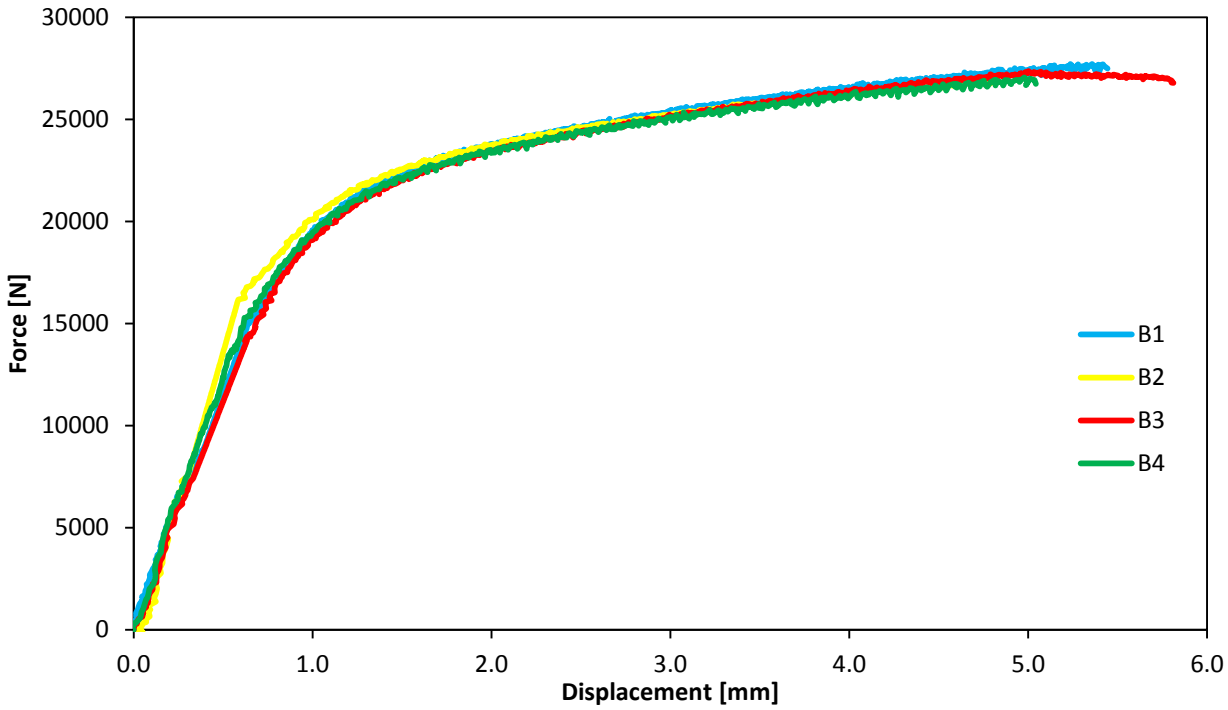

Figure 49: Load-displacement response for fully bainitic 10° butterfly test

In comparison with the fully bainitic butterfly specimens that were tested in the 0° orientation, fewer specimens tested in the 10° orientation exhibited fracture at the through-thickness machined radii. The major and minor true surface strains measured in the gauge section of the specimens is shown in Figure 50. Evidently, the strain path that resulted from this test is between that of simple shear and uniaxial tension, which are also indicated in this plot by dotted and dashed lines, respectively. This strain path is reasonably proportional. Table 13 lists the major, minor, and equivalent strains at failure measured for the four repeats presented here.

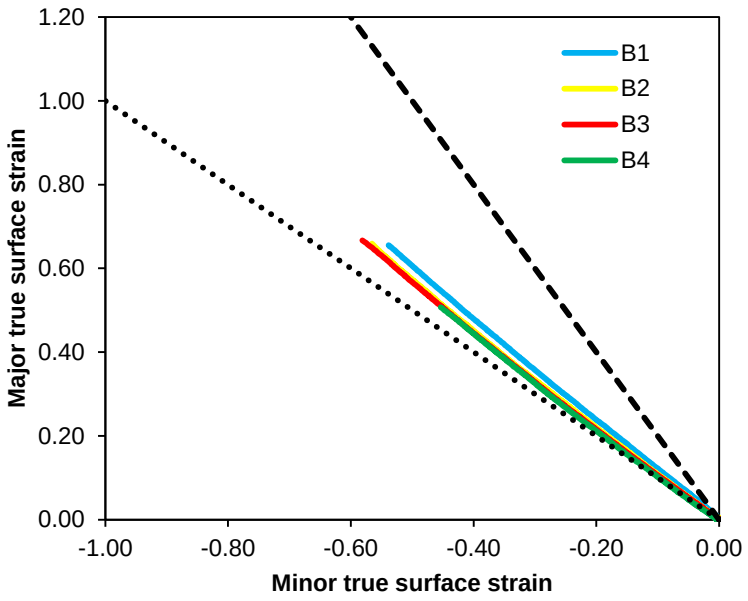

Figure 50: Major true surface strain vs. minor true surface strain for fully bainitic 10° butterfly test

Table 13: Failure strains for fully bainitic 10° butterfly test

Sample	1	2	3	4	Average	Standard Deviation
ε_1	0.66	0.66	0.67	0.51	0.62	0.08
ε_2	-0.54	-0.57	-0.58	-0.45	-0.53	0.06
ε_{eq}	0.77	0.80	0.84	0.66	0.77	0.08

For the material quench conditions included in Appendix H:

- The other two material conditions tested in this orientation generated much more consistent strain paths up to fracture, lacking the necking observed in the fully bainitic specimens.
- In comparison with the fully bainitic butterfly specimens tested in the 10° orientation, the strain paths of the fully martensitic specimens were somewhat closer to that of simple shear.
- Fairly consistent strains at fracture were measured for most of the intermediate forced-air quench specimens, although sample 2 exhibited noticeably higher strains at failure.

However, the elongation at failure of this specimen was consistent with the remainder of the tests. Although the cause of this variation is unknown, material inhomogeneity as a result of the quenching methodology is a possibility.

4.4 15° Butterfly – 700 °C Tailored Hot Stamped

Since the fully bainitic, fully martensitic, and intermediate forced air quench butterfly specimens were tested when the butterfly apparatus was still undergoing development, an analytical relation for determining the stress triaxiality [65] from the loading angle was used to determine appropriate loading angles for combined shear-tension loading. Unfortunately, as a result of later analysis of the resulting strain paths, using a von Mises assumption to estimate major and minor stresses, it was determined that this relation did not predict the expected stress state. For the butterfly specimens produced from the tailored axial crush rails formed at 400 and 700 °C, the previously completed butterfly tests of the other 3 material conditions were used as a starting point to determine a suitable loading angle, which would induce a stress state between simple shear and uniaxial tension. As a result, one test of each of the 400 and 700 °C butterflies was completed initially using a loading angle of 15°. As analysis of these 2 tests showed that this loading angle resulted in a stress state with a triaxiality of approximately 0.1 (discussed in more detail in section 5.1), the remainder of the 400 and 700 °C butterflies were tested using this loading angle.

The specimens produced from the formed axial crush rails quenched in dies at a temperature of 700 °C were the last experiments that were conducted. As a result, the quality of the DIC techniques applied, both in terms of speckling and analysis of these specimens, was likely the best of all the specimens that were tested in this work. The resulting force-displacement response of the 15° tests is shown in Figure 51. The macroscopic response is evidently consistent in terms

of material yielding and hardening behaviour, although there is a small amount of variation in the measured displacements to fracture.

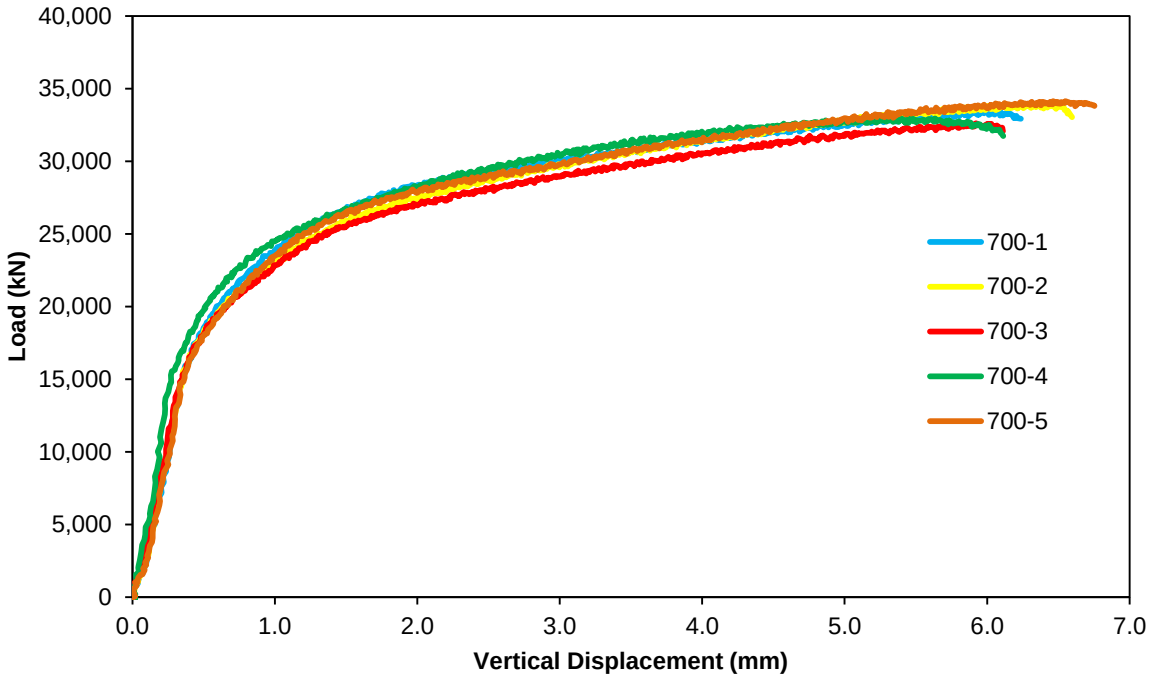

Figure 51: Load-displacement response for 700 °C quench 15° butterfly test

The strain paths that resulted at the centre of the specimen, where fracture was observed to initiate in this test, are shown in Figure 52. As this was the most ductile material condition investigated, the strains measured in this test are the largest of all of the butterfly specimens tested at 15°. As indicated by the fairly linear response between major and minor strains, this test induced proportional loading in the specimen up until fracture. The tests were also very repeatable, with nearly identical strain paths resulting in this test. A summary of the major, minor, and equivalent true surface strains of the five repeats is shown in Table 14. On average 0.96, -0.77, and 1.02 were measured as major, minor, and equivalent strains at failure.

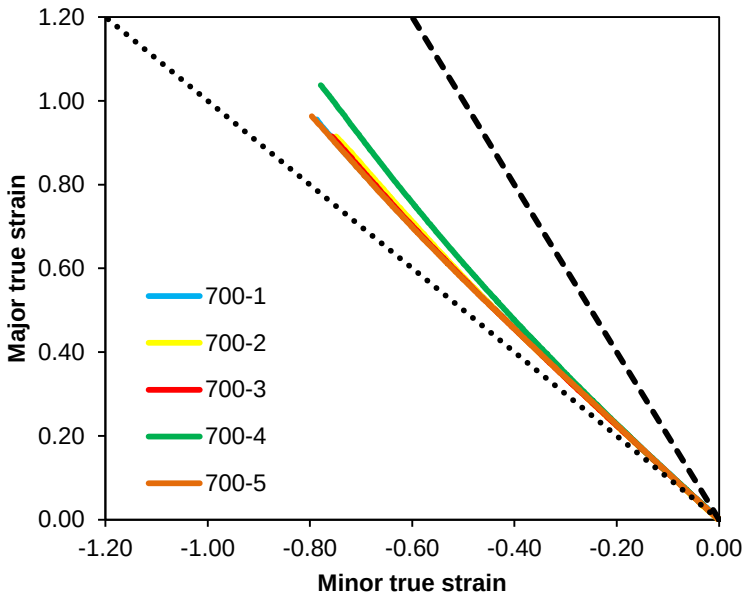

Figure 52: Major true surface strain vs. minor true surface strain for 700 °C quench 15° butterfly test

Table 14: Failure strains for the 700 °C quench 15° butterfly test

Sample	1	2	3	4	5	Average	Standard Deviation
ε_1	0.96	0.92	0.92	1.04	0.96	**0.96**	**0.05**
ε_2	-0.79	-0.75	-0.76	-0.78	-0.80	**-0.77**	**0.02**
ε_{eq}	1.02	0.97	0.98	1.08	1.03	**1.02**	**0.04**

For the material quench condition included in Appendix I:

- The five repeats tested were extremely consistent in terms of load, total elongation, and measured principal strains. Centre fracture was observed in each test.

4.5 30° Butterfly – Fully Bainitic Material Quench Condition

The fourth orientation of butterfly specimens used for this work was the 30° orientation. In terms of stress state, this orientation induces a combined shear-tension stress state. In comparison with the specimens tested in the 10° and 15° orientations, the 30° orientation induces comparatively more tensile stress and less shear stress. Figure 53 illustrates specimen orientation for this test.

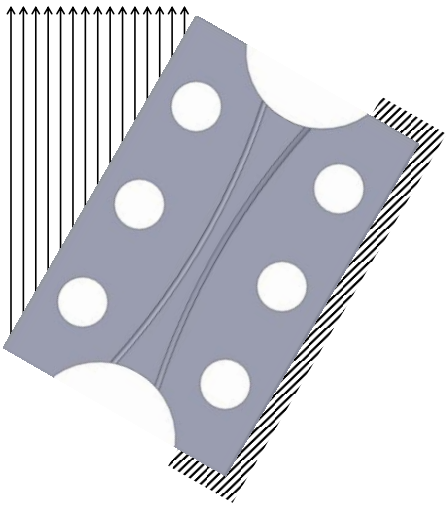

Figure 53: 30° butterfly specimen orientation

For the fully bainitic butterfly specimens tested in the 30° orientation, three specimens were tested. Unfortunately, during testing of one of the specimens, a pre-amplifier in the controller ceased functioning, resulting in load data for this test not being captured. Since the apparatus is run using displacement control, however, the test could be continued up until fracture in order to obtain fracture strains for this specimen. The load-displacement data from the two tests in which it was recorded is shown in Figure 54. Macroscopic response of these two specimens appears to be reasonably similar. Despite the load data corresponding to the third specimen being lost, the displacement at failure was still recorded. The displacements at fracture for all three specimens are noted in Table 15. This table also indicates the major, minor, and equivalent strains at failure that were measured in each of the three tests. Overall, the results from these tests are reasonably consistent. Ideally, a greater quantity of specimens would have been available to test, granting greater confidence to the fracture strains obtained from this test.

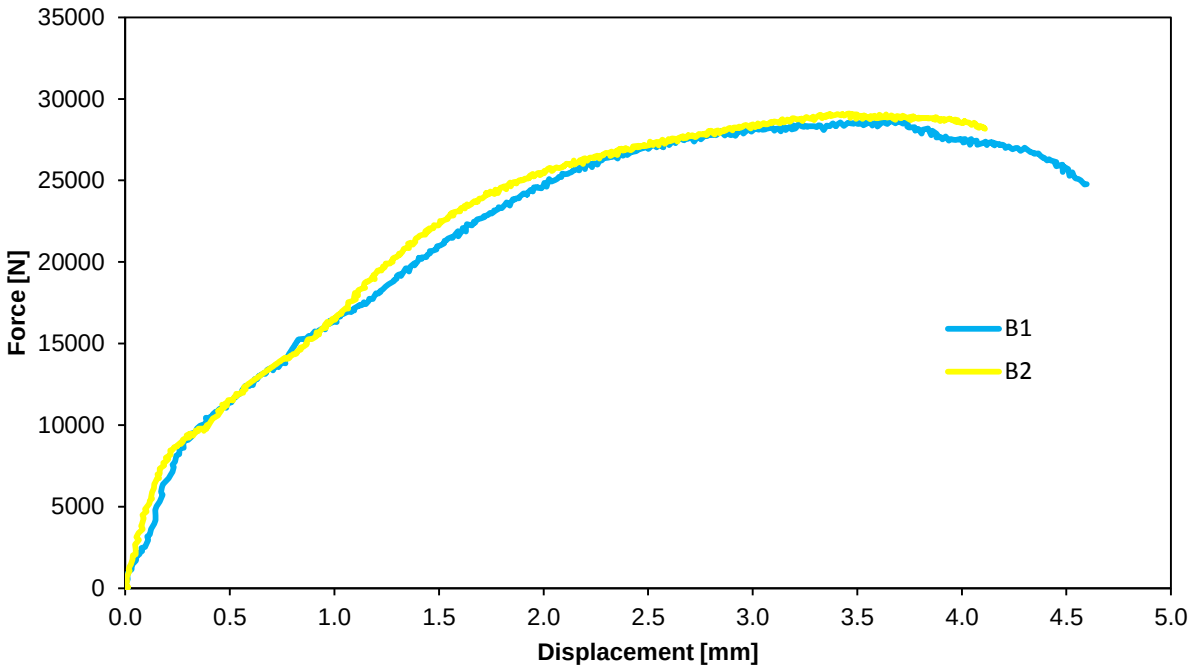

Figure 54: Load-displacement response for fully bainitic 30° butterfly test

For all three of the fully bainitic butterfly specimens that were tested in the 30° orientation, the major and minor strains are plotted in Figure 55. As expected, this particular specimen orientation resulted in a combined shear-tension loading, slightly closer to uniaxial tension than simple shear. In this figure, the theoretical strain ratios for uniaxial tension and simple shear are shown as black lines, dashed and dotted, respectively. For the specimens tested, it is apparent that the strain path that was observed for each specimen was largely proportional. For two of the three tests, the strain ratio appears to remain consistent throughout the test, up until fracture. However, in the third test, the major strain begins to increase much more rapidly than the minor strain towards the end of the test. Of the three orientations in which fully bainitic butterfly specimens were tested, this orientation resulted in the lowest fracture strains, with average true equivalent strains at fracture of 0.74 being measured.

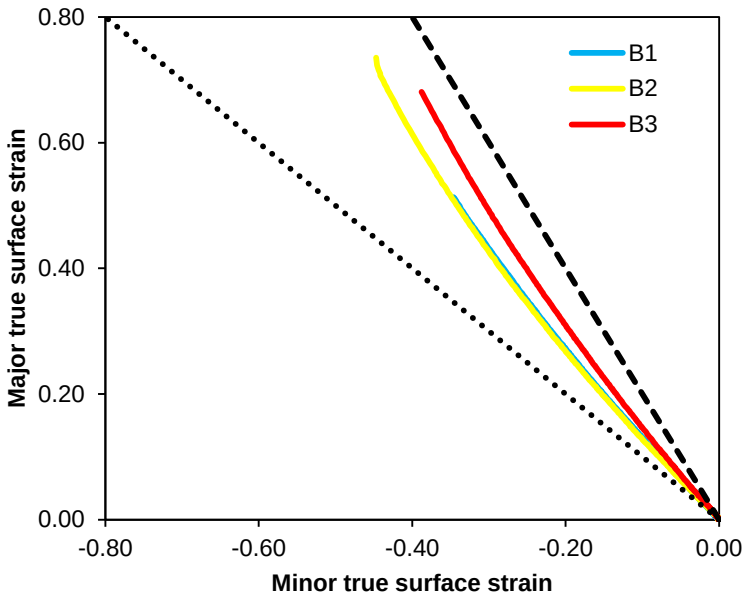

Figure 55: Major true surface strain vs. minor true surface strain for fully bainitic 30° butterfly test

Table 15: Failure strains for fully bainitic quench 30° butterfly test

Sample	1	2	3	Average
$\boldsymbol{\varepsilon_1}$	0.51	0.74	0.68	**0.64**
$\boldsymbol{\varepsilon_2}$	-0.35	-0.45	-0.39	**-0.39**
$\boldsymbol{\varepsilon_{eq}}$	0.66	0.84	0.75	**0.74**

For the material quench conditions included in Appendix J:

- Three fully martensitic and four intermediate forced air quench specimens were tested. For both of these material quench conditions, the macroscopic and localized behaviour was very consistent. Measured strain paths are also extremely proportional.
- Limited specimens were available for testing, due to inconsistent machining.

4.6 Hole Expansion – Fully Bainitic Material Quench Condition

For the hole expansion test, punch load and displacement are not recorded. The sole metric considered in this test is the diameter of the hole at the moment that a crack is observed through the specimen thickness. From this measurement, knowing the initial diameter of the hole, equivalent strain at failure can easily be derived, from the following equation:

$$\varepsilon_{equivalent} = \ln \frac{D_{final}}{D_{initial}}$$

where D_{final} is the outer diameter of the hole at failure [44].

To avoid the influence of a shear affected zone, the holes in all specimens were produced using a lubricated 10 mm reamer on a drill press. Prior to using the reamer, 3 smaller drill bits were used to incrementally increase the hole diameter. The specimen was flipped over before drilling with each successive drill bit in order to prevent the formation of a large burr. During the reaming operation, once the reamer had gone through the thickness of the material, the drill press was stopped and the reamer removed, in order to avoid creating scratches on the inner surface of the hole. The hole was then polished using sandpaper, beginning with 180 grit and successively increasing up to 800 grit in order to eliminate any scratches induced by the reaming process. A tested hole expansion specimen is shown in Figure 56, while the equivalent strain at fracture is plotted as a function of material quench condition in Figure 57.

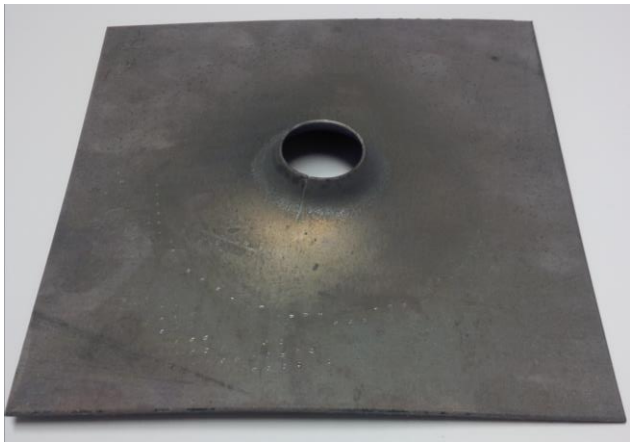

Figure 56: Tested hole expansion specimen (fully bainitic material quench condition)

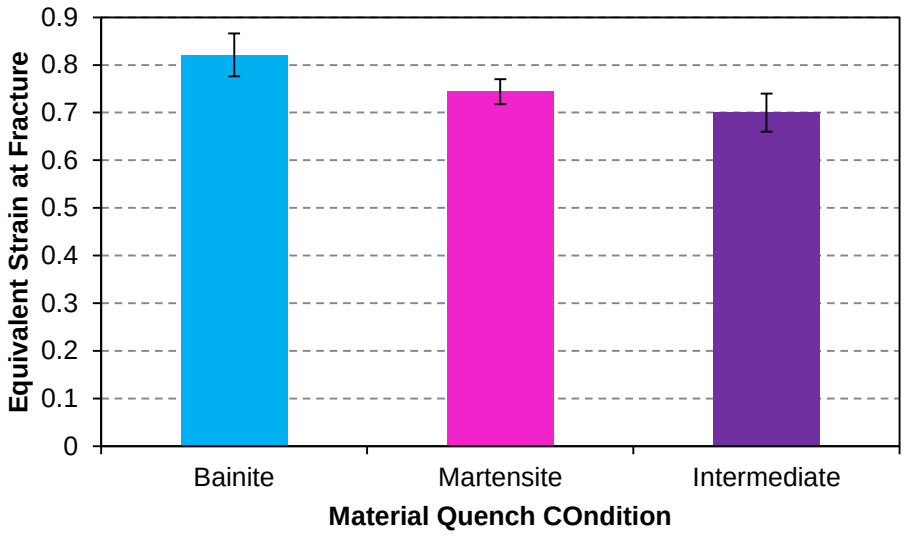

Figure 57: Equivalent strains at fracture for different material quench conditions

For the fully bainitic condition, the experimental results are listed in Table 16. As would be expected the fully bainitic material condition exhibited the greatest equivalent strain at failure of the material conditions investigated. The results were fairly consistent, with the exception of specimen number 8, which produced fracture strains that were more than 10% below the recorded average for this test. Since the material heat treatment for the fully bainitic material condition simply required removing the specimen from the furnace at 930 °C and allowing it to cool standing in still air, this material condition was likely the most consistent of those tested. Perhaps a more likely cause of the comparatively lower hole expansion and fracture strain observed in specimen 8 is the machining process used to produce these specimens. Although it was attempted to produce specimens as consistently as possible, using the methodology outlined in the previous section, it is possible that perhaps this specimen was not polished as consistently as the other specimens tested.

Table 16: Hole expansion results for fully bainitic material condition

Sample	1	2	3	4	5	6	7	8	Average	Standard Deviation
D_{final}	23.47	23.00	23.36	24.2	22.71	22.49	22.26	20.65	**22.77**	**1.05**
$\boldsymbol{\varepsilon_{eq}}$	0.85	0.83	0.85	0.88	0.82	0.81	0.80	0.73	**0.82**	**0.05**

For the material quench conditions included in Appendix K:

- The fully martensitic hole expansion specimens yielded the greatest consistency of the three material quench conditions tested.
- The FA-Q2 proved to be extremely finicky for producing consistent blanks for hole expansion, thus an excess of blanks were produced once a reasonably consistent microhardness could be achieved through the quenching process. However, some of these specimens were damage during the reaming operation. For the sake of consistency with the other two material quench conditions that were investigated in hole expansion, eight repeats were tested.

4.7 Hole Tensile – Intermediate Gleeble

The hole tensile test was only used for the intermediate quench condition produced on the Gleeble and the specimens produced from actual hot stamped parts with tailored properties. As noted in Section 2.2.1, this test was only used for these material conditions due to the fact that it was not possible to produce large enough blanks for hole expansion specimens with these microstructures. Various works have utilized tensile specimens with a central hole in order to generate a stress state of uniaxial tension at the free surface on the inner edge of the hole, as shown by Bao [42], Roth & Mohr [50], and Kofiani *et al*. [66]. Although the hole expansion test would have been preferred, due to ease of testing, since it does not require CNC-machined specimens or stereoscopic DIC, the hole tensile test was deemed an acceptable alternative.

However, since this was the only case in which this type of specimen geometry was used, it would have been preferable to do work to optimize this geometry prior to testing. Although Section 2.2.1 noted that the work of Bao investigated the influence of sheet thickness on fracture behaviour, and the conclusions of his work were used in developing the geometries used, there was insufficient material, particularly of the 400 and 700 °C tailored hot stamped material to do testing with more than one specimen geometry. In the future, if hole tensile specimens are to be used for fracture characterization work, preliminary work should be done to characterize the influence of the ratio of sheet thickness to ligament width for the material being investigated prior to using this specimen to obtain experimental fracture data. As this was not possible within the scope of this work, some of the tests that were conducted using hole tensile geometries exhibited fracture initiation slightly behind the edge of the hole, where the stress state is not uniaxial tension. A typical area of interest (AOI) for obtaining macroscopic information is shown in Figure 58a, while Figure 58b shows a typical local AOI.

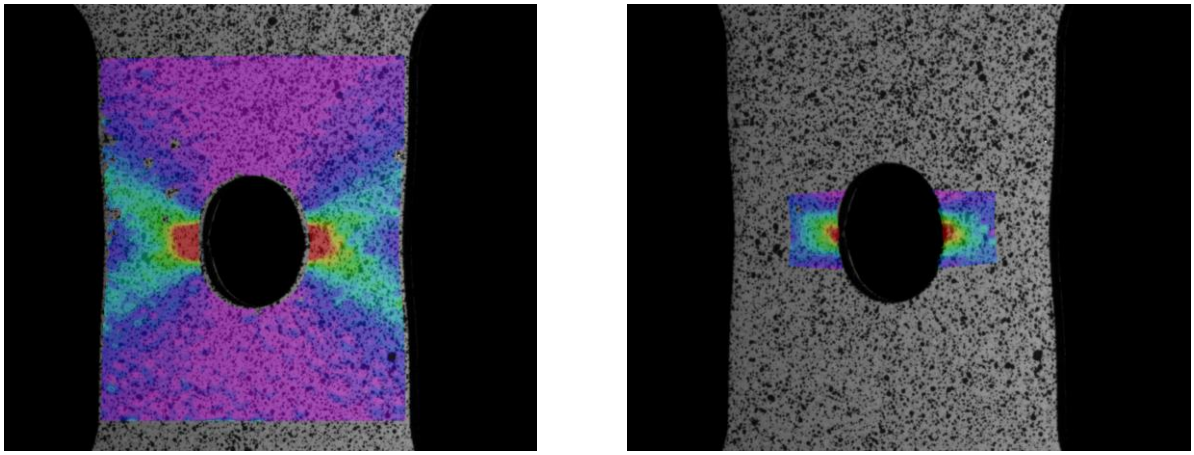

Figure 58a: full AOI, b: local AOI

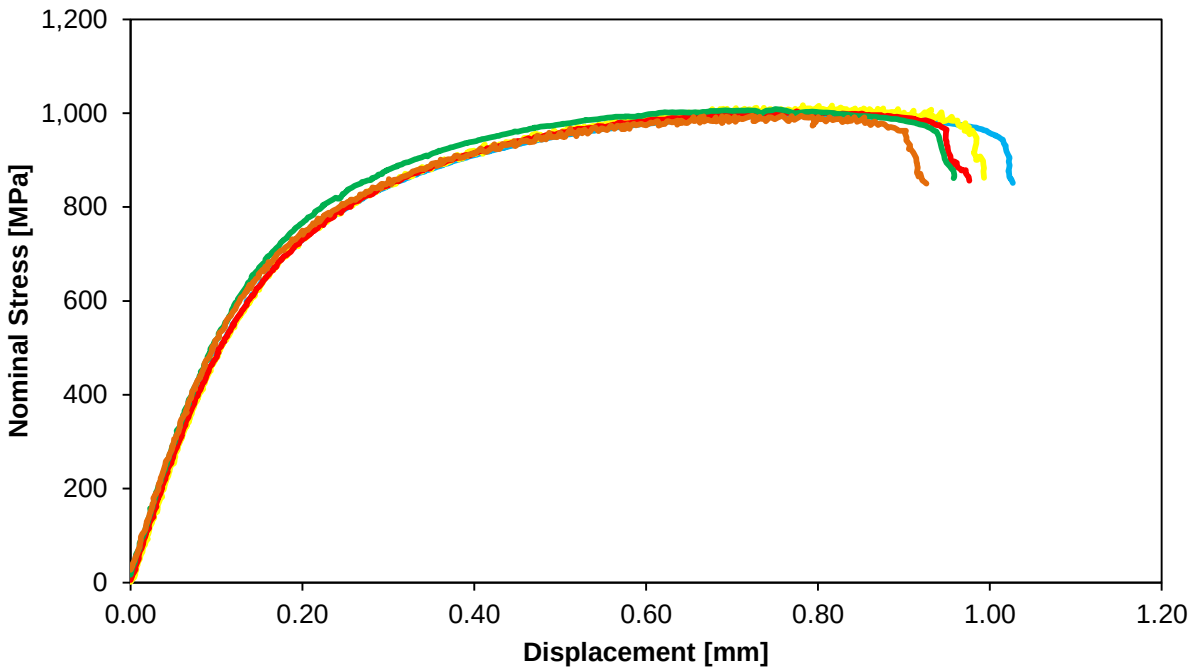

Figure 59: Nominal stress-displacement response for Gleeble intermediate quench hole tensile specimens

Due to the nature of DIC, measuring local strains at the hole edge is difficult, due to the fact that displacement and strain fields can only be computed for an area slightly smaller than the AOI [67]. More precisely, this means that there is an area at the perimeter of the selected AOI, with a width of ½ the selected subset size, in which these fields cannot be computed without expanding the AOI to include a region slightly beyond the edge of the specimen. The large strains observed near the hole edge necessitated the use of incremental correlation, an analysis option in Vic-3D, in which displacement and strain fields are computed by comparing each successive image with the previous image, rather than with the reference image of the undeformed specimen.

Nominal stress is plotted against displacement for this experiment, shown in Figure 59. The specimens were machined fairly consistently, as the hole size and ligament width were very consistent for all the specimens tested. Table 17 notes the measured dimensions of all of the

specimens that were tested. For the local AOIs, strain paths for the hole edge are plotted in Figure 60, while local strains at failure are compiled in Table 17. Evidently there is some variation in the strain paths for the specimens that were tested, with some specimens producing largely proportional strain paths that stayed close to uniaxial tension up until fracture, while the strain paths in other specimens evolved over the course of the test in a non-proportional manner, going towards plane strain.

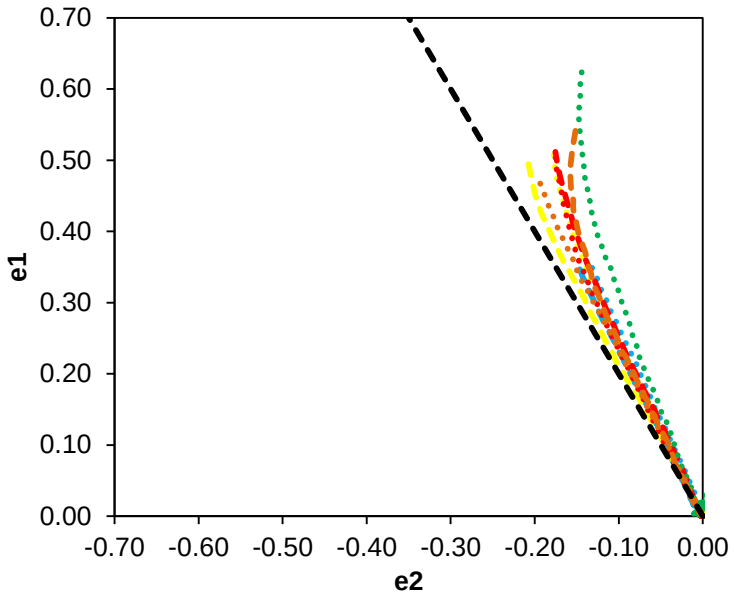

Figure 60: Major true surface strain vs. minor true surface strain for Gleeble intermediate quench hole tensile specimens

Table 17: Properties of Gleeble intermediate quench hole tensile specimens

Sample	1	2	3	4	5	Average	Standard Deviation
UTS (MPa)	996	1017	1005	1009	995	**1004**	**9.35**
Elongation	1.02	0.98	0.95	0.94	0.90	**0.96**	**0.04**
$\boldsymbol{\varepsilon_1}$	0.35	0.51	0.51	0.62	0.52	**0.50**	**0.10**
$\boldsymbol{\varepsilon_2}$	-0.14	-0.19	-0.18	-0.05	-0.17	**-0.15**	**0.06**
$\boldsymbol{\varepsilon_{eq}}$	0.36	0.51	0.52	0.70	0.53	**0.52**	**0.12**

Another challenge posed by the hole tensile geometry is the fact that two ligaments undergo similar straining. In most cases, fracture appeared to initiate simultaneously, but in some cases,

fracture was observed to occur in one ligament first. Slight variations in material thickness and ligament width, as well as the existence of defects or slight misalignment in the grips of the tensile frame are the most likely reasons for this discrepancy in response.

For the material quench conditions included in Appendix L:

- The 400 and 700 °C die quench tailored hot stamped hole tensile tests were produced from material with a nominal thickness of 1.8 mm. Unfortunately, due to the limited availability of material with this quench condition, it was not possible to optimize the geometry for this material. In each of the tests, fracture was observed slightly behind the hole edge, where the strain path tends towards plane strain tension, rather than uniaxial tension. The typical fracture location is indicated in Figure 61.

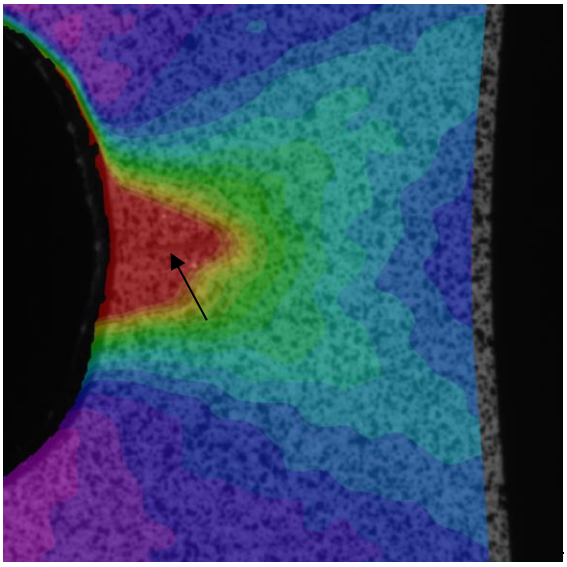

Figure 61: Contour plot showing fracture initiation behind specimen edge

4.8 90° Butterfly – 700 °C Tailored Hot Stamped

The butterfly apparatus was configured to test specimens in the 90° orientation only for specimens machined from the parts produced using hot stamping with in-die heating. Due to the limited size of the top hat sections, this particular test was used to generate a plane strain stress state, as there was insufficient material to produce dome test specimens. Previous work by

Anderson [68] indicated that the 90° orientation is suitable for generating a plane strain stress state. The same camera configuration and stereoscopic DIC techniques utilized for the previously described butterfly tests were used for these tests.

Five butterfly specimens produced from the 700 °C hot stamped rails were tested in the 90° orientation. The 700 °C hot stamped butterflies were tested after the 400 °C hot stamped butterflies, as this material condition was expected to be the most ductile of all of the material conditions investigated. Figure 62 shows the load-displacement response for each of the specimens. The butterfly specimens produced from 700 °C hot stamped parts exhibited extremely repeatable load-displacement behaviour, as well as similar displacement to failure.

The local strain measurements for each specimen, including major and minor strains, as well as equivalent strain at fracture are listed in Table 18. For this test, fracture was observed to initiate in the centre of the specimen for each of the specimens tested. The strain paths are shown in Figure 63, indicating that this test does induce a plane strain tension loading condition up until fracture, as the minor strains are extremely close to zero. Of all the plane strain tests conducted in this work, the 90° butterfly test of specimens created from axial crush rails exhibited the largest measured strains at failure.

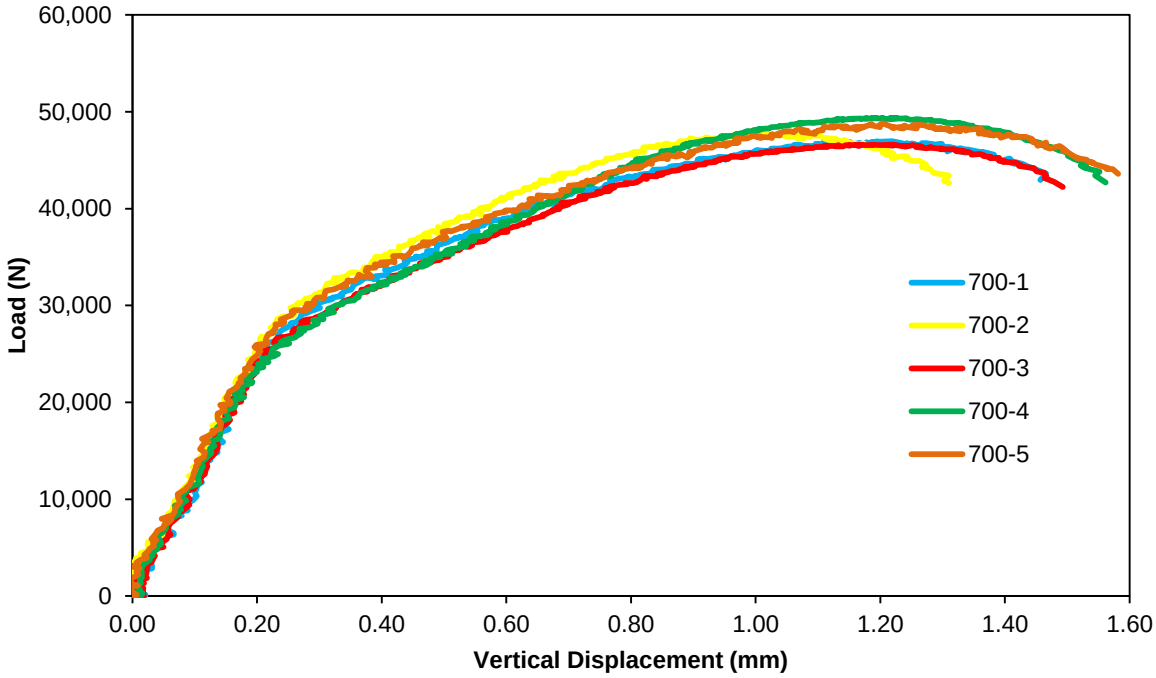

Figure 62: Load-displacement response for 700 °C quench 90° butterfly test

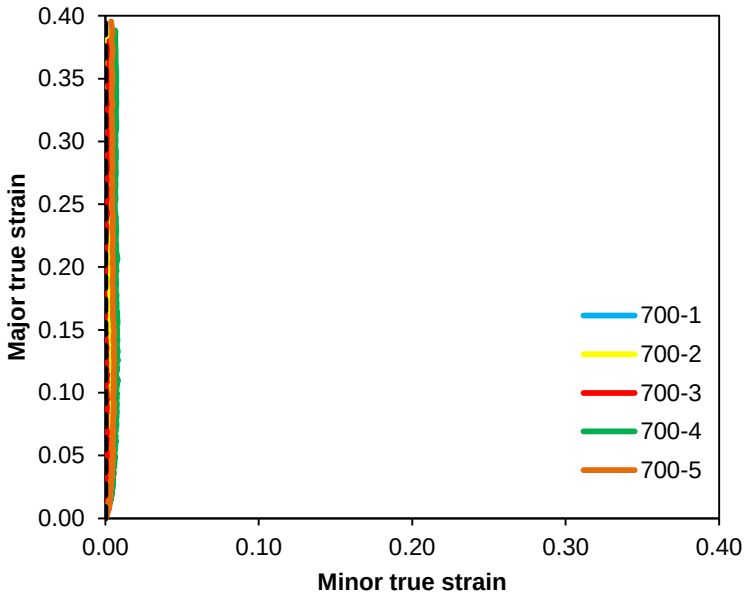

Figure 63: Major true surface strain vs. minor true surface strain for 700 °C quench 90° butterfly test

Table 18: Failure strains for the 700 °C quench 90° butterfly test

Sample	1	2	3	4	5	Average	Standard Deviation
$\boldsymbol{\varepsilon_1}$	0.35	0.39	0.38	0.39	0.40	**0.38**	**0.02**
$\boldsymbol{\varepsilon_2}$	0.00	0.00	0.00	0.01	0.00	**0.00**	**0.00**
$\boldsymbol{\varepsilon_{eq}}$	0.41	0.45	0.44	0.45	0.46	**0.44**	**0.02**

For the material quench condition included in Appendix M:

- The five repeats tested produced extremely repeatable results, with an average equivalent strain of 0.38 measured at fracture.

4.9 Plane Strain Dome – Fully Bainitic Material Quench Condition

For the plane-strain dome tests on each of the different material conditions, force and displacement output was obtained from the dome tester and synchronized with the images captured using Vic-Snap 8. Using Vic3-D stereoscopic DIC, dome height, major and minor strains, and local true equivalent strain at failure was obtained. In order to obtain strains at failure, for each of the tests, a circle with a diameter of 1.2 mm was centred at the location where the crack was initially observed. Since the initiation of a crack at the surface has the tendency to compromise the correlation, the measured failure strains were measured in the image corresponding to one frame before the image in which fracture was visible.

In order to minimize quenching induced warping of the blanks from which these specimens were machined, 8” x 8” blanks of USIBOR® 1500-AS in its as received state were clamped in the tooling of the MTS dome tester. Clamping in the tooling formed the impression of the lock bead in the 8” x 8” blank, enhancing the stiffness of the blank, which significantly reduced the extent of warping induced by the quenching process. The specimen geometry outlined in Section 2.2.3 was then machined from the quenched blanks.

For the fully bainitic material condition, 8 repeats of the plane-strain dome test were conducted. The punch load is plotted against dome height for this test in Figure 64. In comparison with the equi-biaxial test of this material condition (Section 4.10), punch loads in the plane strain dome test are substantially lower and appear to show somewhat greater variability between repeats. The measured dome heights at failure are also markedly lower than in the equi-biaxial case.

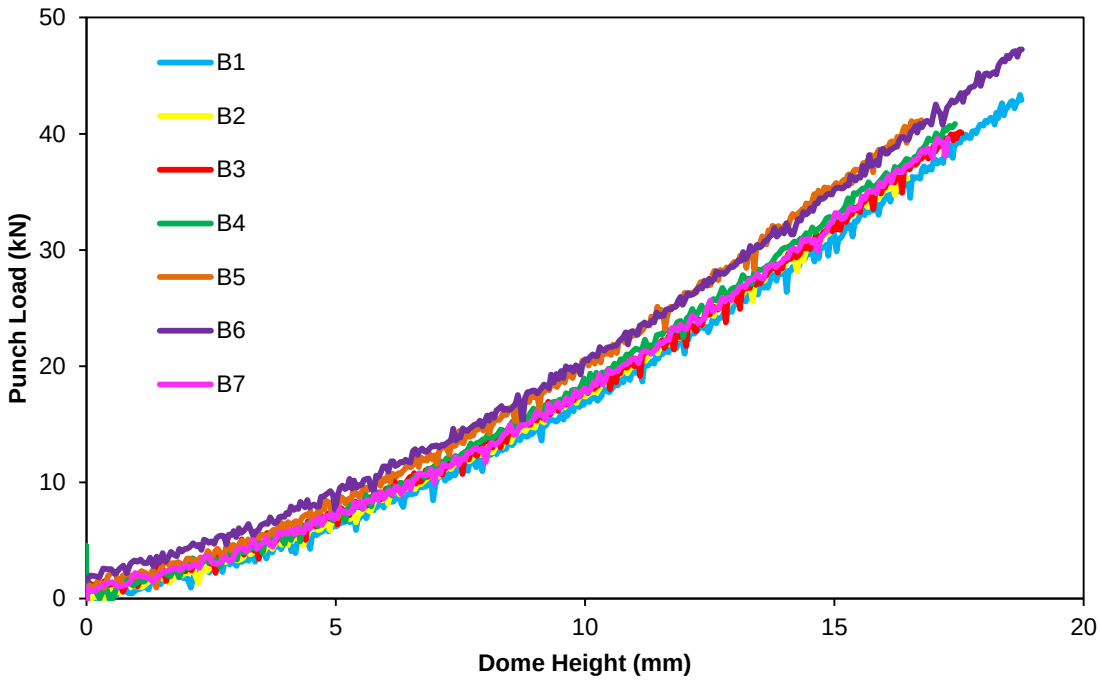

Figure 64: Punch load vs. dome height for fully bainitic plane strain dome test

Analyzing the strain state of the material in the area where fracture is initially observed, Figure 65 plots major strain against minor strain, while Figure 66 is a plot of minor strain/major strain ratio against dome height. Some variability between the test specimens is evident in both these figures, but it is also evident that the strain state evolves over the course of the test. Although the minor strain initially increases, largely due to bending and the dome curvature is formed, the minor strain begins to decrease at approximately 5% major strain, decreasing

sufficiently such that a strain state that is effectively plane strain is induced in the material. The plot of minor strain/major strain ratio provides an alternate means of demonstrating the how the strain state goes to that of plane strain over the course of the test. A perfectly plane strain test would have a strain ratio of zero for its entirety. The initial increase of the minor strain approximately equally to the major strain can likely be attributed to the use of a hemispherical punch for this test, which initially induces a strain path that is approximately equi-biaxial. To use a dome test apparatus to induce a strain path without this initial equi-biaxial portion, a flat punch is sometimes used, as in a Marciniak test [69].

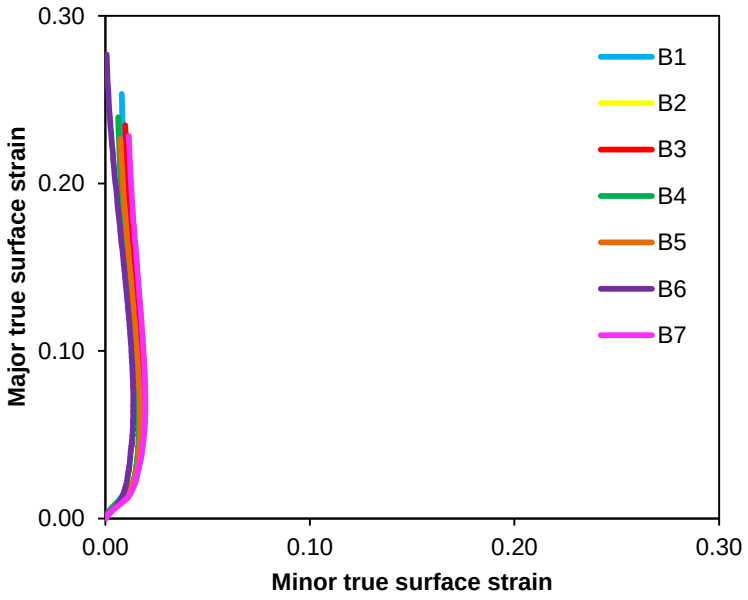

Figure 65: Major true surface strain vs. minor true surface strain for fully bainitic plane strain dome test

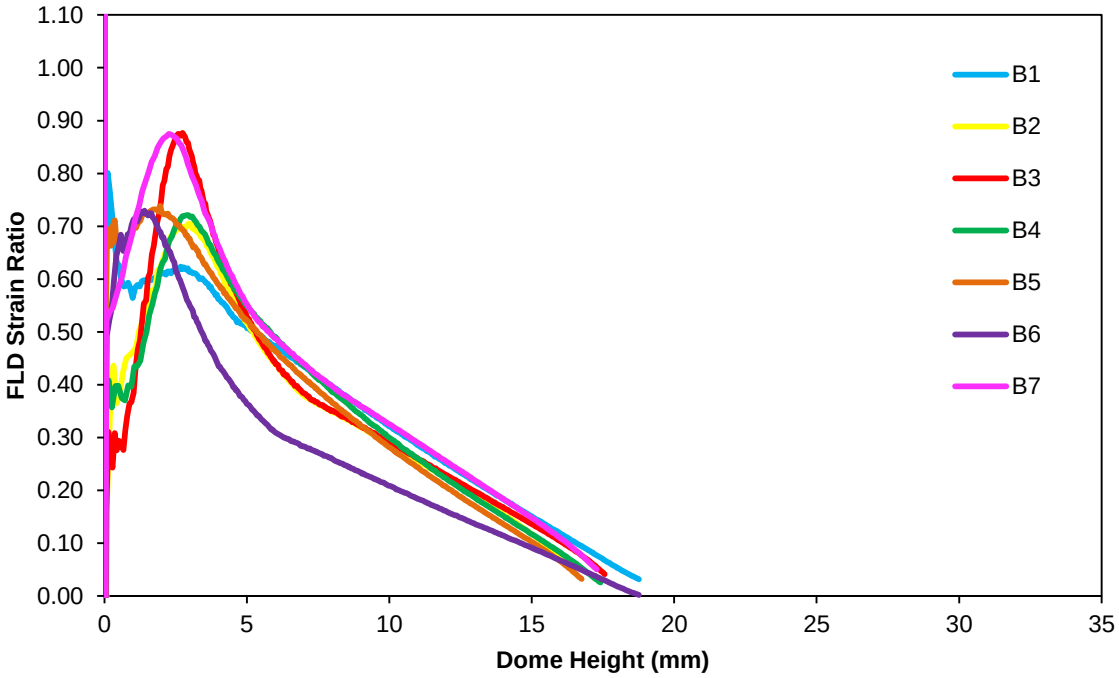

Figure 66: Minor true surface strain/major true surface strain vs. dome height for fully bainitic plane strain dome test

Figure 67 shows a typical contour plot of equivalent true strain for the fully bainitic plane strain dome test. The failure strain measurements are tabulated in Table 19. Most of the tests produced similar contour plots. Observable in this contour plot is a single necking region, indicated by the high levels of equivalent strain in a single band across the width of the specimen. Some tests unfortunately exhibited twin necking locations. The lubrication condition was observed to have a direct effect on both the fracture location and the precipitation of multiple necking regions, with insufficient lubrication resulting in multiple necking regions and a fracture location somewhat further away from the centre of the specimen. With additional lubrication, only one neck is observed and it is located somewhat closer to the centre of the specimen.

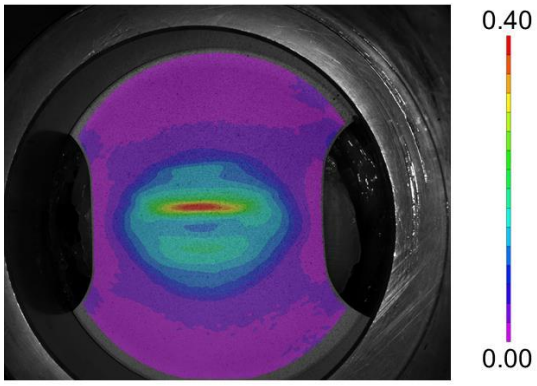

Figure 67: Typical equivalent strain contour plot for fully bainitic plane strain dome test

Table 19: Failure strains for fully bainitic plane strain dome test

Sample	1	2	3	4	5	6	7	Average	Standard Deviation
$\boldsymbol{\varepsilon_1}$	0.20	0.17	0.19	0.19	0.20	0.24	0.19	**0.18**	**0.04**
$\boldsymbol{\varepsilon_2}$	0.01	0.01	0.01	0.01	0.01	0.00	0.01	**0.01**	**0.00**
$\boldsymbol{\varepsilon_2/\varepsilon_1}$	0.05	0.07	0.06	0.04	0.04	0.01	0.06	**0.06**	**0.05**
$\boldsymbol{\varepsilon_{eq}}$	0.39	0.34	0.35	0.36	0.35	0.38	0.34	**0.36**	**0.02**

For the material quench conditions included in Appendix N:

- Due to the comparatively lower ductility of the fully martensitic and intermediate forced air quench material quench conditions, the initial biaxial strain path that resulted from conducting this test with a hemispherical punch appears more significant than in the fully bainitic case.

4.10 Equi-biaxial Dome – Fully Bainitic Material Quench Condition

For the fully bainitic equi-biaxial dome tests, the testing methodology used was the same as that of the plane strain dome tests, discussed in Section 4.9. Plots of punch load versus dome height, major true surface strain versus minor true surface strain, and minor true surface strain/major true surface strain ratio versus dome height are shown in Figure 68, Figure 69, and Figure 70, respectively. Figure 68 shows extremely good repeatability for all of the repeats of this test, as the force-dome height response is nearly identical for all of the specimens tested.

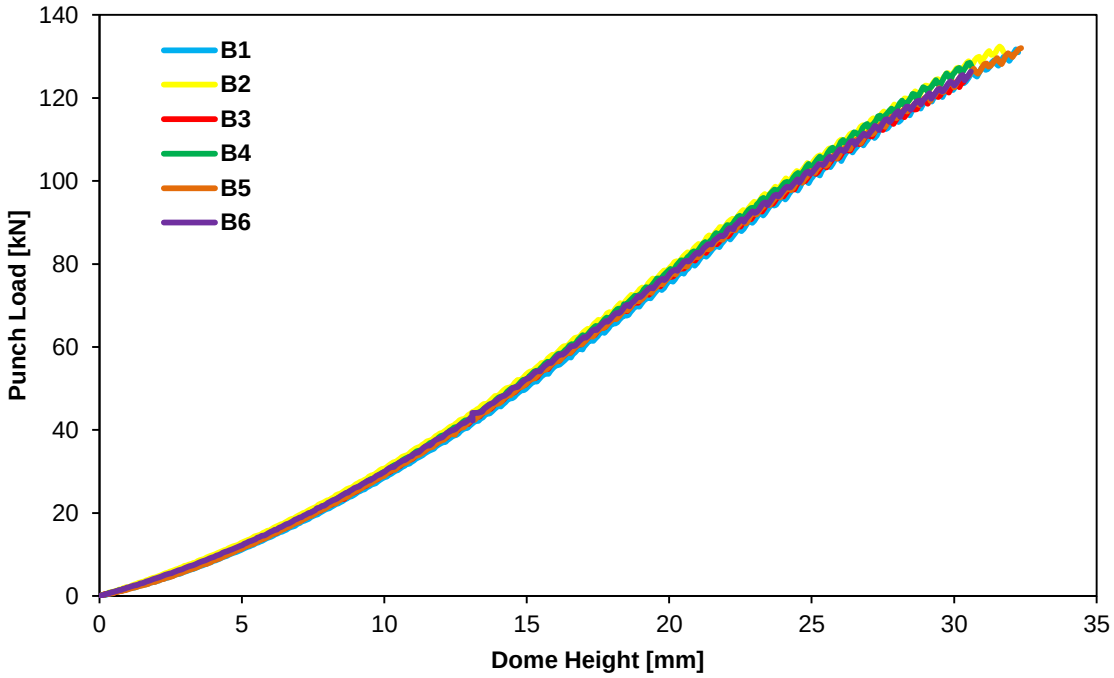

Figure 68: Punch load vs. dome height for fully bainitic equi-biaxial dome test

Using Figure 69 and Figure 70 to make inferences about the strain state of the specimen at the location where fracture was first observed, it is evident that the strain state for this test is effectively equi-biaxial; major and minor strains are almost identical for the entire test, yielding an FLD ratio very close to unity. Necking appears to occur in a few of the repeats just prior to failure, evidenced by the major strain increasing disproportionately to the minor strain near the end of the test. For each repeat, the strains plotted are those at the location of fracture, which was close to the centre of the specimen in all cases. Figure 70 presents this in an alternative form, showing the variation of minor to major strain prior to fracture.

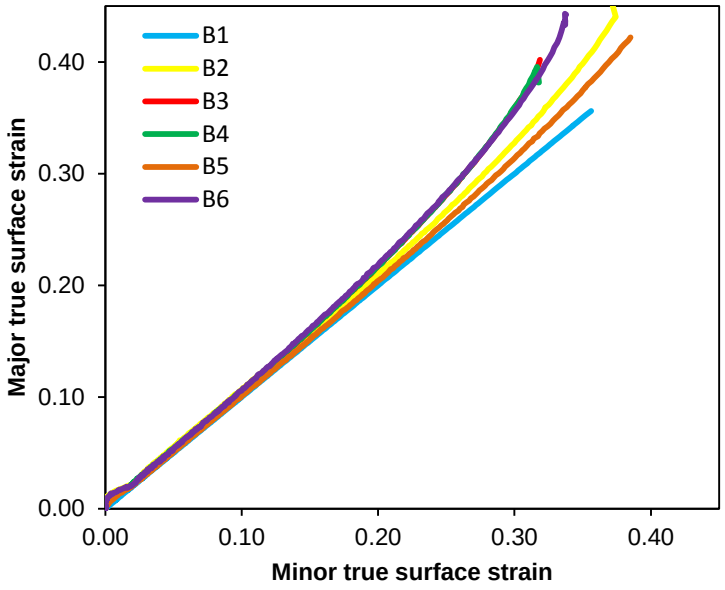

Figure 69: Major true surface strain vs. minor true surface strain for fully bainitic equi-biaxial dome test

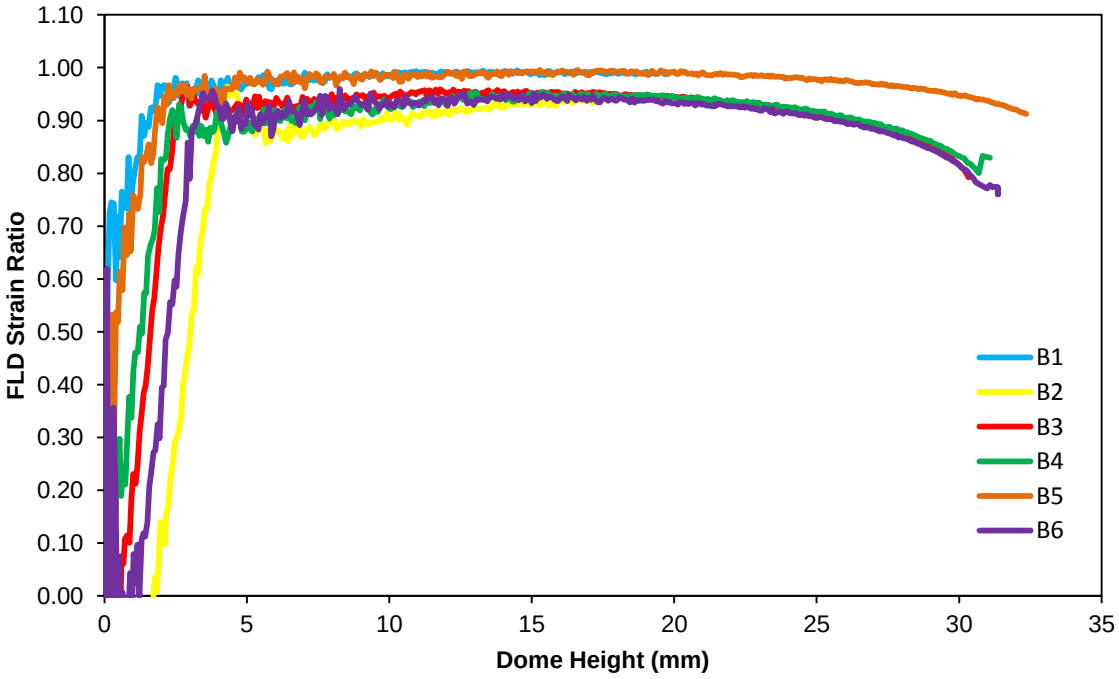

Figure 70: Minor true surface strain/major true surface strain vs. dome height for fully bainitic equi-biaxial dome test

Figure 71 shows a characteristic contour plot of equivalent strain, as well as the typical location of fracture for this test. The true surface strains at failure for this test are tabulated in

Table 20. The ratio of minor to major strain included in Table 20 deviate somewhat from unity, as they are the ratio of the strains one frame prior to the appearance of a crack. As Figure 70 shows, the ratio for the majority of the test was closer to unity.

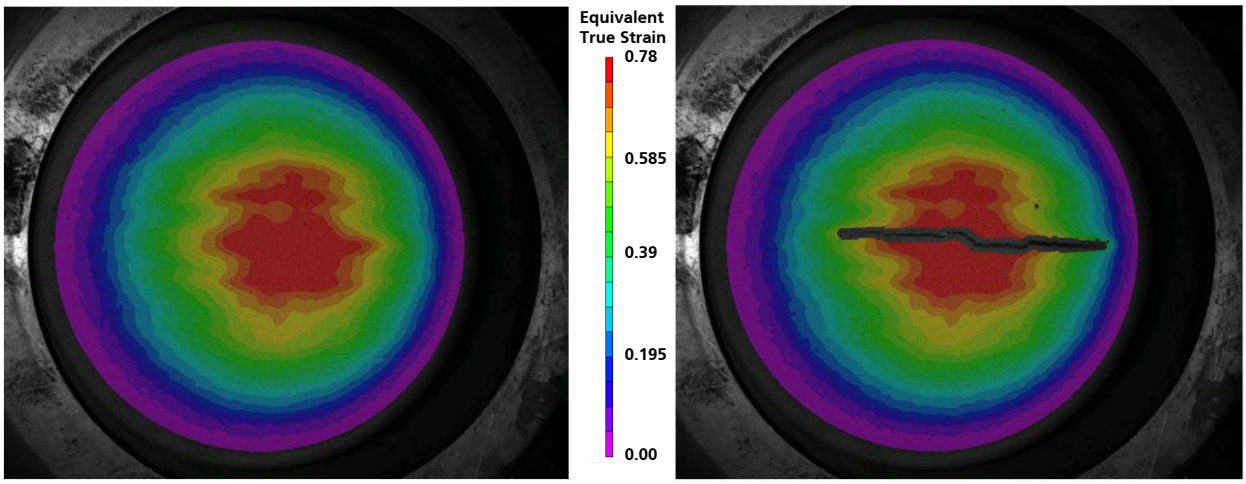

Figure 71: Equivalent strain contour showing typical fracture location for fully bainitic equi-biaxial dome test. The contour plot on the left corresponds to the image one frame before fracture is observed

Table 20: Failure strains for fully bainitic equi-biaxial dome test

Sample	1	2	3	4	5	6	Average	Standard Deviation
$\boldsymbol{\varepsilon_1}$	0.38	0.44	0.40	0.39	0.42	0.43	**0.41**	**0.02**
$\boldsymbol{\varepsilon_2}$	0.36	0.37	0.32	0.32	0.39	0.33	**0.35**	**0.03**
$\boldsymbol{\varepsilon_2/\varepsilon_1}$	0.93	0.85	0.79	0.80	0.91	0.78	**0.85**	**0.06**
$\boldsymbol{\varepsilon_{eq}}$	0.74	0.83	0.72	0.71	0.81	0.76	**0.76**	**0.05**

Table 20 indicates that for the 6 repeats, this test was extremely consistent. While the FLD strain ratio at failure of specimens #3, 4, and 6 is markedly lower than that of the other repeats, the test parameters such as lubrication, frame rate, and punch speed were kept consistent for all six repeats. The average measured equivalent strain at failure is considerable. Compared to the performance of the fully bainitic microstructure in the other experiments, the equibiaxial dome test was bested only by the 0° and 10° butterflies, as well as the hole expansion test.

For the material quench conditions included in Appendix O:

- For the fully martensitic material quench condition, no necking prior to fracture was observed.
- Considerable time was expended attempting to produce blanks with homogenous microhardness using the FA-Q2. This second-rate material quench condition consistently exhibited fracture away from the centre of the specimen, with the measured strain paths indicating a strain state between plane strain and equi-biaxial tension.

5 FRACTURE CHARACTERIZATION

In this section, the approaches used to develop fracture loci for the various material quench conditions investigated in this work are outlined. Fracture characterization using the experimental results presented in Chapter 4, is performed using the experimentally determined strain paths and fracture strains. By assuming a von Mises yield criterion for this material, the experimentally derived strain ratios can be used to obtain an estimate of the stress state in the form of stress triaxiality. Following [70], the ratio of minor strain to major strain is denoted as α:

$$\alpha = \frac{\varepsilon_2}{\varepsilon_1}$$

from which β is calculated:

$$\beta = \frac{2\alpha + 1}{2 + \alpha}$$

Adopting assumptions of von Mises yielding and plane stress loading, the stress triaxiality, η, can be defined in terms of β:

$$\eta = \frac{\beta + 1}{3\sqrt{\beta^2 - \beta + 1}}$$

5.1 Butterfly Fracture Strains

In the case of the butterfly tests that were conducted, the DIC was able to maintain correlation up until the specimens fractured, enabling direct measurement of the limit strains at onset of failure.

For the all of the butterfly tests, the average stress state and fracture strain for the butterfly tests conducted on the fully bainitic, fully martensitic, and intermediate forced air quench material conditions are listed in Table 21.

Table 21: Comparison of strains at fracture and stress states for butterfly tests

	Equivalent strain	Stress triaxiality
0° Fully bainitic	0.90	0.005
10° Fully bainitic	0.77	0.064
30° Fully bainitic	0.74	0.187
0° Fully martensitic	0.54	0.028
10° Fully martensitic	0.52	0.040
30° Fully martensitic	0.46	0.120
0° Intermediate forced air quench	0.68	0.013
10° Intermediate forced air quench	0.64	0.059
30° Intermediate forced air quench	0.46	0.176
15° 400 °C tailored hot stamped	0.94	0.09
90° 400 °C tailored hot stamped	0.38	0.59
15° 700 °C tailored hot stamped	1.02	0.09
90° 700 °C tailored hot stamped	0.44	0.58

Slight variation in the stress states obtained from the strain paths is observed, with the less brittle material quench conditions generating stress states closer to the theoretical triaxiality for simple shear, zero.

For the 10° butterfly tests, the failure strain and stress triaxiality for these three material quench conditions are listed in Table 21. As discussed earlier, in Section 4.4, an analytical relation between loading angle and stress triaxiality had been used initially to estimate the resulting stress state that corresponded to various mixed mode loading conditions. Considering this relation, there had been expected to be a greater variation in stress state induced by rotating the grips of the butterfly apparatus from 0° to 10°. However, after analyzing the strain paths, it is evident that the resulting stress state induced by the 10° butterfly test is very similar to that of the 0° butterfly test, particularly for the fully martensitic material condition. For the fully martensitic and intermediate forced air quench material conditions, the measured fracture strains in the 0° and 10° butterfly specimen orientations are similar in magnitude, while there is a decrease of

approximately 15% for the fully bainitic specimens when comparing the results from the 0° and 10° orientations.

The final orientation in which the butterfly specimens of these three material conditions were tested is the 30° orientation. The average equivalent strains at failure and stress triaxialities obtained from these tests are listed in Table 21. Again, for this orientation, the stress triaxialities obtained from the fully bainitic and intermediate forced air quench material conditions are very similar, while that of the martensitic material condition is significantly lower. Considering measured equivalent strains at fracture, the fully bainitic specimens tested in the 30° orientation were very similar to those measured in the 10° orientation. In contrast, the equivalent strains measured at fracture for the fully martensitic and intermediate forced air quench material conditions tested in the 30° orientation are the lowest of the three butterfly orientations investigated.

For the butterfly specimens that were machined from the top sections of the tailored hot stamped axial crush rails, the specimens were tested with the grips oriented in the 15 and 90° orientations, as discussed in sections 4.4 and 4.8. The 15° orientation resulted in a combined shear-tension loading condition, while the 90° orientation generated a stress state of plane strain tension. The two die quenched material conditions exhibited similar levels of ductility to fracture and following analysis of the strain histories, also yielded similar stress triaxialities in this test.

5.2 Mini Shear Fracture Strains

As with the butterfly tests, the mini shear tests enabled strains at fracture to be obtained through the use of DIC. For the two die quenching conditions that were used to produce the tailored hot stamped axial crush rails, the stress triaxiality and equivalent strain at fracture are listed in Table 22. Additionally, as part of non-proportional loading tests that are discussed in

Chapter 6, mini shear specimens were also produced from material that had been quenched to the fully bainitic material quench condition to use as a baseline. The result of these experiments is also listed in Table 22.

Table 22: Comparison of strains at fracture and stress states for mini shear tests

	Equivalent strain	Stress triaxiality
400 °C tailored hot stamped	1.01	0.00
700 °C tailored hot stamped	1.05	0.00
Fully bainitic	0.89	0.00

5.3 Hole Expansion Fracture Strains

For the hole expansion simulation, a model was set up to represent the experimental setup used in this experiment. However, rather than model the 5" x 5" blank in as a square, for the purpose of creating a axisymmetric model, a circular blank of equivalent area was modeled, resulting in a blank with a diameter of 5.64". For the model with an element length of 0.1 mm, the blank consists of 153,600 constant stress, solid hexahedral elements (solid element formulation 1 in LS-DYNA). Puso enhanced assumed strain stiffness hourglass viscosity [57] was used in this model, to minimize hourglassing around the outer edge of the hole. The tooling in this model has all been modeled as meshed rigid bodies. While no mass scaling was used in this simulation, time scaling was used in order to reduce computation time.

For contact between the different components, surface to surface contacts were defined between the blank-punch, blank-die, and blank-binder interfaces, with the blank defined as the slave surface in each case. Between the blank and punch, a coefficient of friction of 0.05 was applied. Quarter symmetry boundary conditions were applied to reduce the size of the model. Velocity control was used to control punch movement, while a 50 [kN] load was applied to the binder to clamp the blank. The model is shown in Figure 72, with the blank shown in red, the conical punch in blue, the die in yellow, and the binder in green.

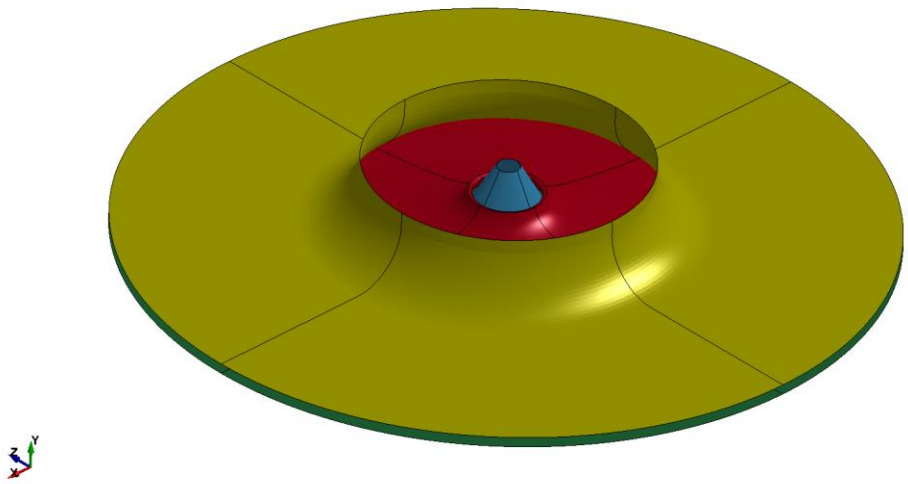

Figure 72: Hole expansion model

Since the only metric obtained from the hole expansion test is the initial hole diameter and the hole diameter at fracture, the model is used to confirm the assumption of a uniaxial tensile stress state being induced at the upper edge of the specimen. The test apparatus was not fitted with a load cell, so correlating punch loads and displacements from model with experimental results is of no value. For each of the fully bainitic, fully martensitic, and intermediate forced air quench material conditions, the measured diameters at fracture from the experiments were used to determine termination times for the models. For the fully bainitic material quench condition Figure 73 plots stress triaxiality and Lode angle parameter against the equivalent strain at the edge of the hole.

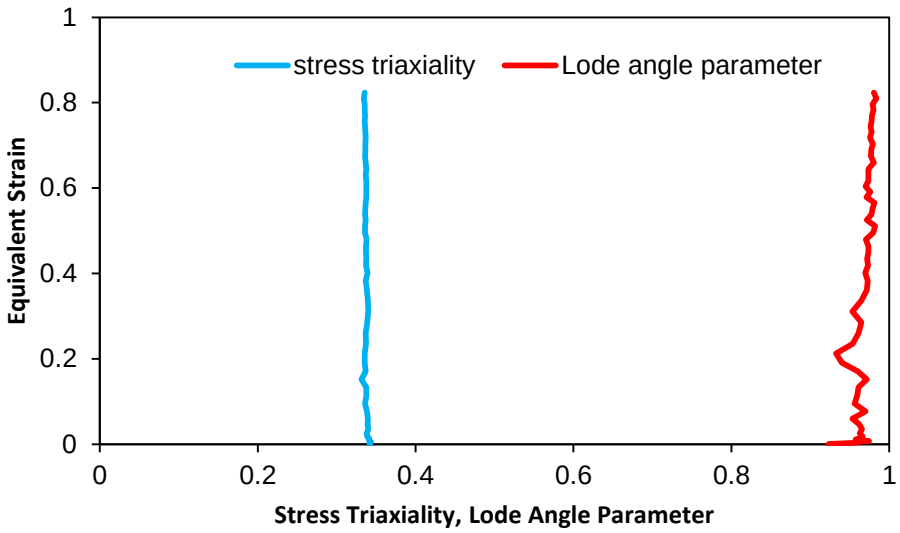

Figure 73: Evolution of stress triaxiality and Lode angle parameter at outer edge for fully bainitic hole expansion model

Evidently, for each of the material conditions tested, at the outer edge of the hole (which is never in contact with the punch), the material is under a stress state of uniaxial tension (stress triaxiality of 1/3 and Lode angle parameter near unity)for the duration of the test. This is the location where fracture was observed to initiate in the experiments. Also obtained from the models of the hole expansion test are equivalent strains of individual elements at the hole diameters corresponding to fracture. The strains from the model are comparable to those measured directly from the experiments, as Table 23 indicates.

Table 23: Comparison of equivalent strains at fracture for hole expansion experiment and model

	Fully bainitic	**Fully martensitic**	**Intermediate forced air quench**
Experiment	0.82	0.74	0.70
Model	0.80	0.74	0.68

5.4 Plane Strain Dome Fracture Strains

For the plane strain dome test, the strain paths are again used from the tests for the three different material conditions in order to approximate stress triaxiality. The fact that this test

generated a plane strain stress state for the three different conditions is highlighted in Table 24, which shows the equivalent strains and stress triaxiality at fracture.

Table 24: Comparison of strains at fracture and stress states for plane strain dome tests

	Equivalent strain	Stress triaxiality
Fully bainitic	0.36	0.59
Fully martensitic	0.15	0.60
Intermediate forced air quench	0.22	0.62

5.5 Equi-biaxial Dome Fracture Strains

For the equi-biaxial dome test, in each of the experiments conducted, fracture was observed to initiate near the centre of the blank. In order to determine the stress state that corresponded to the fracture strains measured in these tests, the ratios of the major and minor strain are considered, and are used to obtain an estimate of stress triaxiality. Considering the three material conditions for which equi-biaxial dome tests were conducted, the equivalent strains at failure and stress triaxiality are noted in Table 25. The fully martensitic and fully bainitic material quench conditions indicate a near biaxial triaxiality of 2/3.

Table 25: Comparison of strains at fracture and stress states for equi-biaxial dome tests

	Equivalent strain	Stress triaxiality
Fully bainitic	0.76	0.67
Fully martensitic	0.35	0.67
Intermediate forced air quench	0.30	0.65

As discussed in Section 4.10, the strain ratio for the intermediate forced air quench stress state is significantly less than unity (a strain ratio of unity indicates perfectly biaxial tension).

5.6 Fracture Loci

While the experiments conducted successfully induce a range of stress states and also allow for failure strains to be obtained for each, the use of sheet material limits the range of stress states achievable. In order to accurately predict fracture for a broad range of stress states, a fracture locus can be calibrated using the experimental points, yielding a surface of equivalent strain as a function of stress triaxiality and Lode angle parameter. The current work considers

sheet material with an inherent plane stress assumption for which the maximum triaxiality is limited to 2/3. While a multitude of fracture loci have been postulated in literature, in this work, the fracture locus proposed by Bai [30] (introduced in Section 1.3.2) is used.

Another popular fracture locus in the literature is the modified Mohr-Coulomb fracture locus, often seen in the works of Wierzbicki [31] [32] and Mohr [52], which is also introduced in Section 1.3.2. While the MMC criterion considers some physical influence of the stress triaxiality and Lode angle parameter on fracture strain, the locus developed by Bai is more flexible, considering these two parameters as independent variables. However, for the case of plane stress, where there are only two non-zero principal stresses, since the stress triaxiality can uniquely define the stress state, as discussed in Section 1.3.3:

$$\xi = -\frac{27}{2}\eta\left(\eta^2 - \frac{1}{3}\right)$$

Since the final application of this fracture characterization work will be in simulations, which use shell elements and thus assume plane stress for this work, only plane stress fracture is considered, thus rather than using a surface of fracture strain as a function of stress triaxiality and Lode angle parameter, a curve of fracture strain as a function of stress triaxiality will suffice. For this case, the Bai locus often provides better agreement with the experimental points than the MMC criterion.

Due to the fact that the notched tensile specimens demonstrated considerable variation in stress state from the beginning of the test to the end and fracture initiation location could not be definitively determined, these tests were not considered when calibrating fracture loci. Since the test programme of the intermediate Gleeble-produced material consisted almost entirely of notched tensile specimens, no fracture loci were fit for this material condition. This particular microstructure was not found in any appreciable quantity in the tailored hot stamped parts of

Omer [37] or Prajogo [71] but was rather a laboratory novelty [7]; thus, it is of limited usefulness in this work. The fit for the fully bainitic material quench condition is shown in Figure 74, while the other material quench conditions are included in Appendix Q. The symbols plotted indicate the individual measured strains at failure and are plotted to indicate the degree of scatter. For each material quench condition, the fracture loci presented here consist of a hybrid of the Bai and MMC fits. The physically-influenced MMC criterion is used for extrapolating the fracture locus in the triaxiality domain corresponding to compression, while the Bai criterion is used to fit the region of the fracture locus between triaxiality of zero and 2/3. To contrast the fracture loci for the different material conditions investigated in this thesis, all of the fracture loci are overlaid in Figure 75 (curves are plotted without scatter bands for clarity). Overall, the fracture loci produced for the material quench conditions investigated in this thesis indicated a correlation between material hardness and fracture strain, with the fully martensitic material (485HV) possessing the lowest ductility, while the material produced through die quenching at 700 °C (185HV) was the most ductile. Although the fully martensitic material quench condition fracture strains in uniaxial tension are comparable to some of the other material quench conditions, under most stress states, it is the least ductile material by a considerable margin. The greatest variation in fracture strain is around the simple shear stress state (triaxiality of zero).

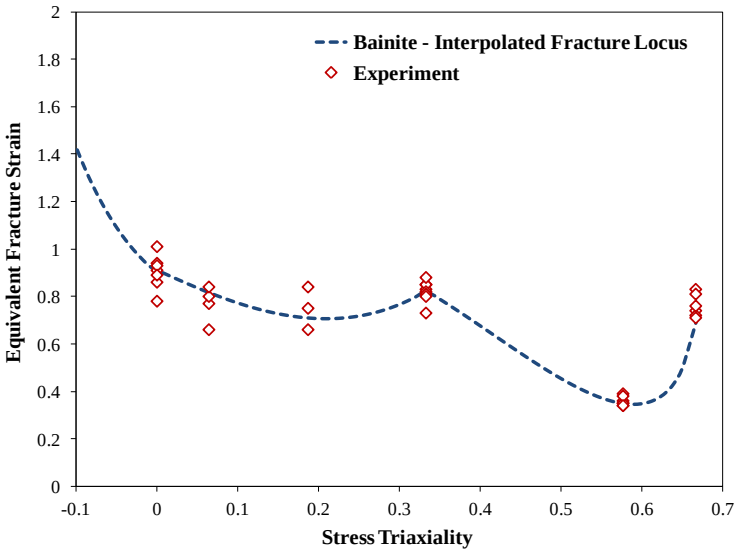

Figure 74: Fracture locus for fully bainitic material condition

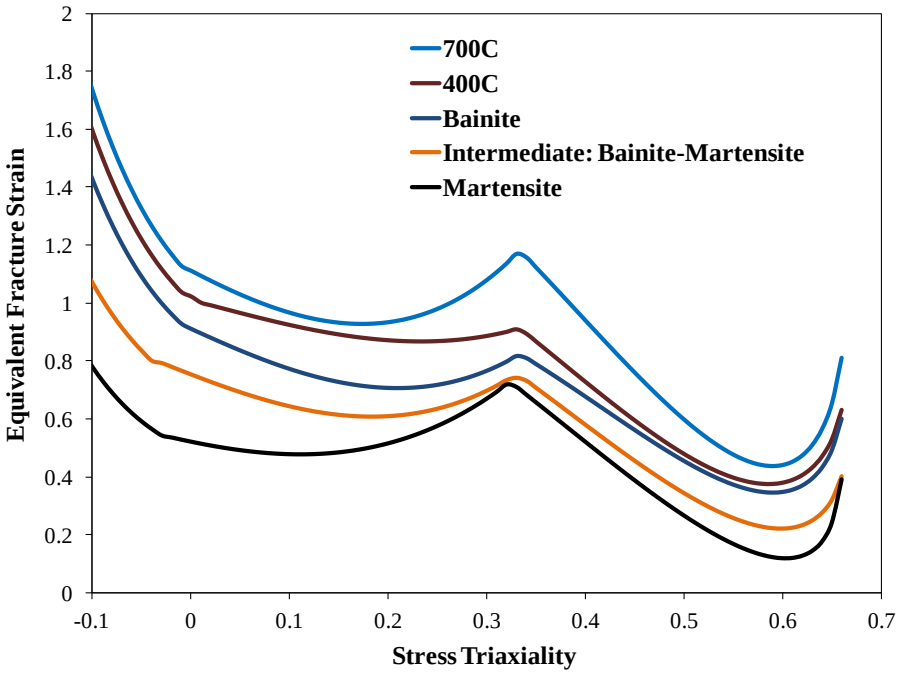

Figure 75: Fracture loci for five material quench conditions

6 FAILURE PREDICTIONS UNDER NON-PROPORTIONAL LOADING PATHS

In order to investigate the suitability of the phenomenological approach to damage modeling that is considered in this thesis, a series of experiments was conceived, in order to induce large changes of strain path. The approach used was as follows: initially, a 203.2 mm x 203.2 mm blank is austenized and quenched, using the same thermal processing route that was used for the fully bainitic material condition in this work. This blank was subsequently biaxially stretched in the centre of the specimen, to 22-25% equivalent strain (measured using stereoscopic DIC), using a flat punch, in a Marciniak test. The Marciniak test employs a carrier blank with a central hole in order to eliminate friction between the punch and the centre of the blank, a schematic of which is provided in Figure 76 [69]. It should be noted, while the tooling depicted in this figure indicates a lock bead, whereas the actual tooling adopted for the biaxial stretching comprised flat dies without a lock bead.

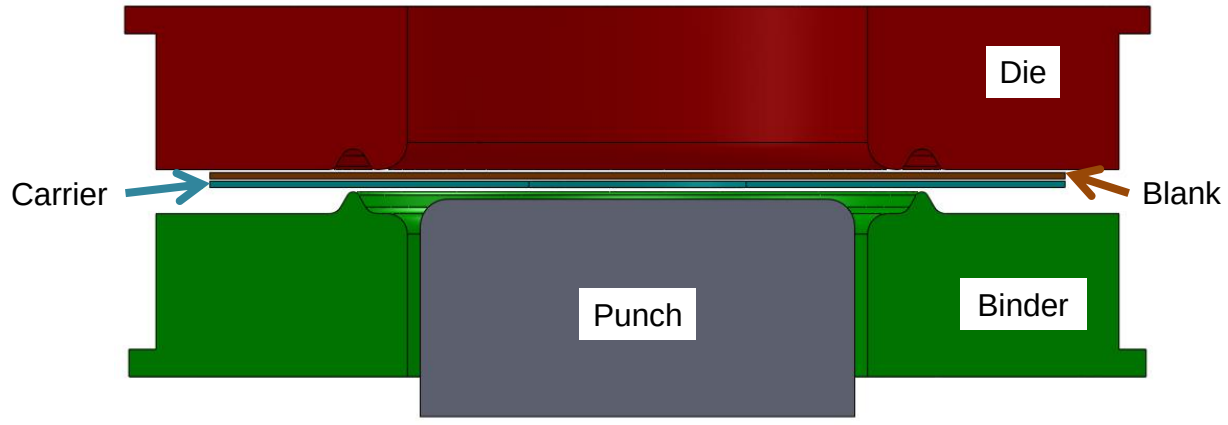

Figure 76: Schematic of a Marciniak test

Since no knurled die set was available, rings of sandpaper were mounted between the blank and the die to increase friction. An example of the relatively uniform strain distribution in the centre section of the blank is shown in Figure 77.

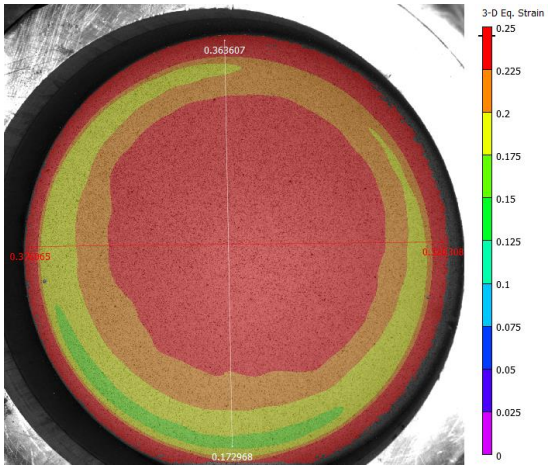

Figure 77: Contour plot showing distribution of equivalent strain in biaxially stretched Marciniak specimen [72]

Following this biaxial stretching operation, the stretched portions of the specimens were then machined to extract pre-strained mini shear and mini dog bone uniaxial tensile specimens, as shown in Figure 78. These specimens were then tested in the hydraulic Instron mechanical test apparatus shown in Figure 18, under quasi-static (0.003 s^{-1}) loading conditions, while applying stereoscopic DIC.

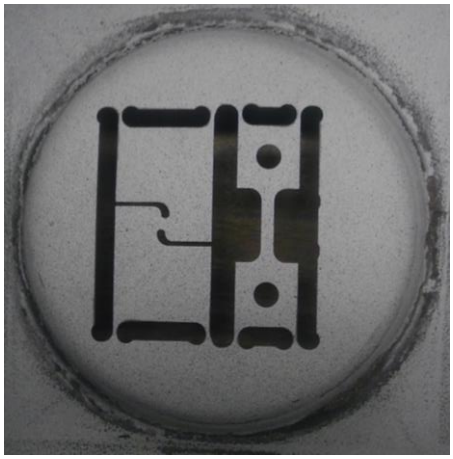

Figure 78: Specimens machined from centre section of biaxially pre-strained blank

The strain paths for the mini shear and mini dog bone uniaxial tensile specimens were then converted to stress triaxiality *versus* equivalent strain histories, using the methodology outlined in Chapter 5. Plotting equivalent strain as a function of stress triaxiality, the evolution of the

stress state for these two sets of strain histories can be observed, as shown in Figure 79. In addition, mini shear and mini dog bone uniaxial tensile specimens that were produced at this time from material that had not been pre-strained were also tested as a baseline. Stress state evolution for these additional tests are also included in Figure 79.

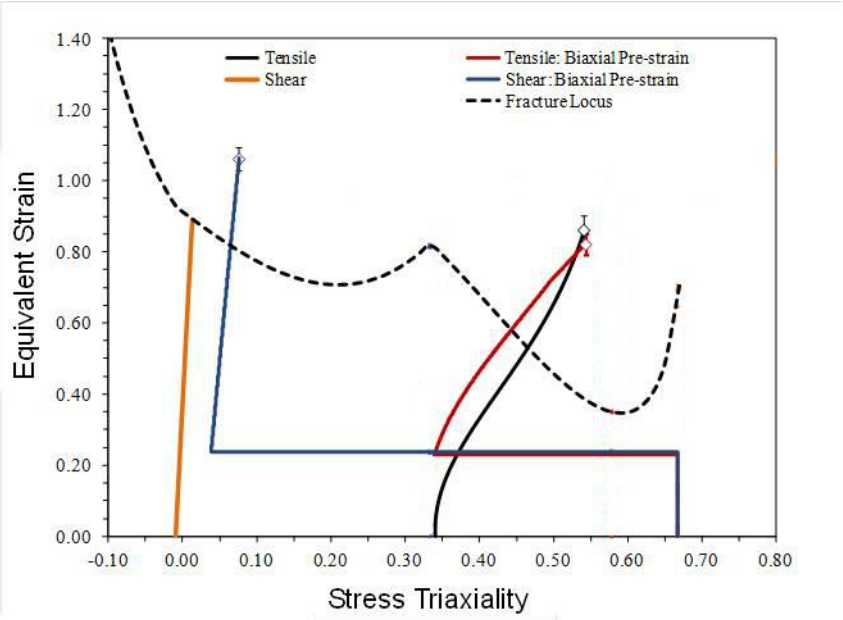

Figure 79: Stress state evolution of tests with and without biaxial prestraining overlaid on fracture locus for fully bainitic material condition [72].

Using the approach to damage that is utilized in the GISSMO model [73], the damage was integrated for each of the different loading histories, using a value of 2 for the damage exponent. Computing damage accumulation incrementally, it was possible to determine the onset of fracture for each of the different loading paths investigated. The GISSMO damage model considers fracture to occur when the damage parameter has a value of unity. The resulting fracture strains predicted by the damage model are compared to those measured in the experiment, presented in Table 26. For the experiments that included pre-straining, the equivalent strain induced during the biaxial stretching operation was simply added to the equivalent strain measured at fracture in each of the subsequent tests. Due to slight variation in

the biaxial pre-strains induced from blank to blank, the mini shear and mini dog bone uniaxial tensile specimens were tracked to their respective blanks, in order to account for this variation.

Table 26: Experimental and predicted fracture strains for non-proportional loading [72]

Experiment	Experimentally measured fracture strain	Predicted fracture strain using damage model
Mini shear	0.89 ±0.08	0.92
Mini dog bone uniaxial tensile	0.86 ±0.04	0.66
Pre-strained mini shear	1.06 ±0.03	1.08
Pre-strained mini dog bone uniaxial tensile	0.83 ±0.03	0.85

Evidently, the damage model proved adequate for prediction of strains at fracture for the pre-strained loading cases. It should be noted, however, that for the mini dog bone uniaxial tensile specimen, the predicted fracture strain was considerably less than what was measured. The most likely reason for this is due to the way in which damage is accrued using this approach. Since this strain path is highly non-linear, the stress triaxiality begins to evolve from uniaxial tension towards plane strain very early on. Since the fracture strain for plane strain is the minimum of all of the stress states investigated, damage is accumulated fastest under plane strain deformation. While the pre-strained mini dog bone uniaxial tensile specimens also exhibited a highly non-linear loading history following the biaxial stretching operation, the influence of the biaxial pre-straining is nearly negligible, as a result of the non-linear damage accumulation in the damage model, since the fracture strain in equi-biaxial tension is quite high. Figure 80 provides an illustration in the difference in damage accumulation for the mini dog bone tensile specimens, with and without biaxial pre-straining, with linear and non-linear damage accumulation.

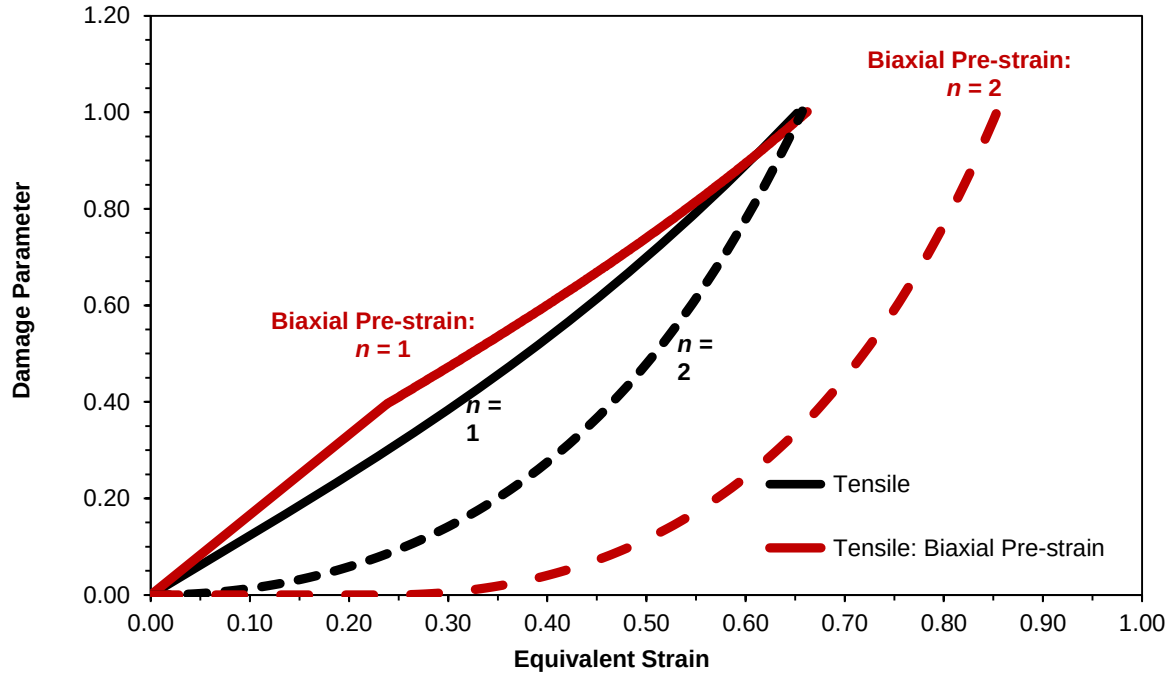

Figure 80: Comparison of damage accumulation for mini dog bone tensile loading cases [72]

7 APPLICATION TO SIMULATION OF HOT STAMPED COMPONENTS

In order to apply the experimentally derived fracture loci to impact simulations of hot stamped components, an inverse approach is used in the interest of pragmatism. Due to limitations and simplifications inherent in the modeling strategy, namely adoption of comparatively large shell elements and the use of the GISSMO damage model as strictly a damage counter to initiate element deletion, discrepancies may arise between experiments and numerical simulations. For instance, while certain experiments indicated considerable necking before failure, the modeling approach does not account for localization prior to element deletion. Thus, "model dependent fracture loci" were constructed, using "critical element" strains from simulations. FE models of fracture experiments are developed and are used to derive stress state and equivalent strain at fracture, conveniently providing a closed-loop approach to fracture characterization. With this approach, the experimentally measured elongation or dome height at fracture is used in the models to determine the strain and stress state of a particular element [33]. A drawback of this approach is that decisions of modeling taste, be it element type, element size, friction coefficients, etc., are inherent in the final fracture locus [31]; hence, the use of the term "model dependent fracture loci" in contrast to the experimentally derived loci in Chapter 5. Mindful of the fact that the tailored hot stamped axial crush and side impact rails studied by Omer [37] and Prajogo [71], respectively, were modeled in LS-DYNA using type 16 shell elements (fully integrated), with seven through thickness integration points, simulations using this element type were developed for selected experiments and used in the model dependent fracture loci calibration. Descriptions of these models and the development of model-dependent fracture loci are the focus of this chapter. For consistency, each simulation described in this section features elements with a length of 0.6 mm in the gage section or at the centre of the

blank. This rather small size was adopted due to the limited size of the gage section in the mini shear specimen geometry. Since the impact simulations of the hot stamped components in [37] [71] had element sizes of 2.5-5.0 mm, element size influence and regularization were also examined as discussed in Section 7.2.

7.1 Numerical Fracture Locus Calibration

For the development of a model dependent fracture locus, models of the experiments that were amenable to shell modeling were developed in order to investigate the existence of discrepancies between the experimentally measured fracture strains and the strains at fracture predicted by these models. The experiments considered included the mini shear, plane-strain dog bone, and equi-biaxial dome. Experiments such as hole expansion and tensile specimens were also simulated using shell elements, however, these experiments were ill-suited to this approach, due to significant stress gradients through the material thickness. These models are not included in the development of the model-dependent facture loci. The methodology used for adjusting the fracture locus was as follows: first, the simulation of the equi-biaxial dome is run using the experimentally derived fracture locus. Since the strain path in the model corresponds to nearly perfect equi-biaxial tension up until fracture, simply scaling the input fracture strain corresponding to a stress triaxiality of 0.667 directly affects the resulting dome height at fracture. Once the simulation of the equi-biaxial dome test predicts fracture initiation at a dome height consistent with the experiment, simulations of the plane-strain dog bone are run. Since the initial strain path of this test using a hemispherical punch is initially equi-biaxial tension before transitioning to plane-strain tension, the fracture strain corresponding to a triaxiality of 0.667 influences the rate of damage accumulation for this portion of the strain path. Once the fracture locus in the region between equi-biaxial tension and plane strain tension has been calibrated to

yield consistent fracture initiation dome heights between model and experiment, the region of the fracture locus around stress triaxiality of zero is tuned, based on the results of the mini shear simulation. Between stress states of simple shear and plane strain tension, it was intended to use a hole expansion model with shell elements in order to calibrate the model dependent fracture locus. However, planar shell elements were found to be less than ideal, given the through thickness stress gradient at the hole edge. Comparing experimental and numerical fracture strains for the stress states of simple shear, plane strain tension, and equi-biaxial tension, the experimental fracture locus is then fit to the numerical results. The results of the equi-biaxial dome, plane strain dome, and mini shear simulations are shown in Sections 7.1.1-7.1.3. It should be noted, for the material produced through die quenching at 700 °C, the only experiment that could be modeled using shell elements was the mini shear. For development of the model-dependent fracture locus under equi-biaxial and plane-strain loading, the differences between the experimental and model-dependent fracture loci for the fully bainitic material condition were considered and applied to the experimental fracture locus of the 700 °C die quench material.

7.1.1 Equi-biaxial Dome Predictions

The mesh used to model the equi-biaxial dome test is shown in Figure 81. This mesh features a 0.6 mm element size in the refined region over the punch; the element size adopted for calibration of model dependent fracture loci for each material condition. Quarter-symmetry boundary conditions have been applied and each component has been modeled using shell elements. In LS-DYNA, contact between the blank and the various tooling components has been defined using the *CONTACT_FORMING_SURFACE_TO_SURFACE contact definition, which is a penalty function-based contact type generally used in metal forming simulations [57]. The coefficient of friction between the blank and the punch has been defined as 0.04,

corresponding to Teflon lubrication, while 0.4 was used as a coefficient of friction between the blank and the other tooling components. Investigations into modeling the binder and die with the lockbead incorporated were conducted, with no appreciable variation in draw-in or load-displacement response. However, due to the tight radius of the lock bead, special attention was required in this region when meshing the blank. As a result, considerably greater simulation times were encountered when running the model that incorporated a lock bead. As a result, the lock bead was neglected in the final simulations. For completeness, meshes that incorporate the lock bead for both the equi-biaxial and plane strain dog bone models are included in Appendix R. This simulation did not incorporate any mass scaling. Although strain rate sensitive constitutive models are not used, the time scaling applied to these models is very conservative, as initial simulations with more aggressive time scaling induced stress waves, and as a result in some cases, plastic strain, in the blank upon initial contact with tooling.

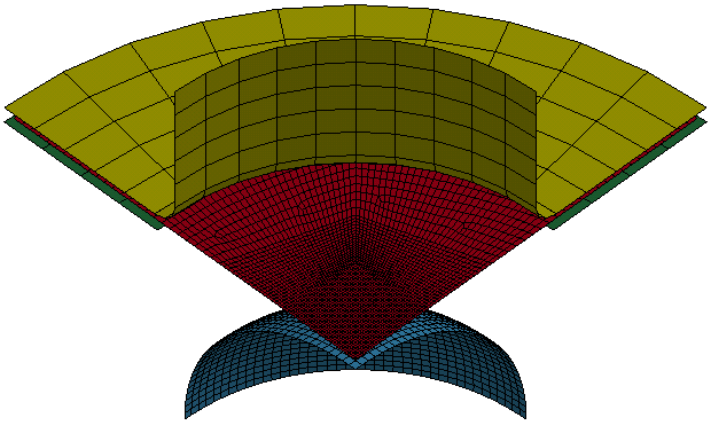

Figure 81: Quarter-symmetry mesh of equi-biaxial dome test. Blank is shown in red, while die, binder, and punch are shown in yellow, green, and blue

Punch force is plotted against dome height in Figure 82 for the bainitic material condition. The corresponding experimental results are included for reference. Good agreement between experiment and simulation is observed.

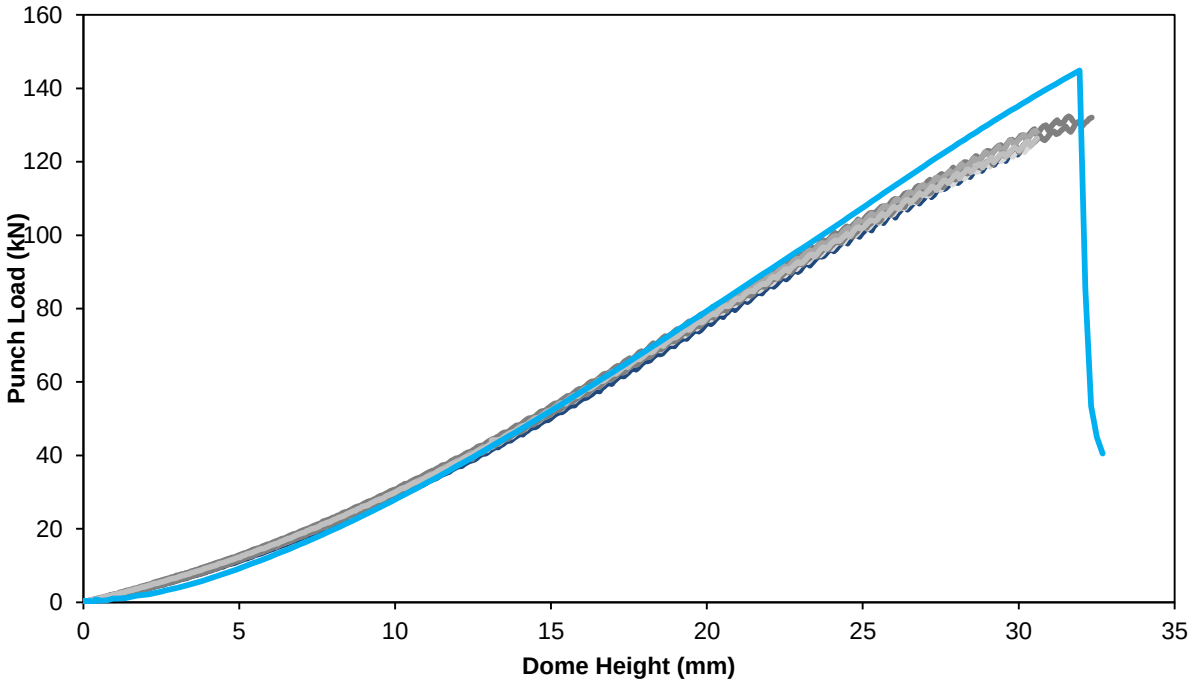

Figure 82: Punch force plotted against dome height for equi-biaxial model and experiment for fully bainitic material quench condition. The grey and blue lines correspond to experiment and simulation, respectively.

7.1.2 Plane Strain Dog Bone

For the model of the plane-strain dog bone geometry, the same tooling from the equi-biaxial dome model is used. The mesh used for this model is shown in Figure 83. In terms of model setup (contacts, coefficients of friction, time scaling), these parameters are identical to the equi-biaxial dome model described in Section 7.1.1.

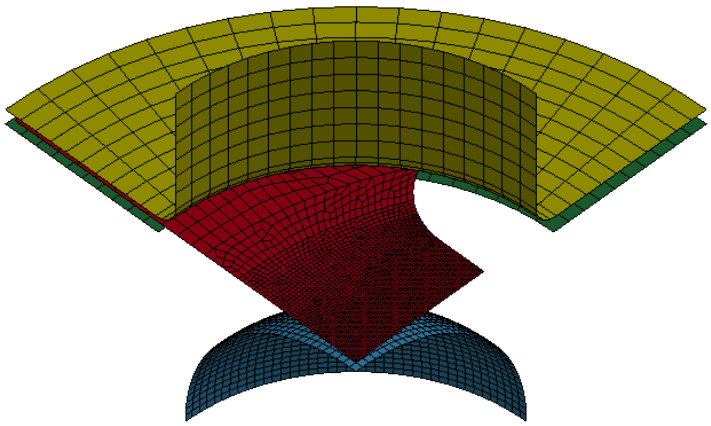

Figure 83: Quarter-symmetry mesh of plane-strain dog bone dome test. Blank is shown in red, while die, binder, and punch are shown in yellow, green, and blue

For the plane strain dome model, punch force is plotted against dome height in Figure 84. The experimental results are also plotted on this figure for reference. Good agreement between simulation and experiment is observed, with dome height at fracture consistent with the experimental median.

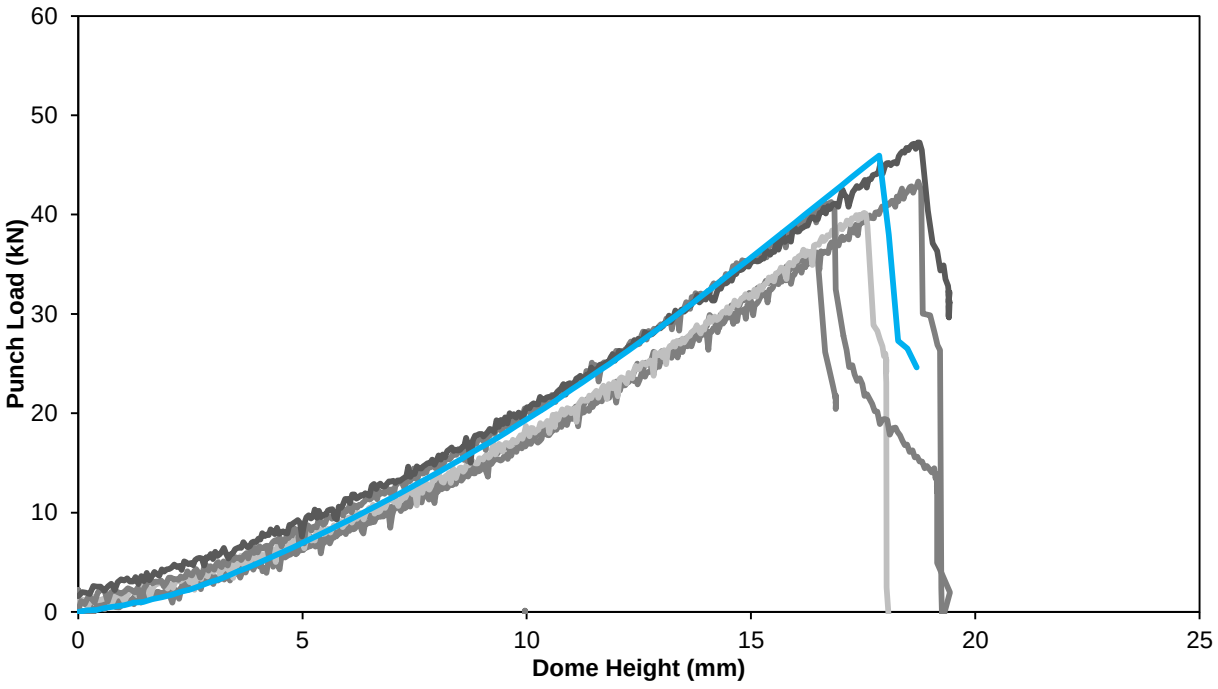

Figure 84: Punch force plotted against dome height for plane-strain dog bone dome model and experiment for fully bainitic material quench condition. The grey and blue lines correspond to experiment and simulation, respectively

7.1.3 Mini Shear

For the mini shear test, the specimen was modeled with 0.6 mm elements through the gauge section in order to maintain consistency with the other shell simulations used for adjustment of the experimental fracture locus. The mesh for this simulation is shown in Figure 85. As with the modeled dome tests, fully integrated shell elements with seven through-thickness integration points were used (shell element type 16 in LS-DYNA). The resulting force-displacement from this simulation is plotted with the experiment repeats in Figure 86. The white circle in this figure identifies the fracture initiation point for two of the three repeats. Overall, the load-displacement response of the mini shear simulations is consistent with the experiments. The fracture initiation of the simulation also indicates good agreement with the experimental results.

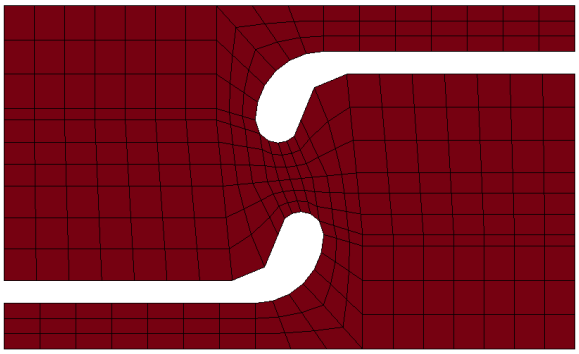

Figure 85: Mini shear mesh with 0.6 mm elements in gauge section

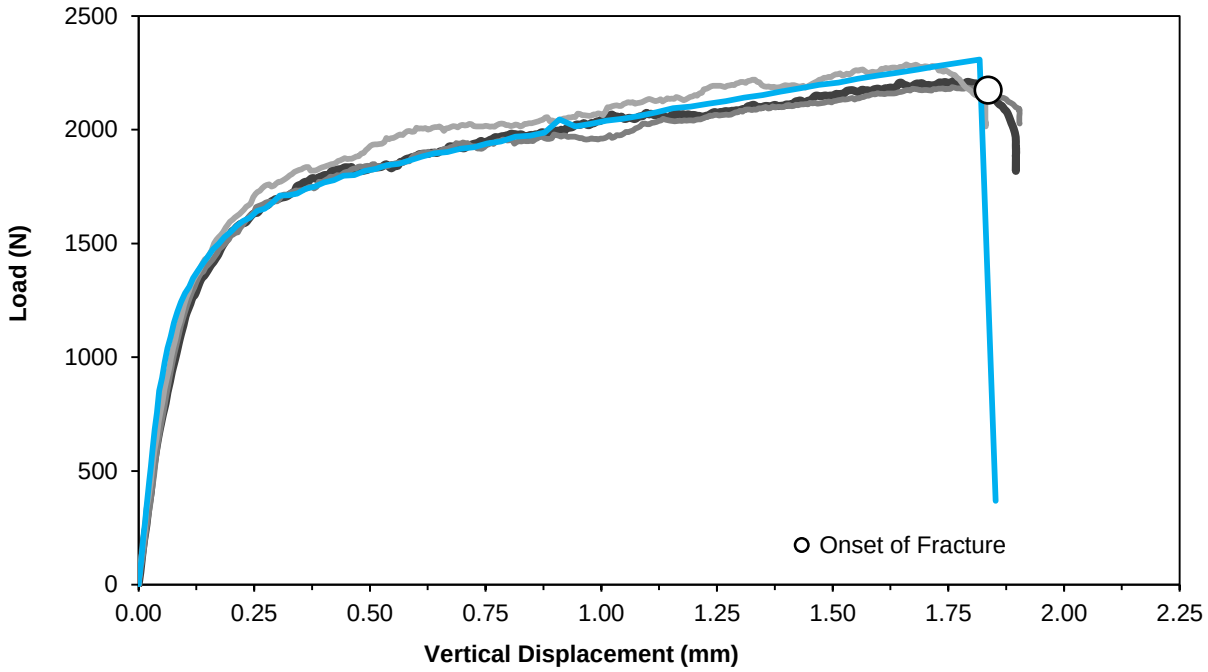

Figure 86: Force plotted against displacement for mini shear experiment and simulation for fully bainitic material quench condition. The grey and blue lines correspond to experiment and simulation, respectively

7.1.4 Model-dependent Fracture Loci

The local strains at failure in the finite element models corresponding to the measured displacement at failure in the experiments were used to adjust the experimental fracture loci presented in Chapter 5, following the procedure described above. The resulting "model dependent fracture loci" for the fully bainitic, fully martensitic, and 700 °C tailored hot stamped material quench conditions are shown in Figure 87. The fully martensitic and 700 °C material quench conditions represent the extremes of those for which fracture was characterized experimentally. The fully bainitic material quench condition was also included in this exercise, as it was the material quench condition investigated most extensively in this thesis.

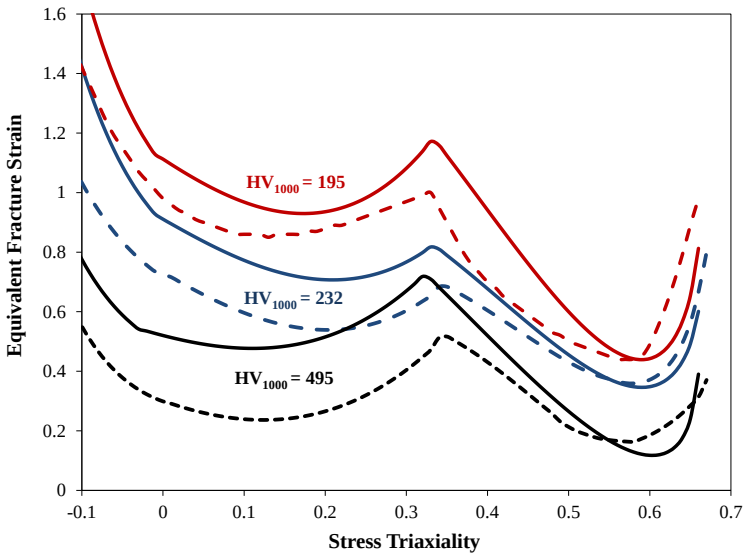

Figure 87: Fracture loci for fully martensitic, fully bainitic, and 700 °C tailored hot stamped material quench conditions. Solid lines denote experimentally derived fracture loci, while dashed lines correspond to those adjusted based on FE simulations

By comparing the experimental and model dependent failure loci, it is apparent that the agreement between the two loci is closest under biaxial and plane strain conditions, at least for the harder, lower ductility conditions. The adjustment under shear loading conditions (zero triaxiality) is larger, with the calibrated loci lying below the measured failure strains.

Of note, although consistent DIC analysis parameters and FE mesh size are used for each, the discrepancy between model and experiment for the fully martensitic and fully bainitic quench conditions is inconsistent. As shown in Figure 32 and Figure 93, the hardening behaviour for these two quench conditions is rather different, with the fully bainitic material quench condition exhibiting considerably greater work hardening than the fully martensitic material quench condition.

7.2 Mesh Regularization

Since a key consideration in the development of the GISSMO damage model in LS-DYNA is the ability to track damage in multi-stage processes, from simulations of metal forming through

to crash (which can feature different mesh densities), provisions exist to eliminate mesh size dependence [73]. Namely, GISSMO offers two approaches for mesh size regularization. The first approach considers Lemaitre's concept of effective stress [74], defined in the equation below, in which damage becomes coupled with the material flow stress curve in order for softening to occur following the onset of localized deformation [73]. In this equation, $\tilde{\sigma}$ is effective stress, σ is the nominal stress, and D is the damage parameter.

$$\tilde{\sigma} = \frac{\sigma}{(1 - D)}$$

In order to yield consistent macroscopic response for various element sizes, a fading exponent can be defined for element sizes of interest, controlling the amount of energy dissipated during element fadeout for elements of different sizes. In this case, above a critical damage threshold, defined as D_{crit}, which can be defined to correspond to the value of D at the point of instability, e_{crit}, the fading exponent, m in the equation below, will control how quickly energy is dissipated.

$$\sigma^* = \sigma\left(1 - \left(\frac{D - D_{crit}}{1 - D_{crit}}\right)^m\right)$$

In the uncoupled approach, the focus of the current work, damage is treated as a "counter" initiating element deletion when the damage parameter reaches unity. An alternative approach to compensate for mesh-size dependence in failure modeling is used, in which the equivalent strain at fracture is simply scaled as a function of element size. This scaling, or so called "mesh regularization", function is tuned in order to yield a consistent macroscopic material response for different element sizes of interest.

In literature which focuses on the phenomenological fracture characterization, regularization is often a topic which is neglected or left for "future work". Some research has supported the use

of a stress state dependent regularization approach [75], however, since regularization is not a focal point of this thesis, less involved methods are considered sufficient. Other papers attempt to show the effect of regularization in the GISSMO model using load-displacement or engineering stress-strain curves for uniaxial tensile specimens which converge and match experimental results for a range of element sizes [73]. This approach was initially considered, however, since there is motivation to apply the fracture model developed in this thesis to crash simulations, the required element sizes exceed those which could be used to mesh the uniaxial tensile specimen geometry used in this work. Rather, the plane strain dome test was chosen as a more appropriate test to use for regularization, since the stress state of the critical element is both fairly constant for the duration of the test as well as quite consistent for a the required range of element sizes. The other motivation for using this approach relates to ductility under plane-strain loading. For many metals, the plane-strain stress state corresponds to a minimum in ductility, considering formability and fracture [69] and it was considered most important to ensure that fracture models exhibit consistency in fracture initiation prediction for the stress state corresponding to the lowest ductility.

Using the model-dependent fracture locus that was developed using models with a consistent 0.6 mm element size, fracture prediction results for models with element sizes of 1.25, 2.5, and 5.0 mm are shown in the form of punch load versus dome height plots, in Figure 88. Evidently, greater dome heights are reached before fracture is predicted, increasing with element size. As a result, a scaling curve for fracture strain as a function of element length was developed and incorporated into the models. This curve is shown in Figure 90. With this regularization curve applied to the plane strain dome simulations with various element sizes, consistent dome heights

at fracture are recorded, as show in Figure 88. The corresponding plots for the fully martensitic material quench condition is shown in Figure 89.

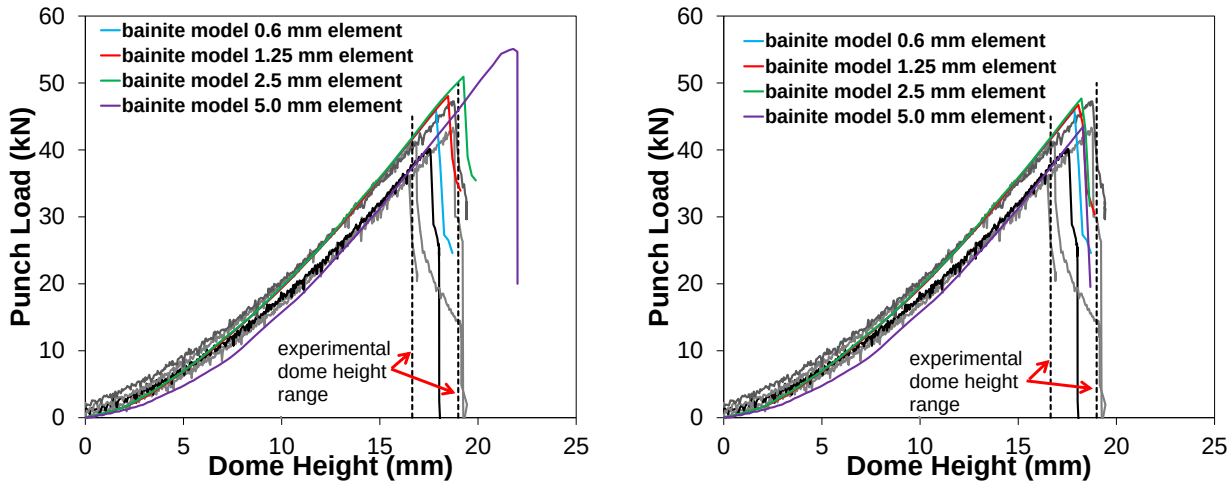

Figure 88: Punch force plotted against dome height for plane-strain dog bone dome model without (left) and with (right) regularization and experiment for fully bainitic material quench condition. The solid blue, red, green, and purple lines correspond to element sizes of 0.6, 1.25, 2.5, and 5.0 mm, respectively.

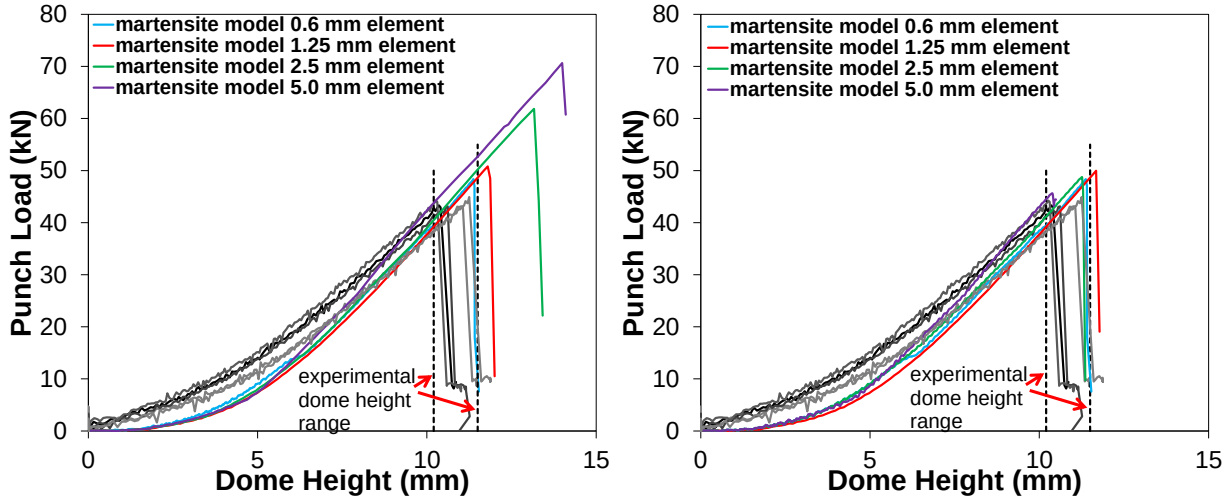

Figure 89: Punch force plotted against dome height for plane-strain dog bone dome model without (left) and with (right) regularization and experiment for fully martensitic material quench condition. The solid blue, red, green, and purple lines correspond to element sizes of 0.6, 1.25, 2.5, and 5.0 mm, respectively.

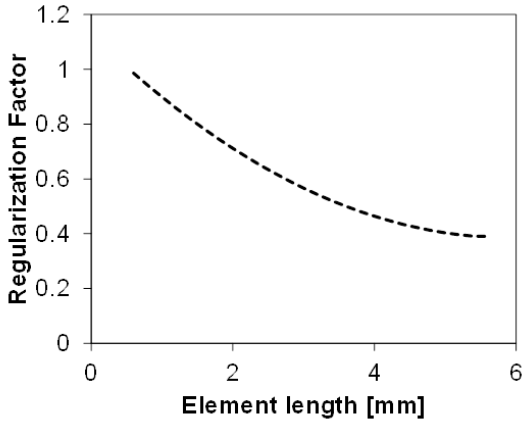

Figure 90: Scaling curve used for fracture strain regularization

8 DISCUSSION, CONCLUSIONS, AND RECOMMENDATIONS

This final chapter provides discussion of the work presented in this thesis. In addition, conclusions drawn from this work and recommendations to consider in subsequent work of this nature are also provided.

8.1 Discussion

Considering the range of stress states probed for development of fracture loci, the improved fracture performance of the softer material quench conditions, relative to the fully hardened material, is notable. In almost all of the experiments conducted to characterize fracture, the lowest measured strains corresponded to the fully martensitic phase, highlighting the potential for improved energy absorption performance through the use of tailored hot stamping to introduce softer, more ductile phases, as investigated by Omer [37] and Prajogo [72]. Of note, however, the performance of the fully martensitic hole expansion tests was somewhat surprising, as the measured strain exceeded that of the intermediate forced air material quench condition and was nearly comparable to that of the fully bainitic material. Although not investigated, it was speculated that this was due to the presence of the single martensitic phase, rather than a mixed microstructure of martensite and bainite, for which a considerable strength differential would exist at interfaces between the two phases. For the softer material quench conditions, the strength differential between the different phases present would not be as dramatic.

Given the extensive use of DIC analysis in the development of fracture loci, while 2-D DIC was used for some tests and 3-D for others, a more coherent experimental strategy would have utilized a consistent DIC approach for all tests. As mentioned in Section 2.2.3, the influence of step, strain filter, and inspection circle size on the measured strains at the onset of fracture was investigated outside of this thesis, however, the influence of image magnification was not. Given the various specimen geometries utilized in this fracture characterization approach, a variety of

lens and camera configurations were used, resulting in various degrees of magnification for different tests. Also, in making extensive use of DIC, certain specimen geometries proved to be less accommodating than others. The use of the mini dog bone tensile geometry, as well as the notched tensile specimens, proved troublesome because of their small size. Due to the large size of the necking region relative to the specimen size, as localization occurred in these experiments, the applied speckle pattern had a tendency to flake off, compromising the fidelity of the DIC analysis. Subsequent experiences with the standard size ASTM E8 tensile geometry proved much more robust in this regard, as local strains could be obtained up to failure. Furthermore, use of a standard, full size tensile specimen could have enabled a more typical mesh regularization approach to be used, rather than using the plane-strain dome test. Although experiments using notched tensile specimens were conducted, the results from these experiments were not used in the final development of fracture loci, due to the fact that the location of failure initiation could not be definitively identified.

For characterization of fracture under uniaxial tensile loading, although numerous tests were utilized in this work, the hole expansion test proved to be the most consistent and also most user friendly. Although commonly used for evaluation of the influence of sheared edges on fracture performance [44], it is also an excellent experiment for fracture characterization, due to the extremely proportional loading path, since necking is suppressed.

Although it was sought to conduct experiments that produced proportional strain paths up to fracture, in the case of the plane-strain dome test, this proved challenging, due to the initial biaxial pre-strain induced due to the use of a hemispherical punch. Alternative tests may have enabled plane strain fracture characterization under a more proportional load path. One such test

is a tight radius bend test [50]. Alternatively, testing the plane strain specimen using a flat punch and carrier blank, as in a Marciniak test may also suffice [69].

For the non-proportional loading paths considered in Chapter 6, the predictive ability of the damage accumulation function of GISSMO was probed. It was apparent that a non-linear damage accumulation approach produced better agreement with the experimental results. However, even the non-linear damage accumulation approach was overly conservative in prediction of fracture in the uniaxial mini dog bone tensile test.

While an inverse approach, in which finite element simulations of various experiments are developed and from which parameters of stress state and fracture strain are typically obtained, was used for developing model-dependent fracture loci, the crux of the research presented in this thesis focused on experimental fracture characterization. Through selection of experiments in which the location of fracture initiation could be identified, it was possible to measure fracture strains and strain paths directly from an experiment. With an assumption of von Mises yielding, the stress triaiality could be inferred from the measured major and minor strains. Some work conducted outside of this thesis analyzed the strain paths of the so-called "critical element" in simulations of mini shear, hole expansion, uniaxial and notched tensile, plane-strain dome, and equi-biaxial dome tests, comparing the performance of solid and shell elements. For the mini shear, plane-strain dome, and equi-biaxial dome tests, solid and shell elements both gave resonable agreement with the experiments, while for the other experiments mentioned, only the models with solid elements proved consistent, serving to further highlight the influence of modeling choices on fracture "behaviour" [77].

Finally, in terms of application of simulations of hot stamped components, it may have been worthwhile to consider alternative damage models to GISSMO, such as a stress based failure

criterion [82]. Comparison between strain and stress based failure criteria could prove useful in future fracture characterization work, in order to assess the performance of different damage models, both in terms of accuracy and ease of calibration.

8.2 Conclusions

The following conclusions stem from this research:

- The range of specimen geometries tested indicated that the measured strain at the onset of fracture is strongly influenced by the stress state under which the material is loaded. For each of the material conditions investigated, the lowest fracture strains were measured in the plane strain tension loading condition. The greatest fracture strains were measured in either the simple shear or uniaxial tensile stress states, depending on the material condition. For the fully bainitic material quench condition, fracture strains of 36% and 90% corresponded to the minimum and maximum measured, respectively, corresponding to plane strain tension and simple shear.
- The fracture loci of the various material conditions correlated reasonably well with the measured microhardnesses of the different material conditions. The greatest ductility was observed in specimens produced from axial crush rails that were produced using a tailored hot stamping approach with die temperatures of 700 °C, which had a measured microhardness of approximately 185HV [37]. In contrast, the fully martensitic material condition, with a measured microhardness of 485HV exhibited the lowest strain at fracture (as shown in Figure 75).
- The hardening behaviour of the different material quench conditions varied considerably, with the fully bainitic material quench condition exhibiting

considerable strain hardening, while the hardening responses of the fully martensitic and intermediate forced air quench material conditions were much flatter.

- To apply the results of this work to simulations of hot stamped components, it was first required to develop model dependent fracture loci, correlating the macroscopic response of selected experiments with finite element simulations. In most cases, the experimental fracture loci had higher fracture strains than their numerically derived counterparts; however, differences between the two loci will depend strongly upon the adopted numerical approximations (element size, type, formulation) and to some extent on the material characteristics (hardening rate).

8.3 Recommendations

From the work carried out in this thesis, the following are recommendations to consider in future fracture characterization work of hot stamped materials:

- Ensure that a consistent number of repeats of each test are performed. In order to assess the statistical uncertainty associated with measured fracture strains, there should be 5-10 repeats of each experiment.
- Utilize a coherent fracture characterization methodology. In order to ensure consistency across various experiments in which fracture strains are measured, care should be taken to maintain DIC analysis settings and image magnification.
- Consider alternative means of microstructural characterization. Microhardness was used as the defining metric for characterization of material conditions, requiring the inherent assumption that a microstructure can be completely defined by its hardness. Askeland and Phulé indicate that hardness should be used "primarily as a qualitative basis for comparison" [81]. More thorough analysis of the microstructures produced

in this work, by identifying phase composition should be considered in future experiments and analysis.

- For development of "model-dependent fracture loci" to be used in large-scale simulations of vehicle crash events, it is important to utilize experiments that are compatible with the modeling strategy mandated by these simulations. Although a multitude of fracture experiments are presented in literature, only some are amenable to modeling using large, shell elements.
- As DIC was used extensively in this work, some recommendations can be drawn from experience applying DIC to a wide range of specimens. For tensile specimens, the mini dog bone geometry should be avoided. This non-standard geometry imposes unnecessary limitations on the usefulness of the DIC. Due to the small size of these specimens, the size of the speckle pattern relative to the specimen requires very large subset sizes be used in analysis. More significantly, since the necking region is larger with respect to the gauge length of this specimen in comparison with a standard tensile geometry [7], even the slightest paint infidelity in this area results in catastrophic loss of correlation. Later testing performed using ASTM E8 full size tensile specimens did not suffer from this limitation, and DIC strains in the neck could be obtained all the way to fracture.
- Process material for test specimens in a manner that is consistent with the production techniques used to manufacture components to which the fracture characterization work will be applied. The hardness within specimens produced using the forced air quench apparatus proved inconsistent. Future work should utilize heated flat dies with cartridge heaters to produce hot stamped material with tailored properties.

- The hole tensile geometries used in this work may have produced better results had an optimized specimen geometry been developed. While results for hole tensile specimens with varying aspect ratios have been presented in literature [42], such a process was not undertaken for this thesis.
- For characterizing failure under plane strain loading, consider using a Marciniak test [69] or tight radius bend test [50] in order to ensure proportional loading up to fracture.

9 WORKS CITED

[1] H. Karbasian and A. Tekkaya, "A review on hot stamping," *Journal of Materials Processing Technology*, pp. 2103-2118, 2010.

[2] A. Bardelcik, C. Salisbury, S. Winkler, M. Wells and M. Worswick, "Effect of cooling rate on the high strain rate properties of boron steel," *International Journal of Impact Engineering*, pp. 1-9, 2009.

[3] A. Barcellona and D. Palmeri, "Effect of plastic hot deformation on the hardness and continuous cooling transformations of 22MnB5 microalloyed boron steel," *Metallurgical and Materials Transactions A*, pp. 1160-1174, 2009.

[4] ArcelorMittal, "Automotive Product Catalogue," [Online]. Available: http://automotive.arcelormittal.com/saturnus/sheets/ArcelorMittal%20Automotive%20product%20offer%20EN.pdf. [Accessed 13 04 2015].

[5] R. George, A. Bardelcik and M. Worswick, "Hot forming of boron steels using heated and cooled tooling for tailored properties," *Journal of Materials Processing Technology*, vol. 212, no. 11, pp. 2386-2399, 2012.

[6] P. Akerstrom, *Modelling and simulation of hot stamping*, Luleå : Luleå University of Technology, 2006.

[7] A. Bardelcik, *High Strain Rate Behaviour of Hot Formed Boron Steel with Tailored Properties*, Waterloo: University of Waterloo, 2012.

[8] D. Mohr and F. Ebnoether, "Plasticity and fracture of martensitic boron steel under plane stress conditions," *International Journal of Solids and Structures*, vol. 46, no. 20, pp. 3535-

3547, 2009.

[9] T. Eller, L. Greve, M. Andres, M. Medricky, A. Hatscher, V. Meinders and A. van den Boogaard, "Plasticity and fracture modeling of quench-hardenable boron steel with tailored properties," *Journal of Materials Processing Technology,* vol. 214, no. 6, pp. 1211-1227, 2014.

[10] R. Östlund, *Modelling and characterisation of fracture properties of advanced high strength steels,* Luleå: Universitetstryckeriet Luleå Tekniska Universitet, 2011.

[11] M. Dunand, *Hybrid experimental-numerical determination of the loading path to fracture in TRIP780 sheets subjected to multi-axial loading,* Cambridge: Massachusetts Institute of Technology, 2010.

[12] M. Dunand and D. Mohr, "Optimized butterfly specimen for the fracture testing of sheet materials under combined normal and shear loading," *Engineering Fracture Mechanics,* vol. 78, no. 17, pp. 2919-2934, 2011.

[13] C. Walters, *Development of a punching technique for ductile fracture testing over a wide range of stress states and strain rates,* Cambridge: Massachusetts Institute of Technology, 2009.

[14] O. Björklund, R. Larsson and L. Nilsson, "Failure of high strength steel sheets: Experiments and modelling," *Journal of Materials Processing Technology,* vol. 213, no. 7, pp. 1103-1117, 2013.

[15] Y. Lou and H. Huh, "Prediction of ductile fracture for advanced high strength steel with a new criterion: Experiments and simulation," *Journal of Materials Processing Technology,* vol. 213, no. 8, pp. 1284-1302, 2013.

[16] A. Gurson, "Continuum theory of ductile rupture by void nucleation and growth: Part I—Yield criteria and flow rules for porous ductile media," *Journal of engineering materials and technology*, vol. 99, no. 1, pp. 2-15, 1977.

[17] J. Weiler and J. Wood, "Modeling fracture properties in a die-cast AM60B magnesium alloy I—Analytical failure model," *Materials Science and Engineering: A,* vol. 527, no. 1, pp. 25-31, 2009.

[18] J. Weiler, J. Wood, R. Klassen, E. Maire, R. Berkmortel and G. Wang, "Relationship between internal porosity and fracture strength of die-cast magnesium AM60B alloy," *Materials Science and Engineering: A,* vol. 395, no. 1, pp. 315-322, 2005.

[19] G. Johnson and W. Cook, "Fracture characteristics of three metals subjected to various strains, strain rates, temperatures and pressures," *Engineering Fracture Mechanics,* vol. 21, no. 1, pp. 31-48, 1985.

[20] T. Børvik, O. Hopperstad, S. Dey, E. Pizzinato, M. Langseth and C. Albertini, "Strength and ductility of Weldox 460 E steel at high strain rates, elevated temperatures and various stress triaxialities," *Engineering Fracture Mechanics,* vol. 72, no. 7, pp. 1071-1087, 2005.

[21] G. Johnson and W. Cook, "A constitutive model and data for metals subjected to large strains, high strain rates and high temperatures," in *Proceedings of the 7th International Symposium on Ballistics*, The Hague, 1983.

[22] Neukamm, F; Feucht, M; Haufe, A, "Considering damage history in crashworthiness simulations," in *7th European LS-DYNA Conference*, Stuttgart, 2009.

[23] A. Haufe, F. Neukamm, M. Feucht, P. DuBois and T. Borvall, "A comparison of recent damage and failure models for steel materials in crashworthiness application in LS-DYNA,"

in *11 International LS-DYNA Users Conference*, Detroit, 2010.

[24] M. Brünig, "An anisotropic ductile damage model based on irreversible thermodynamics," *International Journal of Plasticity*, vol. 19, no. 10, pp. 1679-1713, 2003.

[25] M. Brünig, S. Gerke and V. Hagenbrock, "Micro-mechanical studies on the effect of the stress triaxiality and the Lode parameter on ductile damage," *International Journal of Plasticity*, vol. 50, pp. 49-65, 2013.

[26] Effelsberg, J; Haufe, A; Feucht, M; Neukamm, F; Du Bois, P, "On parameter identification for the GISSMO damage model," in *12th International LS-DYNA Users Conference*, Dearborn, 2012.

[27] Neukamm, F; Feucht, M; Haufe, A, "Consistent damage modelling in the process chain of forming to crashworthiness simulations," in *7. LS-DYNA Anwenderforum*, Bamberg, 2008.

[28] H. Ebelsheiser, M. Feucht and F. Neukamm, "On calibrating advanced damage models using sheet metal coupon tests," in *7. LS-DYNA Anwenderforum*, Bamberg, 2008.

[29] M. Basaran, S. Wolkerling, M. Feucht, F. Neukamm and D. Weichert, "An extension of the GISSMO damage model based on Lode Angle dependence," in *9. LS-DYNA Anwenderforum*, Bamberg, 2010.

[30] Y. Bai and T. Wierzbicki, "A new model of metal plasticity and fracture with pressure and Lode dependence," *International Journal of Plasticity*, vol. 24, pp. 1071-1096, 2008.

[31] M. Luo and T. Wierzbicki, "Numerical failure analysis of a stretch-bending test on dual-phase steel sheets using a phenomenological fracture model," *International Journal of Solids and Structures*, vol. 47, no. 22, pp. 3084-3102, 2010.

[32] Y. Bai and T. Wierzbicki, "Application of extended Mohr–Coulomb criterion to ductile

fracture," *International Journal of Fracture,* vol. 161, no. 1, pp. 1-20, 2010.

[33] M. Basaran, *Stress state dependent damage modeling with a focus on the lode angle influence,* Aachen: Rheinisch-Westfalische Technische Hochschule Aachen, 2011.

[34] A. Bardelcik, *Personal communication,* Waterloo, 2013.

[35] A. Bardelcik, M. Wells and M. Worswick, "The Effect of Cooling Rate on the Mechanical Properties and Energy Absorption Potential of Hardened Boron Steel," *International Conference on Hot Sheet Metal Forming of High-Performance Steel,* 2009.

[36] A. Bardelcik, M. Worswick and M. Wells, "The influence of martensite, bainite and ferrite on the as-quenched constitutive response of simultaneously quenched and deformed boron steel - Experiments and model," *Materials & Design,* vol. 55, pp. 509-525, 2014.

[37] K. Omer, *Development and Testing of a Hot Stamped Axial Crush Member with Tailored Properties,* Waterloo, 2014.

[38] M. Dunand and D. Mohr, "Hybrid experimental-numerical analysis of basic ductile fracture experiments for sheet metals," *Internation Journal of Solids and Structures,* vol. 47, no. 9, pp. 1130-1143, 2010.

[39] R. Smerd, S. Winkler, C. Salisbury, M. Worswick, D. Lloyd and M. Finn, "High strain rate tensile testing of automotive aluminum alloy sheet," *International Journal of Impact Engineering,* vol. 32, no. 1-4, pp. 541-560, 2005.

[40] A. Thompson, *High strain rate characterization of advanced high strength steels,* Waterloo: University of Waterloo, 2006.

[41] D. Kraehling, *Effect of Stress Triaxiality on Constitutive Response and Failure of Super Vacuum Die Cast AM60B Magnesium Alloy,* Waterloo: University of Waterloo, 2015.

[42] Y. Bao, "Dependence of fracture ductility on thickness," *Thin-Walled Structures,* pp. 1211-1230, 2004.

[43] M. Dünckelmeyer, A. Karelová, C. Krempaszky and E. Werner, "Instrumented hole expansion test," in *Proceedings of International Doctoral Seminar 2009*, Smolenice Castle, Slovakia, 2009.

[44] C. Butcher, D. Anderson and M. Worswick, "Predicting Failure during Sheared Edge Stretching Using a Damage-Based Model for the Shear-Affected Zone," *SAE International Journal of Materials and Manufacturing,* vol. 6, no. 2, pp. 304-312, 2013.

[45] B. S. Levy and C. J. Van Tyne, "Failure during sheared edge stretching," *Journal of materials engineering and performance,* vol. 17, no. 6, pp. 842-848, 2008.

[46] F. Stachowicz, "Estimation of hole-flange ability for deep drawing steel sheets," *Archives of Civil and Mechanical Engineering,* vol. 8, no. 2, pp. 167-172, 2008.

[47] ISO-12004-2, *Metallic Materials – Sheet and Strip Determination of Forming Limit Curves – Part 2: Determination of Forming Limit Curves in the Laboratory,* 2008.

[48] C. G. MacLean, *Fracture and plasticity characterization of DH-36 Navy steel,* Cambridge: Massachusetts Institute of Technology, 2012.

[49] A. Beese, M. Luo, Y. Li, Y. Bai and T. Wierzbicki, "Partially coupled anisotropic fracture model for aluminum sheets," *Engineering Fracture Mechanics,* vol. 77, no. 7, pp. 1128-1152, 2010.

[50] C. Roth, *Experimental and Numerical Investigation of Ductile Fracture Initiation at Low, Intermediate and High Strain Rates,* Palaiseau: Ecole Polytechnique, 2015.

[51] Y.-W. Lee, *Fracture prediction in metal sheets,* Massachusetts Institute of Technology,

2005.

[52] M. Dunand and D. Mohr, "On the predictive capabilities of the shear modified Gurson and the modified Mohr–Coulomb fracture models over a wide range of stress triaxialities and Lode angles," *Journal of the Mechanics and Physics of Solids,* vol. 59, no. 7, pp. 1374-1394, 2011.

[53] J. Peirs, P. Verleysen, W. van Paepegem and J. Degrieck, "Determining the stress–strain behaviour at large strains from high strain rate tensile and shear experiments," *International Journal of Impact Engineering,* vol. 38, no. 5, pp. 406-416, 2011.

[54] A. Abedini, C. Butcher, D. Anderson, M. Worswick and T. Skszek, "Fracture Characterization of Automotive Alloys in Shear Loading," *SAE International Journal of Materials and Manufacturing,* vol. 8, no. 3, pp. 774-782, 2015.

[55] L. ten Kortenaar, A. Bardelcik, M. Worswick and D. Detwiler, "The Effect of Stress Triaxiality on the Failure Response of Boron Steel Quenched to a Martensitic and Bainitic Material Condition," in *4th International Conference on Hot Sheet Metal Forming of High-Performance Steel,* Luleå, 2013.

[56] M. Worswick, *ME725: Simulation of Forming and Impact,* Waterloo: University of Waterloo, 2013.

[57] "LS-DYNA Keyword User's Manual," Livermore Software Technology Corporation (LSTC), Livermore, 2014.

[58] J. Hallquist, "LS-DYNA Theory Manual," Livermore Software Technology Company, Livermore, 2006.

[59] Y. Ling, "Uniaxial true stress-strain after necking," *AMP Journal of Technology,* vol. 5, pp.

37-48, 1996.

[60] D. Kraehling, D. Anderson, M. Worswick and T. Skszek, "Effect of Stress Triaxiality on the Constitutive Response of Super Vacuum Die Cast AM60B Magnesium Alloy," *SAE Technical Paper,* vol. 0.1, no. 1015, 2014.

[61] T. Børvik, O. Hopperstad and T. Berstad, "On the influence of stress triaxiality and strain rate on the behaviour of a structural steel. Part II. Numerical study," *European Journal of Mechanics A/Solids,* vol. 22, pp. 15-32, 2003.

[62] K. Wang, M. Luo and T. Wierzbicki, "Experiments and modeling of edge fracture for an AHSS sheet," *Interation Journal of Fracture,* vol. 187, no. 2, pp. 245-268, 2014.

[63] C. C. Roth and D. Mohr, "Effect of strain rate on ductile fracture initiation in advanced high strength steel sheets: experiments and modeling," *International Journal of Plasticity,* vol. 56, pp. 19-44, 2014.

[64] P. Bridgman, Studies in large plastic flow and fracture, New York: McGraw-Hill Book Company Inc., 1952.

[65] D. Mohr and S. Henn, "Calibration of Stress-triaxiality Dependent Crack Formation Criteria: A New Hybrid Experimental–Numerical Method," *Experimental Mechanics,* vol. 47, no. 6, pp. 805-820, 2007.

[66] K. Kofiani, A. Nonn, T. Wierzbicki, C. Kalwa and C. L. Walters, "Experiments and Fracture Modeling of High-Strength Pipelines for High and Low Stress Triaxialities," in *Twenty-second International Offshore and Polar Engineering Conference,* Rhodes, Greece, 2012.

[67] Y. Lai, Y. Li and J. Rock, "A novel full-field experimental method to measure the local compressibility of gas diffusion media," *Journal of Power Sources,* vol. 195, no. 10, pp.

3215-3223, 2010.

[68] D. Anderson, 2014.

[69] Z. Marciniak and K. Kuczynski, "Limit strains in the processes of stretch-forming sheet metal," *International Journal of Mechanical Sciences,* vol. 9, no. 9, pp. 609-620, 1967.

[70] Y. Jia and Y. Bai, "Experimental study on the mechanical properties of AZ31B-H24 magnesium alloy sheets under various loading conditions," *International Journal of Fracture,* vol. 197, no. 1, pp. 25-48, 2016.

[71] Y. Prajogo, *Hot stamping of a boron steel side impact beam with tailored flange properties - Experiments and numerical simulations,* Waterloo, 2015.

[72] C. Butcher, *Personal communication,* Waterloo, 2015.

[73] M. Feucht, F. Neukamm and A. Haufe, "A phenomenological damage model to predict material failure in crashworthiness applications," in *Recent developments and innovative applications in computational mechanics*, Berlin, Springer-Verlag, 2011, pp. 143-153.

[74] J. Lemaitre, "A continuous damage mechanics model for ductile fracture," *Journal of Engineering Materials and Technology,* vol. 107, no. 1, pp. 83-89, 1985.

[75] C. Walters, "Framework for adjusting for both stress triaxiality and mesh size effect for failure of metals in shell structures," *International Journal of Crashworthiness,* vol. 19, no. 1, pp. 1-12, 2014.

[76] D. R. Askeland and P. Phulé, The Science and Engineering of Materials, Fifth Edition, Thomson, 2005.

[77] C. Butcher, *Personal communication,* Waterloo, 2015.

[78] T. B. Stoughton and J. W. Yoon, "A new approach for failure criterion for sheet metals,"

Internation Journal of Plasticity, vol. 27, no. 3, pp. 440-459, 2011.

Appendix A Extended Depth of Field Images

The EDOF images of each of the various uniaxial and notched tensile specimens used for measuring area strains for the material conditions considered are listed in the same order that they were presented in the body of this work. Each image was 2560 x 1920 pixels but they have been scaled for brevity.

Uniaxial – fully bainitic

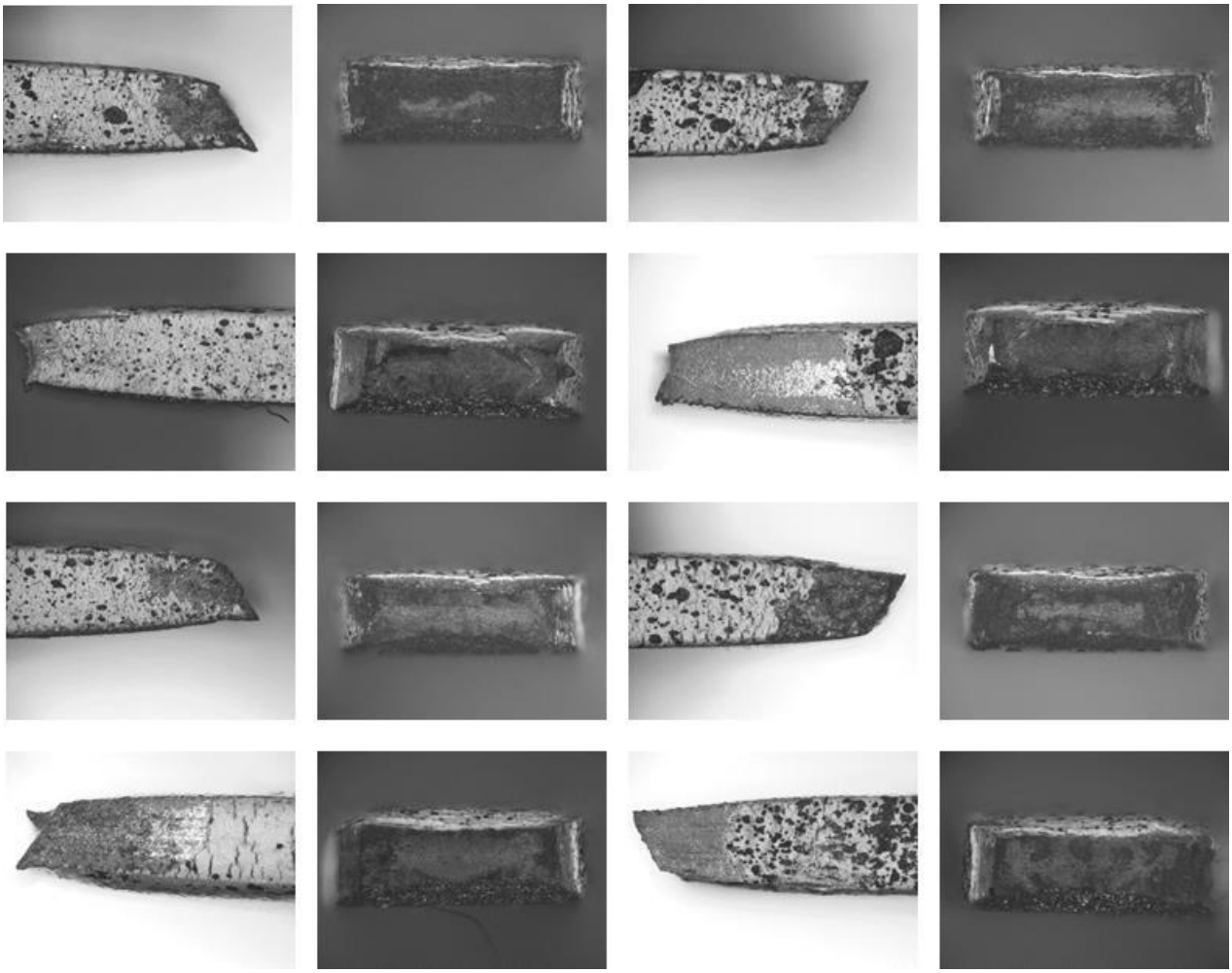

Uniaxial - fully martensitic

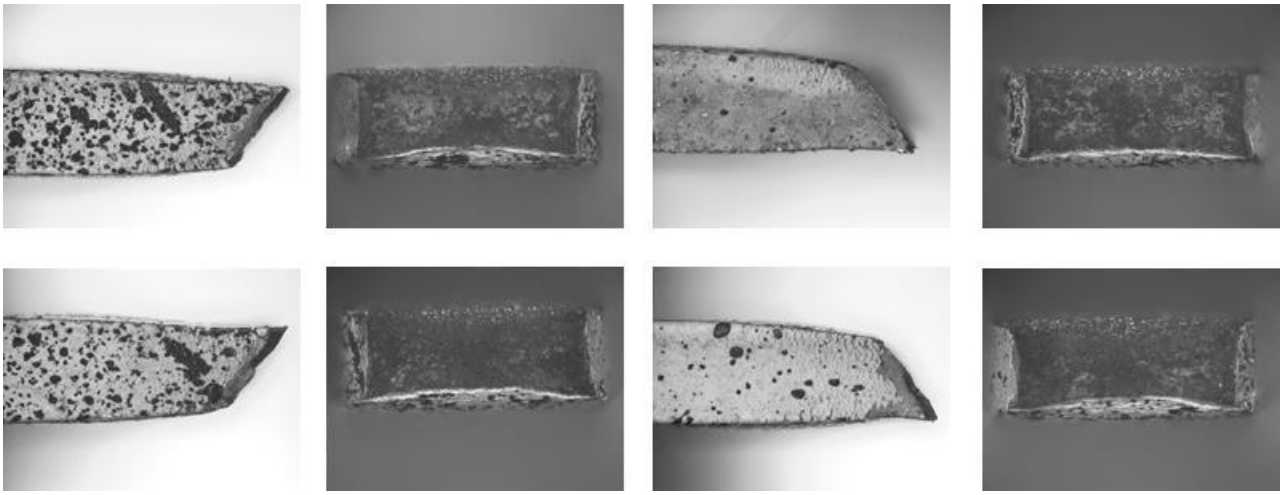

Uniaxial - Intermediate forced air

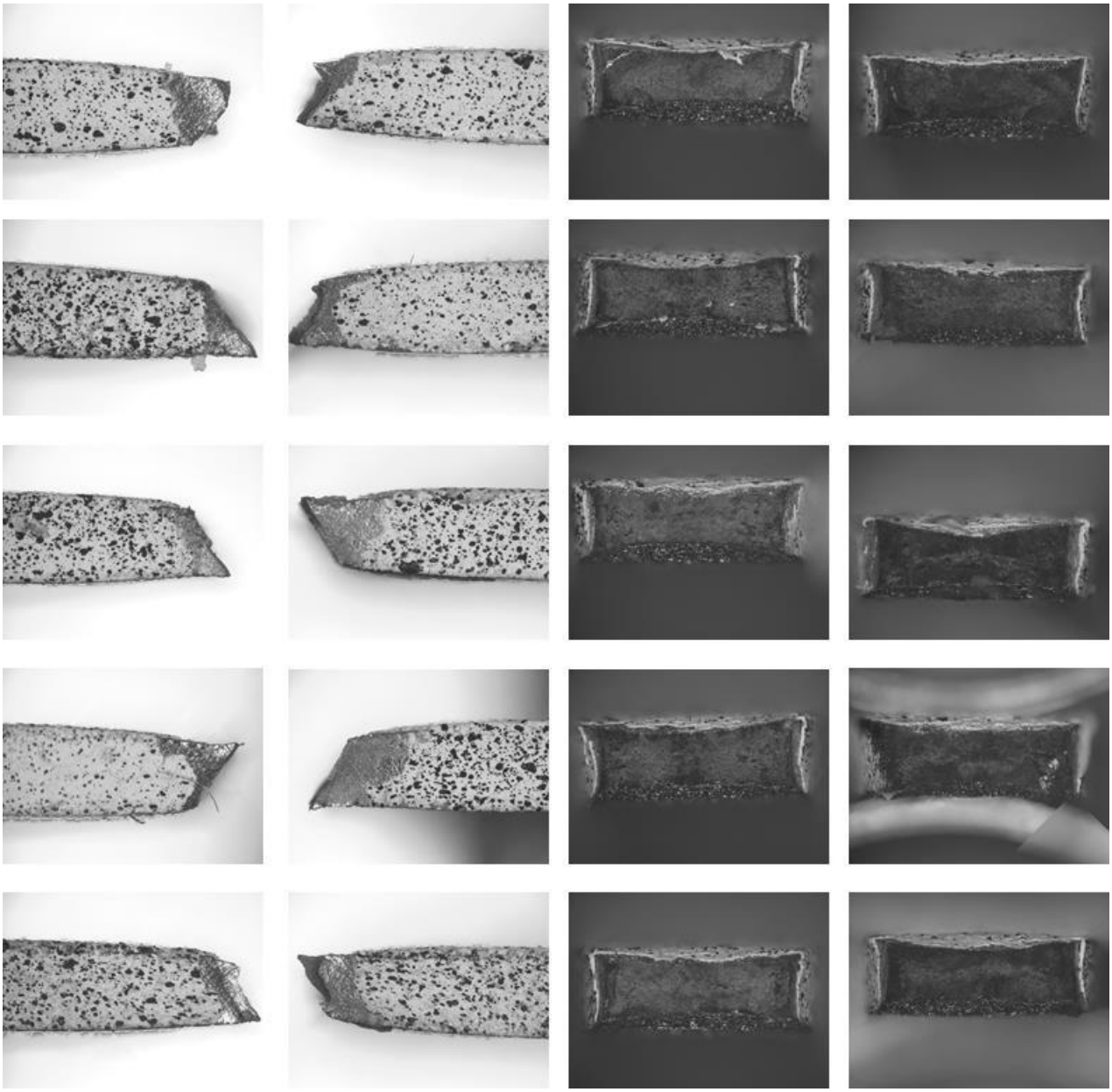

Uniaxial - Intermediate Gleeble

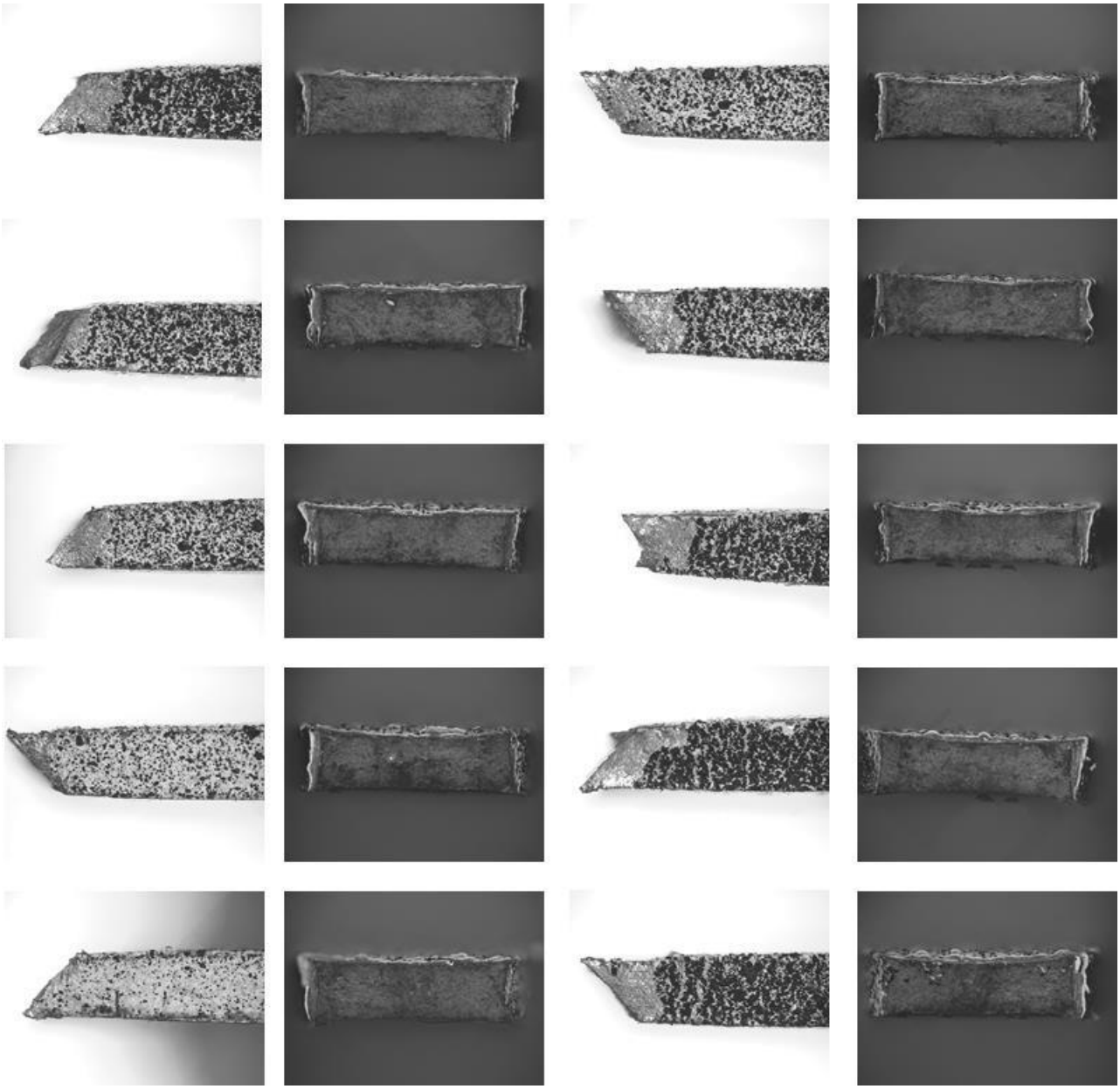

Uniaxial – 400 °C tailored hot stamped

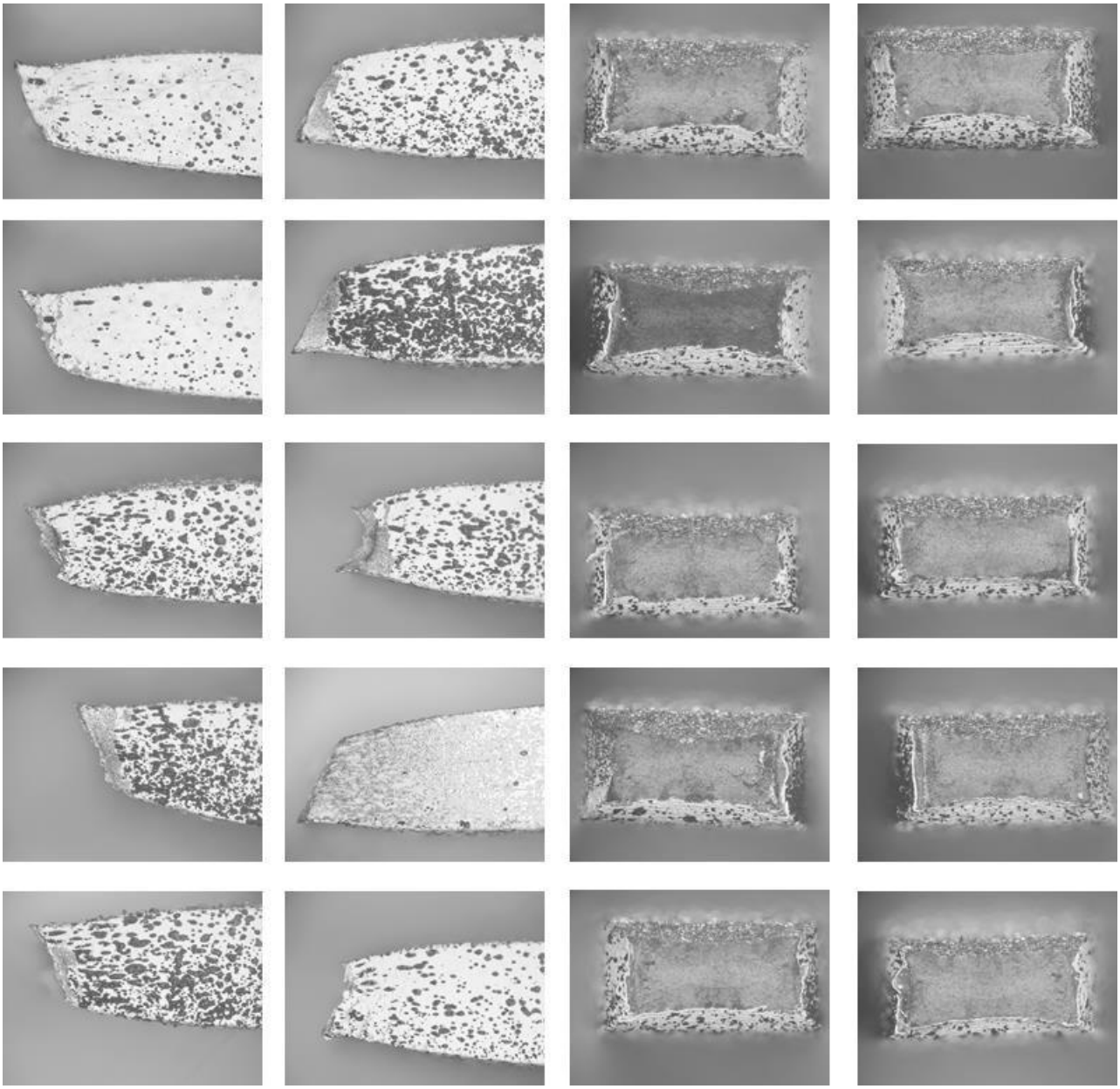

Uniaxial – 700 °C tailored hot stamped

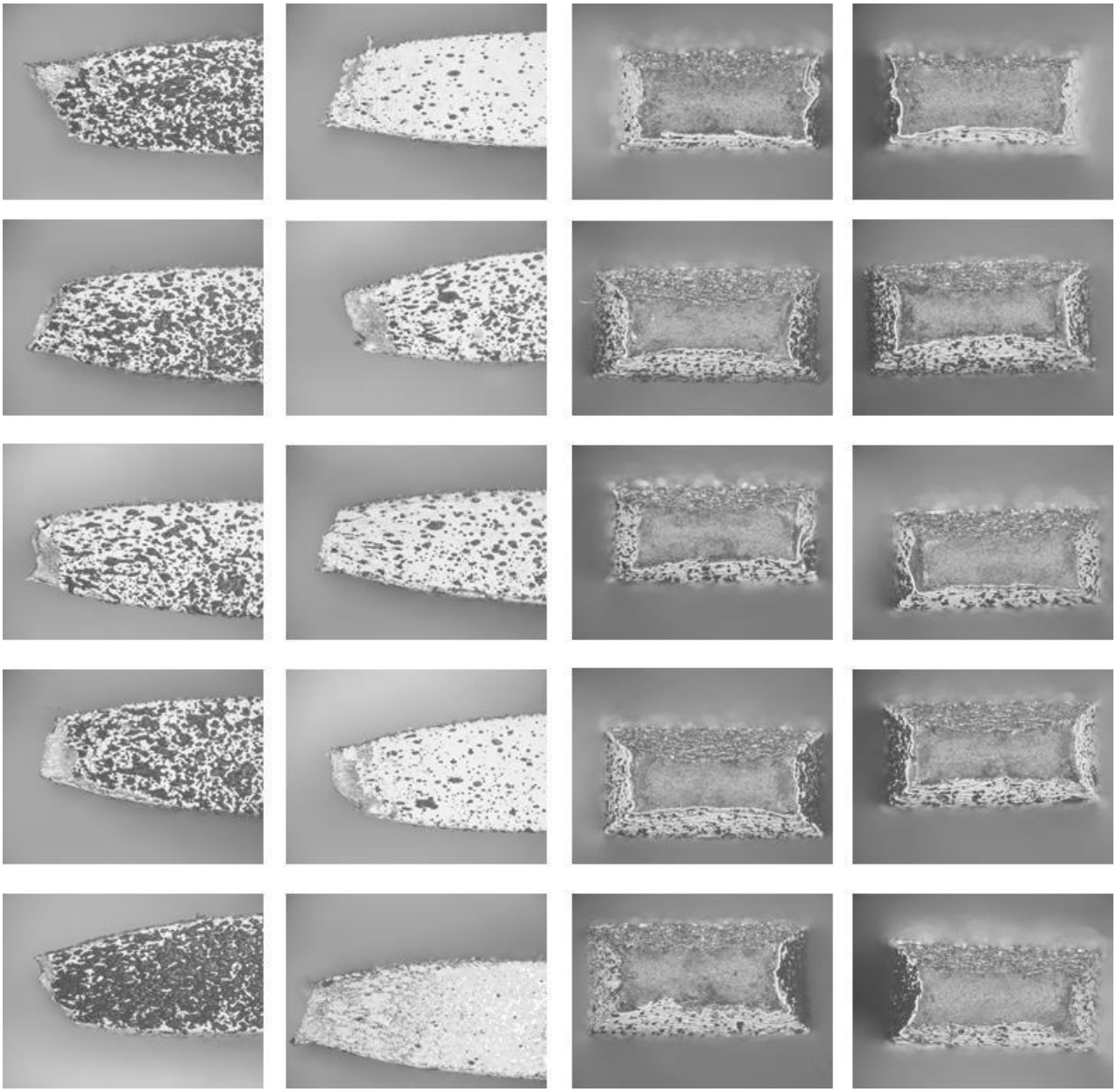

4a notch – fully bainitic

4a notch – fully martensitic

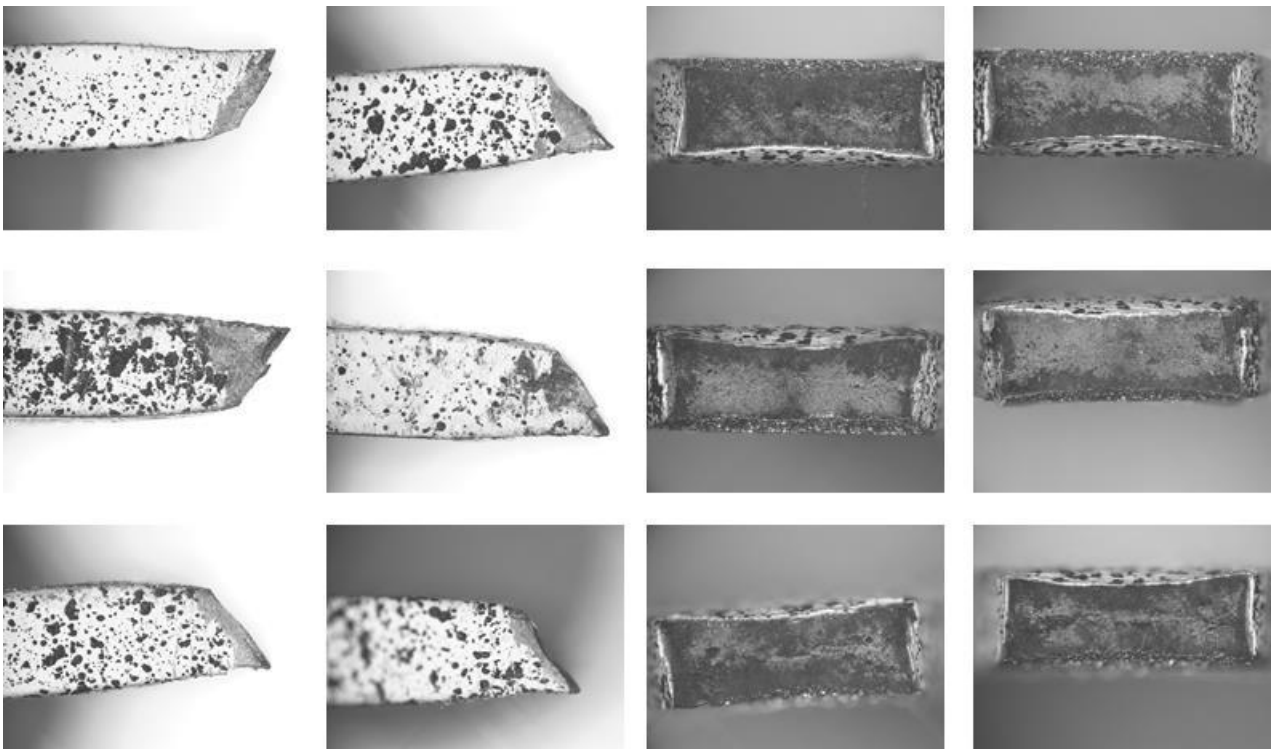

4a notch – intermediate forced air

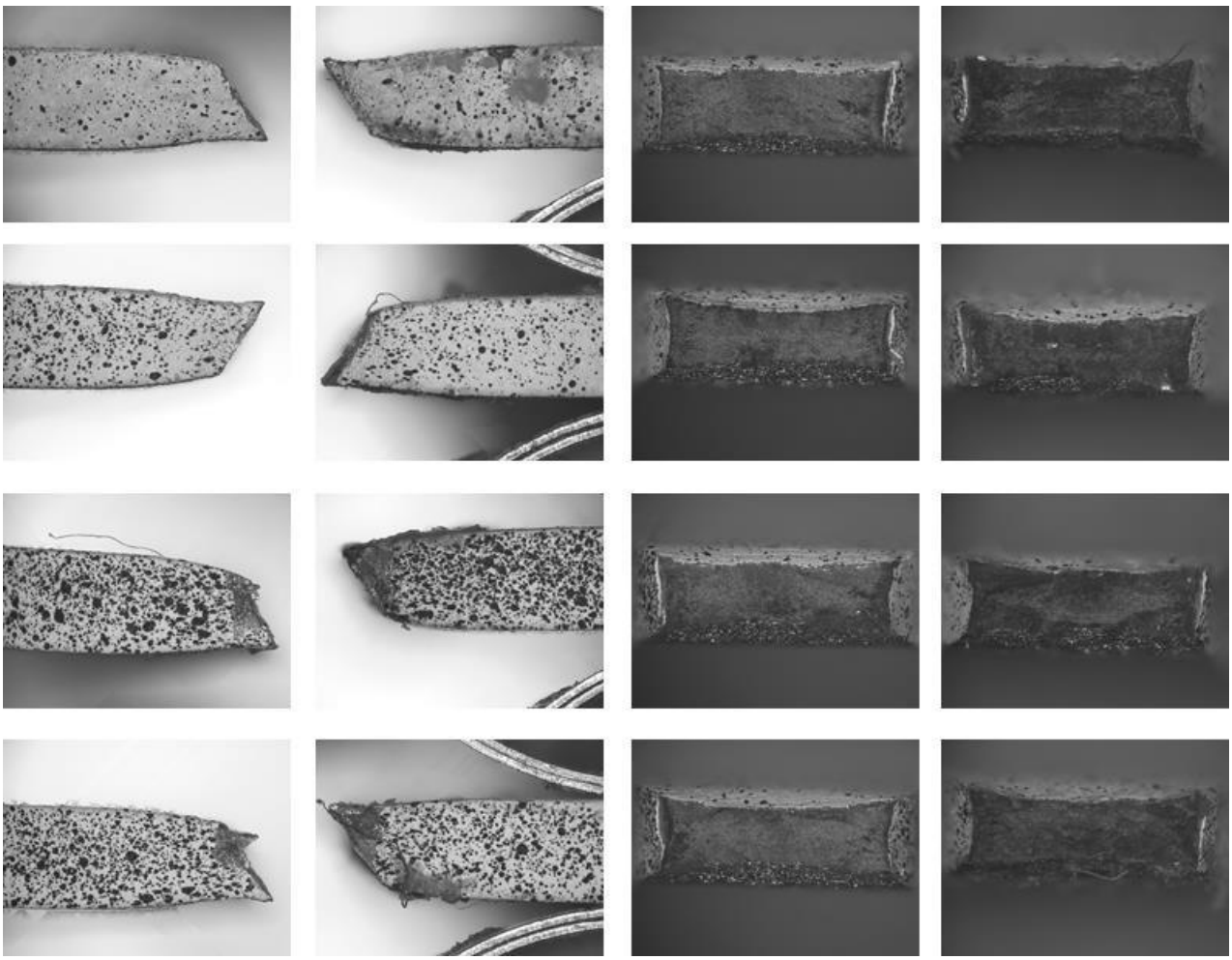

4a notch – intermediate Gleeble

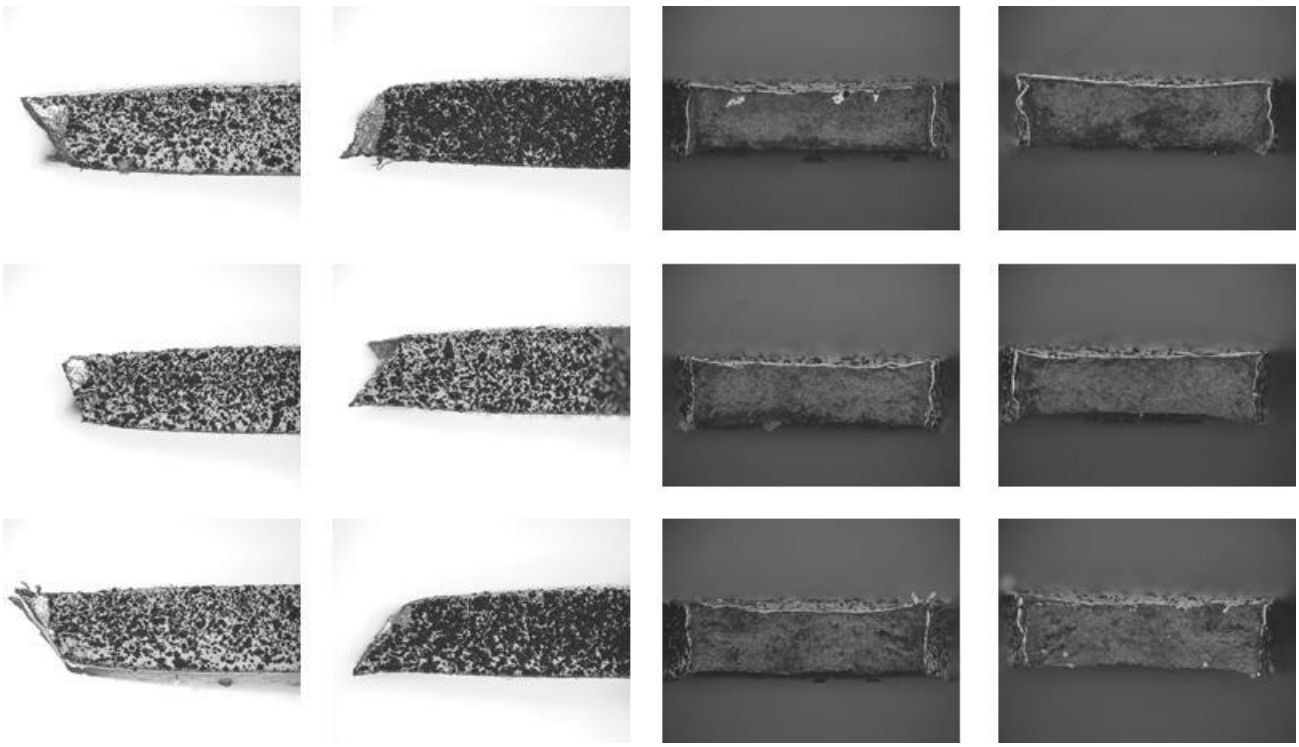

1a notch – fully bainitic

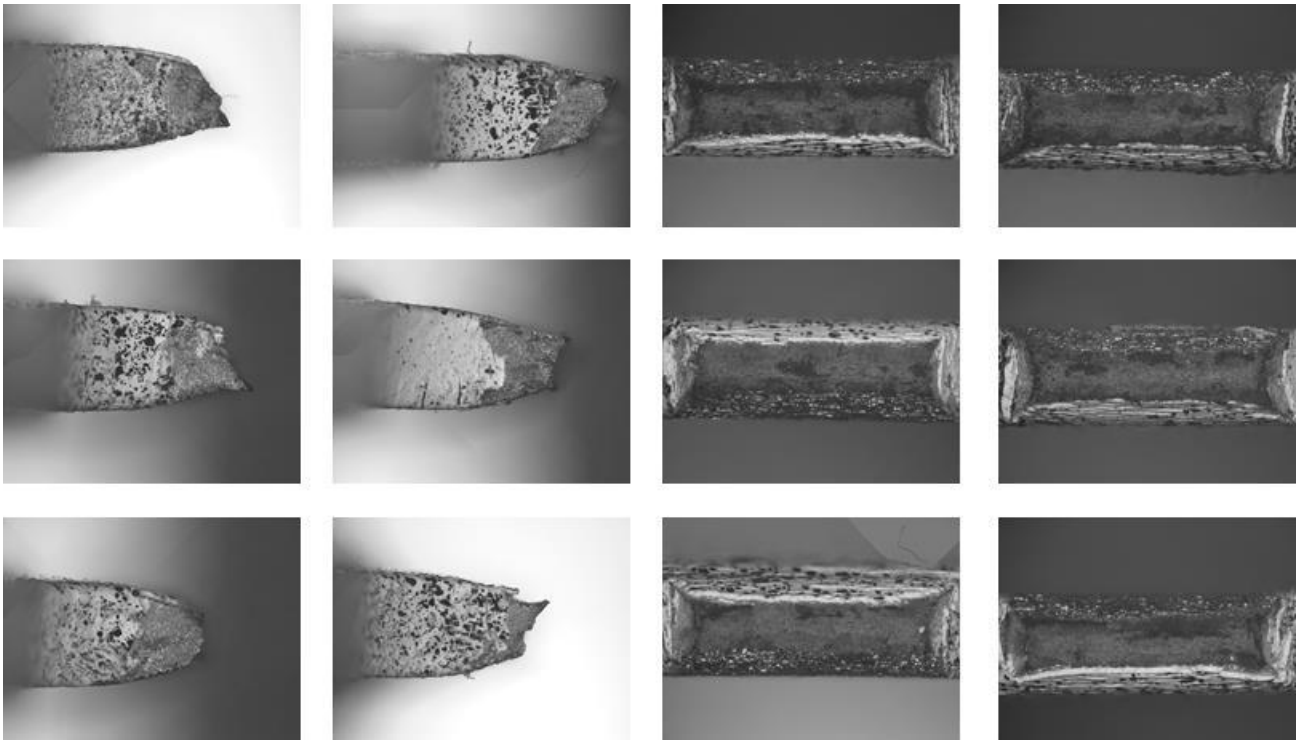

1a notch – fully martensitic

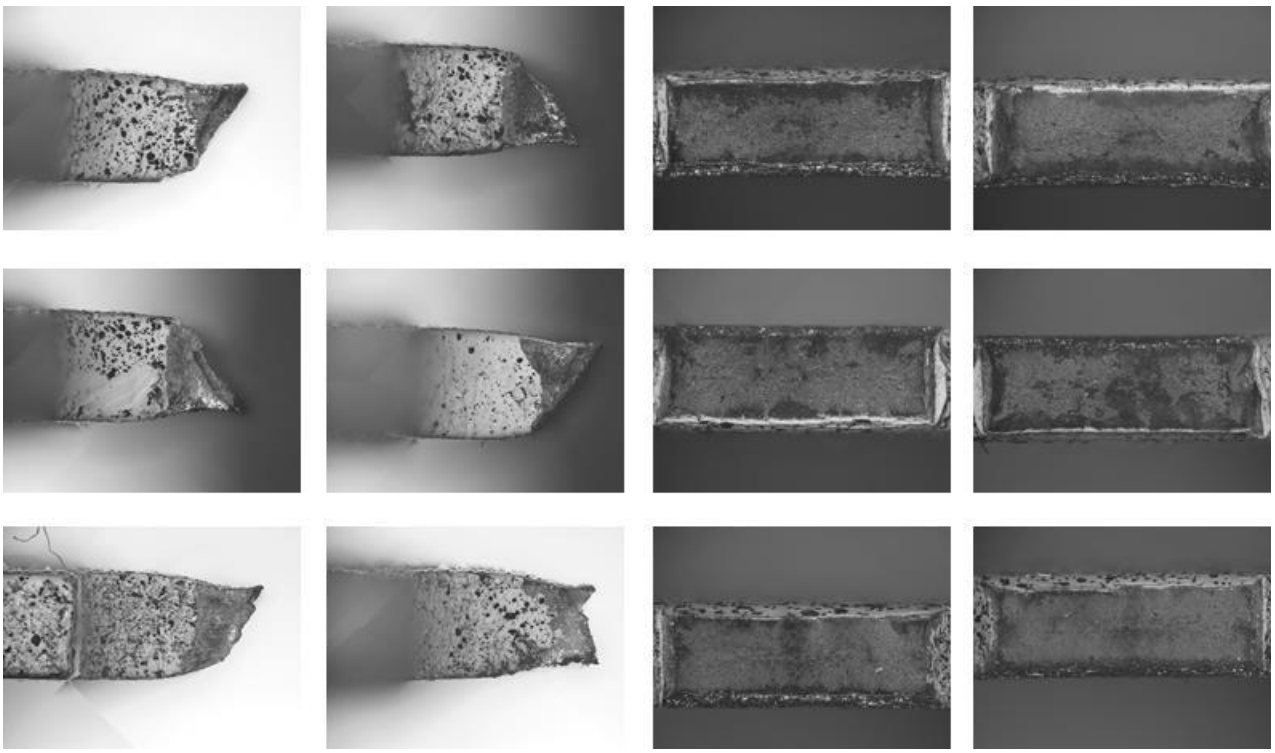

1a notch – intermediate forced air

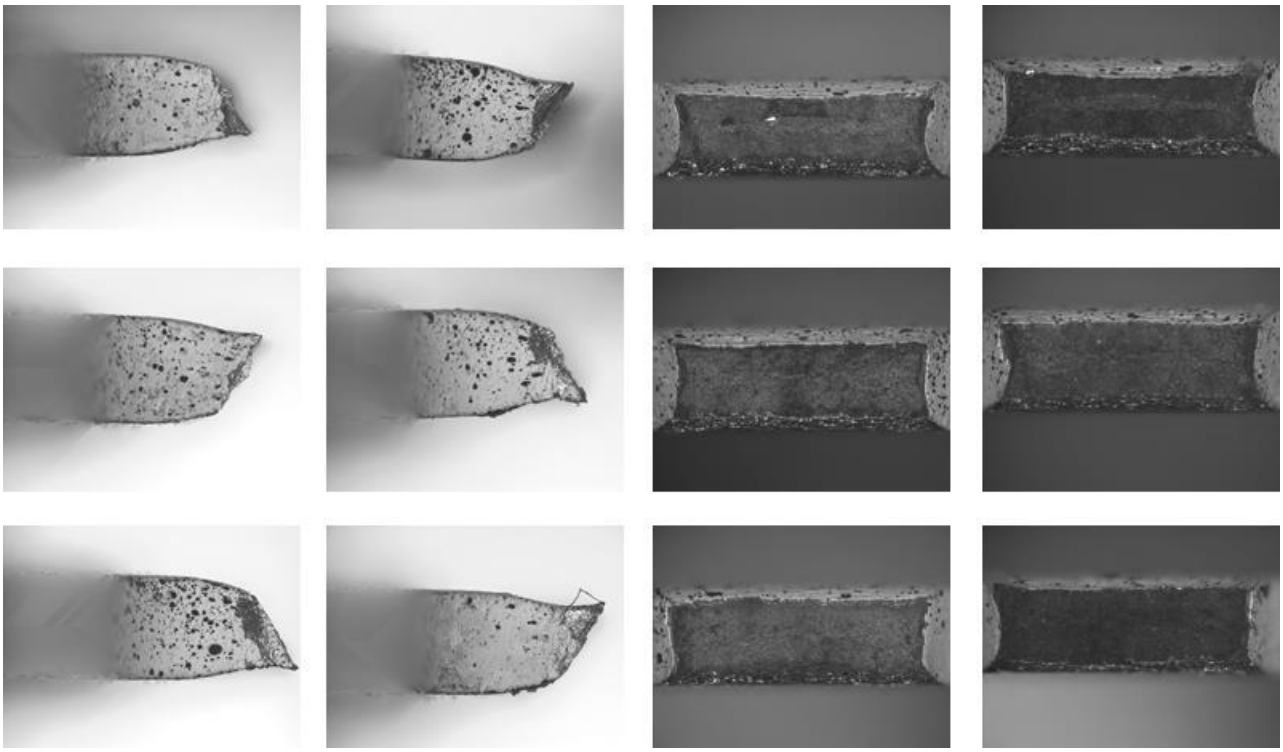

1a notch – intermediate Gleeble

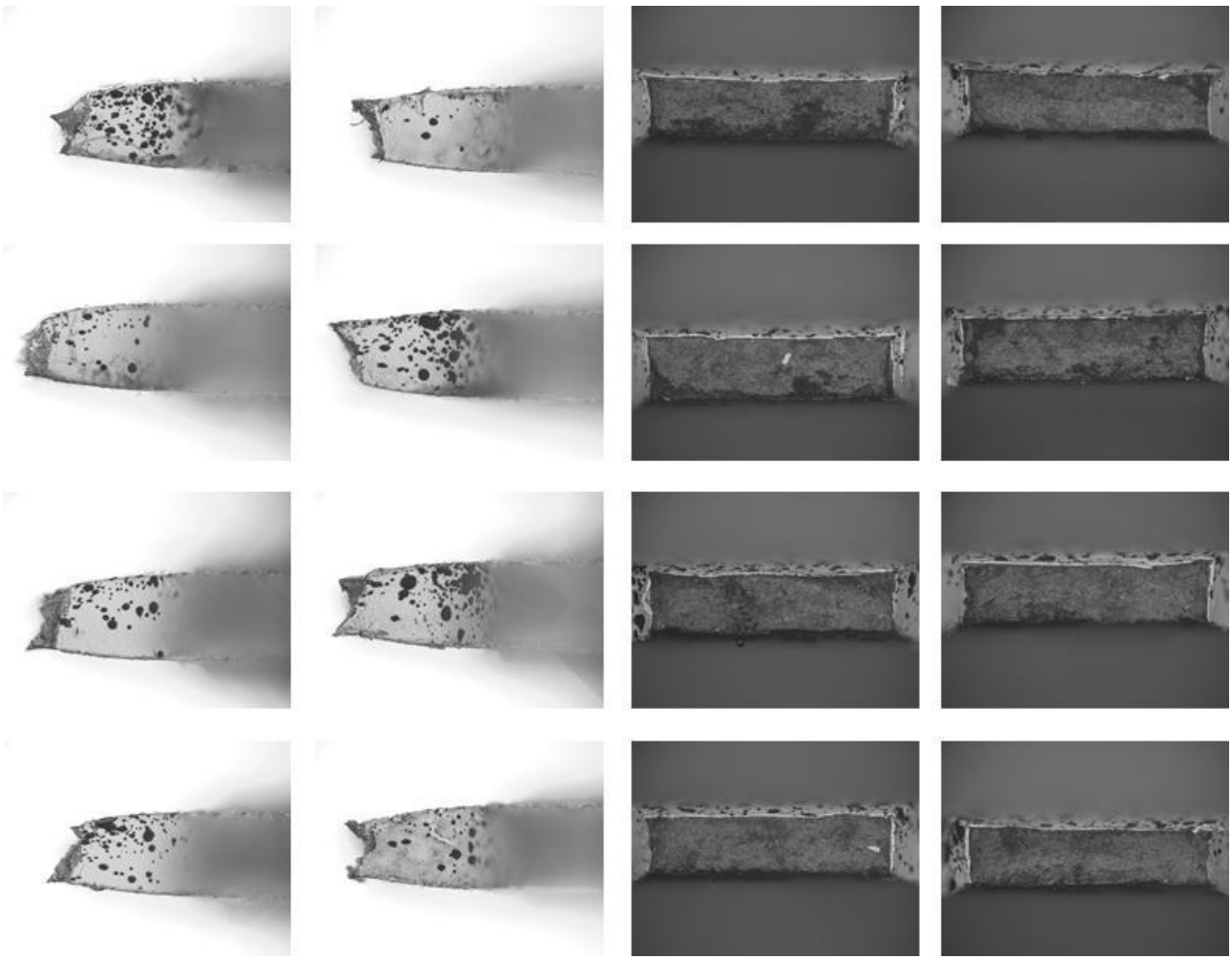

Appendix B Results for Miniature Uniaxial tensile

Fully martensitic material quench condition

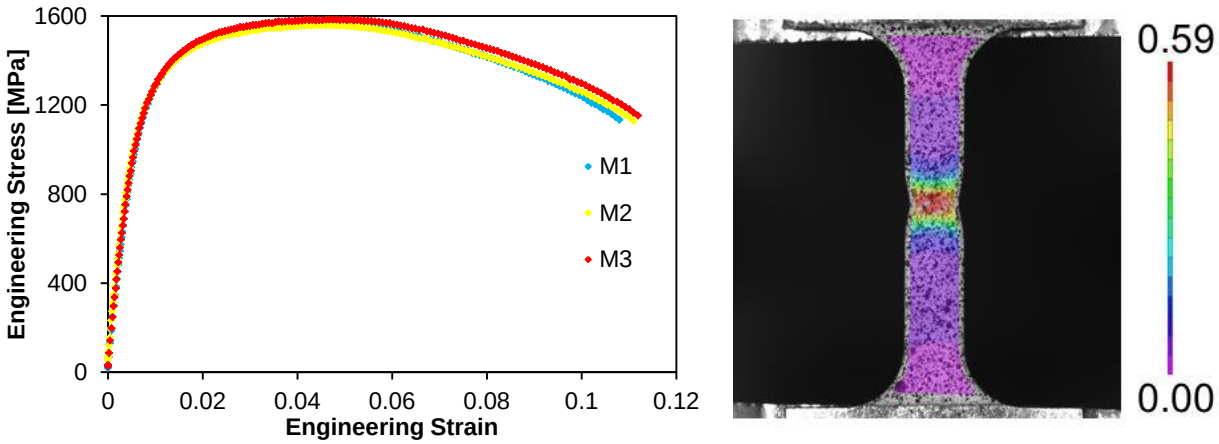

Figure 90: Engineering stress-strain curve for fully martensitic uniaxial tensile tests and typical contour plot of equivalent strain one frame before fracture.

Table 27: Properties of fully martensitic uniaxial tensile specimens

Sample	M1	M2	M3	Average
UTS (MPa)	1571	1559	1583	**1571**
Elongation	0.11	0.11	0.11	**0.11**
Initial Area (mm^2)	3.72	3.71	3.69	**3.70**
Final Area (mm^2)	2.63		2.45	**2.54**
Area strain	0.35		0.41	**0.38**

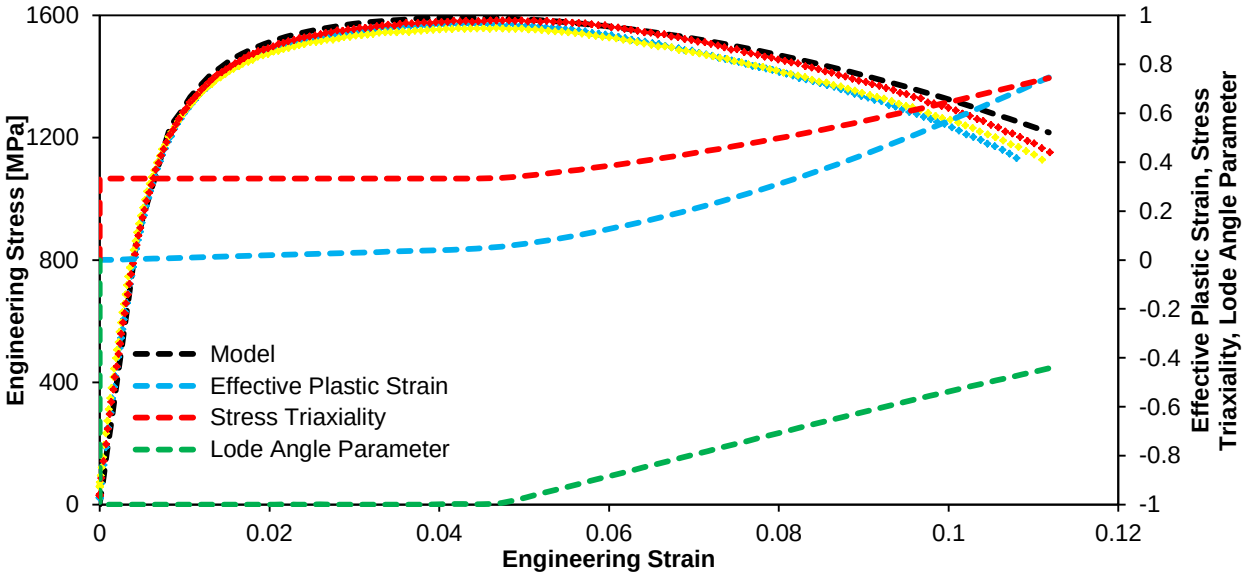

Figure 91: Uniaxial tensile model results for fully martensitic material condition

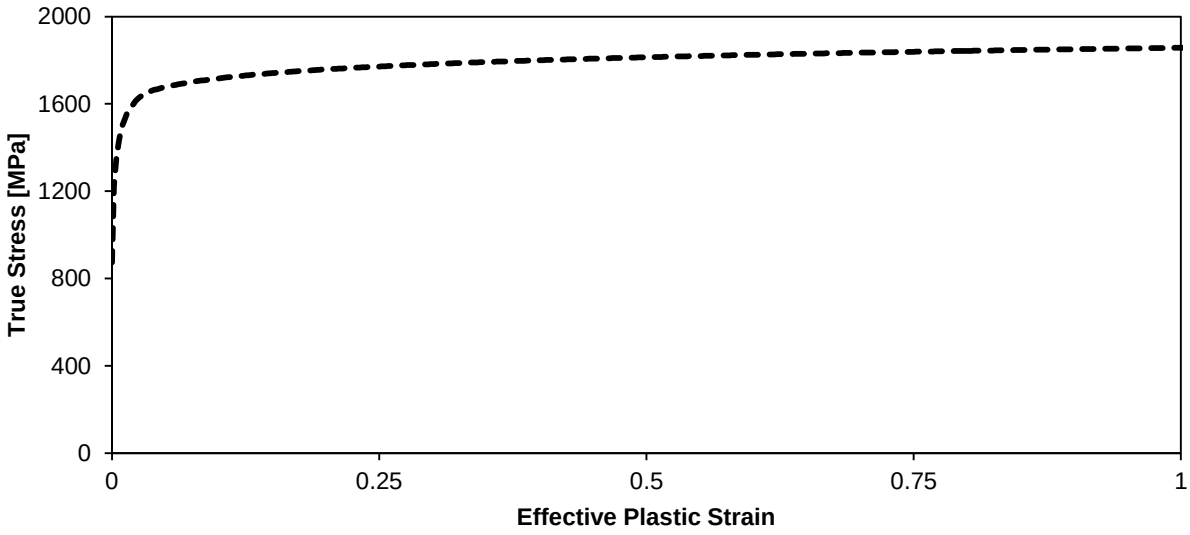

Figure 93: Flow stress curve for fully martensitic material condition

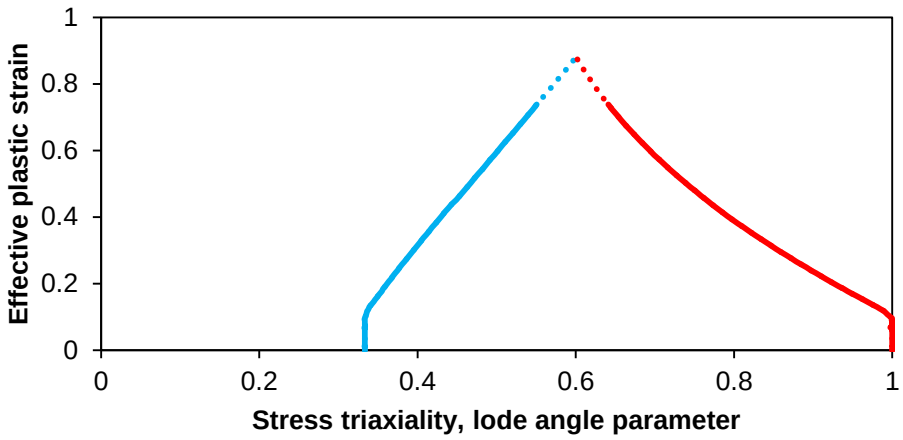

Figure 93: Stress state evolution for fully martensitic uniaxial tensile specimen

Intermediate forced-air material quench condition

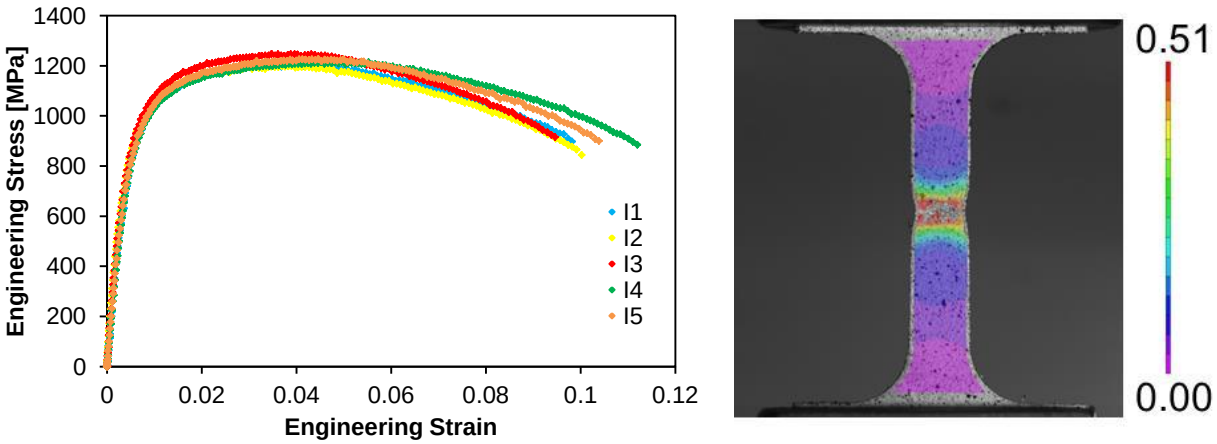

Figure 94: Engineering stress-strain curve for intermediate forced-air quench uniaxial tensile tests

Table 28: Properties of intermediate forced air quench uniaxial tensile specimens

Sample	I1	I2	I3	I4	I5	Average	Standard Deviation
UTS (MPa)	1206	1199	1215	1227	1248	**1219**	**17.3**
Elongation	0.10	0.10	0.11	0.10	0.09	**0.10**	**0.01**
Initial Area (mm^2)	3.67	3.68	3.56	3.49	3.43	**3.56**	**0.10**
Final Area (mm^2)	2.29	2.28	0.00	2.10	2.18	**1.77**	**0.89**
Area strain	0.47	0.48	0.00	0.50	0.45	**0.38**	**0.19**

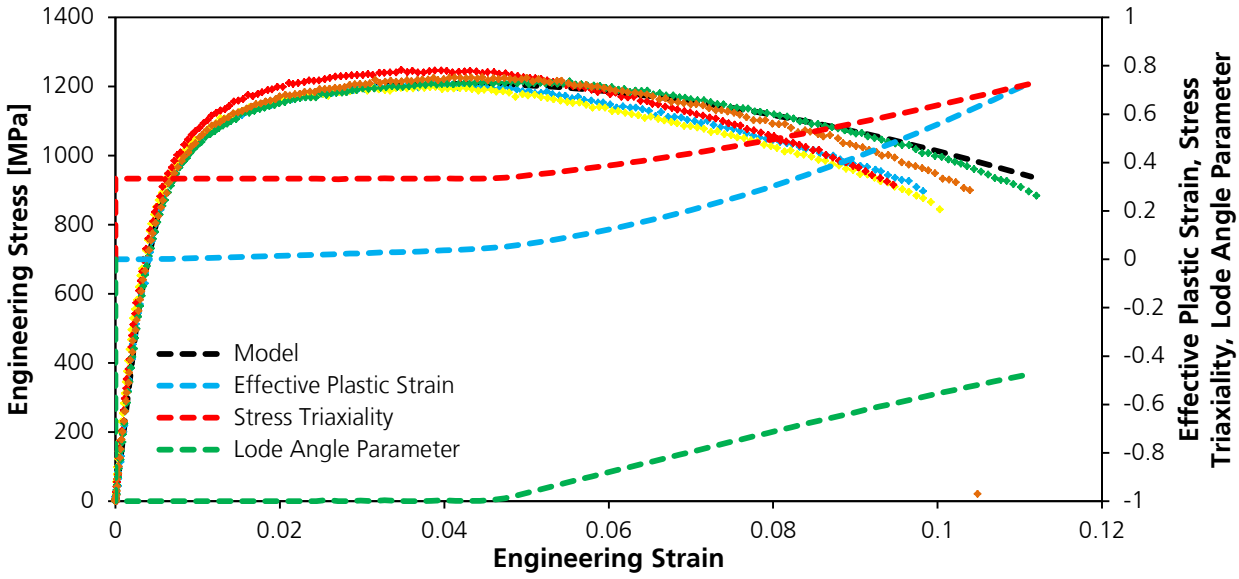

Figure 95: Uniaxial tensile model results for intermediate forced air quench material condition

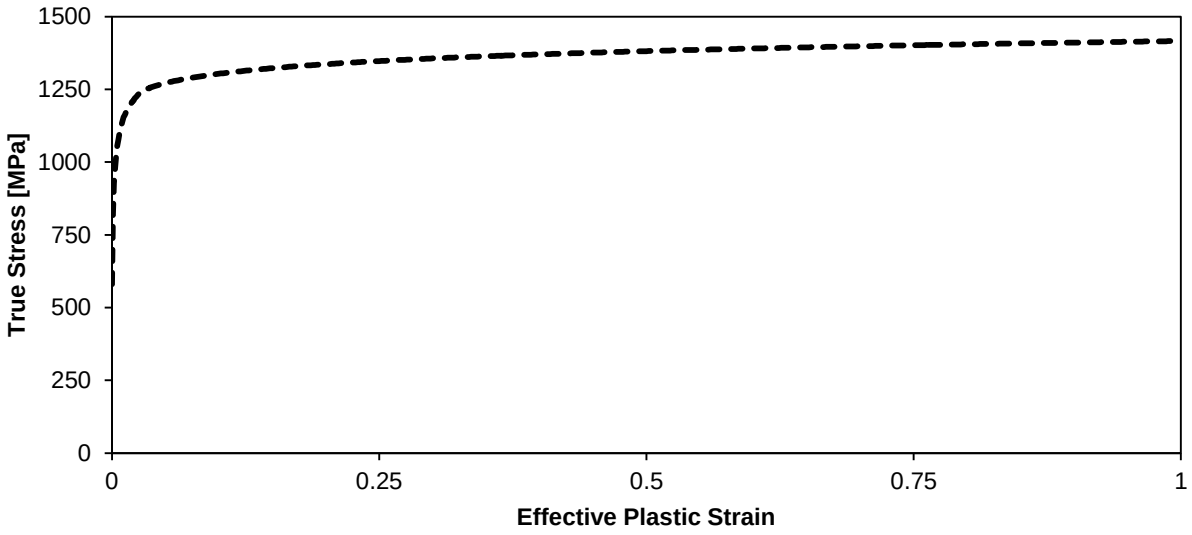

Figure 96: Flow stress curve for intermediate forced air quench material condition

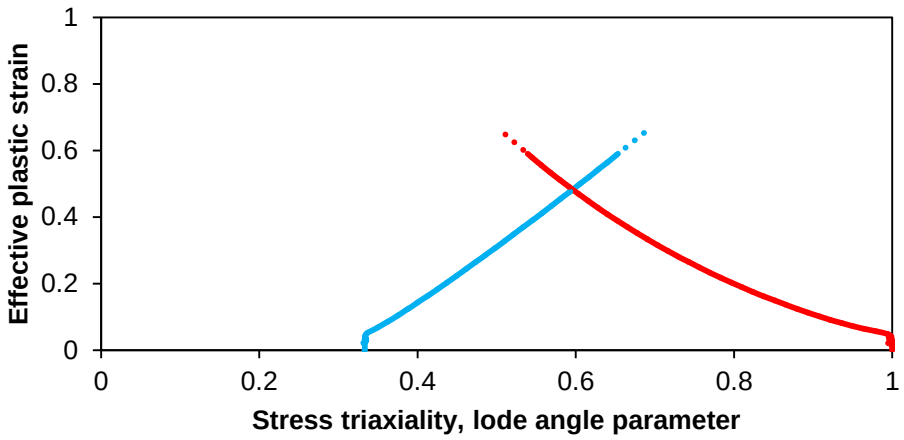

Figure 97: Stress state evolution for intermediate forced air quench uniaxial tensile specimen

Intermediate Gleeble material quench condition

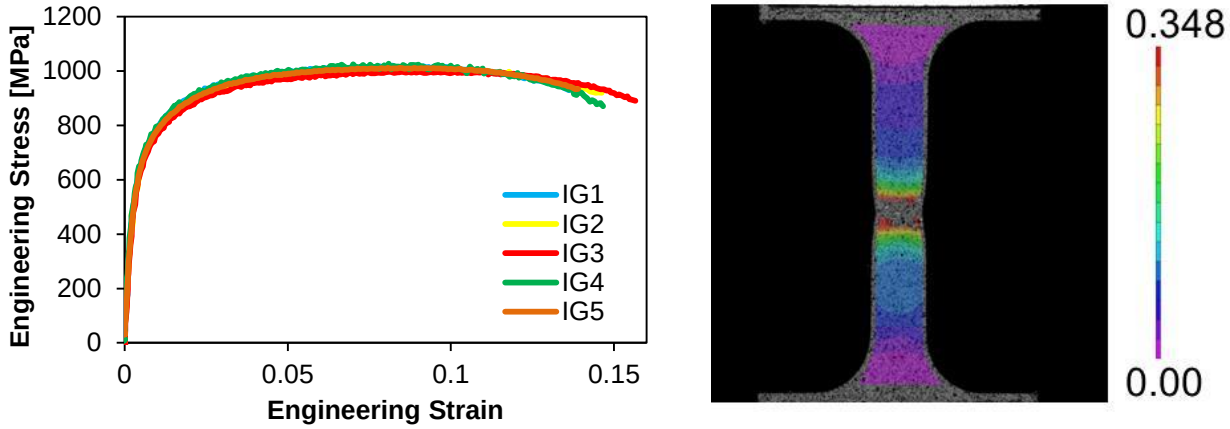

Figure 98: Engineering stress-strain curve for intermediate Gleeble uniaxial tensile tests and typical contour plot of equivalent strain one frame before fracture

Table 29: Properties of intermediate Gleeble uniaxial tensile specimens

Sample	IG1	IG2	IG3	IG4	IG5	Average	Standard Deviation
UTS (MPa)	1019	1010	999	1026	1012	**1013**	**10.1**
Elongation	0.14	0.15	0.16	0.15	0.14	**0.15**	**0.01**
Initial Area (mm^2)	3.18	3.18	3.17	3.18	3.17	**3.18**	**0.00**
Final Area (mm^2)	2.26	2.19	2.03	2.34	2.37	**2.24**	**0.14**
Area strain	0.34	0.37	0.45	0.31	0.29	**0.35**	**0.06**

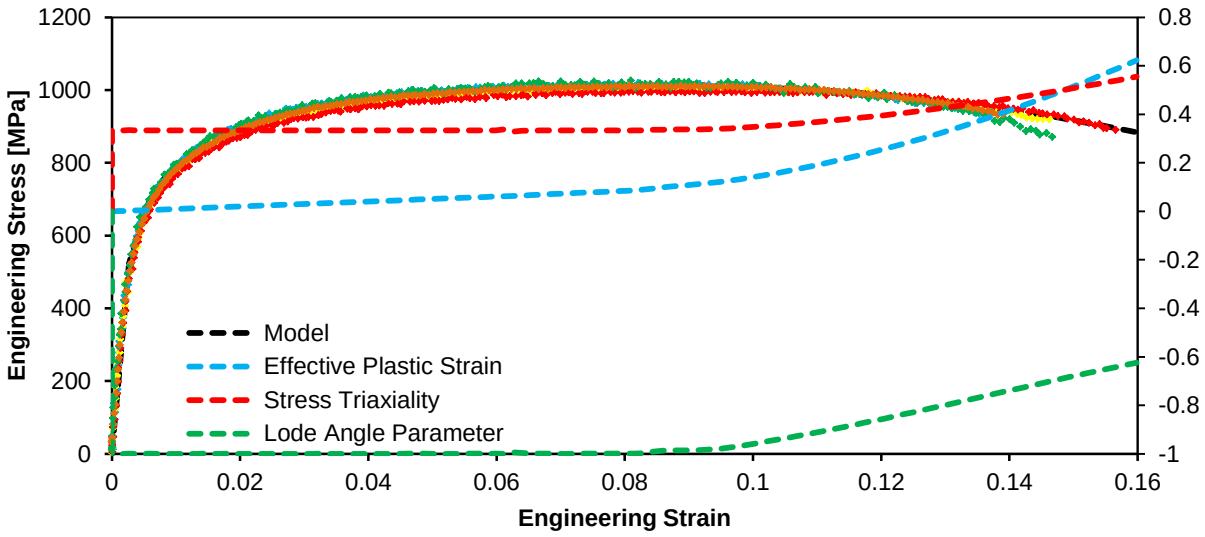

Figure 99: Uniaxial tensile model results for intermediate Gleeble quench material condition

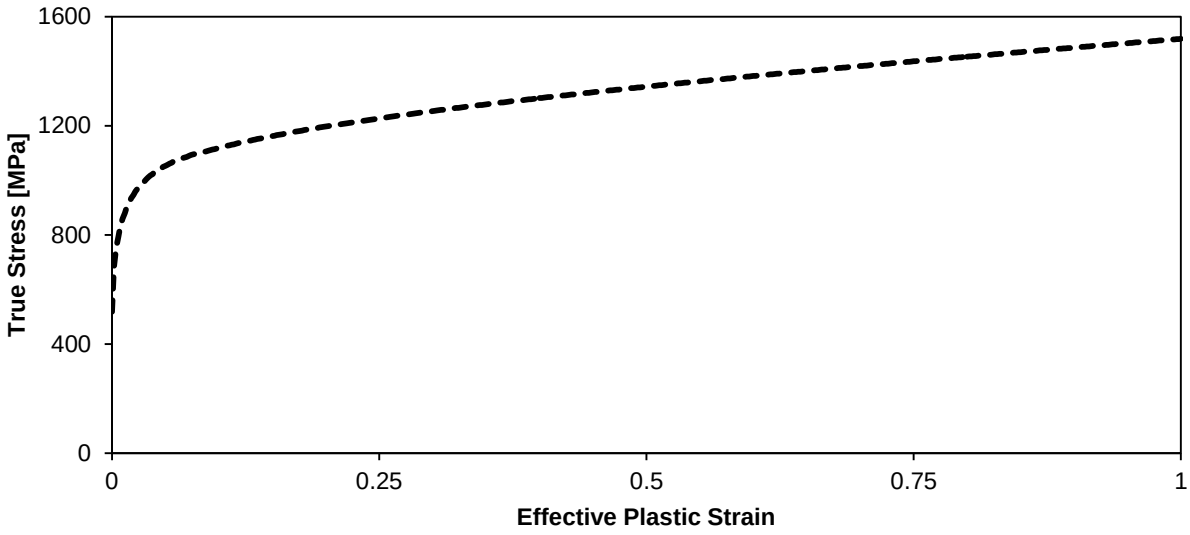

Figure 100: Flow stress curve for intermediate quench with deformation material condition

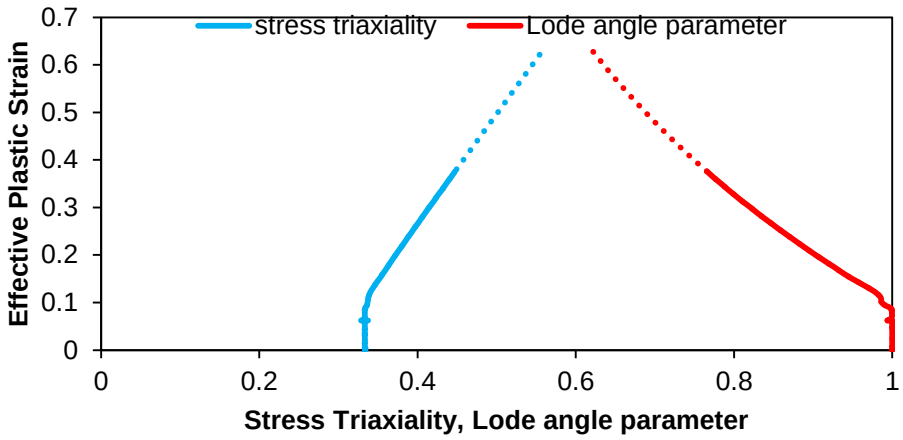

Figure 101: Stress state evolution for intermediate Gleeble quench uniaxial tensile specimen

400 °C Tailored Hot Stamped material quench condition

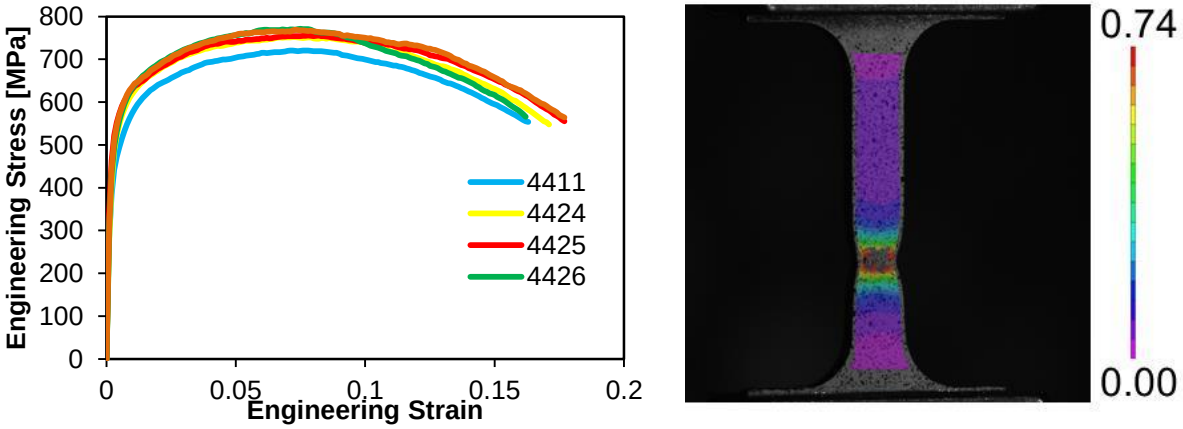

Figure 102: Engineering stress-strain curve for 400 °C quench uniaxial tensile tests and typical contour plot of equivalent strain one frame before fracture

Table 30: Properties of 400 °C Tailored Hot Stamped uniaxial tensile specimens

Sample	4-1	4-2	4-3	4-4	4-5	Average	Standard Deviation
UTS (MPa)	721	752	756	771	769	**754**	**20.3**
Elongation	0.18	0.18	0.19	0.17	0.19	**0.18**	**0.01**
Initial Area (mm^2)	5.71	5.38	5.41	5.31	5.30	**5.42**	**0.17**
Final Area (mm^2)	2.11	2.10	2.26	2.17	2.30	**2.18**	**0.09**
Area strain	1.00	0.94	0.87	0.90	0.84	**0.91**	**0.06**

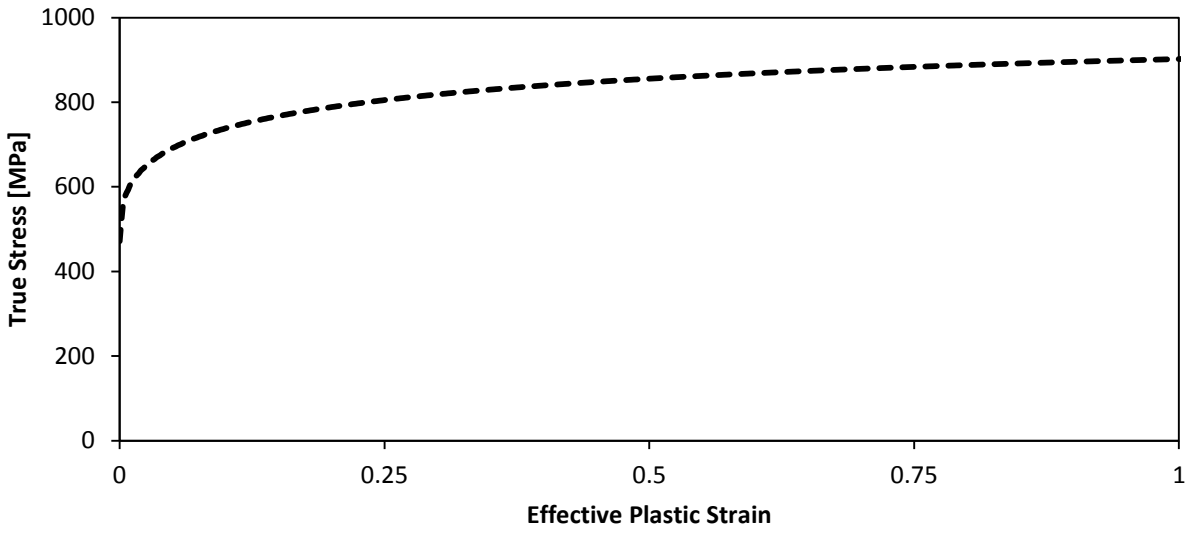

Figure 103: Flow stress curve for 400 °C tailored hot stamped material condition

700 °C Tailored Hot Stamped material quench condition

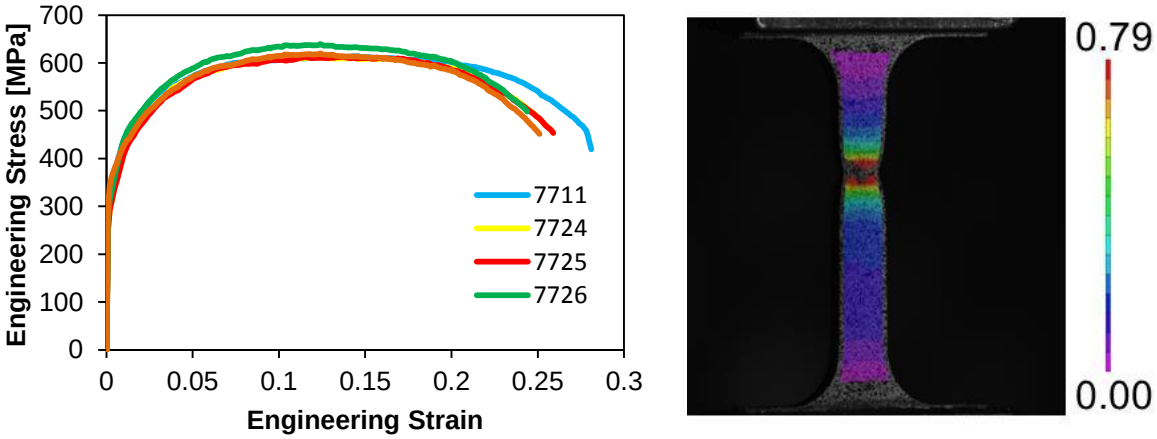

Figure 104: Engineering stress-strain curve for 700 °C quench uniaxial tensile tests and typical contour plot of equivalent strain one frame before fracture

Table 31: Properties of 700 ° C Tailored Hot Stamped uniaxial tensile specimens

Sample	700-1	700-2	700-3	700-4	700-5	Average	Standard Deviation
UTS (MPa)	614	612	613	632	620	618	**8.27**
Elongation	0.28	0.28	0.28	0.27	0.27	0.28	**0.01**
Initial Area (mm^2)	5.49	5.41	5.50	5.48	5.52	5.48	**0.04**
Final Area (mm^2)	2.02	1.56	1.53	1.56	1.82	1.70	**0.22**
Area strain	1.00	1.24	1.29	1.26	1.11	1.18	**0.12**

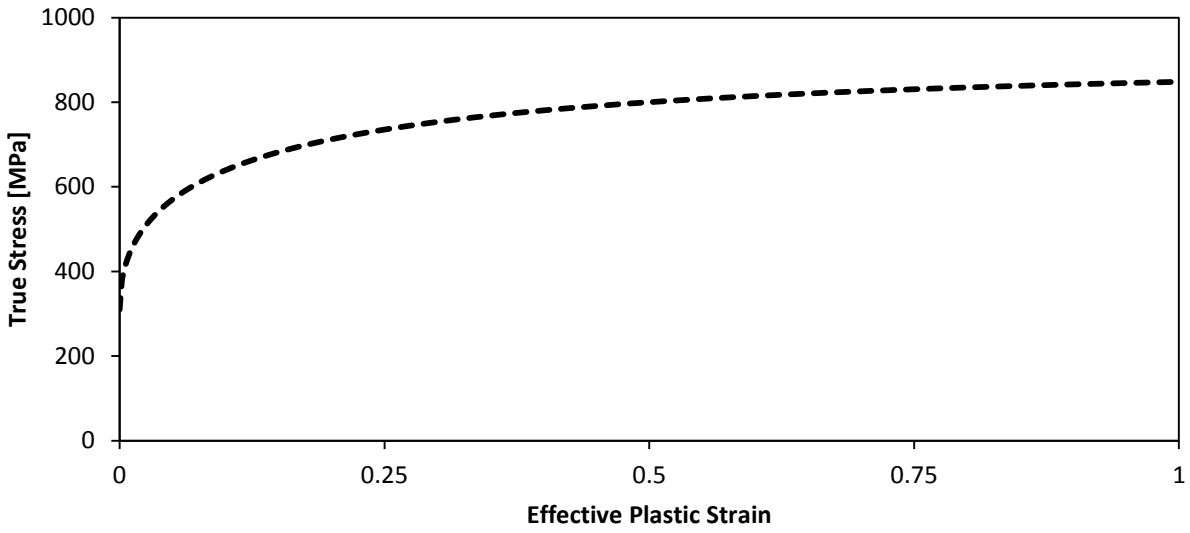

Figure 105: Flow stress curve for 700 °C tailored hot stamped material condition

Appendix C Results For 4a Notched Tensile

Fully martensitic material quench condition

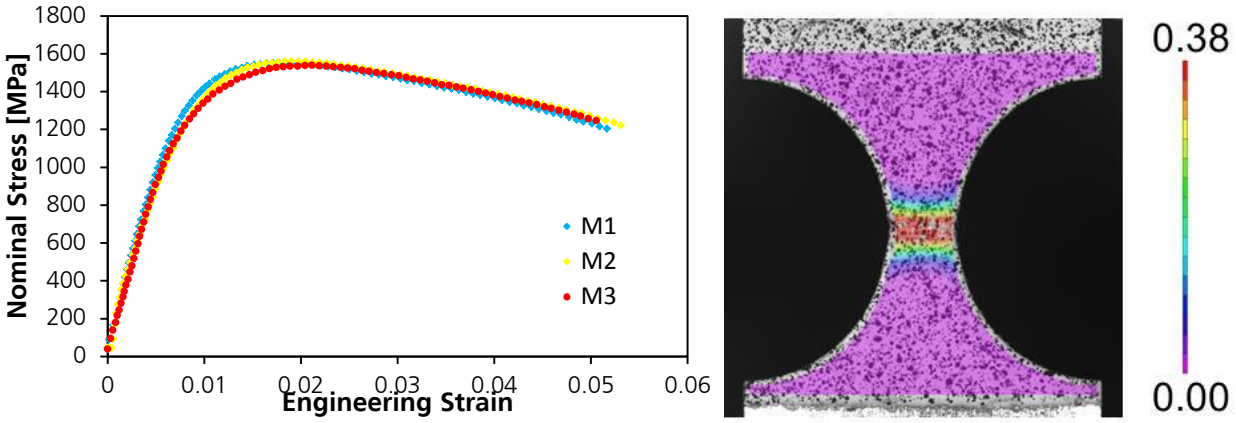

Figure 106: Nominal stress-strain curve for fully martensitic 4a notch tensile tests

Table 32: Properties of fully martensitic 4a notch tensile specimens

Sample	M1	M2	M3	Average
UTS (MPa)	1539	1552	1560	**1550**
Elongation	0.05	0.05	0.05	**0.05**
Initial Area (mm^2)	3.99	3.97	3.99	**3.99**
Final Area (mm^2)	2.81	2.83	2.87	**2.84**
Area strain	0.35	0.34	0.33	**0.34**

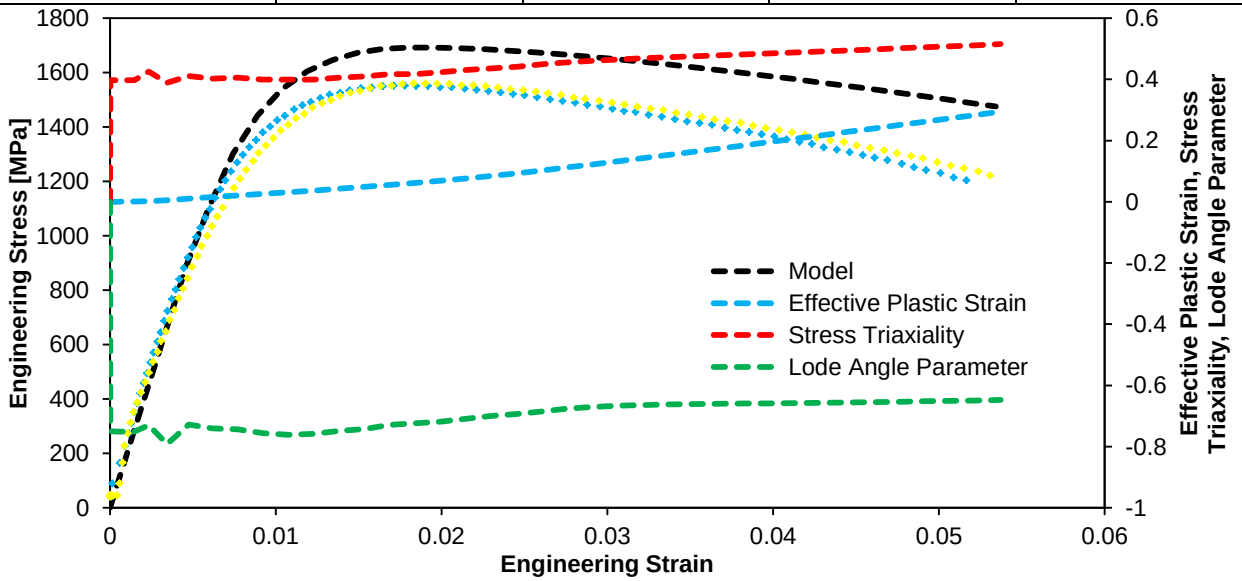

Figure 107: 4a notched tensile model results for fully martensitic material condition

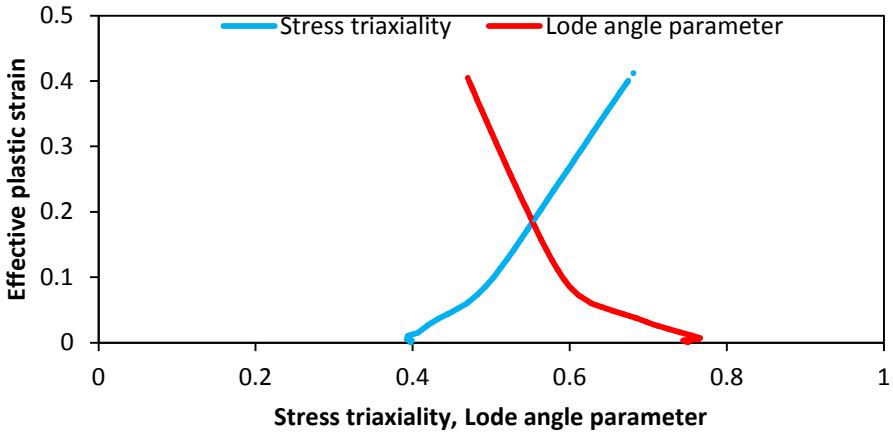

Figure 108: Stress state evolution for fully martensitic 4a notched tensile specimen

Intermediate forced-air material quench condition

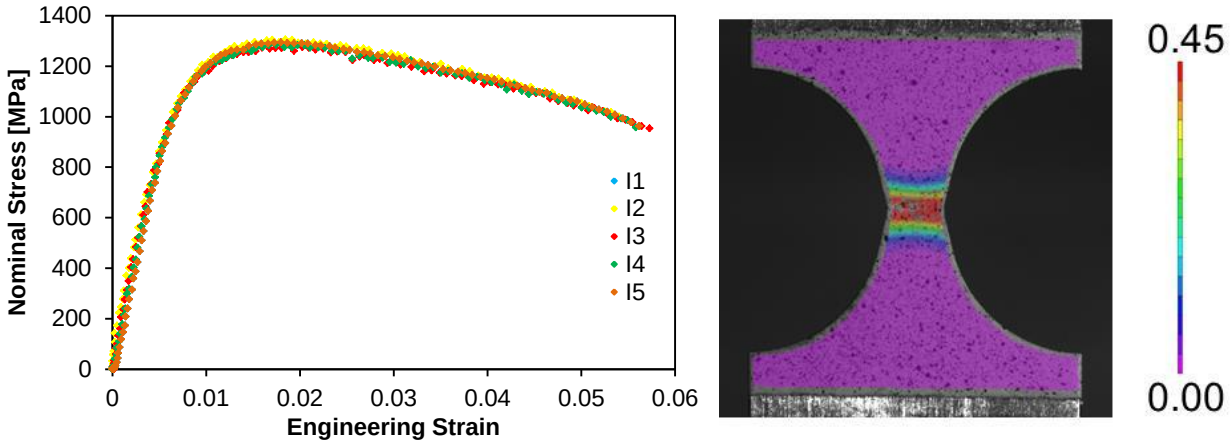

Figure 109: Nominal stress-strain curve for intermediate forced-air quench 4a notch tensile tests

Table 33: Properties of intermediate forced-air quench 4a notch tensile tests

Sample	I1	I2	I3	I4	Average	Standard Deviation
UTS (MPa)	1306	1286	1284	1294	**1293**	**9.90**
Elongation	0.05	0.06	0.06	0.06	**0.71**	**0.02**
Initial Area (mm^2)	3.49	3.46	3.57	3.57	**3.52**	**0.06**
Final Area (mm^2)	2.62	2.34	2.38	2.53	**2.47**	**0.13**
Area strain	0.29	0.39	0.40	0.34	**0.36**	**0.05**

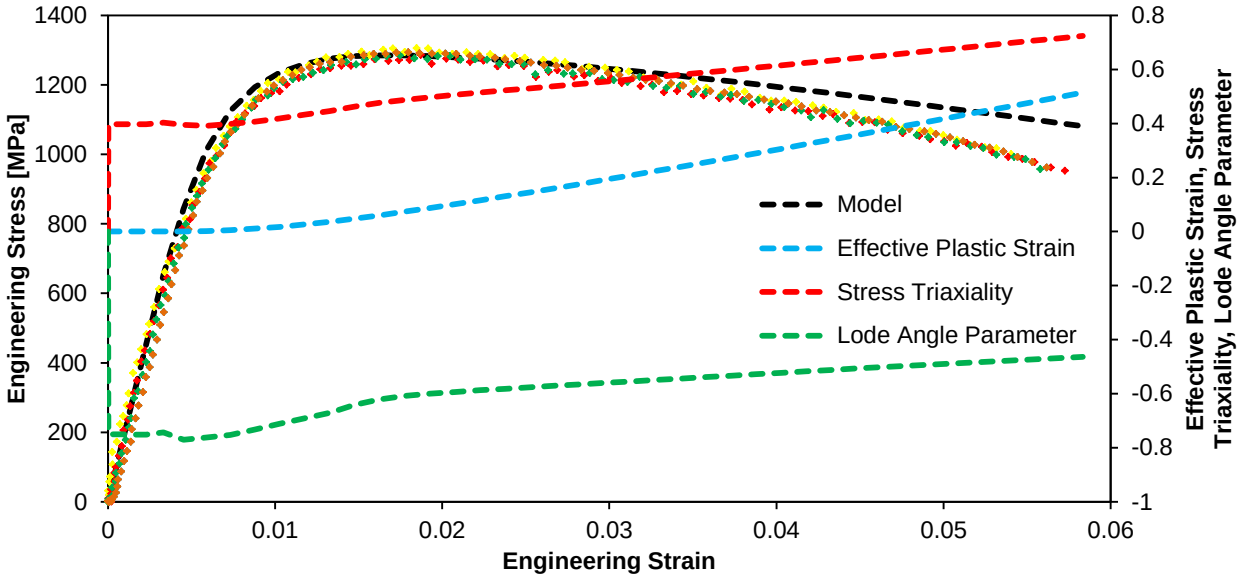

Figure 110: 4a notched tensile model results for intermediate forced air quench material condition

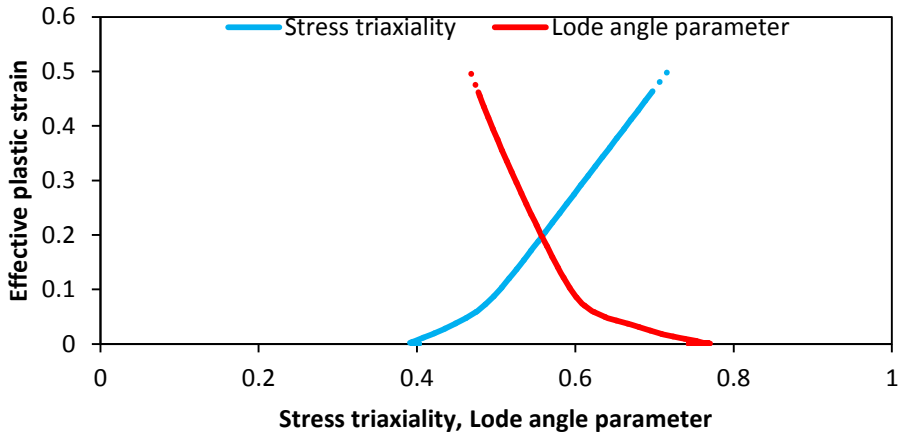

Figure 111: Stress state evolution for intermediate forced air quench 4a notched tensile specimen

Intermediate Gleeble material quench condition

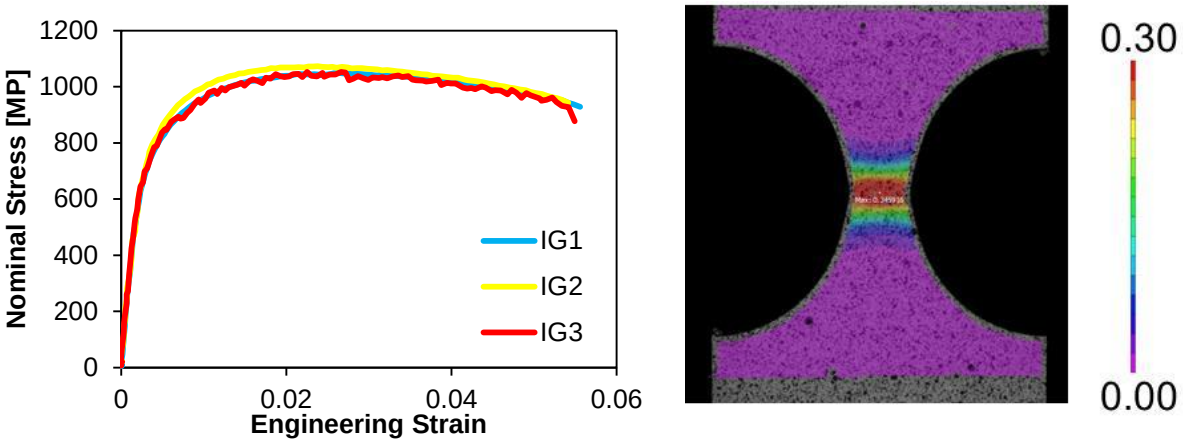

Figure 112: Nominal stress-strain curve for intermediate Gleeble 4a notch tensile tests

Table 34: Properties of intermediate Gleeble 4a notch tensile tests

Sample	IG1	IG2	IG3	Average
UTS (MPa)	1049	1073	1053	**1058**
Elongation	0.06	0.05	0.05	**0.05**
Initial Area (mm^2)	3.22	3.23	3.19	**3.22**
Final Area (mm^2)	2.37	2.15	2.51	**2.34**
Area strain	0.31	0.41	0.24	**0.32**

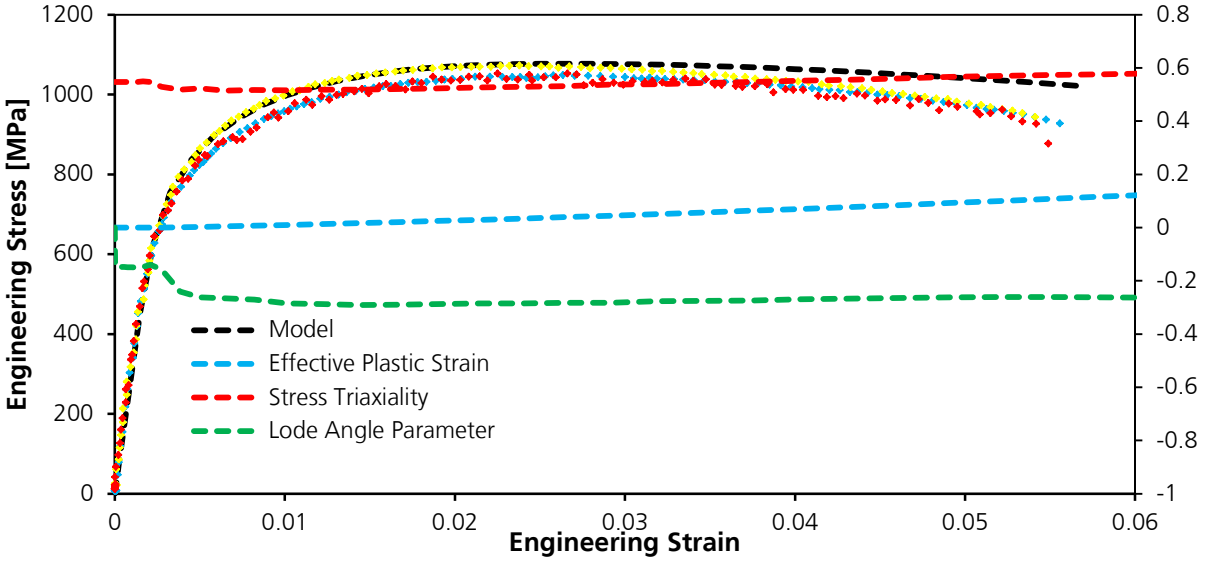

Figure 113: 4a notched tensile model results for intermediate Gleeble quench material condition

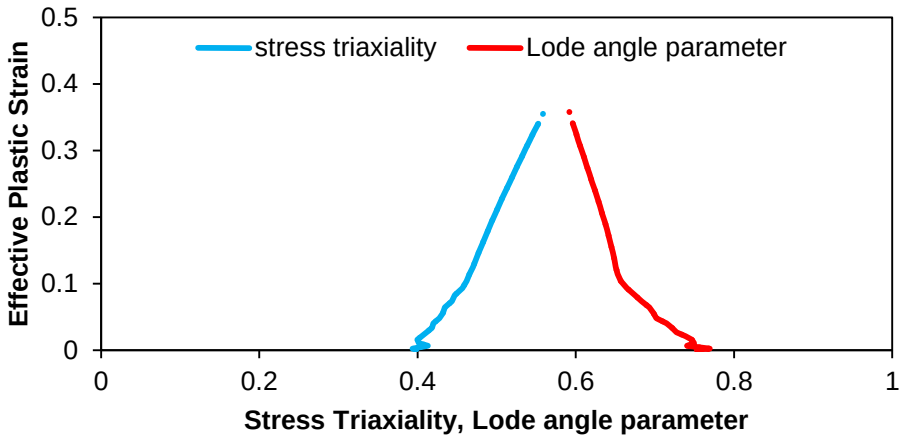

Figure 114: Stress state evolution for intermediate Gleeble quench 4a notched tensile specimen

Appendix D Results For 1a Notched Tensile

Fully martensitic material quench condition

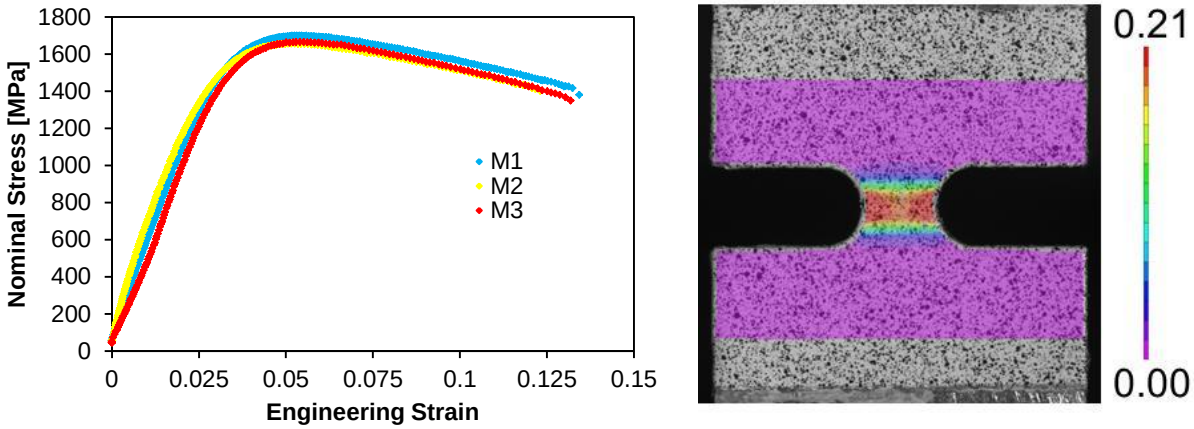

Figure 115: Nominal stress-strain curve for fully martensitic 1a notch tensile tests

Table 35: Properties of fully martensitic 1a notch tensile specimens

Sample	1	2	3	Average
UTS (MPa)	1699	1656	1665	**1673**
Elongation	0.13	0.12	0.13	**0.13**
Initial Area (mm^2)	3.98	3.97	3.99	**3.98**
Final Area (mm^2)	3.31	3.60	2.91	**3.28**
Area strain	0.19	0.10	0.31	**0.20**

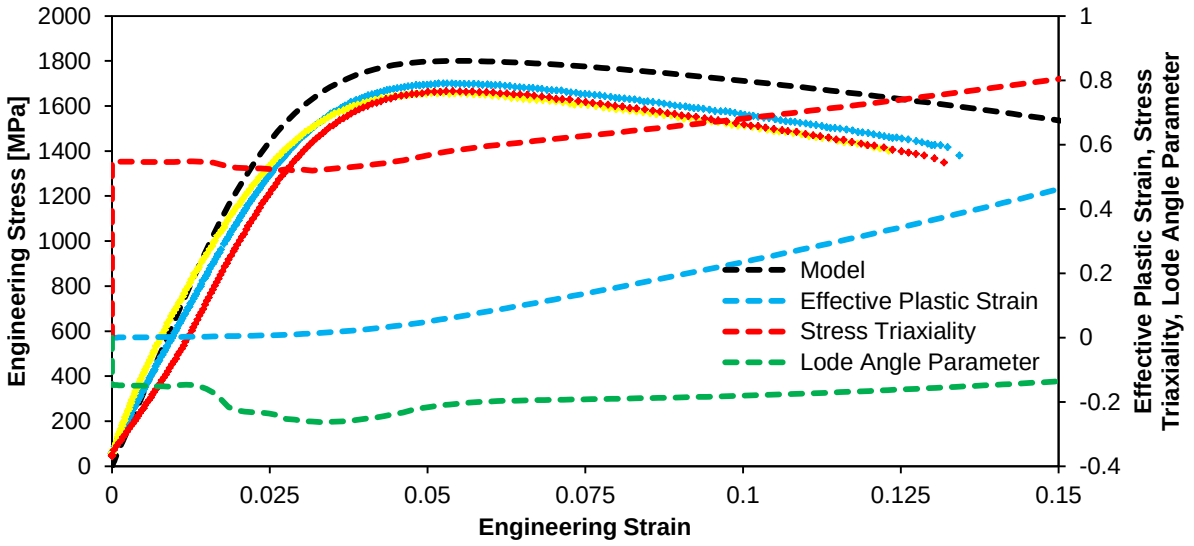

Figure 116: 1a notched tensile model results for fully martensitic material condition

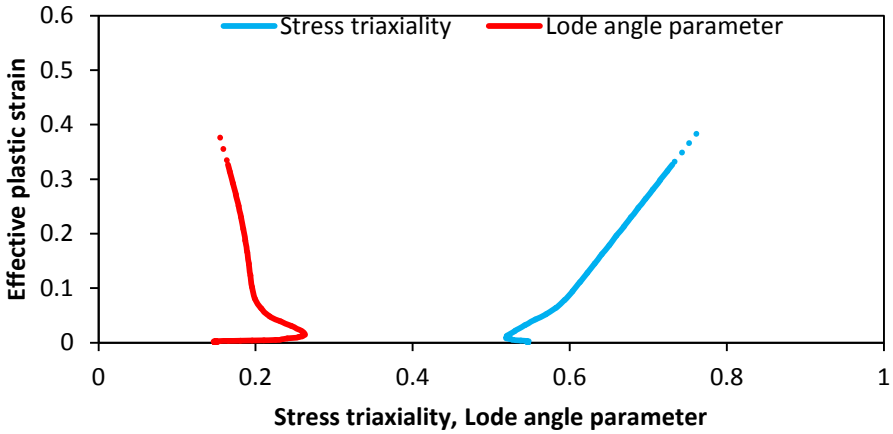

Figure 117: Stress state evolution for fully martensitic 1a notched tensile specimen

Intermediate forced-air material quench condition

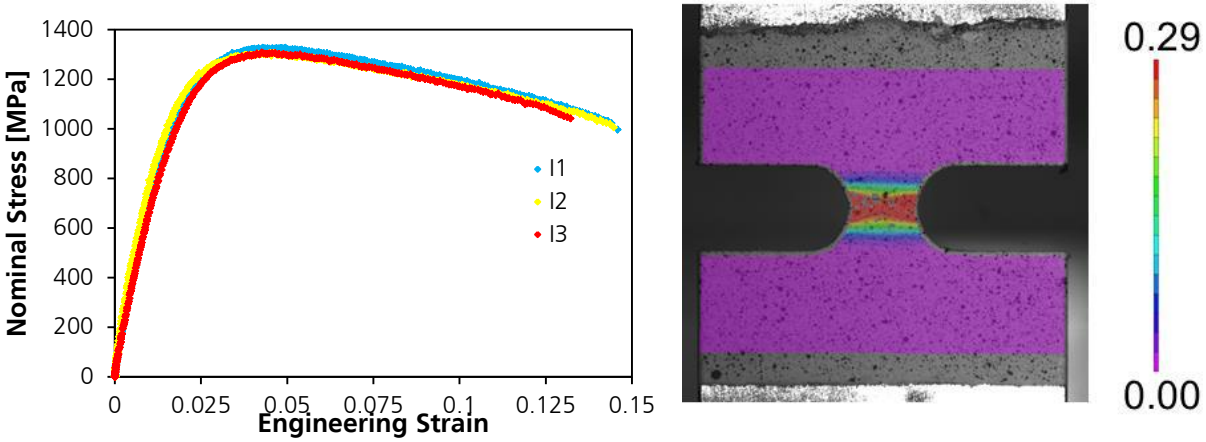

Figure 118: Nominal stress-strain curve for intermediate forced-air quench 1a notch tensile tests

Table 36: Properties of intermediate forced-air quench 1a notch tensile specimens

Sample	1	2	3	Average
UTS (MPa)	1327	1306	1307	**1313**
Elongation	0.15	0.14	0.13	**0.14**
Initial Area (mm^2)	3.39	3.71	3.67	**3.59**
Final Area (mm^2)	2.54	2.79	2.81	**2.71**
Area strain	0.29	0.29	0.27	**0.28**

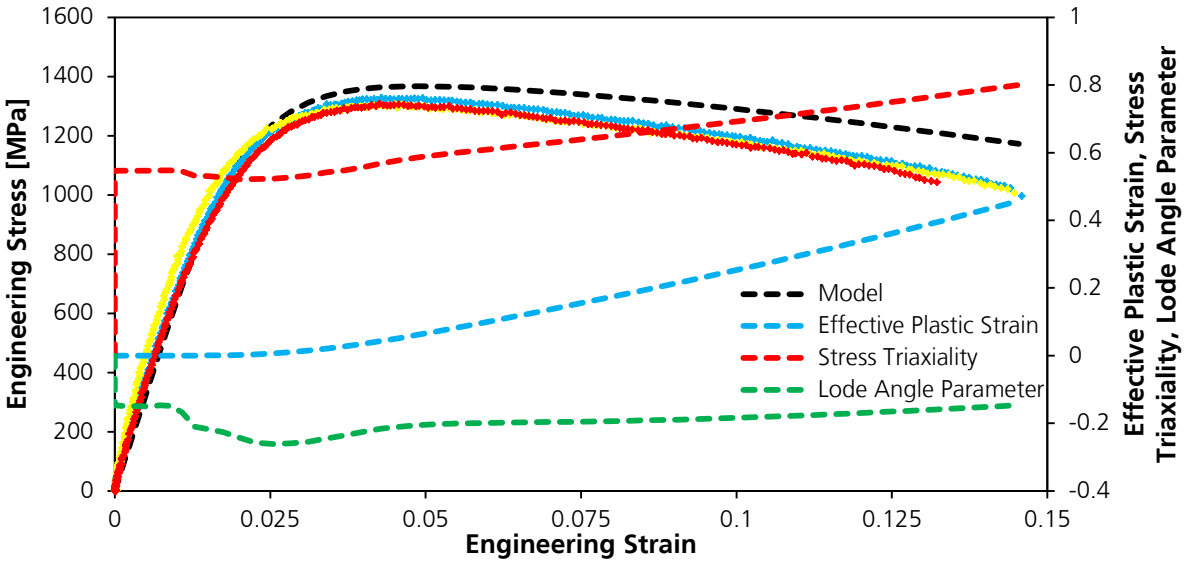

Figure 119: 1a notched tensile model results for intermediate forced air quench material condition

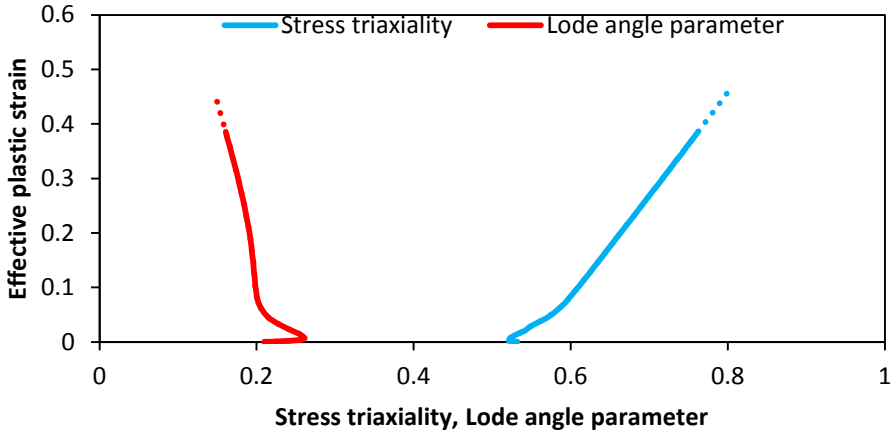

Figure 120: Stress state evolution for forced air intermediate quench 1a notched tensile specimen

Intermediate Gleeble material quench condition

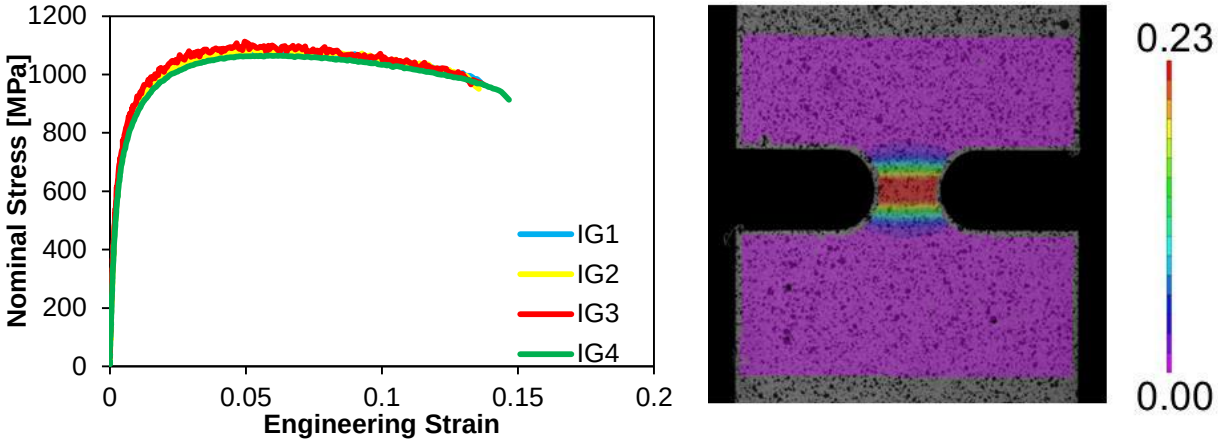

Figure 121: Nominal stress-strain curve for intermediate forced-air quench 1a notch tensile tests

Table 37: Properties of intermediate Gleeble 1a notch tensile specimens

Sample	I1	I2	I3	I4	Average	Standard Deviation
UTS (MPa)	1093	1092	1113	1065	**1091**	**19.7**
Elongation	0.14	0.13	0.14	0.15	**0.14**	**0.01**
Initial Area (mm^2)	3.17	3.25	3.20	3.14	**3.19**	**0.05**
Final Area (mm^2)	2.21	2.32	2.32	2.24	**2.27**	**0.06**
Area strain	0.36	0.34	0.32	0.34	**0.34**	**0.02**

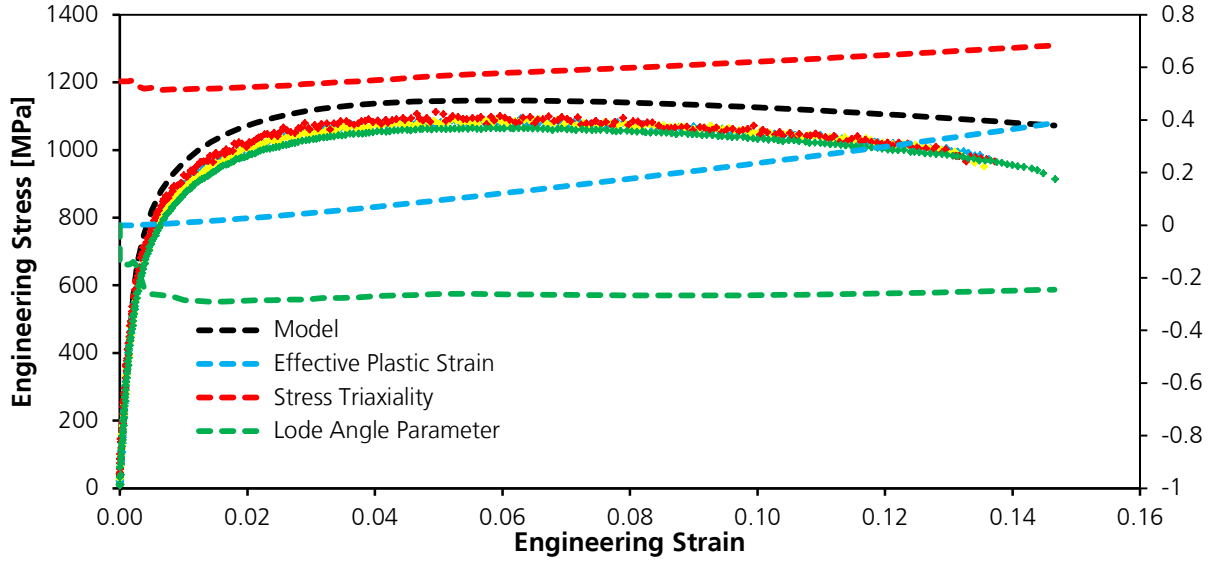

Figure 122: 1a notched tensile model results for intermediate Gleeble quench material condition

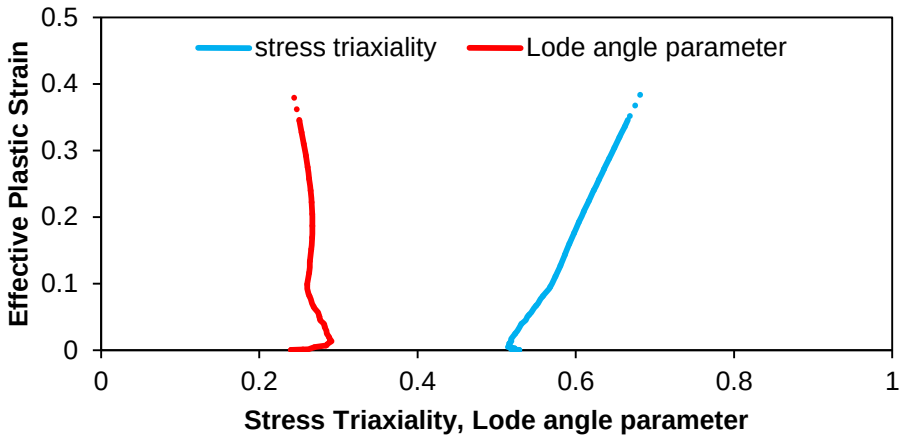

Figure 123: Stress state evolution for intermediate Gleeble quench 1a notched tensile specimen

Appendix E Alternative Tensile Specimen Meshes

For the tensile geometries that were used in this work, numerous mesh sizes were considered.

These meshes are depicted below:

Uniaxial tensile meshes (0.2 mm, 0.05 mm)

4a notched tensile meshes (0.2 mm and 0.05 mm)

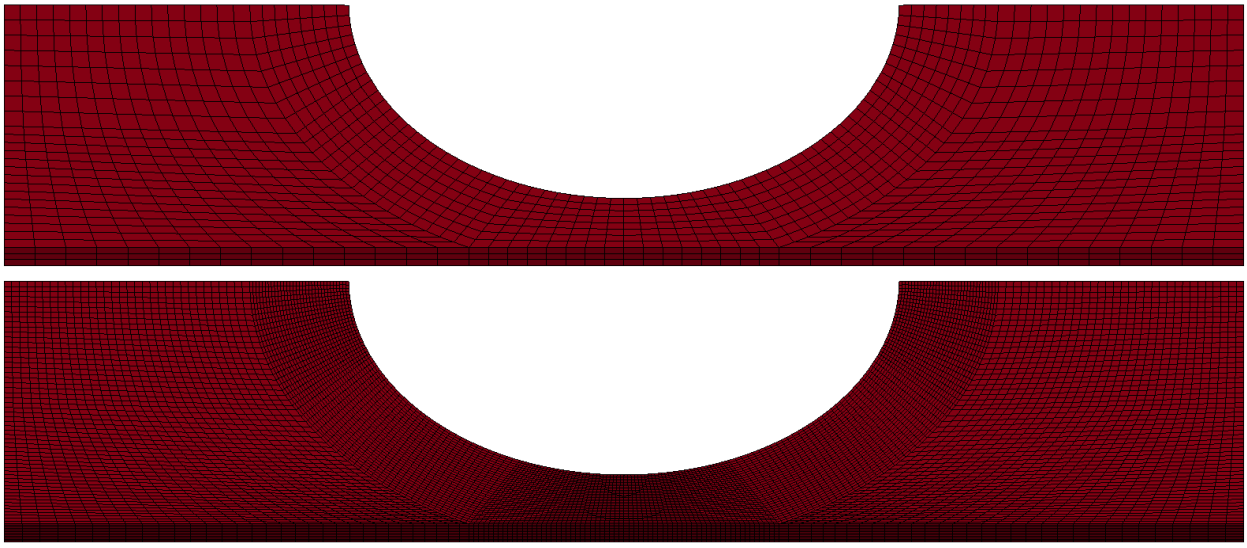

1a notched tensile meshes (0.2 mm, and 0.05 mm)

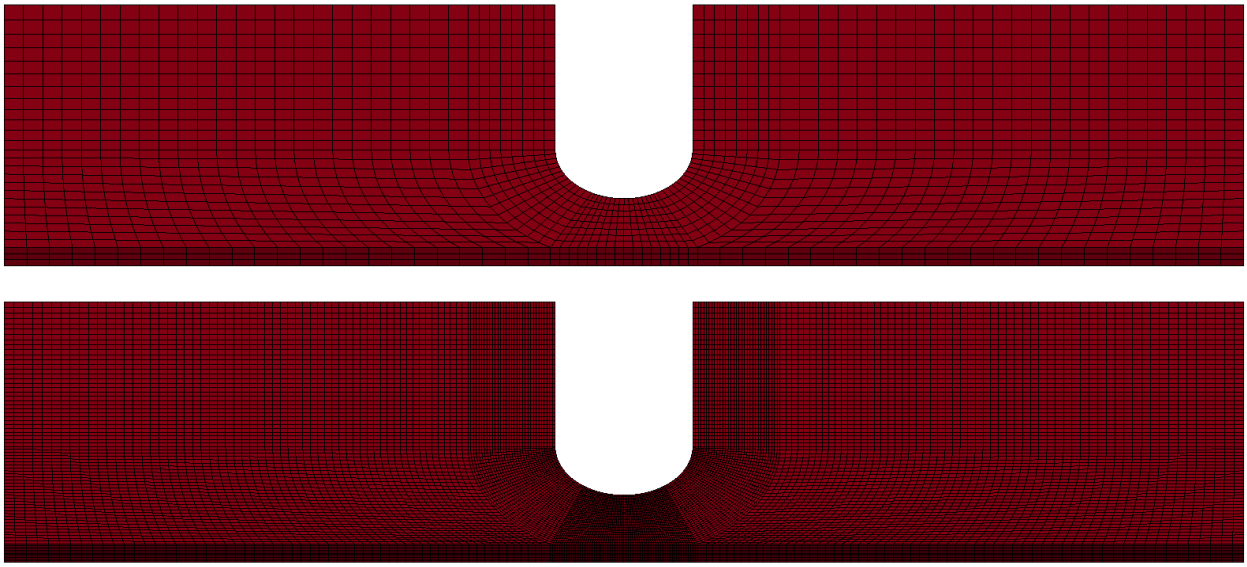

Appendix F Results For 0° Butterfly

Fully martensitic material quench condition

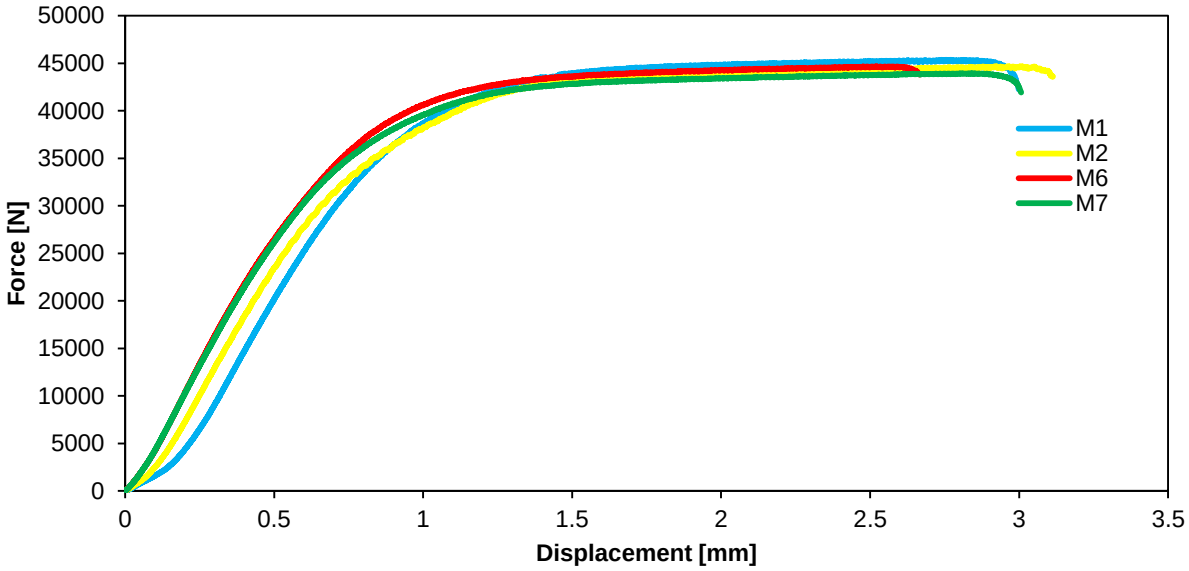

Figure 124: Load-displacement response for fully martensitic 0° butterfly test

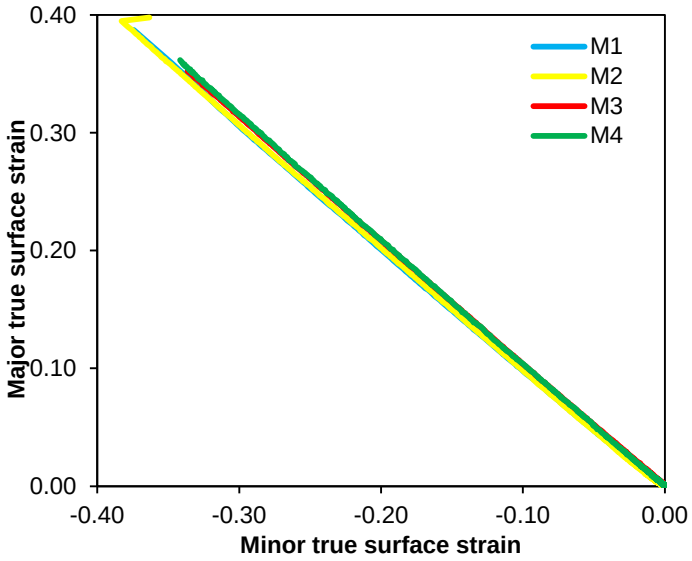

Figure 125: Major true surface strain vs. minor true surface strain for fully martensitic 0° butterfly test

Table 38: Failure strains for fully martensitic 0° butterfly test

Sample	1	2	3	4	Average	Standard Deviation
ε_1	0.39	0.40	0.35	0.36	**0.39**	**0.03**
ε_2	-0.37	-0.36	-0.34	-0.34	**-0.37**	**0.03**

ε_{eq}	0.46	0.54	0.46	0.59	**0.54**	**0.08**

Intermediate Forced Air Quench

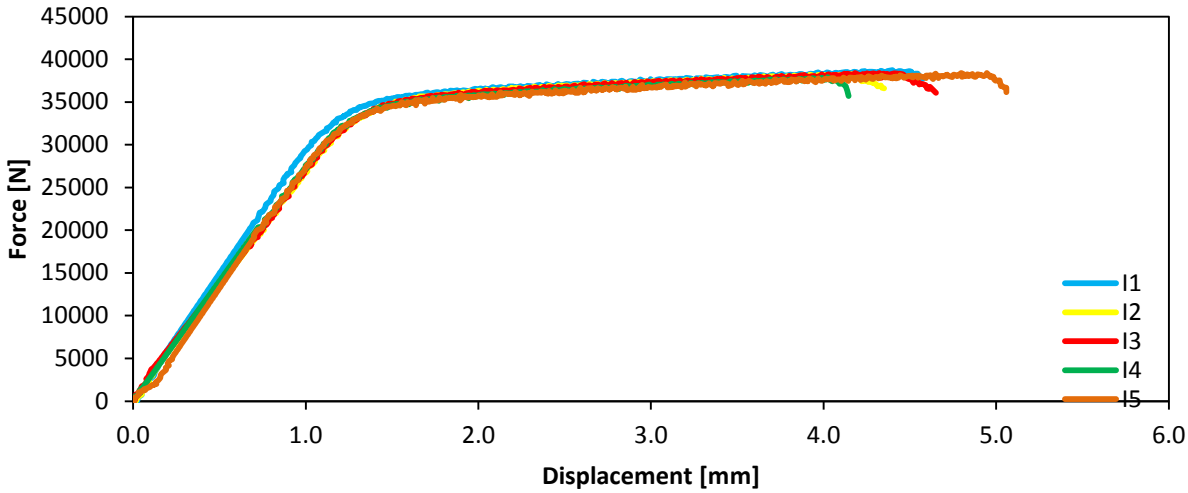

Figure 126: Load-displacement response for intermediate forced-air quench 0° butterfly test

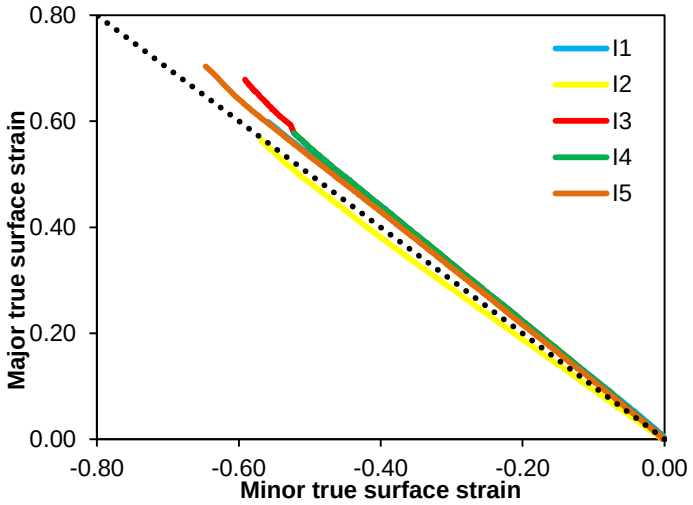

Figure 127: Major true surface strain vs. minor true surface strain for intermediate forced-air quench 0° butterfly test

Table 39: Failure strains for fully intermediate forced-air quench 0° butterfly test

Sample	1	2	3	4	5	Average	Std. Dev.
ε_1	0.60	0.56	0.59	0.58	0.70	**0.61**	**0.06**
ε_2	-0.56	-0.57	-0.53	-0.52	-0.65	**-0.56**	**0.05**
ε_{eq}	0.67	0.65	0.65	0.64	0.78	**0.68**	**0.06**

Appendix G Results For Mini Shear

400 °C Tailored Hot Stamped material quench condition

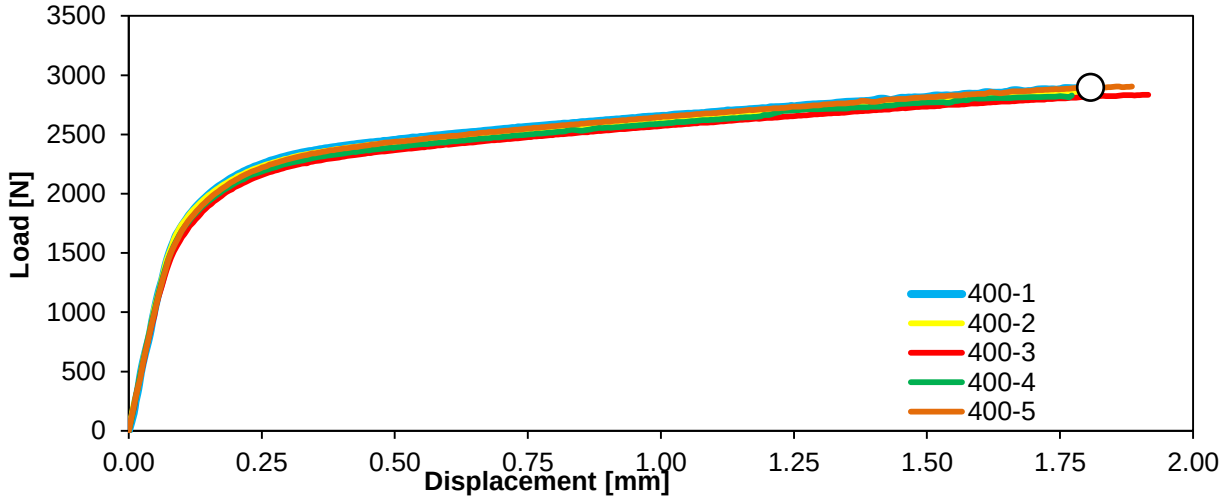

Figure 128: Load-displacement response for 400 °C quench mini shear test

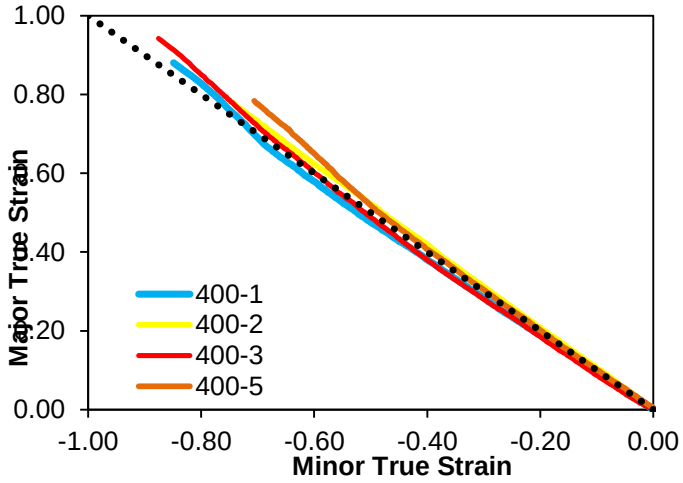

Figure 129: Major true surface strain vs. minor true surface strain for 400 °C quench mini shear

Table 40: Properties of 400 °C quench mini shear specimens

Sample	400-1	400-2	400-3	400-4	400-5	Average	Std. Dev.
Peak Load [N]	2896	2866	2834	2828	2904	**2866**	**34.6**
Elongation [mm]	1.81	1.80	1.92	1.77	1.89	**1.84**	**0.06**
ε_1	0.88	0.79	0.94		0.78	**0.85**	**0.08**
ε_2	-0.85	-0.75	-0.88		-0.71	**-0.80**	**0.08**
ε_{eq}	1.06	0.94	1.11		0.92	**1.01**	**0.09**

Appendix H Results For 10° Butterfly

Fully martensitic material quench condition

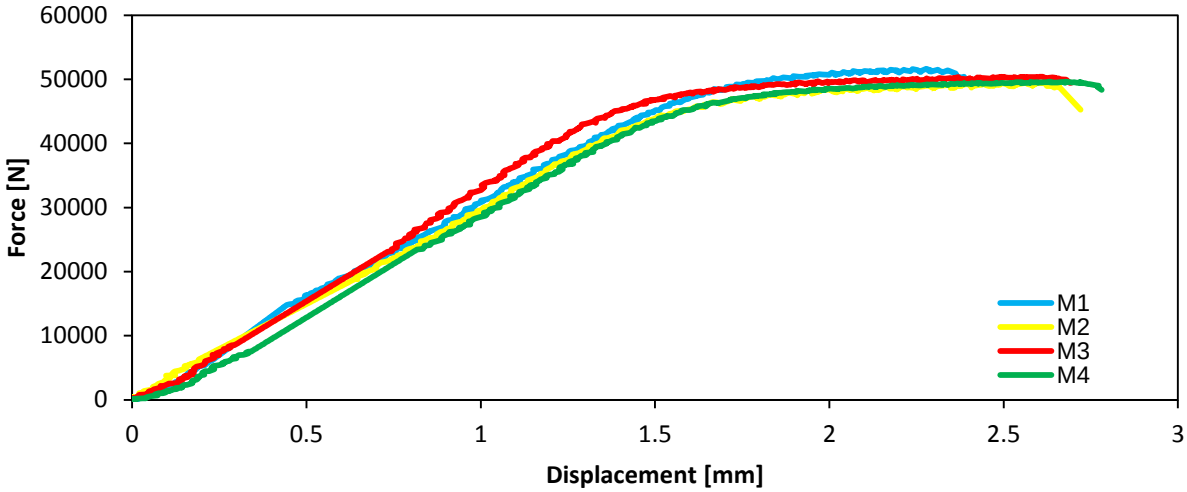

Figure 130: Load-displacement response for fully martensitic 10° butterfly test

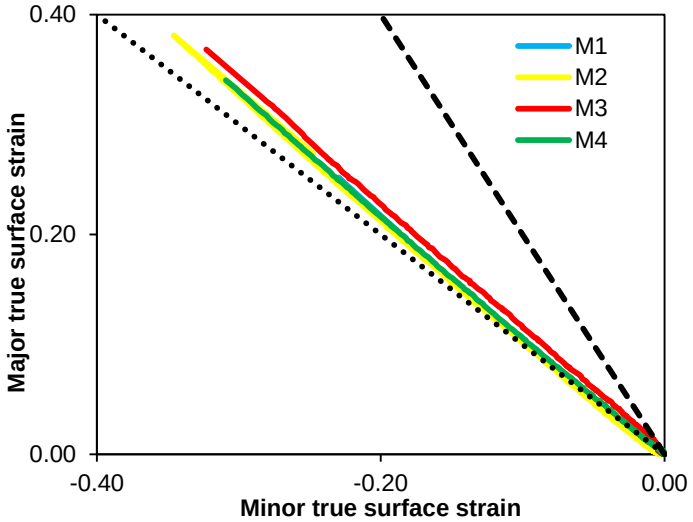

Figure 131: Major true surface strain vs. minor true surface strain for fully martensitic 10° butterfly test

Table 41: Failure strains for fully martensitic 10° butterfly test

Sample	1	2	3	4	Average	Standard Deviation
ε_1	0.25	0.37	0.38	0.34	**0.34**	**0.05**
ε_2	-0.23	-0.32	-0.35	-0.31	**-0.30**	**0.04**
ε_{eq}	0.41	0.60	0.56	0.52	**0.52**	**0.07**

Intermediate Forced Air Quench Material Condition

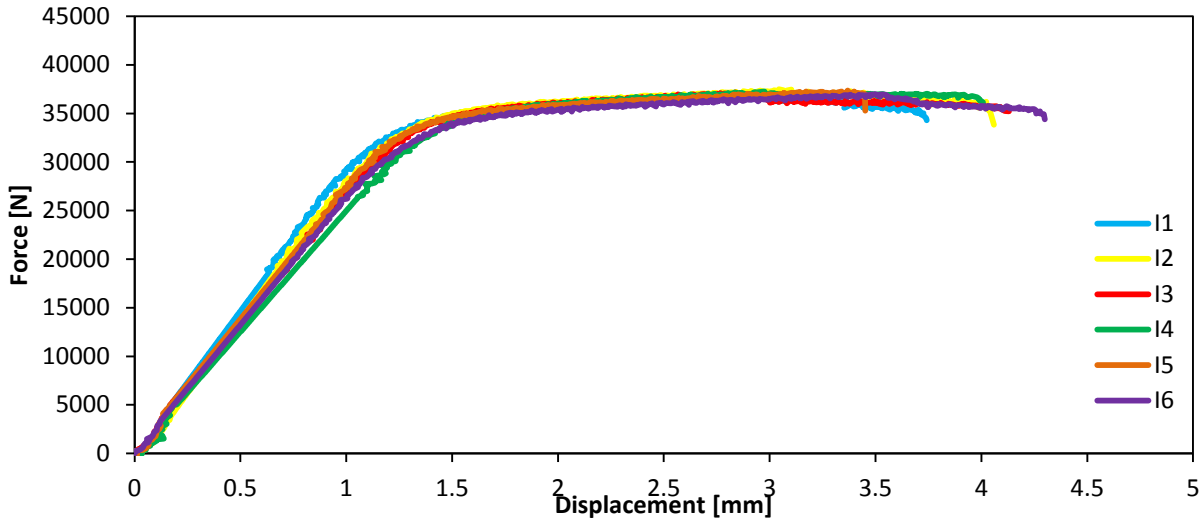

Figure 132: Load-displacement response for intermediate forced-air quench 10° butterfly test

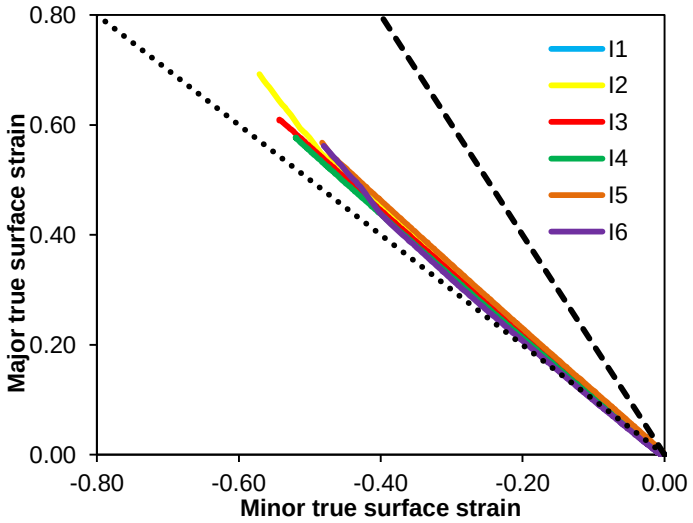

Figure 133: Major true surface strain vs. minor true surface strain for intermediate forced-air quench 10° butterfly test

Table 42: Failure strains for fully intermediate forced-air quench 10° butterfly test

Sample	1	2	3	4	5	6	Average	Standard Deviation
ε_1	0.53	0.69	0.61	0.58	0.57	0.56	**0.59**	**0.05**
ε_2	-0.48	-0.57	-0.54	-0.52	-0.48	-0.48	**-0.51**	**0.04**
ε_{eq}	0.58	0.74	0.67	0.64	0.61	0.61	**0.64**	**0.05**

Appendix I Results For 15° Butterfly

400 °C Tailored Hot Stamped material quench condition

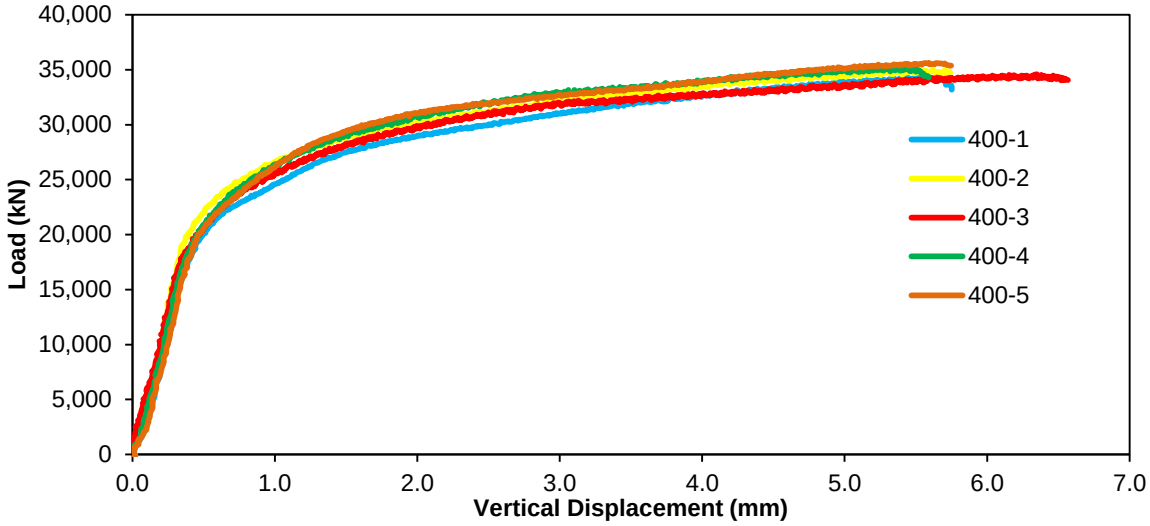

Figure 134: Load-displacement response for 400 °C quench 15° butterfly test

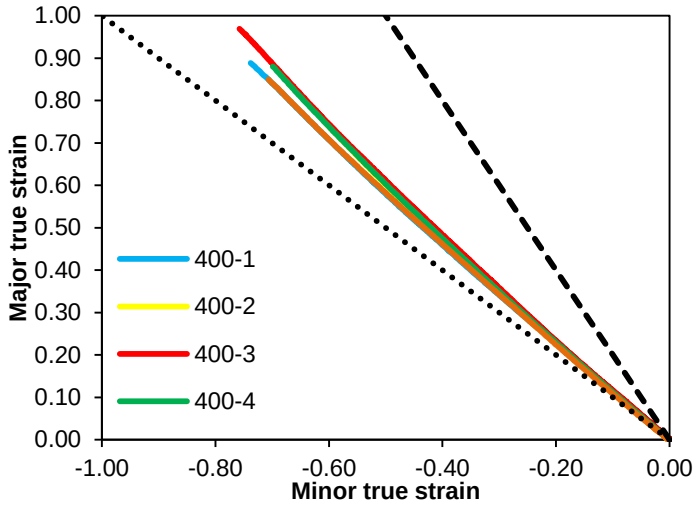

Figure 135: Major true surface strain vs. minor true surface strain for 400 °C quench 15° butterfly test

Table 43: Failure strains for the 400 °C quench 15° butterfly test

Sample	1	2	3	4	5	Average	Standard Deviation
ε_1	0.89	0.84	0.97	0.88	0.85	**0.89**	**0.05**
ε_2	-0.74	-0.67	-0.76	-0.70	-0.71	**-0.71**	**0.03**
ε_{eq}	0.95	0.89	1.02	0.93	0.91	**0.94**	**0.05**

Appendix J Results For 30° Butterfly specimens

Fully martensitic material quench condition

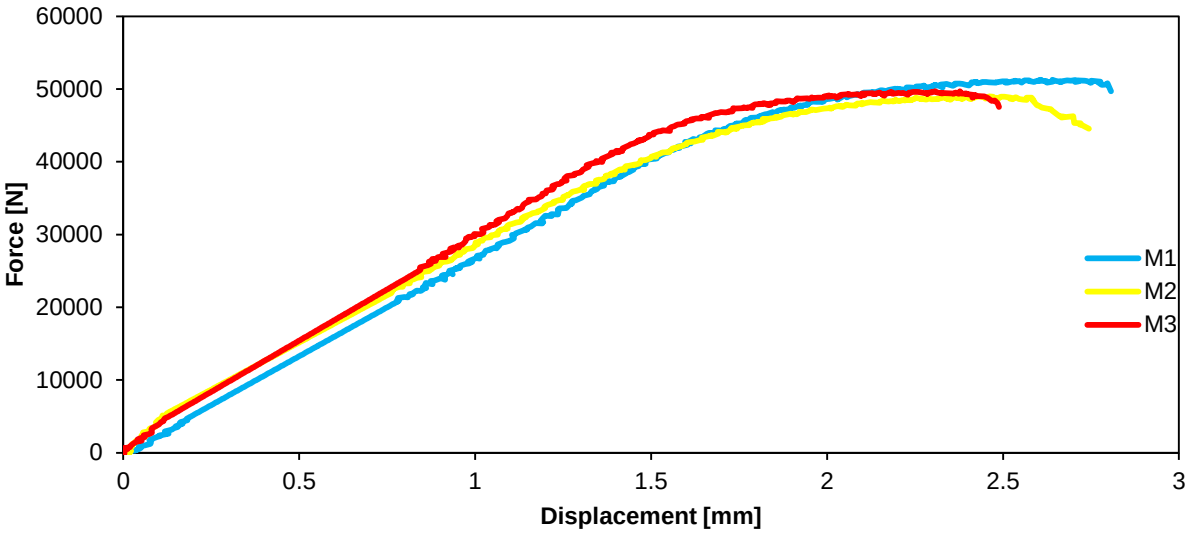

Figure 136: Load-displacement response full martensitic 30° butterfly test

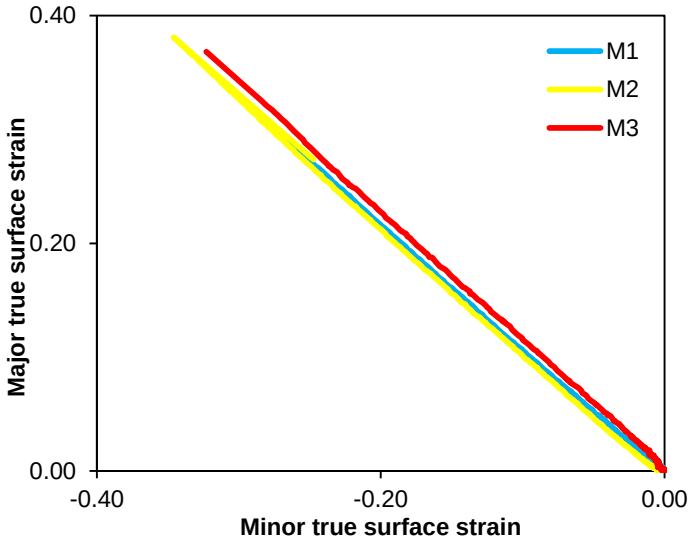

Figure 137: Major true surface strain vs. minor true surface strain for fully martensitic 30° butterfly test

Table 44: Failure strains for fully martensitic quench 30° butterfly test

Sample	1	2	3	Average
ε_1	0.33	0.30	0.32	**0.32**
ε_2	-0.26	-0.25	-0.24	**-0.25**
ε_{eq}	0.49	0.44	0.46	**0.46**

Intermediate forced-air material quench condition

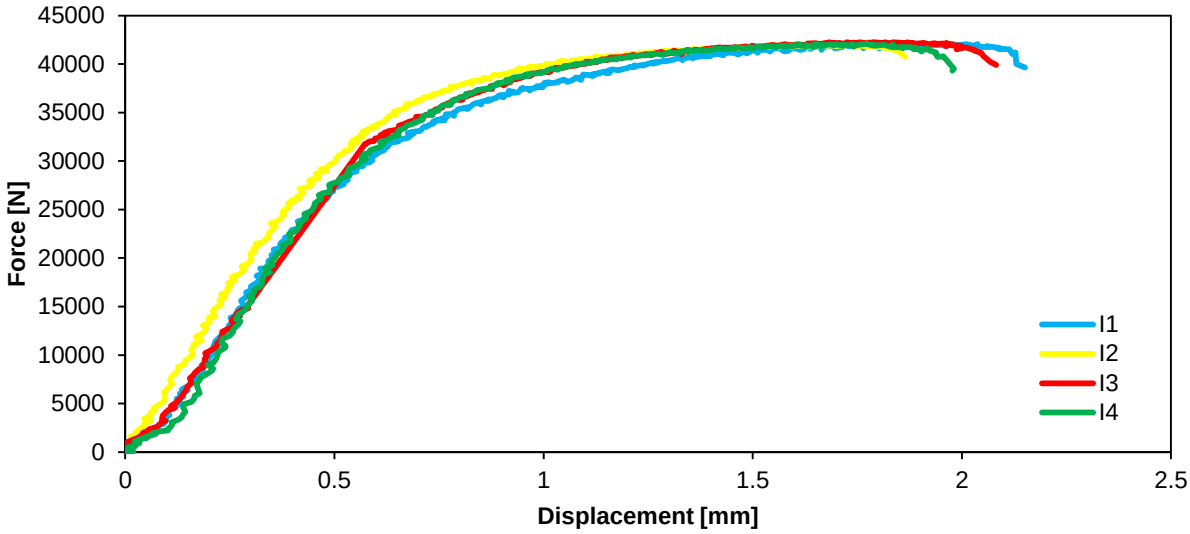

Figure 138: Load-displacement response for intermediate forced-air quench 30° butterfly test

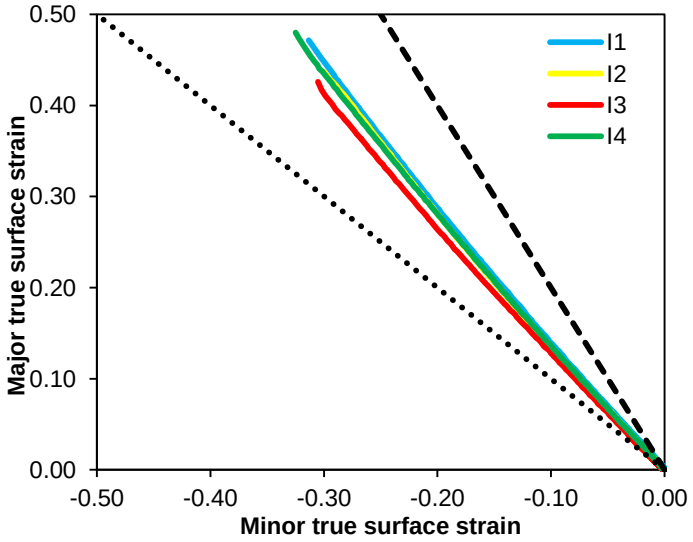

Figure 139: Major true surface strain vs. minor true surface strain for intermediate forced-air quench 30° butterfly test

Table 45: Failure strains for intermediate forced-air quench 30° butterfly test

Sample	1	2	3	4	Average	Standard Deviation
ε_1	0.47	0.44	0.43	0.48	**0.45**	**0.03**
ε_2	-0.31	-0.30	-0.31	-0.32	**-0.31**	**0.01**
ε_{eq}	0.48	0.45	0.44	0.49	**0.46**	**0.02**

Appendix K Results For Hole Expansion

Fully martensitic material quench condition

Table 46: Hole expansion results for fully martensitic material condition

Sample	1	2	3	4	5	6	7	8	Average	Std. Dev.
D_{final}	20.49	21.01	22.18	21.64	20.59	21.28	20.84	21.02	**21.13**	**0.56**
ε_{eq}	0.71	0.74	0.79	0.77	0.72	0.75	0.73	0.74	**0.74**	**0.03**

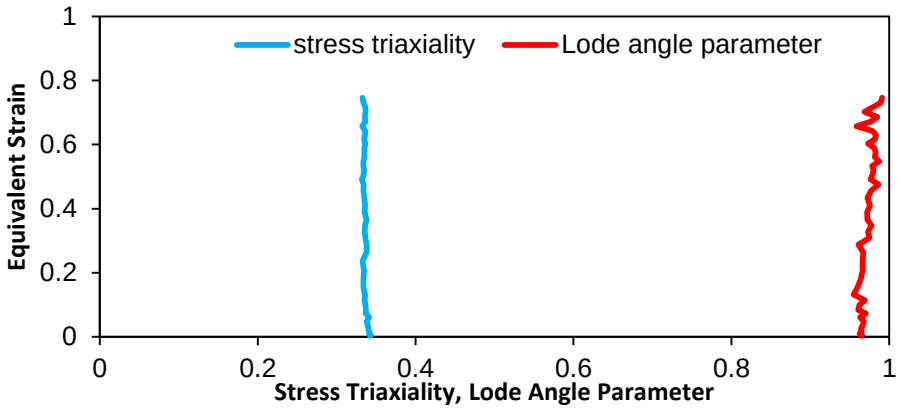

Figure 140: Evolution of stress triaxiality and Lode angle parameter at outer edge for fully martensitic hole expansion model

Intermediate forced-air material quench condition

Table 47: Hole expansion results for intermediate forced air quench material condition

Sample	1	2	3	4	5	6	7	8	Average	Std. Dev.
D_{final}	19.53	19.09	20.04	20.08	21.18	21.30	19.29	20.27	**20.10**	**0.81**
ε_{eq}	0.67	0.65	0.70	0.70	0.75	0.76	0.66	0.71	**0.70**	**0.04**

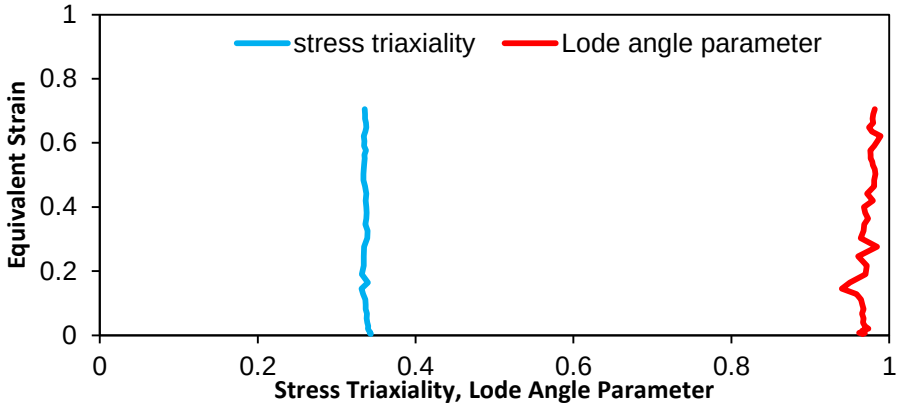

Figure 141: Evolution of stress triaxiality and Lode angle parameter at outer edge for intermediate forced air quench hole expansion model

Appendix L Results For Hole Tensile specimens

700 °C Tailored Hot Stamped material quench condition

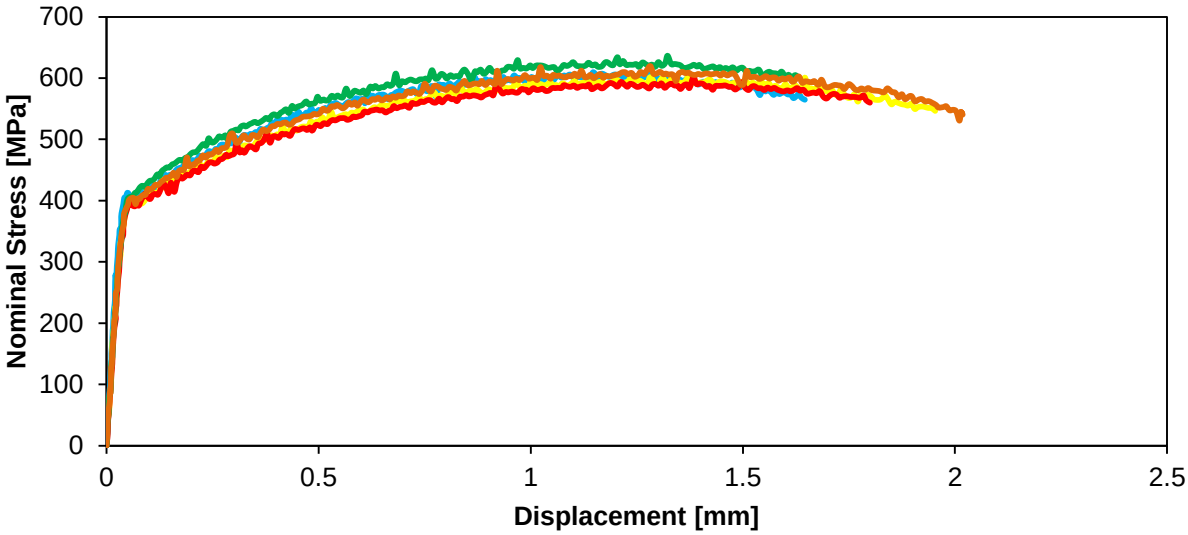

Figure 142: Nominal stress-displacement response for 700 °C quench hole tensile specimens

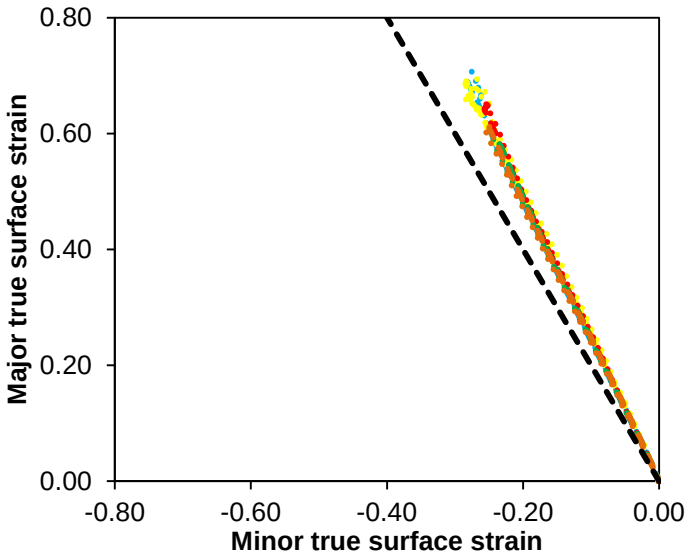

Figure 143: Major true surface strain vs. minor true surface strain for 700 °C quench hole tensile specimens

400 °C Tailored Hot Stamped material quench condition

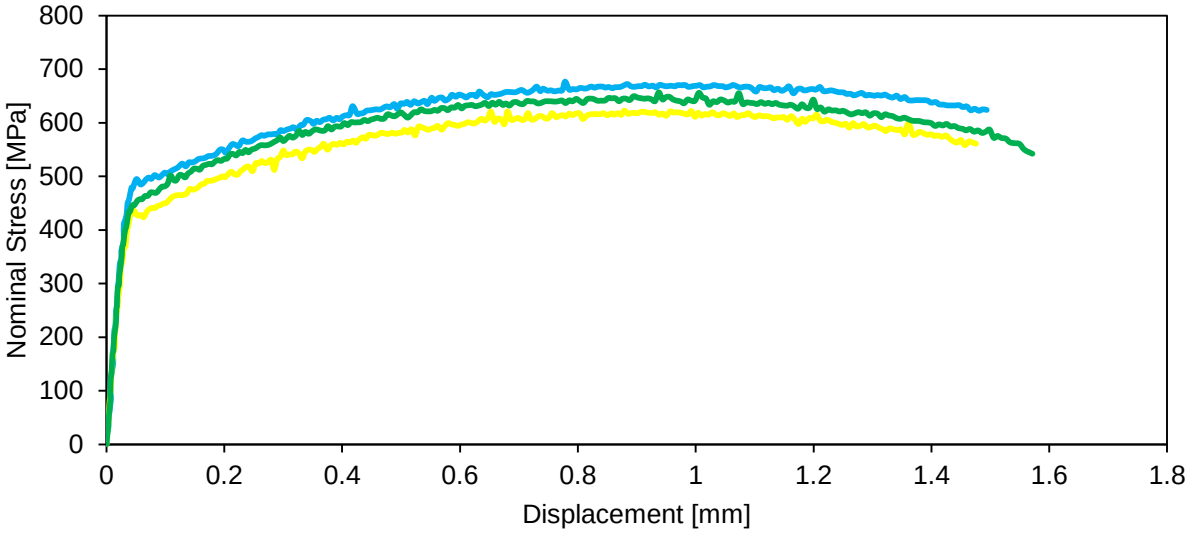

Figure 144: Nominal stress-displacement response for 400 °C quench hole tensile specimens

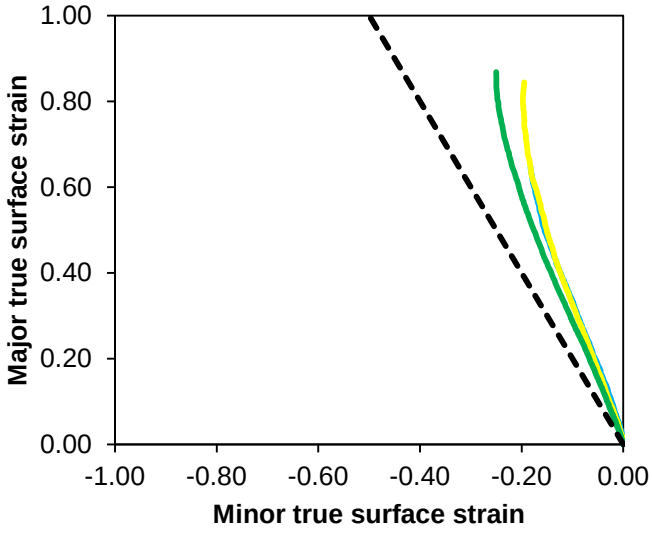

Figure 145: Major true surface strain vs. minor true surface strain for 400 °C quench hole tensile specimens

Appendix M Results For 90° Butterfly specimens

400 °C Tailored Hot Stamped material quench condition

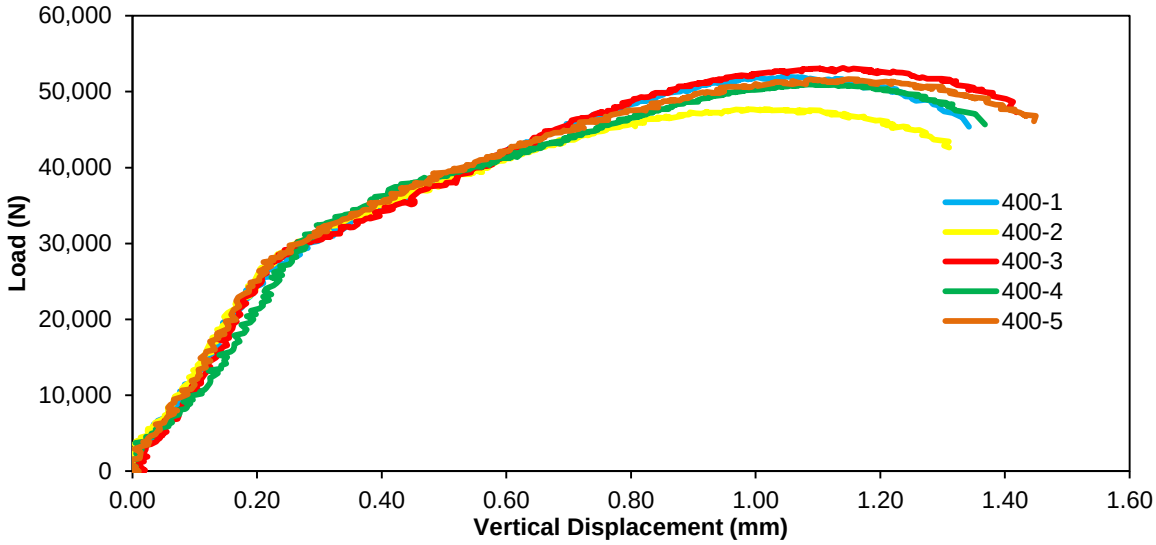

Figure 146: Load-displacement response for 400 °C quench 90° butterfly test

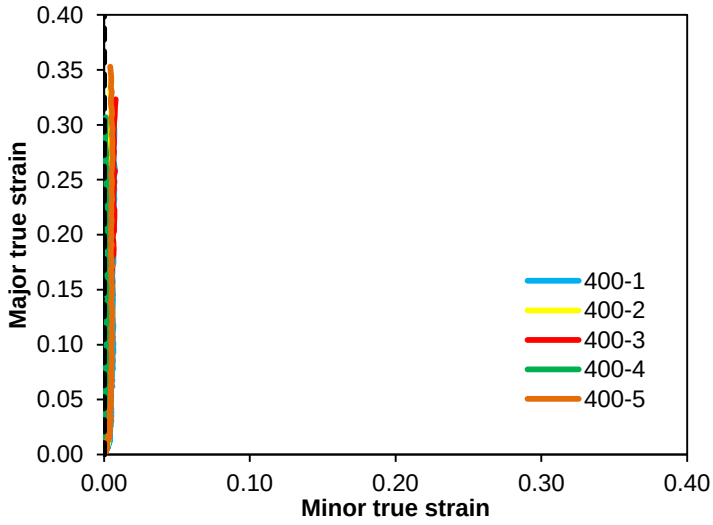

Figure 147: Major true surface strain vs. minor true surface strain for 400 °C quench 90° butterfly

Table 48: Failure strains for the 400 °C quench 90° butterfly test

Sample	1	2	3	4	5	Average	Standard Deviation
ε_1	0.32	0.34	0.32	0.31	0.35	**0.33**	**0.02**
ε_2	0.01	0.01	0.01	0.00	0.00	**0.01**	**0.00**
ε_{eq}	0.37	0.40	0.38	0.36	0.41	**0.38**	**0.02**

Appendix N Results For Plane Strain Dome

Fully martensitic material quench condition

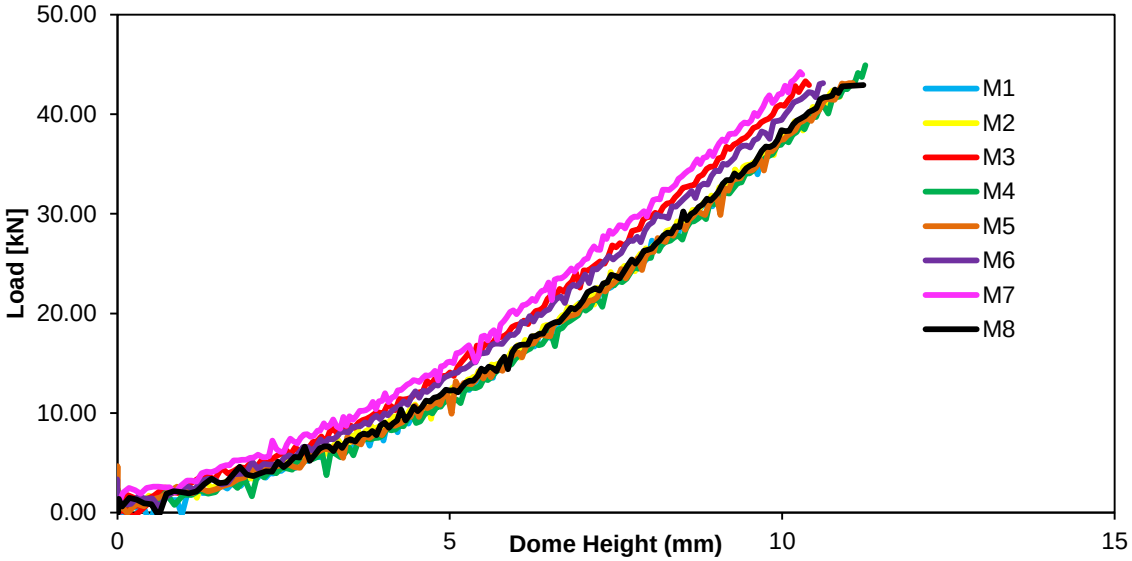

Figure 148: Punch load vs. dome height for fully martensitic plane strain dome test

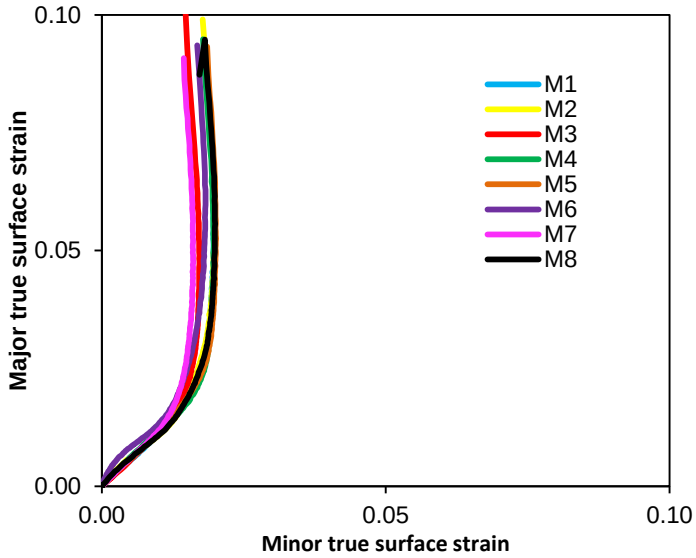

Figure 149: Major true surface strain vs. minor true surface strain for fully martensitic plane strain dome test

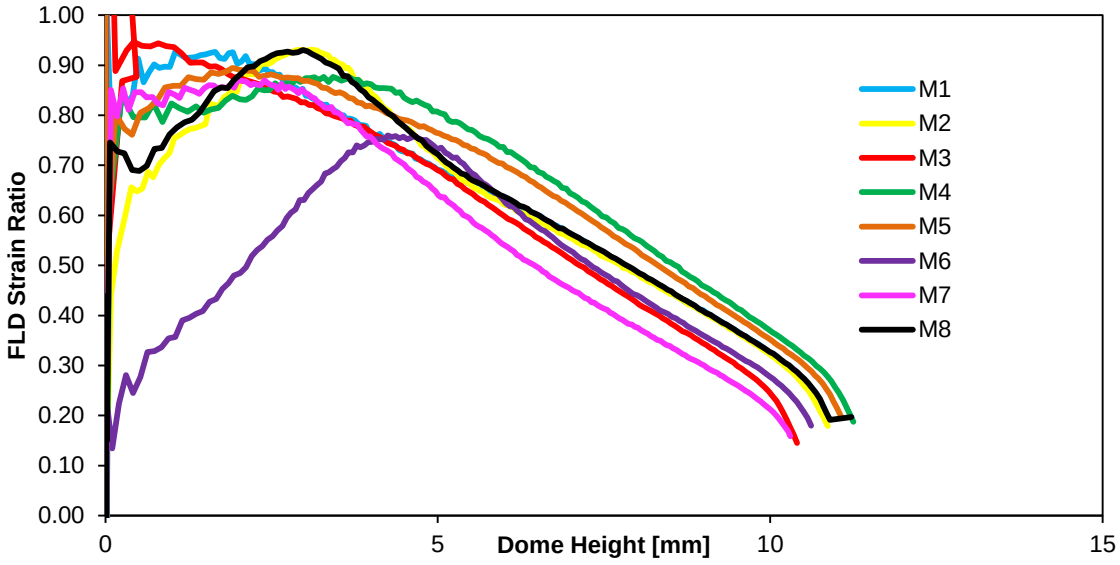

Figure 150: Minor true surface strain/major true surface strain vs. dome height for fully martensitic plane strain dome test

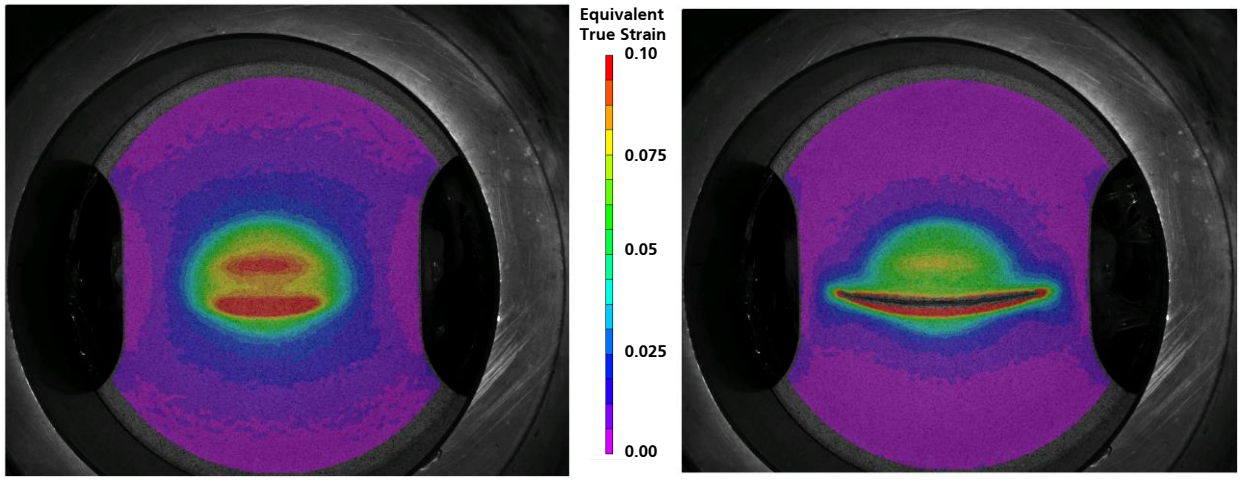

Figure 151: Equivalent strain contour showing typical fracture location for fully martensitic plane strain dome test. The contour plot on the left corresponds to the image 1 frame before fracture is observed

Table 49: Failure strains for fully martensitic plane strain dome test

Sample	1	2	3	4	5	6	7	8	Average	Standard Deviation
ε_1	0.08	0.09	0.08	0.08	0.07	0.09	0.08	0.09	**0.08**	**0.01**
ε_2	0.02	0.02	0.01	0.02	0.02	0.02	0.01	0.02	**0.02**	**0.00**
$\varepsilon_2/\varepsilon_1$	0.20	0.20	0.18	0.19	0.24	0.19	0.16	0.20	**0.19**	**0.02**
ε_{eq}	0.14	0.15	0.17	0.14	0.15	0.13	0.13	0.13	**0.15**	**0.01**

Intermediate forced-air material quench condition

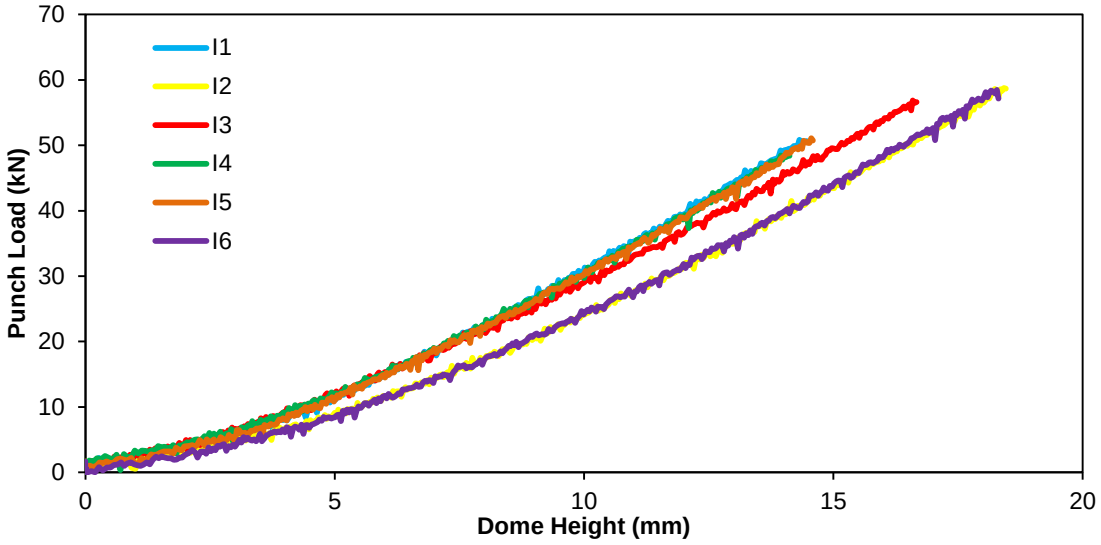

Figure 152: Punch load vs. dome height for intermediate forced air quench plane strain dome test

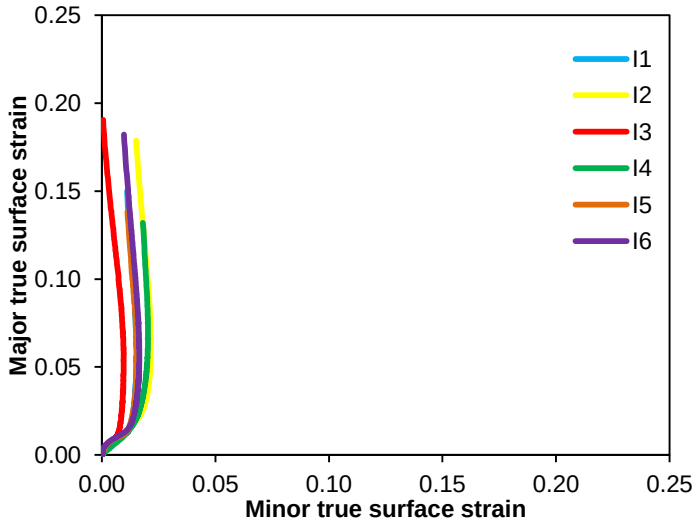

Figure 153: Major true surface strain vs. minor true surface strain for intermediate forced air quench plane strain dome test

Table 50: Failure strains for intermediate forced air quench plane strain dome test

Sample	1	2	3	4	5	6	Average	Standard Deviation
ε_1	0.14	0.16	0.17	0.12	0.12	0.18	**0.15**	**0.04**
ε_2	0.01	0.02	0.00	0.02	0.01	0.01	**0.01**	**0.01**
$\varepsilon_2/\varepsilon_1$	0.07	0.10	0.01	0.14	0.09	0.06	**0.08**	**0.06**
ε_{eq}	0.21	0.25	0.26	0.20	0.20	0.24	**0.22**	**0.04**

Appendix O Results for Equi-biaxial Dome

Fully martensitic material quench condition

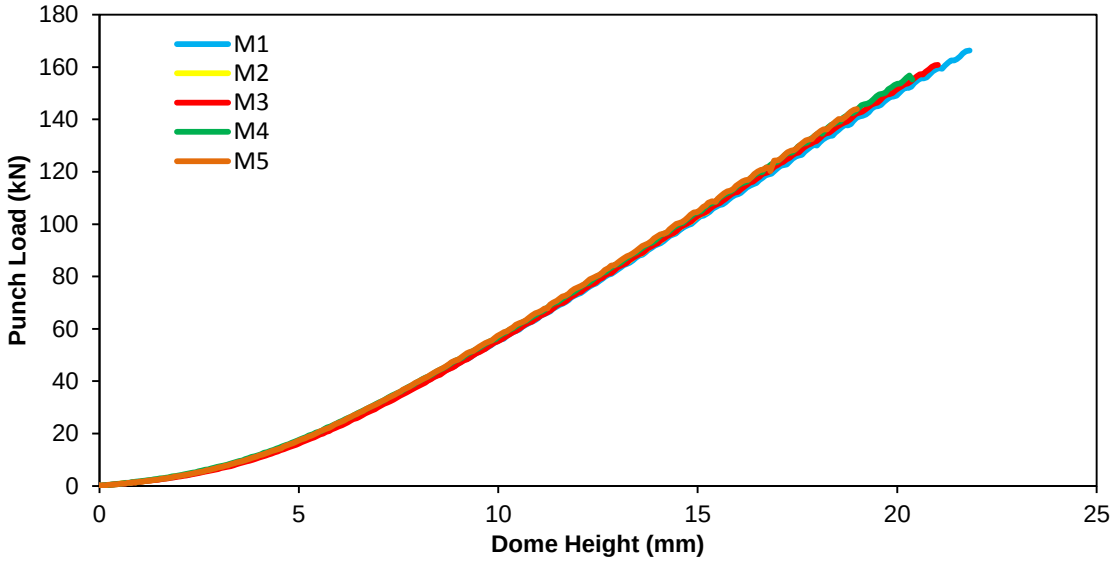

Figure 154: Punch load vs. dome height for fully martensitic equi-biaxial dome test

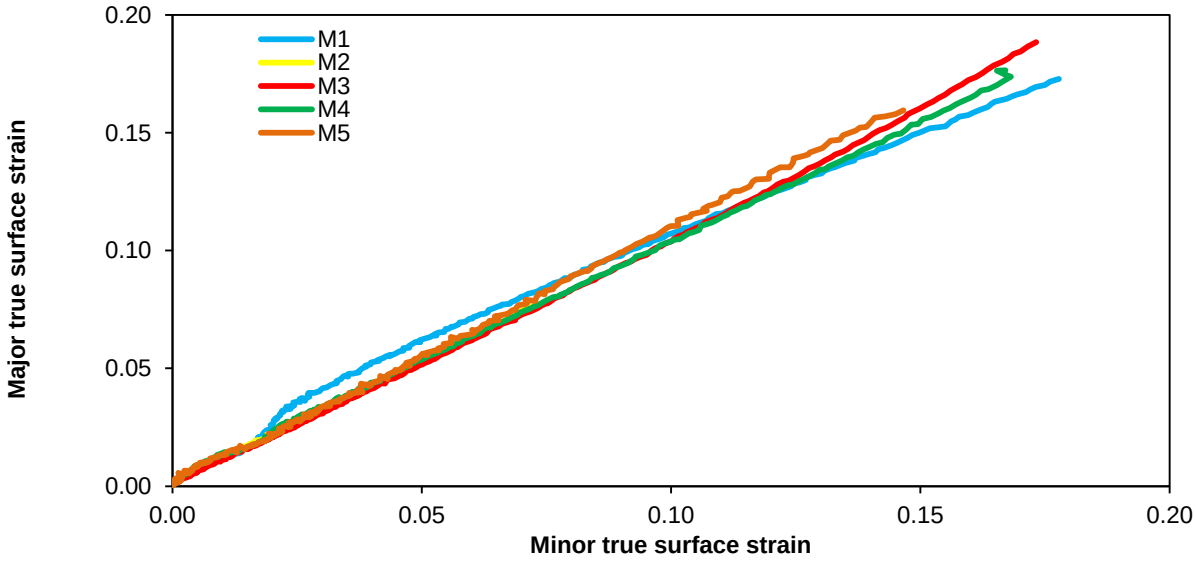

Figure 155: Major true surface strain vs. minor true surface strain for fully martensitic equi-biaxial dome test

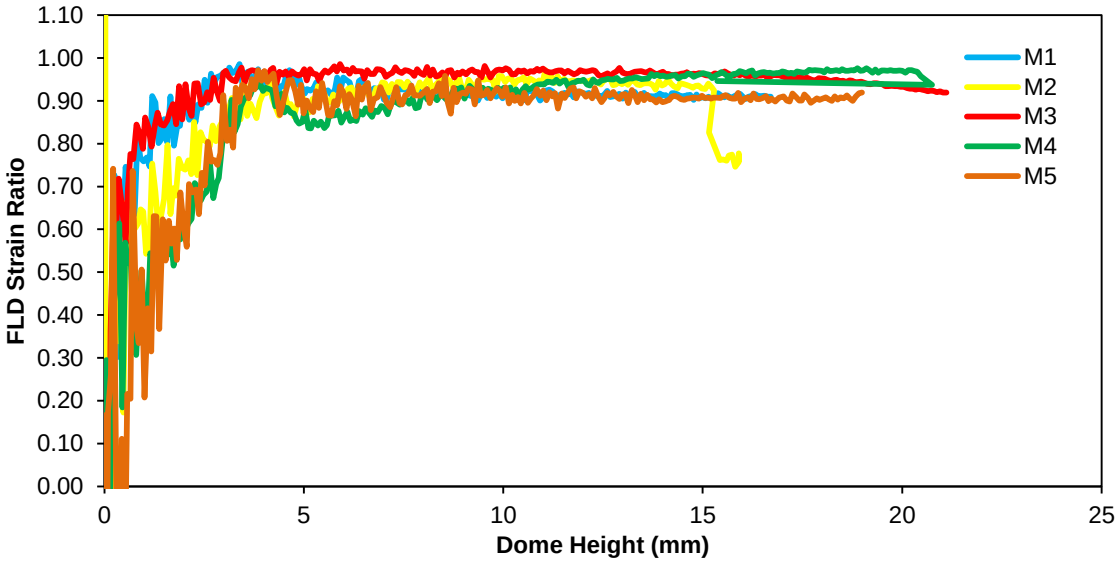

Figure 156: Minor true surface strain/major true surface strain vs. dome height for fully martensitic equi-biaxial dome test

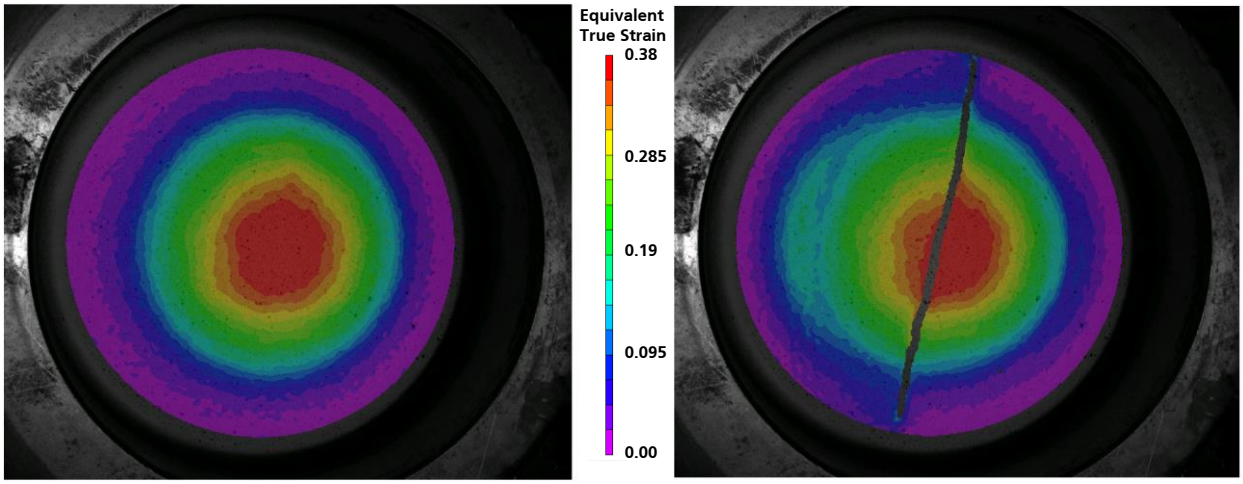

Figure 157: Equivalent strain contour showing typical fracture location for fully martensitic equi-biaxial dome test. The contour plot on the left corresponds to the image 1 frame before fracture is observed

Table 51: Failure strains for fully martensitic equi-biaxial dome test

Sample	1	3	4	5	Average	Standard Deviation
ε_1	0.20	0.19	0.17	0.16	**0.18**	**0.02**
ε_2	0.18	0.17	0.17	0.15	**0.17**	**0.01**
$\varepsilon_2/\varepsilon_1$	0.90	0.92	0.97	0.92	**0.93**	**0.03**
ε_{eq}	0.38	0.36	0.34	0.31	**0.35**	**0.03**

Intermediate forced-air material quench condition

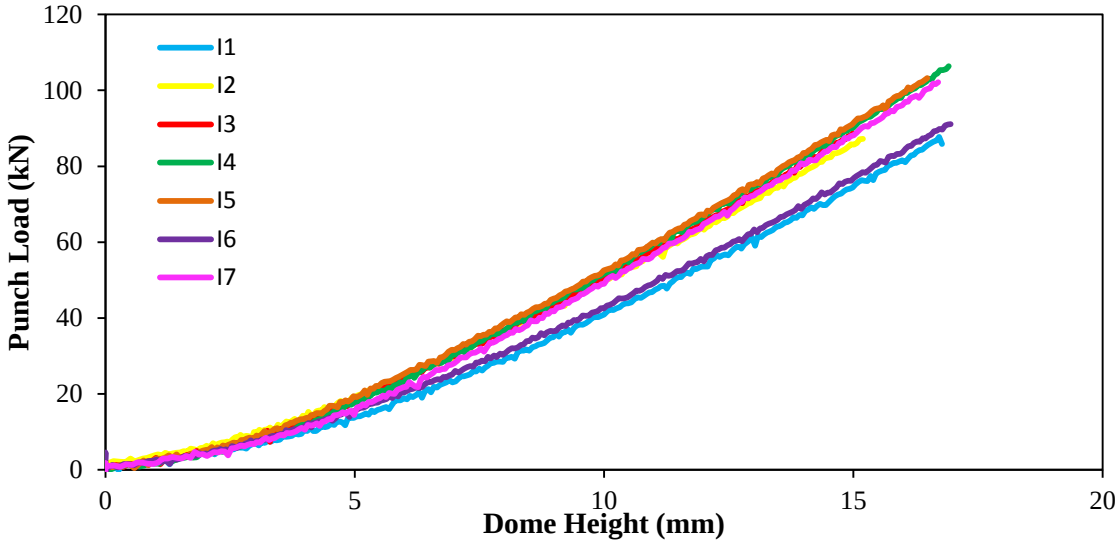

Figure 158: Punch load vs. dome height for intermediate forced air quench equi-biaxial dome test

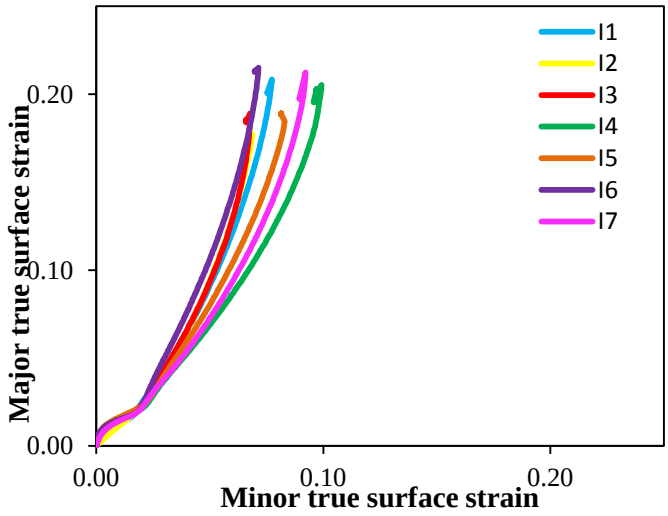

Figure 159: Major true surface strain vs. minor true surface strain for intermediate forced air quench equi-biaxial dome test

Table 52: Failure strains for intermediate forced air quench equi-biaxial dome test

Sample	1	2	3	4	5	6	7	Average	Standard Deviation
ε_1	0.20	0.17	0.18	0.20	0.19	0.21	0.20	**0.19**	**0.01**
ε_2	0.08	0.07	0.07	0.10	0.08	0.07	0.09	**0.8**	**0.01**
$\varepsilon_2/\varepsilon_1$	0.37	0.40	0.36	0.48	0.43	0.33	0.45	**0.40**	**0.05**
ε_{eq}	0.31	0.27	0.28	0.32	0.28	0.31	0.34	**0.30**	**0.02**

Appendix P FA-Q2 Microhardness Calibration

Since [7] used microhardness as the metric to uniquely define microstructure, this practice was the de-facto standard adopted for most of the work in this project. For calibration of the FA-Q2, the microstructure of the quenched material was measured to characterize it. Due to the multitude of blank sizes required for the different specimens used in this work, in order to ensure a consistent microstructure was produced for each, the distance from the nozzle to the blank and the pressure of the air flow were the only two parameters to vary. To maintain microstructural consistency with the intermediate forced air quench tensile specimens, which were the first blanks produced using the FA-Q2, the nozzle distance and air pressure were adjusted for the production of subsequent blanks until satisfactory results were obtained. As a more direct measurement, measurement of the cooling response for different combinations of blank size, nozzle distance, and air pressure was initially considered and attempted. Unfortunately, issues of thermocouple durability and questions regarding the use of the same blank for repeated thermal cycles limited the implementation of this approach. The 8” x 8” blanks that were used for plane strain and equi-biaxial dome specimens presented the greatest challenge in terms of obtaining a consistent microhardness in the quenched blanks. The locations in which microhardness was measured are indicated by the red rectangles in Figure 160. Microhardness measurements for different air pressures are included in Table 53.

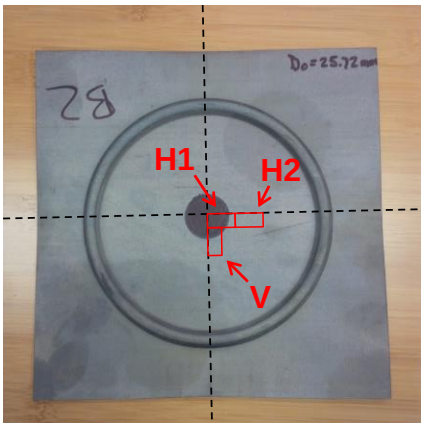

Figure 160: Microhardness measurement locations for 8” x 8” blank

Table 53: Microhardness for intermediate forced-air quench 8” x 8” specimens. 7.1 psi setting was used for production of specimens

Pressure (psi)-Sample	Location	1	2	3	4	5
7.0-1	**H1**	403	388	392	380	374
	H2	395	395	386	389	390
	V	357	361	376	366	
7.0-2	**H1**	393	409	407	384	304
	H2	400	410	381	376	378
	V	397	390	380	371	
7.1-1	**H1**	373	372	378	384	413
	H2	410	407	415	388	427
	V	378	393	393	395	
7.1-2	**H1**	364	380	418	425	412
	H2	413	425	419	416	413
	V	404	393	415	419	
7.5-1	**H1**	404	395	404	395	415
	H2	410	412	410	418	416
	V	397	396	389	389	
7.5-2	**H1**	384	386	395	415	410
	H2	412	409	415	413	409
	V	395	418	402	396	
8.0-1	**H1**	396	393	390	389	386
	H2	399	406	409	415	406
	V	403	419	412	409	
8.0-2	**H1**	418	418	429	409	407
	H2	415	407	402	418	419
	V	404	390	382	395	

Appendix Q Fracture Loci

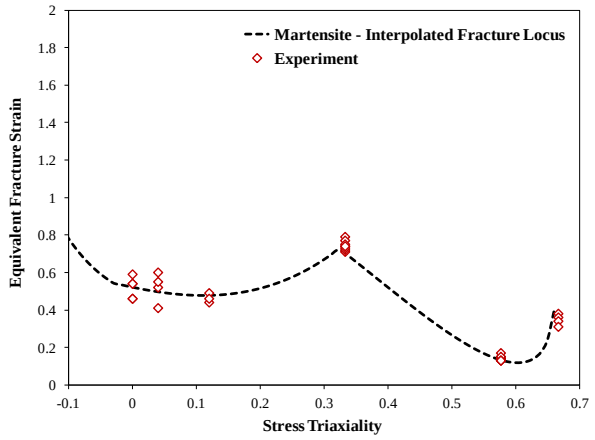

Figure 161: Fracture locus for fully martensitic material condition

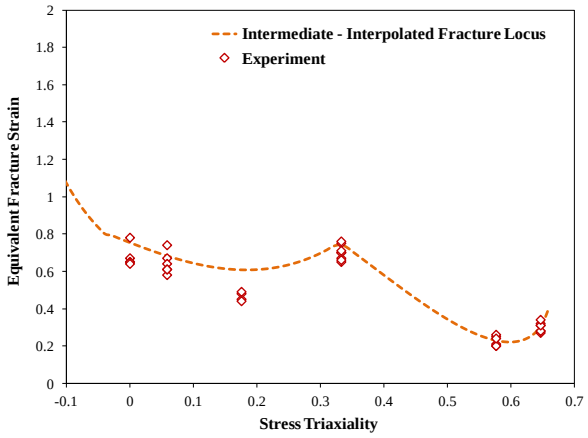

Figure 162: Fracture locus for intermediate forced air quench material condition

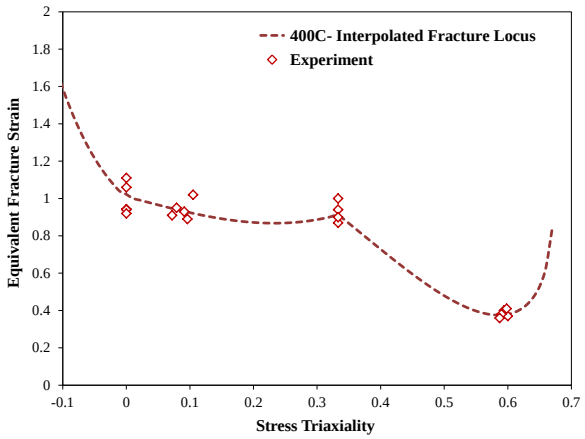

Figure 163: Fracture locus for 400 °C die quench hot stamped material condition

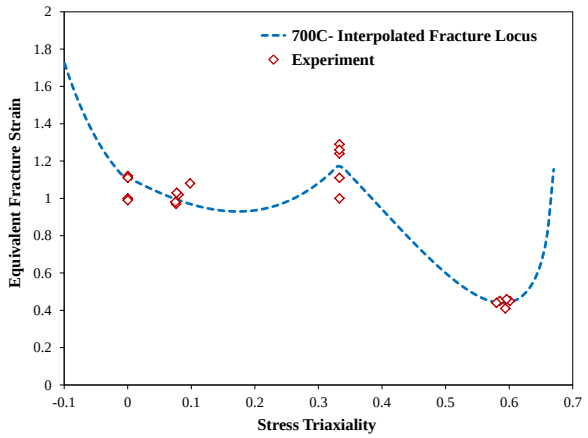

Figure 164: Fracture locus for 700 °C die quench hot stamped material condition

Appendix R Additional Shell Models

<u>Meshes with lock bead:</u> equi-biaxial (0.6 mm), plane strain (0.6 mm), plane strain (1.25 mm)

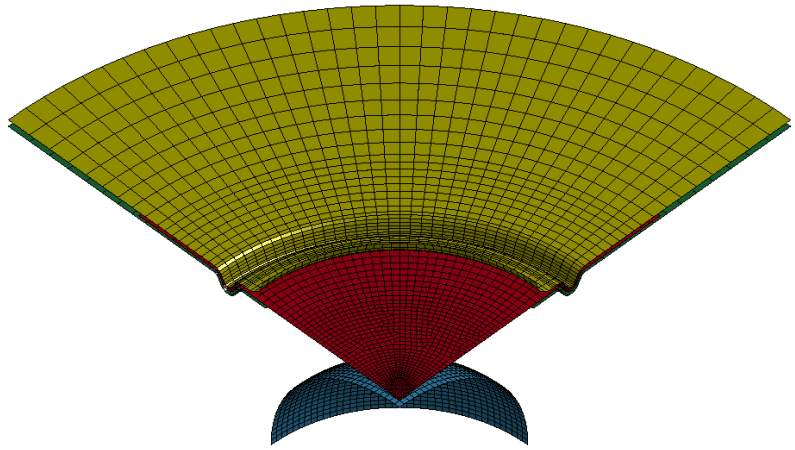

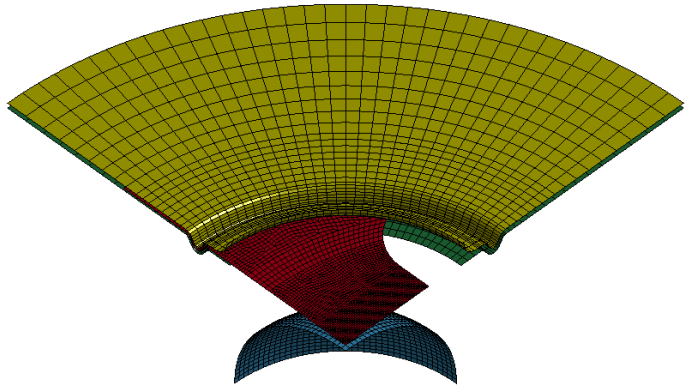

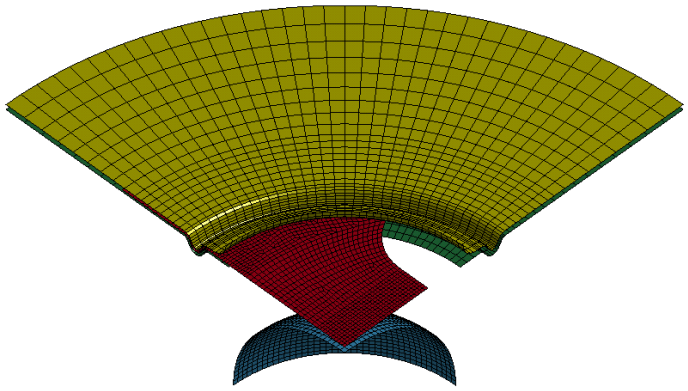

<u>Plane strain regularization meshes:</u> 1.25 mm, 2.5 mm, and 5.0 mm